Chemically programming redox-active nanovaccines and theranostic nanoparticles for combination cancer immunotherapy

Marc Bilbao Asensio

Submitted to Swansea University in fulfilment of the requirements for the Degree of Doctor of Philosophy

Swansea University
Prifysgol Abertawe

2021

Summary

Cancer immunotherapies have established their relevance in the clinic in recent years. These therapies have increased patient survival rates with few toxic side-effects. However, they still suffer from low patient response rates. With the progression of the disease, tumors become increasingly heterogeneous, which poses limits to the development of universal, “off the shelf” cures. Nanotechnology allows insight over novel therapy strategies to better suit the specificities and uniqueness of each patient’s cancer.

In this work, a chemistry and material science approach enabled the development of iron oxide nanoparticle-filled nanovaccines (IONVs) to exploit the biochemical features of the tumor microenvironment for cancer immunotherapy and combination therapy. A systematic nanoparticle engineering rationale is stablished to “programme” IONVs for: (i) cancer cell sensitization to oxidative damage and ferroptosis; (ii) pH-catalysed disassembly and drug release; (iii) macrophage repolarization towards tumor-suppressing phenotypes; (iv) optimization of tumor-antigen processing and cross-presentation; (v) optimization of platinum-based prodrug delivery for chemotherapy and chemoimmunotherapy; (vi) integration of directing ligands for active targeted drug delivery; (vii) monitorable therapy biodistribution; and (viii) synergy with state-of-the-art antibody-based immunotherapies.

Systematic IONV engineering provided control over distinguishable device properties such as size, charge, stability, chemical reactivity, bioactive molecule loading and particle surface functionalization. The device integrated iron catalysis for cancer-cell specific activation of ferroptosis, immunostimulatory redox stress and site-specific disassembly for targeted drug release. IONVs were visualized to accumulate into the tumor tissue as well as immune cell-rich tissues such as spleen and lymph nodes. Their high biocompatibility enabled immune cell activation for multipronged antitumor action. The results show how IONVs can unite and improve concurrently effective anticancer strategies, resulting in complete elimination of established aggressive tumors and acquisition of protective long-term immunity. Overall, this work demonstrates the suitability of programmable IONVs to act as generalizable platforms for cancer immunotherapy enhancement.

Declarations and statements

Declarations

This work has not previously been accepted in substance for any degree and is not being concurrently submitted in candidature for any degree.

Signed... [redacted] MARC BILBAO ASCENSO

Date..... 13.12.21

This thesis is the result of my own investigations, except where otherwise stated. Other sources are acknowledged by footnotes giving explicit references. A bibliography is appended.

Signed..... [redacted] MARC BILBAO ASCENSO

Date..... 13.12.21

I hereby give my consent for my work, if relevant and accepted, to be available for photocopying and for inter-library loans **after expiry of a bar on access approved by the University.**

Signed..... [redacted] MARC BILBAO ASCENSO

Date..... 13.12.21

The University's ethical procedures have been followed and, where appropriate, that ethical approval has been granted.

Signed..... [redacted] MARC BILBAO ASCENSO

Date..... 13.12.21

Table of Contents

Table of Figures

List of Tables

Acknowledgements

First of all, I would like to thank my supervisor Prof. Juan Mareque-Rivas for giving me the opportunity to join and complete this PhD. His guidance, dedication and advice allowed me to grow both professionally and personally, specially through these exceptional last two years. What I learned I will carry for the rest of my career. I would also like to thank my second supervisor, Dr. Mariolino Carta, for his support and encouragement.

I would like to thank Dr. James Cronin for his kindness and assistance. James remained always open and willing to offer his help and advice, and that is something that is sincerely appreciated. I would also like express my gratitude to Dr. Nick Jones, Dr. Stephen Evans, Dr. Rachel Lawrence, Dr. Martin Clift and Prof. Cathy Thornton, as well as to each of their group members and colleagues, for the support that was extended to me during the entirety of this work. Similarly, I would like to thank Dr. Ane Ruiz the Angulo who, perhaps unknowingly, has been of reference to me during my entire PhD. Finally, I would also like to express my gratitude for all the work done by Dr. Jordi Llop's group and all the people in CIC biomaGUNE.

This work would not have been possible without the help from the university staff in Grove Extension building, CNH and ILS1, who welcomed and advized me in every step of the way.

Finally, on a more personal note, I would like to express my most sincere gratitude to the friends I have made throughout these years. Primero, a Saul, como veteranos del departamento que somos, ha sido un placer compartir contigo estos años tanto dentro como fuera del laboratorio. To Joel, our first master's student and then PhD candidate, I wish you all the best for the rest of your PhD and carreer. A Chiara, for your warmth and our friendship that I value so much. To Kadie, Michael, Edward, Natasha, Arianna, to the many that came most recently, Denise, John, Natalia, Ben, to the friends that came and went, Max and Wei, and to the many I shared my livelihood with, Robin, Astrid, Ahsan, Shu, you are all amazing people and I wish you the very best.

A la Martina, for the wonderful time we have spent and the many more things to happen.

A la meva mare, al meu pare, al meu germà i a la meva germana, per tot.

List of Abbreviations

APC	Antigen presentinc cell
BCA	Bicinchoninic acid
BSA	Bovine serum albumin
CTLA-4	Cytotoxic T-cell-associated antigen-4
DAMP	Damage-associated molecular pattern
DC	Dendritic cell
DLS	Dynamic Light Scattering
DOTAP / TAP	1,2-dipalmitoyl-3-trimethylammonium-propane
EDTA	Ethylenediamine-tetraacetate
ELISA	Enzyme-linked immunosorvent assay
FBS	Fetal bobine serum
HRP	Horseradish peroxidase
ICB	Immune checkpoint blockade
ICD	Immunogenic cell death
ICP-AES	Inductively coupled plasma atomic emission spectroscopy
IFN	Interferon
IL	Interleukin
iNOS	Inducible nitric oxide synthase
IONP	Iron oxide nanoparticle
IONV	Iron oxide-based nanovaccine
LN	Lymph node
MDSC	Myeloid-derived suppressor cells
MHC	Major histocompatibility complex
MHT	Magnetic hyperthermia therapy
mIONP	Iron oxide nanoparticle-filled micele
MRI	Magnetic resonance imaging
NP	Nanoparticle
OPD	Ortho-phenylenediamine
OVA	Ovalbumin
PAMP	Pathogen-associated molecular pattern
PBS	Phosphate buffer saline
PD-1	Programmed cell death type 1
PD-L1	Programmed cell death ligand type 1
PDI	Polydispersity index
PET	Positron Emission Tomography
PEG	Polyethylene glycol
PEG-PL	Polyethylene glycol phospholipid
Poly (I:C) / pIC	Polyinosinic:polycytidylic acid

PRR	Pattern-recognition receptors
PUFA	Poly unsaturated fatty acid
ROS	Reactive oxygen species
SPECT	photon emission computerized tomography-
SPION	Superparamagnetic iron oxide nanoparticle
TAA	Tumor-associated antigen
TAM	Tumor-associated macrophage
TCR	T-cell receptor
TDLN	Tumor-draining lymph node
TEM	Transmission Electron Microscopy
TGF	Tumor growth factor
TLR	Toll-like receptor
TLRa	Toll-like receptor agonist
TMB	3,3′,5,5′-tetramethylbenzidine
TME	Tumor microenvironment
TNF	Tumor necrosis factor
Treg	Regulatory T-cell
TSA	Tumor-specific antigen
XPS	X-ray photoelectron spectroscopy

Chapter 1 :

Current Understanding and Challenges in Cancer Immunotherapy

1.1. Overview

Cancer is the term for diseases in which abnormal cells divide without control and invade nearby tissues. Cancer is characterized by cells that, upon the accumulation of a set of mutations, start growing without restrain. Their uncontrolled growth leads to the formation of chaotic clumps of tissue, the tumors. At advanced stages of disease, cancer cells can migrate around the organism forming new tumors and propagate the disease – a process called metastasis. If untreated, tumor growth will eventually press against tissue, blood vessels and nerves, and induce life-threatening organ failure.

Cancer ranks as the first or second leading cause of death before the age of 70 years in most countries (Fig 1.1, a) [1]. It is predicted that one in every 5 people will develop cancer during their lifetime, and that one out of 8 men and one out of 11 women will die from the disease. Breast, lung and colorectum cancers were estimated to be the most diagnosticated cancers in 2020 worldwide. Lung, colorectum and liver cancers accumulated the highest mortal rates (Fig. 1.1, b).

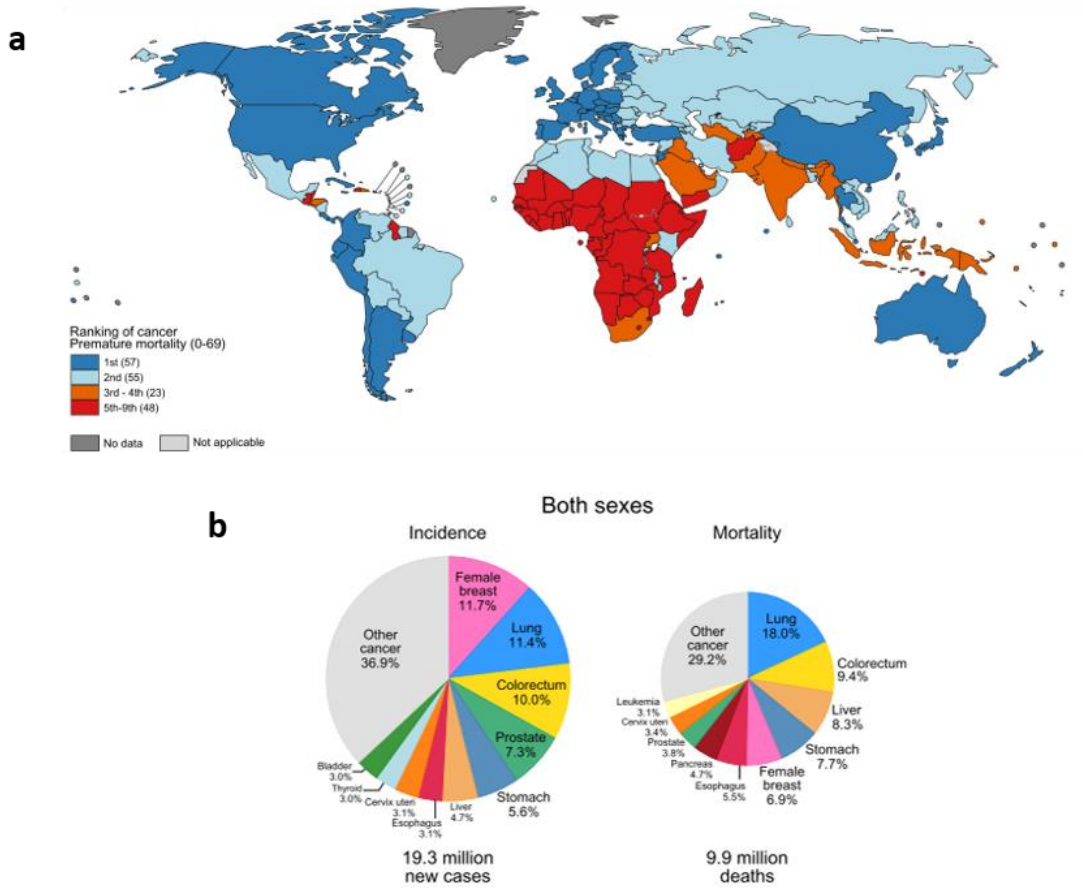

Figure 1.1. Cancer as a cause of death in 2020. *(a) Ranking of cancer as a cause of death per country for ages <70 years. (b) incidence and mortality per type of cancer for both sexes. Image taken from* [1].

There has been a long pressing medical need for the development of effective and safe cancer therapies. Classically, cancer therapies have been based on the administration of powerful cytotoxic chemical agents (cancer chemotherapies). Indeed, many of these therapies still serve today as the first front in anticancer treatments. However, the well-known side-effects of chemotherapy have a negative impact on the well-being of cancer patients and limit the therapeutic doses that can be administered, which in many cases compromizes the ability to successfully treat cancer patients [2–4].

In the last decade, cancer immune-based therapies (immunotherapies) gathered increasing interest. Instead of directly killing the cancer cells, immunotherapies aim to train or enable the immune system to combat the tumor. On their own, these new therapies have been proven effective in showing fewer toxic side-effects than conventional chemotherapies. When combined with chemotherapies (combination cancer therapies, or

chemoimmunotherapy), they can maximize therapeutic benefits and attenuate the limitations of each treatment modality. Cancer immunotherapies have been able to increase long-term survival rates and patient quality-of-life for a wide range of cancer types [5].

However, cancer immunotherapies still suffer from limited affordability and low patient response rates. Additional concerns are that immunotherapies have the potential to induce severe auto-immune toxicity [6]. In the last few years, thanks to advances in nanotechnology, immunology and chemistry, more and more resources are available to address for these challenges. Increasing research has shown the intricate and complex nature of cancer and the many self-reinforcing mechanisms of resistance that the tumor presents against therapy [7,8]. Hence, for the development of effective anticancer immunotherapies, it is first necessary to understand cancer development and its relationship with the immune system.

1.2. Tumor development

1.2.1. Cancer as "the wound that never heals"

Cancer develops in a micro-scaled Darwinist fashion. Malignant cells progressively acquire traits to sustain their uncontrollable growth in a "survival of the fittest" trend. It is typically understood that cancerous traits mainly include the deactivation of cell cycle regulators and the development of mechanisms to sustain their large nutrient demand. However, extensive research has demonstrated the crucial ability of cancerous tissue to use the immune system to support its growth and establishment [9].

In normal conditions, the immune system is prepared to identify aberrant or malfunctioning tissue and eliminate it (immunosurveillance) (Fig. 1.2.) However, cancer cells progressively acquire mechanisms to avoid its action - a process called immunoediting [9]. For instance, between 40%-90% of cancers are reported to avoid immunity by downregulating the major histocompatibility complex class-I (MHC-I) [10]. In normal conditions, MHC-I decorates the membrane of cells with recognizable biomolecules (antigens) for the immune system to distinguish endogenous ("self") from exogenous ("non-self", and therefore pathogenic) agents. The progressive accumulation of cancerous mutations yields the expression of tumor associated antigens (TAAs). A

particular class of TAAs are “non-self” tumor specific antigens (TSAs), known as neoantigens, which are unique to the tumor and thus susceptible to immune identification and “elimination”. Evolutionary MHC-I downregulation thus manages to hide TSA-expression from immunosurveillance. In many cancers, MHC-I downregulation is accompanied by an upregulation of membrane receptors working as “immune checkpoints”, which actively promote deactivation and anergy among approaching immune cells [11–13]. Cancer cells are known for their unrestrained, aberrantly active metabolism. The tumor site, or tumor microenvironment (TME), is thus characterized by nutrient deficiency and accumulation of metabolic subproducts. For instance, due to local lactate accumulation, the TME typically shows a characteristic acidity (pH ~6.5) in comparison to normal physiological pH (pH~7.4). Together with other typical traits of the tumor site like high levels of H_2O_2, hypoxia or glucose-deprivation, TME biochemistries have been reported to contribute towards local deactivation of the immune system [14].

The immunoedited tumor can reach an “equilibrium” of tolerance with the immune system. Tumor growth is contained but the cancer cells are not recognized as a pathogen and therefore are not attacked. In that scenario, additional cancer mutations may manage to overcome or “escape” the immune system action and facilitate further tumor growth (Fig. 1.2).

Immunoediting results in a TME that is rich in tolerant and deactivated immune cells. The tumor site typically accumulates tolerogenic T-regulatory cells (Treg), myeloid-derived suppressor cells (MDSCs) [15] and M2-phenotype tumor-associated macrophages (TAMs), all together responsible for maintaining a strong pro-tumoral environment [16,17]. Most notably, exhausted or deactivated immune cells remaining in the TME will not only stop further cytotoxic immune infiltration but will also promote wound healing-like mechanisms that facilitate cancer growth and tumor tissue repair. Hence, the cancer disease has been acknowledged as “a wound that never heals” [18,19].

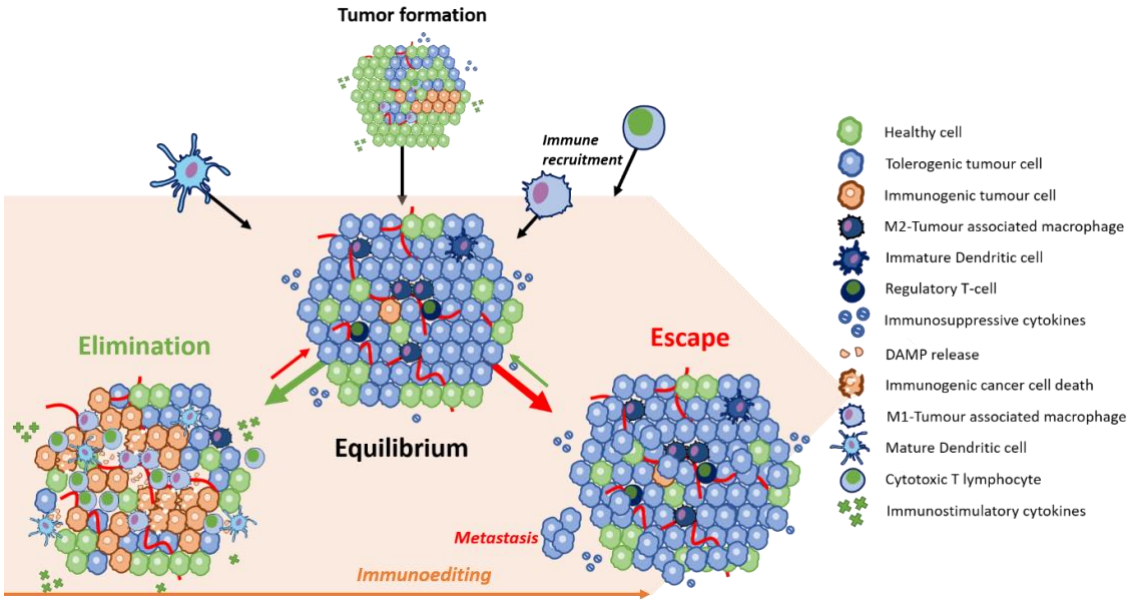

Figure 1.2. Cancer immunoediting leads to immune tolerance and escape. *The dynamic tumor-immune cell interaction can be differentiated into three reversible stages: Equilibrium, when the immune system manages to contain tumor growth but is not able to kill it; Escape, when the tumor manages to avoid the immune system action and grow further; and Elimination, when the immune system manages to overcome the protective cancer immunoediting and induce anticancer cell killing.*

1.2.2. "Hot" and "Cold" Tumors

The reversal of tumor immunoediting mechanisms is fundamental to induce effective anticancer immune responses. Although immunoediting occurs in a patient-specific fashion, a set of common cancerous immunosuppressive traits can be distinguished (Fig. 1.3). To combat them, key immunotherapy strategies are: (i) overcoming or inhibiting the immunosuppressive mechanisms of the TME; (ii) depletion of immune-suppressive cell populations from the TME; (iii) immune cell recruitment and activation into the TME; (iv) restoration of neoantigen-presentation mechanisms to facilitate the identification of cancer cells by the immune system; and (iv) inhibition of pro-tumoral immune checkpoints [20–23].

Overall, cancer immunotherapies aim to turn tolerated or tolerogenic "*cold*" tumors into targetable, immunogenic, "*hot*" tumors (see Fig. 1.3) [24]. In a "*hot*" tumor environment, the therapeutic effect of the treatment is facilitated by mechanisms of cancer immunogenic cell death (ICD). ICD typically involves the release of damage-associated

molecular patterns (DAMPs) and reactive oxygen species (ROS) which can provide (i) immune cell activation through immunostimulatory "danger signals" or cytokines and (ii) cancer-specific targets through TAA and TSA release. ICD may thus work as an *in situ* vaccine for the immune system and promote both immediate and long-lasting antitumor immunity [25–27].

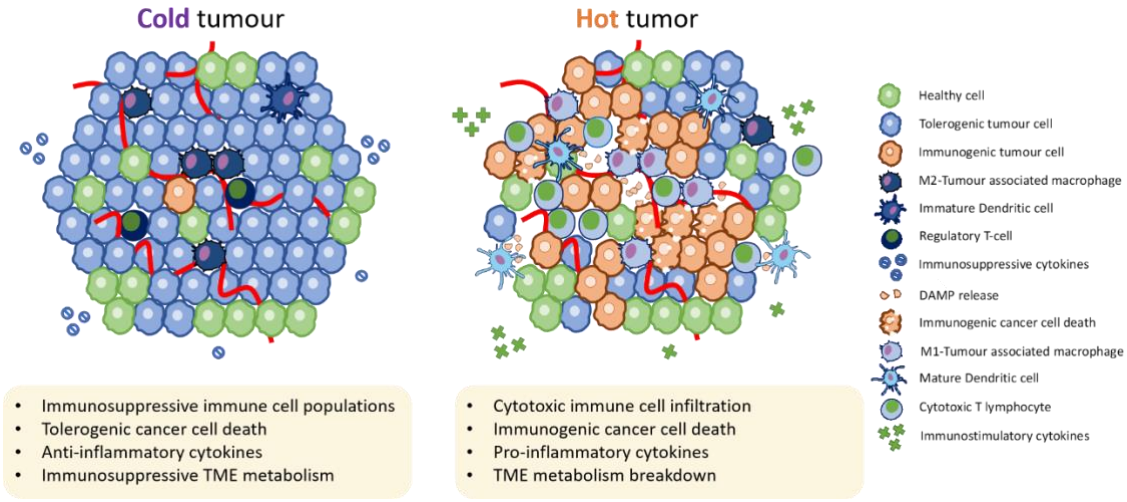

Figure 1.3. Schematic representation of distinctive characteristics of cold and hot tumors. *Cold tumors are characterized by a dense concentration of immunosuppressive and exhausted cell populations (Tregs, M2-TAMs, immature DCs) and immunosuppressive cytokine signalling. Hot tumors are characterized by a dense concentration of activated cytotoxic cell populations (T-cells, M1-macrophages, mature DCs) facilitating ICD and immunostimulatory cytokine signalling.*

1.2.3. ROS as key cancer therapy modulators

ROS are a ubiquitous product of intracellular oxygen metabolism. They are highly reactive radical species (e.g. hydrogen peroxide, peroxyl and hydroxyl radicals) that quickly oxidize their immediate surrounding tissue. High local ROS concentrations can degrade vital cellular components such as polyunsaturated fatty acids in the cellular membrane, induce mitochondrial dysfunction, deactivate essential enzymes or damage deoxyribonucleic acid (DNA) chains inducing cell death [28,29]. Hence, to maintain a healthy oxidative homeostasis, cells produce protective intracellular antioxidants like glutathione (GSH) [30].

The alterations in metabolic pathways in tumor cells (i.e. mitochondrial dysfunction, NADPH oxidase overexpression) have been linked with the elevated ROS levels in the

TME [31]. Cancer cells thus find themselves in a delicate oxidative state, where their antioxidant capacity can be exceeded and trigger irreversible oxidative damage. The recently described mechanism of ferroptosis, a ROS-and iron-mediated non-apoptotic programmed cell death, has gathered enormous interest as means to exploit this cytotoxic pathway for cancer therapy (Fig. 1.4, a) [32]. Oxidative stress-inducing therapies have been shown to trigger cancer-specific damage in a much safer/selective fashion than classic chemotherapies targeting apoptotic cell death [28,33–43] In addition, ferroptosis has been reported to favor cancer ICD via TAA and DAMP release [44,45]. ROS also play a key role as immunostimulatory messengers. ROS favor release of DAMPs and function as "eat me" signals for cytotoxic anticancer immunity [26,46,47]. "Eat me" signals are inducers of immunogenic phagocytosis, the process by which activated immune cells kill and scavenge cancer cells from the tumor-site [48,49]. Overall, ferroptosis shows distinctive features (biochemical regulators, cell morphology, immune features) that separate it from other mechanisms of cell death like apoptosis and necrosis (Fig. 1.4, c). However, ROS are regarded as a double-edged sword for cancer therapy as they have potential for exerting both pro and anti-cancerous action [50]. Chronic ROS generation in the TME has been shown to trigger mechanisms of tissue repair and cancer cell proliferation [51]. Hence, ROS-mediated anticancer activity is seen as a spectrum that can range from immunogenic to semi-tolerogenic and tolerogenic responses (Fig. 1.4, b).

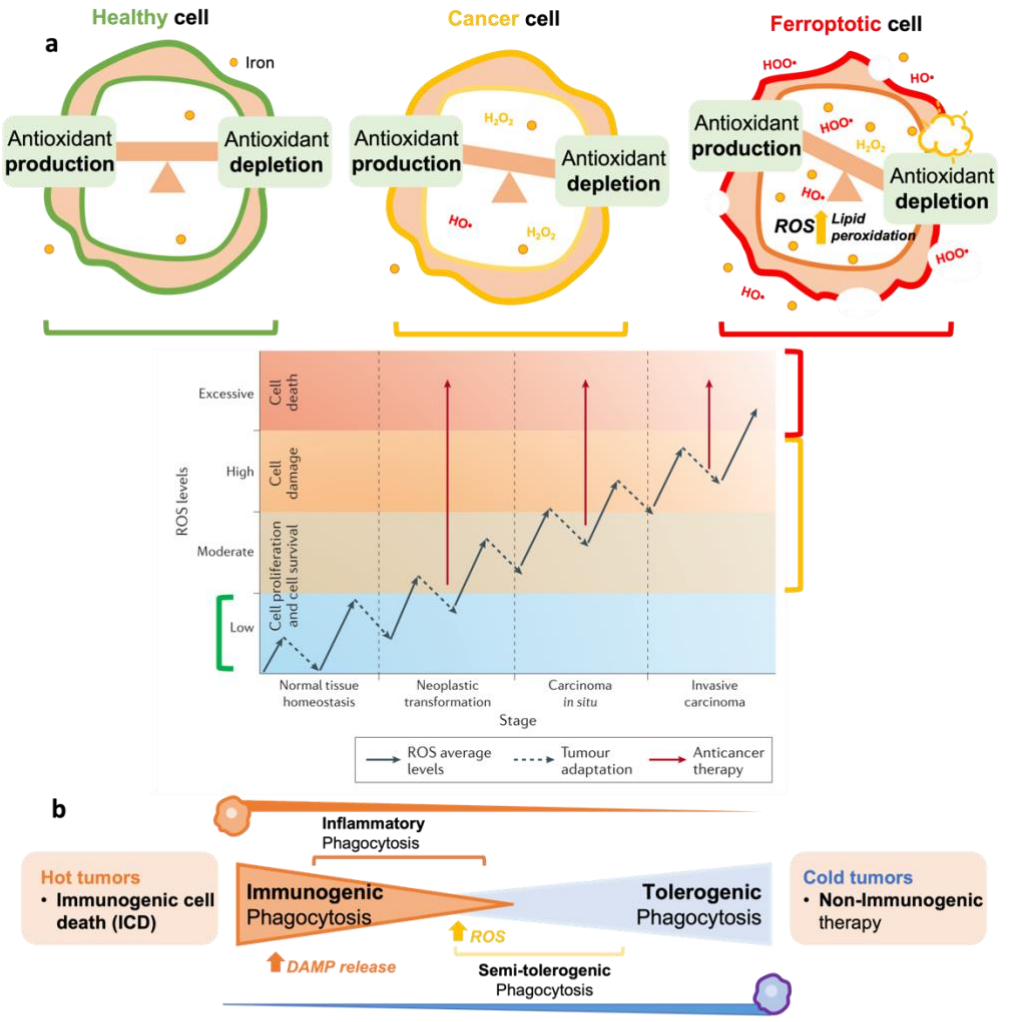

c

	Apoptosis	Ferroptosis	Necrosis
Regulation	Programmed cell death regulated by intrinsic biochemical pathways.	Programmed cell death regulated by intrinsic biochemical pathways.	Non-programmed cell death triggered by external factors (i.e. trauma, burning, etc.)
Key biochemical features	Activation of caspases (proteases) for DNA fragmentation and controlled cell component degradation. Conserved signalling proteins.	Inhibition of reduced GSH. Increased iron accumulation and lipid peroxidation. Conserved signalling proteins.	Membrane integrity loss. ATP depletion.
Cell morphology	Plasma membrane blebbing; cellular and nuclear volume reduction; nuclear fragmentation	Mitocondria dysfunction and atrophy; Membrane rupture; Cell lysis; Cellular swelling	Membrane rupture, Cellular swelling, Cell lysis
Immune features	Mostly anti-inflammatory	Pro-inflammatory	Pro-inflammatory

Figure 1.4. Schematic representation of tumor interplay with ROS production and cell death mechanisms comparison. *All cells experience ROS production during oxygen metabolism. The potential cell damaging effects are typically contained by antioxidant production. However, increased cancer metabolism induces ROS overproduction, yielding a delicate oxidative equilibrium. Redox stress-inducing therapies can therefore be used to give a "fatal push" towards irreversible oxidative damage and trigger cancer cell-specific ferroptosis. Image adapted from* [28]*; (b) Schematic representation of the*

immunological spectrum between immunogenic phagocytosis typical of hot tumors and tolerogenic phagocytosis typical of cold tumors. Image adapted from [52]*. (c) Comparison between apoptosis, ferroptosis and necrosis cell death mechanisms.*

1.3. State-of-the-art strategies for cancer immunotherapy

Two subtypes of immunity can be distinguished: (a) innate immunity, a nonspecific immunity subtype prepared to react as a first line of defence against non-identified pathogens; and (b) adaptive or acquired immunity, a specialized immunity subtype aimed at the elimination of previously identified "non-self" pathogens. Adaptive immunity develops potent pathogen-specific responses and long-term memory after innate immunity fails.

The process acknowledged as "immunization" occurs after the assimilation of disease-specific "non-self" antigens by the immune system. Cross-presentation is the process by which antigen-presenting cells (APCs) present "non-self" antigens to cytotoxic T-cells ($CD8^+$). $CD8^+$ T-cells are then able to recognize and attack targeted pathogen. APCs are a broad category of cells, formed primarily by DCs and macrophages. APCs expose the tumor antigen on their membrane through MHC-I proteins. T-cells bind to them through membrane T-cell receptors (TCR) to recognize the antigen. Efficient antigen presentation requires the simultaneous recognition of co-stimulatory receptors. Transmembrane proteins CD86 and CD80 are key co-stimulatory APC receptors that bind transmembrane protein CD28 receptors in T-cells (Fig. 1.5, c).

Adoptive cell transfer (ACT) therapies give testimony of the promising outcomes of effective TAA and TSA processing and immunization. ACTs use extracted immune cells from the patient and activate them *ex vivo* by exposure to TSA and immunostimulatory drug cocktails. Once activated, immune cells are re-introduced into the patient as readily specialized, anti-cancerous immune cells. Although exuberantly costly, these therapies have shown promising results in several clinical trials [53,54].

The main hurdle when trying to induce antitumor immunity are the barriers set by cancer immunoediting. Breaking through the defensive immunosuppressive features of the TME is indispensable for immunotherapy success. To this end, an increasing number of research articles have highlighted the relevance of at least three key immunotherapy

objectives: TAM reprogramming, pro-tumoral immune checkpoint blockade and enhancement of antigen cross-presentation mechanisms [16, 21, 24, 26.]

1.3.1. TAM reprogramming

TAMs represent the most predominant immune cell population in the TME [55]. Macrophages display two main phenotype groups which determine their functional activity: classical activated (M1) and alternative activated (M2). Activation (or polarization) towards a specific phenotype is strongly influenced by external signalling mechanisms. Macrophage polarization towards M2-like phenotypes (typical of TAMs) is thought to be promoted by the hypoxic character of the TME as well as by emission of immunosuppressive cytokines like interleukin 10 (IL-10), tumor growth factor type-β (TGF-β) or epidermal growth factor (EGF) by some cancers [56,57]. The M2-polarized macrophages (e.g. IL-10, TGF-β or Arginase I) promote mechanisms of tumor tissue repair and growth, metastasis and depletion of proximal immune activation [58]. In contrast, M1-like macrophages display increased cytotoxic phagocytotic activity, promote antigen presentation through co-stimulatory CD80/86 transmembrane proteins and induce the release of immunostimulatory signals like tumor necrosis factor-α (TNF-α), interferon-γ (IFN-γ), ROS and inducible nitric oxide synthase (iNOS) (Fig. 1.5, a) [59]. Hence, M2-to-M1 macrophage repolarization represents a key new cancer immunotherapy strategy [16].

M2-to-M1 macrophage repolarization can be achieved through chemical stimulation. Administration of potent immunostimulatory drugs (e.g. DAMP-like molecules), inhibition of crucial immunosuppressive receptors and signalling pathways (e.g. TGF-β generation), modulation of the immunosuppressive TME biochemistries (e.g. hypoxia relief) or controlled increases of oxidative stress are some of the many strategies used to this end [60–62]. By achieving M2-to-M1 re-polarization, these new therapeutic strategies overcome a key immunosuppressive mechanism whilst recruiting anti-tumor immune cells from within the TME.

1.3.2. Immune checkpoint inhibitors

One of the mechanisms that cancer cells use for T-cell deactivation and M2-TAM polarization is the overexpression of programmed death ligand-1 (PD-L1) [63]. PD-L1 is a transmembrane protein functioning as immune checkpoint that in healthy conditions

serves to protect against immune hyperactivity. PD-L1 binds to the programmed death type-1 (PD-1) membrane protein expressed on cytotoxic T-cells ($CD8^+$ T-cells) to induce immune cell anergy. Other TME immunosuppressive populations like Tregs, deactivated T-cells and M2-TAMs may also express PD-L1. The immune checkpoint interaction downregulates the expression of important co-stimulatory signalling (e.g. IFN-γ, TNF-α), stabilizes M2-like macrophage phenotypes and ultimately raises the threshold required for T-cells to become cytotoxic, thus reinforcing the immunosuppressive character of the TME [64].

Immunotherapies that aim to block pro-tumoral immune checkpoints like PD-L1/PD-1 binding are part of the current immune-checkpoint blockade (ICB) therapies. These ICB therapies target any of the two receptors of the PD-L1/PD-1 pathway with anti-PD-1 or anti-PD-L1 antibodies which then impede the binding [65]. Other important ICB strategies are aimed at the blockade of the cytotoxic T-cell-associated antigen-4 (CTLA-4) immune checkpoint, although their use is limited due to safety concerns [6,66]. ICB strategies are conceptualized as if they were "releasing the brakes" that halt the immune system action (Fig. 1.5., b).

New generations of ICB therapies currently under investigation in clinical trials combine PD-L1/PD-1 blockade strategies with co-administration of antibody-based stimulatory agents like OX40 [67]. Interaction of OX40 with its ligand (OX40L) favors $CD8^+$ T-cell expansion and T-reg depletion thus stimulating the immune cytotoxic action [66,68]. Combinatory immune checkpoint strategies that simultaneously stimulate and deactivate suppressing mechanisms of the immune system have reported very promising therapeutic benefits [67,69]. However, these strategies are only effective for PD-L1 positive cancers, which account for less than 20% of all clinical cases. Treatment dosage and timing are conditions that still require careful optimization to maximize benefits and reduce potential auto-immunity side-effects [6,70–76].

1.3.3. Antigen cross-presentation enhancement

By potentiating the efficiency of antigen cross-presentation mechanisms, the threshold of immunogenic cargo needed to drive powerful anticancer responses may be reduced. Oxidative damage-inducing therapies may enhance DC antigen cross-presentation

mechanisms through enhanced intracellular trafficking (occurring through endosome escape; see below) [77]. ICB therapies have been reported to upregulate the generation of IFN-γ [78,79], which plays a pivotal role in antitumor immunity by restoring tumor-surface MHC-I expression [22,80]. Various immunostimulatory drugs have also reported capacity for enhancing DC maturation, expression of co-stimulatory receptors (CD40/80/86) and expansion. [81,82] Therapy-inducing TCR clustering have also facilitated increased $CD8^+$ T-cell activation and expansion [83].

Most notably, nanomedicine research enabled the development of effective antigen-presenting devices and controlled site-specific delivery of immunostimulatory drugs for adaptive immunity enhancement [84,85]. As we will see in the sections that follow, these therapeutic nanodevices provide important therapeutic benefits through controllable drug delivery and reactivity. Hence, several of these systems have already been approved for clinical use [86,87].

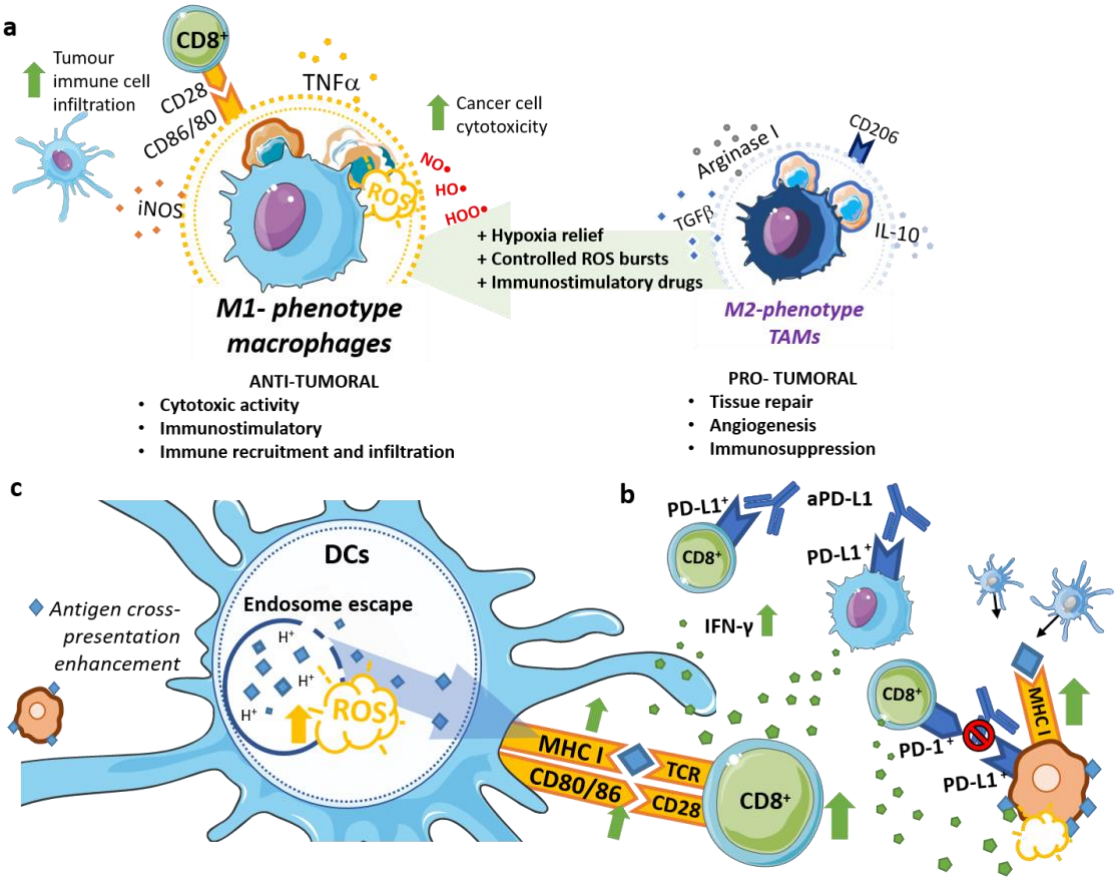

Figure 1.5. Three key immunotherapy strategies for enhanced cytotoxic anticancer immune responses. *(a) M2-to-M1 TAM reprogramming is key to break through one of*

the main protective tumor mechanisms and facilitate cytotoxic immune infiltration; (b) ICB therapies prevent key immunosuppressive tumor mechanisms and enable immunostimulatory signalling; (c) antigen cross-presentation enhancement strategies provide enhanced recognition of the malign tissue and facilitate adaptive immune action.

1.4. Cancer Nanomedicine

Cancer immunotherapies can benefit strongly from the development of interdisciplinary fields like nanomedicine, biological inorganic chemistry and chemical immunology. For their immunogenic nature, immunotherapy drugs are especially susceptible to early degradation and off-target processing [88]. Furthermore, therapeutic synergies that may be established between complex multidrug cocktails are only possible when they act in a coherent time and space-controlled manner. Hence, therapeutic cargo protection and biodistribution control are key for successful anticancer immunization [85]. By turning to chemistry and material sciences, cancer therapies gathered increasingly safer and efficient means for cancer diagnosis, multidrug administration, smart site-specific drug delivery and fundamental research on immunoediting and cancer development dynamics [89].

1.4.1. Common nanodevice features

Briefly, nanodevices provide two key characteristics for effective immunotherapy administration:

(i) Physical and chemical means to load, protect and deliver the therapeutic agents.
(ii) High surface-to-volume ratios allowing functional particle surface decoration for tissue targeting.

Pharmacokinetic control (i.e. control over absorption, biodistribution, metabolism and excretion of the therapeutic cargo by the patient) can be achieved by tuning the physicochemical properties of the nanodevice. Some key features are:

(i) Safe loading of multidrug cocktails.
(ii) Target tissue recognition by surface nanodevice decoration.
(iii) Control over drug biodistribution and intracellular trafficking through stimuli-responsive reactivity.

A wide range of nanosystems can be found in the literature, each conferring their own degree of control over features like chemical reactivity, stability or biocompatibility. Among them, several nanodevice families can be distinguished (Fig. 1.6):

(i) **Soft organic particles:** These are soft and flexible organic structures showing a very wide application range. Their organic nature allows a very high degree of chemical tunability governing particle decoration and multidrug loading [90–93]. These structures are typically inert, safe and biocompatible. Clinically approved examples of these formulations are Doxil and Myocet, which use lipidic bilayers as vehicles (liposomes) to carry powerful chemotherapy drugs [86]. However, the soft and flexible nature of these systems can lead to stability issues and cargo leakage. Notable components in this family of vehicles are polyethyleneglycol (PEG) polymeric chains. These are long polymeric chains that form meshes around the particle, thus providing physical protection by steric hydration [94]. PEG chains are commonly used as particle stabilizers and took part, for example, in the formulation of Doxil as well as some COVID-19 vaccine formulations [95].

(ii) **Inorganic nanoparticles:** Inorganic or metallic nanoparticles are solid and robust carriers. They enable enhanced physiological stability and longer retention times. Most notably, these particles provide interesting material-specific chemical features for redox and external stimuli reactivity (e.g. upon the incidence of magnetic, photonic fields). Clinically relevant examples are iron oxide nanoparticles (IONPs), which show ferroptosis-inducing redox reactivity and sensitivity to magnetic-based therapies [96,97], and gold nanoparticles (AuNPs), which show high tunability and sensitivity to light-based therapies [98]. Inorganic/metallic materials can suffer from limited biodegradability, off-target accumulation and toxicity issues [99–101]. Hence, inorganic nanoparticle features are typically modulated and enhanced through metal doping and heterogeneous composite structures [102–107].

(iii) **Mesoporous structures:** Mesoporous materials provide solid carriers that show distinctively high porosity. They are characterized by their high physiological stability and high surface-to-volume ratios. Their porous structure enables excellent particle tunability, multidrug loading and surface decoration. Some representative examples are silicon oxide particles [108–111], polymeric particles

[112,113] and carbon nanotube meshes (CNTs) [114]. These carriers form typically large non-discrete structures, which can limit biodegradability and biodistribution. Hence, in many cases they are used *ex vivo* or as localized implantable devices [115–117].

(iv) **Metal-organic Frameworks (MOFs)**: MOFs are uniquely tuneable and reactive organic-inorganic crystalline constructs. They are formed by a regular array of interactions between a metal centre and organic linkers, which yields a repetitive cage-like structure (Fig. 1.6, b). MOFs show well-defined porosity and tailorable composition, thus enabling drug loading and versatile chemical reactivity [118]. They typically show potent redox catalytic features and sensitivity to external stimuli [119,120]. However, their strong reactivity can induce stability and toxicity issues, which has posed strong limits to their clinical approval [121,122].

Increasing research enabled the design of hybrid nanodevices combining these families of nanomaterials and nanoparticle-based systems to better suit the specificities of each clinical case. Some representative examples like: inorganic particle-enriched mesoporous silicon mesoporous structures, which typically allow for multidrug loading combined with redox and exogenous stimuli reactivity (Fig. 1.6, a) [105,112]; inorganic particle-enriched drug-loaded polymeric micelles, allowing synergistic therapeutic drug loading and redox stimuli reactivity (Fig. 1.6, c) [102,123,124]; or complex inorganic particles and composites, allowing heterogeneous surface coating and anisotropic reactivity (Fig 1.6, d) [96,125–127].

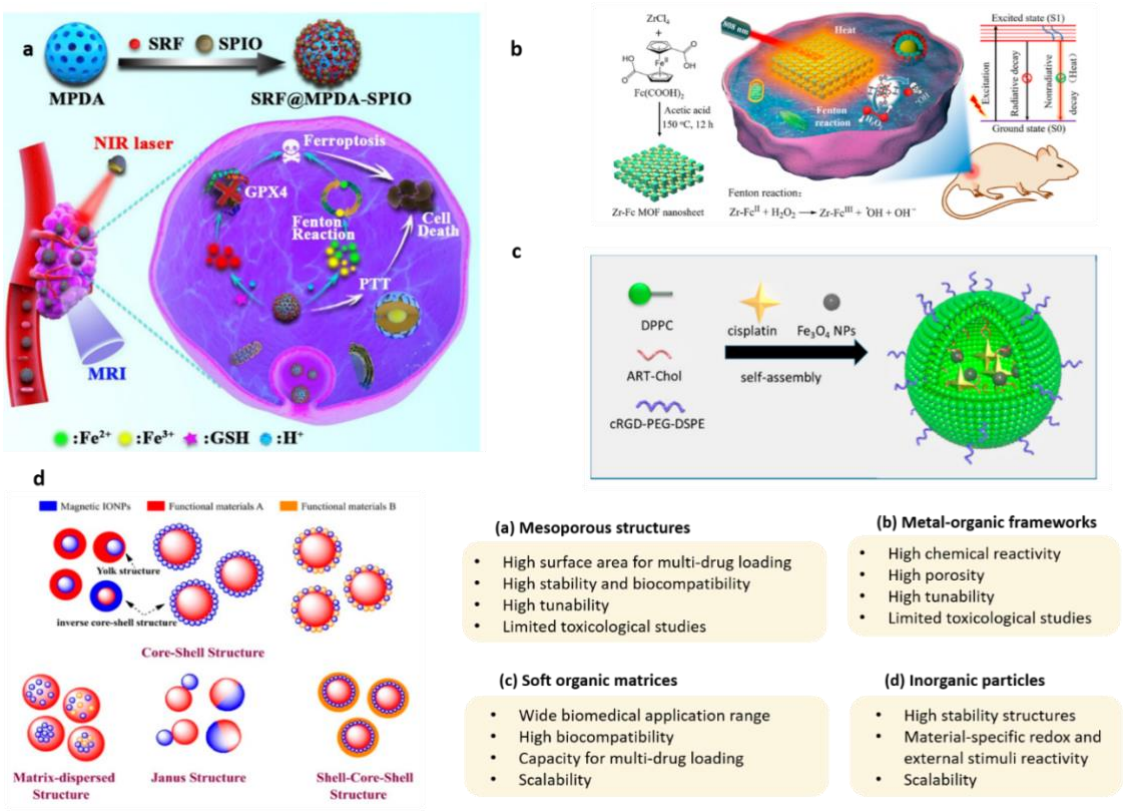

Figure 1.6. Common nanomedicine structures for cancer therapy *(a) Schematic representation of redox-active IONPs embedded into mesoporous polydopamine for cancer ferroptosis in combination with light-based therapies. Image adapted from* [112]*; (b) Schematic representation of zinc and iron-rich MOFs for enhanced oxidative chemistry and combination cancer therapy. Image adapted from* [128]*; (c) Schematic representation of magnetite-containing liposomes in combination with chemotherapy for enhanced ROS generation and cancer chemotherapy. Image adapted from* [123]*. (d) Common morphologies of inorganic composite nanomaterials. Figure adapted* [96]

1.4.1.1. Cancer nanovaccines

Vaccines are biological preparations used to induce adaptive immunity against a particular disease [129]. A vaccine typically contains an active compound, the antigen, that resembles the disease-causing agent and becomes the target for subsequent immune system action. The active compound is typically accompanied by a "danger signal", the adjuvant, an innate immunostimulatory compound that does not provide immunity by itself but potentiates and facilitates the processing of the active compound by the immune system.

DAMPs and pathogen-associated molecular patterns (PAMPs) are recognized as "danger signals" by pattern-recognition receptors (PRRs) in cells of the immune system. An important PRR family are Toll-like receptors (TLRs), which are primarily found in DCs and macrophages [26]. On accounts of their relevance in cancer therapy, various TLR agonists have been proposed as some of the "twelve immunotherapy drugs that could cure cancer" [130]. Chemotherapy and ferroptosis-inducing agents may trigger ICD through TAAs and DAMPs release and thus be used for their adjuvant-like properties [44,45,131].

Vaccines may be administered to fight an already existing disease (therapy) or in prevision of that disease (prophylaxis). Vaccines are most active when administered prophylactically. Indeed, the advent of the COVID-19 pandemic showed that development of potent adaptive memory requires time (and multiple booster doses) [132]. However, the chaotic, patient-specific development of the tumor and immunoediting impedes the development of universal generalizable prophylactic vaccines for cancer [133].

Antigen-presenting nano-vehicles (or nanovaccines) are gathering increasing interest as means of therapeutic anticancer immunization [134–136]. These systems can be used to overcome the inherent limits of therapeutic vaccination and break through tumor immunoediting mechanisms. Nanovehicles can protect the antigen from early degradation and powerful adjuvants can be co-loaded onto the construct to enhance immunization [137].

Smart construct design offers unique opportunities to improve tissue targeting and intracellular trafficking, ensuring efficient antigen presentation and developing immunological memory against the tumor [89]. In the chapters that follow, it will be shown how cancer nanovaccines can be "chemically programmed" to be delivered into the tumor site and lymphoid tissues to induce effective anticancer immunization to fight the disease [124].

1.4.2. Nano-enabled pharmacokinetic control

Five key pharmacokinetic characteristics can be controlled through nanomedicine: improved drug circulation, tissue accumulation, tissue penetration, cell internalization, and drug release (shortened as CAPIR) [138]. For any given nanovehicle, it will be key to

find an optimal equilibrium between mechanisms of drug protection from early degradation and drug release in the target tissue (Fig. 1.7).

We can broadly distinguish two main strategies for controlled therapy delivery [85,139]:

a) **Passive Targeting**, which aims to gain control over therapy biodistribution, tissue penetration and retention by tuning passive physicochemical parameters of the vehicle such as particle size, surface charge or shape.
b) **Active Targeting,** which aims to enhance target-specific delivery through "directing ligand" particle surface decoration and "stimuli-responsive" reactivity. Directing ligands are biomolecules functioning as agonists of receptors that are unique or overexpressed in the target tissue. The carrier is thus able to distinguish target from off-target tissue. Additionally, reactive moieties of various nature (e.g. moieties sensitive to changes in pH, redox potential, enzyme concentration, etc.) can be incorporated onto the vehicle structure to trigger site-specific drug release.

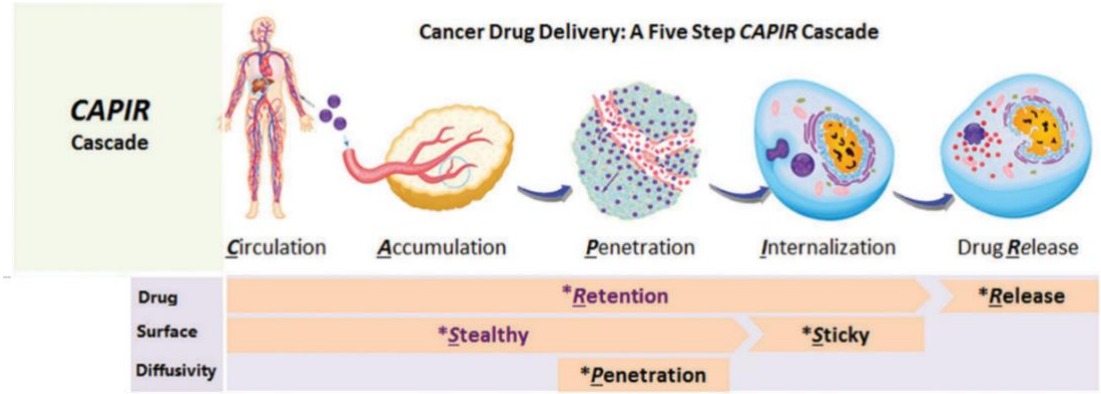

Figure 1.7. **CAPIR pharmacokinetic indications for efficient nanomedicine therapy.** Drug circulation, tissue accumulation, tissue penetration, cell internalization, and drug release are key pharmacokinetic features of the therapy that may be controlled through smart nanomedicine design. Figure adapted from [138].

1.4.2.1. Passive tissue targeting

Inherent physicochemical features of the nanovehicle such as size, shape or surface charge have long been revealed to influence their biodistribution. The tuning of these basic features can be used to improve therapy biodistribution among different organs and tissues of interest:

- **Size, stiffness and shape:** Treatment accumulation in the tumor has been reported to be optimal for medium-sized particles (30 - 80 nm) [138]. Very small vehicles (<7nm) can penetrate deeper into the tumor but are readily excreted by renal filtration. Larger vehicles (>100nm) demonstrate increased circulation times but can also lead to clearance by the reticuloendothelial system (RES) and struggle to penetrate into the tumor [140]. Depending on the specificities of each cancer type and TME dynamics, shape or stiffness can also be tuned to influence biodistribution, tissue penetration and cell uptake [141,142].
- **Surface charge:** Positive surface charges facilitate cell uptake through interaction with anionic lipids of the cellular membrane. Although this could enable enhanced intracellular delivery to the targeted cells (e.g. cancer cells), the effect is also true for untargeted cells. Positively charged vehicles might thus induce off-target therapy internalization before reaching the tissue of interest. Instead, negatively charged surfaces might avoid early uptake and provide longer circulation times. Krantz et al. demonstrated how negative liposome-based formulations accumulated into the spleen and lymph nodes, crucial neuralgic centres of the immune system, whereas positive formulations accumulated in the lung [143].

1.4.2.1.1. Cellular uptake and intracellular trafficking control

Reaching the target tissue remains very challenging and yet it offers no guarantee for therapeutic success. Gold-standard chemotherapy drugs like cisplatin need to reach the nucleus to impair DNA replication [144]. Immunotherapeutic activation of certain TLRs (i.e. TLR3, TLR7, TLR8 and TLR9) requires TLR agonist trafficking into intracellular endosome and lysosome compartments [145]. Antigens need to be transported into the cytosol to be processed and presented by APCs [146]. Hence, a key objective in cancer nanomedicine design is to seize control over drug uptake and intracellular trafficking.

Transfection is the process of deliberately introducing foreign nucleic acid structures into the intracellular space by crossing the lipid membrane [147]. The transit is governed by the dynamic electrostatic interactions of the semi-fluid, anionic lipid membrane. Molecular structures designed to facilitate transfection are called transfecting agents. Typically, these agents are enriched with positively charged moieties that facilitate membrane trespassing through:

i. **Ion-pair-induced defects**. Cationic particles accommodated onto anionic membrane lipids may induce structural deformations. These defects may develop into pores through which the particles can diffuse into the cell [147–150]. Inclusion of hydrophobic chains into the structure may further stabilize amphiphilic membrane trespassing [151–155].

ii. **Facilitated endocytosis**. Endocytosis mediates the cellular uptake of agents that are too big to diffuse through the membrane. Nanoparticles are thus typically uptaken through endocytosis pathways [156] (Fig. 1.8, a). Cationic particles, by remaining proximal to the anionic membrane, as well as directing ligand-decorated devices, by attaching to specific cell receptors (see below), have higher chances of cellular uptake. The cell is thus able to engulf the particle and internalize it inside intracellular vesicles (endosomes and lysosomes) [143].

One of the major functions of endosomes and lysosomes is the digestion of material and nutrients uptaken by the cell. These compartments have thus been exploited by biodegradable carriers to trigger site-specific intracellular drug release (Fig. 1.8, b-c; see below) [156]. However, endosome and lysosome digestion can also degrade and deactivate many therapeutic agents. In such cases, various strategies have been devised to promote endosome escape, by which the therapeutic cargo is relocated into the cytosol (Fig. 1.8, d-f) [157]:

i. **Proton sponge effect**: The introduction of structures that can be highly-protonable in the acidic endosome will induce absorption of protons and counter anions into the vesicle. The process produces an increase in osmotic pressure stress that ruptures the endosome (Fig 1.8, d).

ii. **Mechanical destabilization**: Structures that once they are highly protonated can induce mechanical vesicle rupture by: (a) swelling and pressing against the vesicle (Fig. 1.8, e); or (b) disassembling into multiple ion-pair-inducing fragments (Fig. 1.8, f).

iii. **Membrane oxidation**: ROS generation through redox-active and photosensitive agents loaded into the endosome have been used to transform H_2O_2 and incident light into oxidative stress (see below), yielding lipid peroxidation, membrane defects and rupture [158].

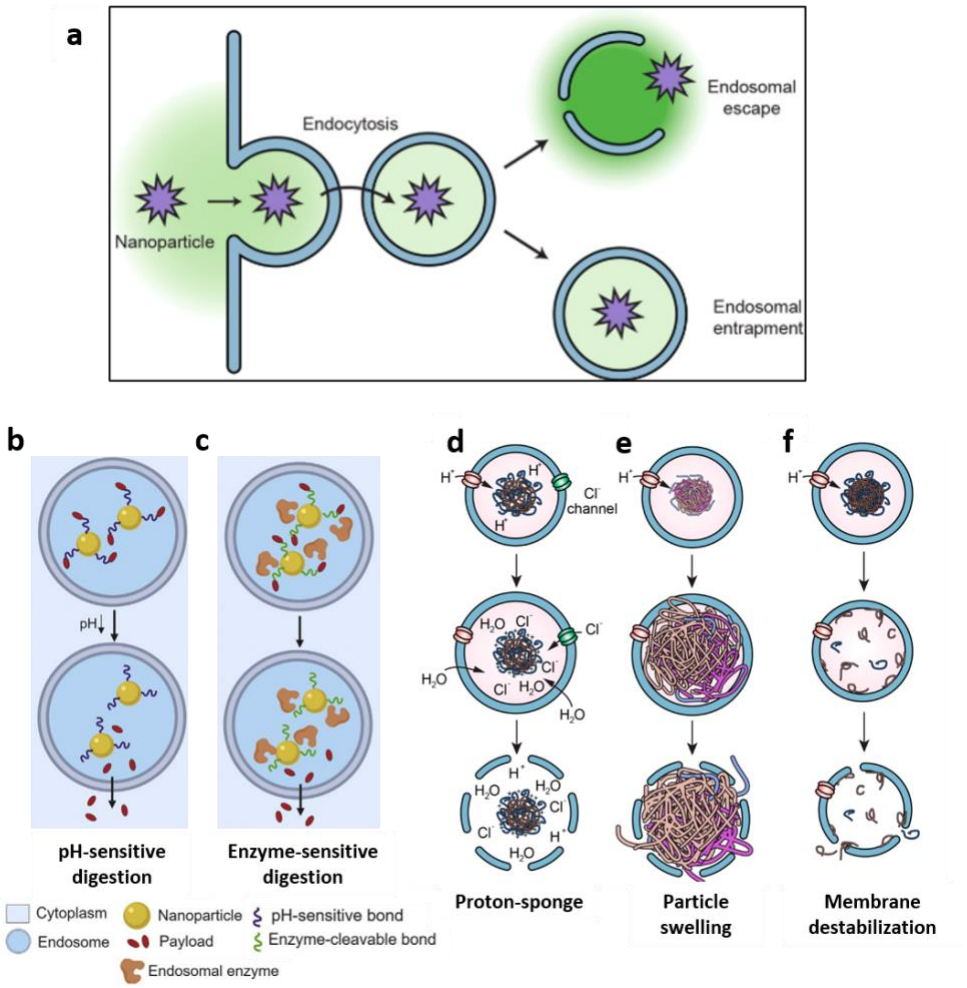

Figure 1.8. Schematic representation of nanoparticle endocytosis and opportunities for intracellular drug trafficking control. *(a) Owing to their size, nanoparticles are mainly uptaken into the cell by mechanisms of endocytosis. Nanovehicles can then incorporate (b-c) cleavable bonds for site-specific drug release in the endosome. Two common mechanisms of site-specific drug release can occur through (b) pH-sensitive and (c) enzyme-sensitive digestion. Nanovehicles can also incorporate (d-f) mechanisms of endosome escape for cytosol drug delivery. Three common endosome escape mechanisms occur through (d) proton-sponge effects (high osmotic pressure), (e) mechanical strain by particle swelling and (f) vesicle destabilization by multiple ion-pair defect-inducing fragments. Figure (b-c) adapted from* [156]*. Figures (a, d-f) adapted from* [157]*.*

1.4.2.2. Active tissue targeting

In many cases passive targeting is not be sufficient to deliver the nanocarrier to the target tissue. It has been estimated that in most cases only 1-2% of particle dosage accumulates into the targeted tissue [141,159,160]. The two main particle design strategies to "actively"

enhance tissue targeting and intracellular trafficking control are: (i) particle surface decoration with targeting ligands and (ii) stimuli-sensitive drug delivery.

1.4.2.2.1. Ligand-directed targeting

As previously mentioned, directing ligands are biomolecular structures that selectively bind to receptors that are unique or overexpressed on the target tissue [161,162]. These can be biomolecules of a very wide nature (e.g. small peptides, polysaccharide chains, proteins, etc.). By incorporating directing ligands onto the particle surface, the carrier may recognize and attach to specific receptors on the target cells. The therapy can then be site-specifically accumulated and processed (Fig. 1.9).

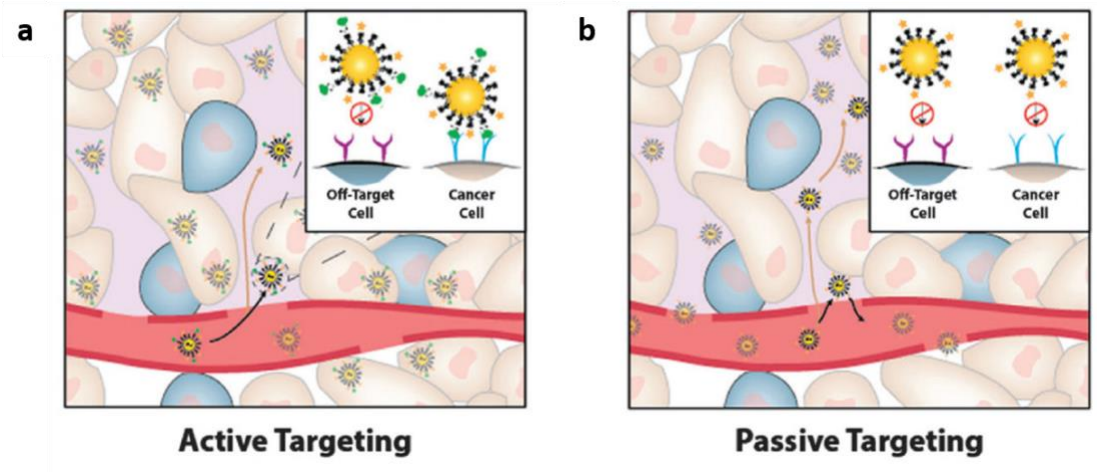

Figure 1.9. Expected outcomes from active ligand-directed targeting. *(a) Upon reaching the TME, ligand-targeting nanoparticles can be designed to recognize and bind cell surface receptors on target cells, like cancer cells, to facilitate accumulation and cell uptake. (b) In contrast, passive targeting nanoparticles may not interact with the target cells, thus remaining in circulation. Figure adapted from* [156].

There are many bioconjugation options to enable particle surface decoration. The chemistry is typically chosen according to two common requirements: (a) to prevent cargo degradation during the bioconjugation process to maintain binding activity; and (b) to provide a particle-ligand bonding that is stable enough to reach the target tissue. It is also desirable that they should be high yielding, versatile, and produce by-products that are easy to remove (*click-chemistry* approaches) [163–165]. Some relevant examples are hydrazone-based conjugation and thiosuccinimide linkage formation [166–168].

1.4.2.2.2. Stimuli-sensitive drug delivery

Nanovehicle stability is key to protect the drug payload from early degradation. However, failure to release the cargo when reaching the target will still result in ineffective treatments. To achieve effective drug release when reaching the target, some nanovehicles incorporate stimuli reactive moieties [169–171].

Stimuli-sensitive moieties can be either organic or inorganic in nature. In response to site-specific or time-controlled stimuli, these moieties react inducing structural rearrangement or breakdown of the vehicle. The process attenuates and cleaves the interactions that hold the therapeutic cargo, which is then released.

According to the origin of the stimuli, two broad categories can be distinguished:

(i) **Endogenous stimuli:** These are caused by gradients in pH, redox potential or enzyme concentrations between cellular compartments and tissue.
(ii) **Exogenous stimuli**: These are caused by the application of external signal, such as the incidence of light, magnetic fields or acoustic waves.

1.4.2.2.2.1. Endogenous stimuli

1.4.2.2.2.1.1. pH-sensitive drug delivery

Certain biological compartments of interest for cancer therapy are distinctively acidic. This is the case for the TME (pH ~ 6.5) and intracellular endolysosomal compartments (pH = 3-6) [172]. Site-specific delivery is thus possible by using moieties that can be protonated/deprotonated and/or hydrolysed within this range of pH gradients. We can distinguish two main strategies for pH-sensitive drug delivery:

(i) **Structural rearrangement:** Protonation-deprotonation processes inside the nanovehicle can modulate the strength of interactions such as hydrogen bonds, hydrophobic and electrostatic interactions. When protonation/deprotonation weakens drug-vehicle interactions the drug is detached and released from the vehicle [173–176]. Alternatively, when it affects vehicle-vehicle interactions, the nanovehicle might swell and rearrange exposing the drug outwards to the environment (Fig. 1.10 a) [177,178]. These are common strategies used in soft

polymeric nanovehicle structures. However, although this can provide a simple strategy for triggering drug release, the weak and non-specific interactions involved in these strategies may result in off-target drug leakage.

(ii) **Structural breakdown:** Hydrolysis-sensitive moieties/bonds can also be used to trigger vehicle breakdown and drug release. Although more elaborate, covalent bond chemistry enables more controlled and precise site-specific drug delivery mechanisms. Amides, oximes, hydrazones, carbonates and esters are common examples of pH-responsive moieties (Fig. 1.10, b) [179]. Customization of the environment surrounding the reactive moiety may be used to obtain very specific windows of acid-catalysed hydrolysis. This approach enabled the development of nanovehicles that can distinguish between biological compartments of different pH [167,180,181]. Hydrolysis-based strategies may be also sensitive to concentration gradients of small molecules and enzymes that catalyse hydrolyzation [182,183].

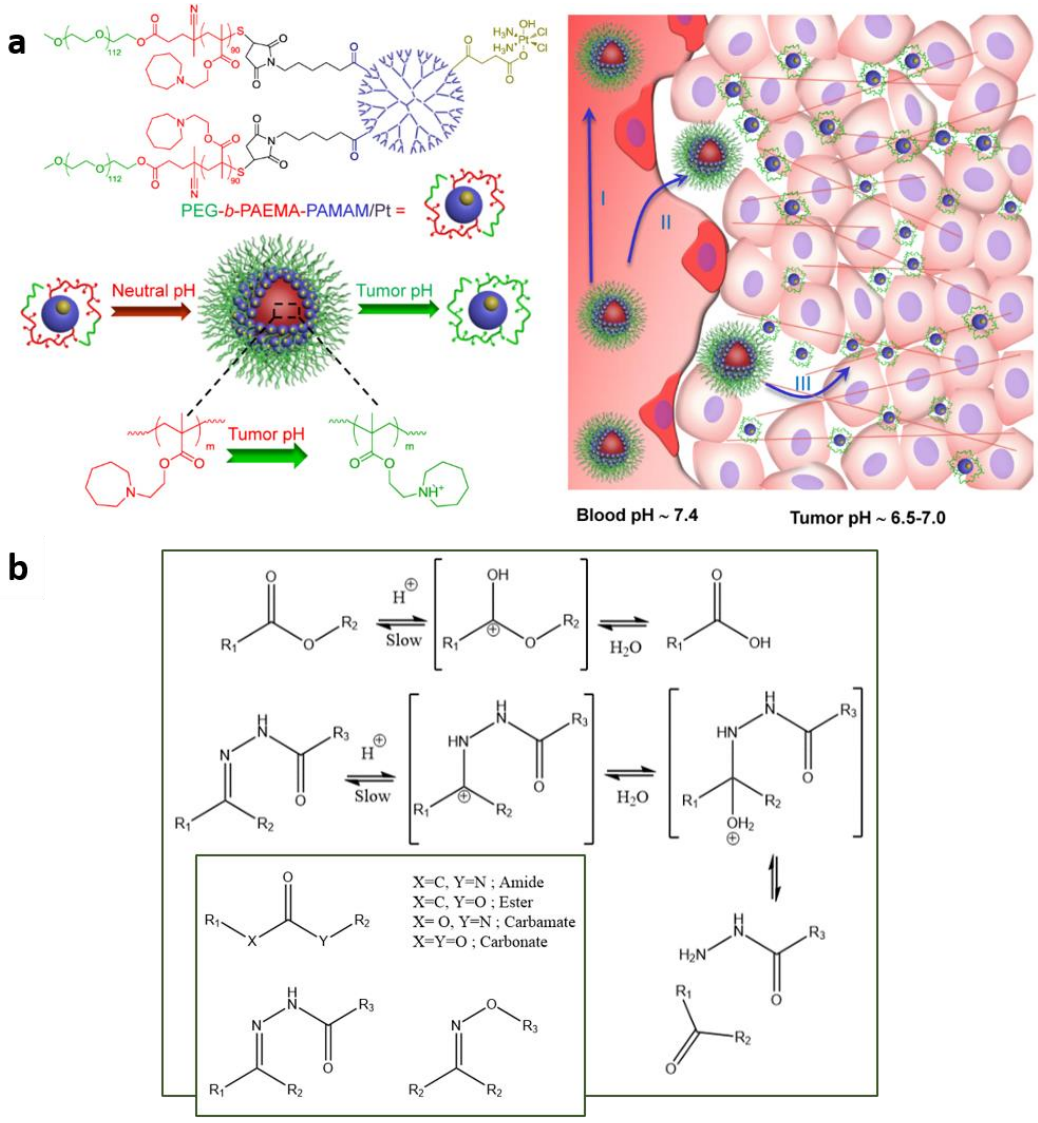

Figure 1.10. Acid-responsive drug release strategies. *(a) Illustrative example of structural rearrangement triggered by nanovehicle protonation in the TME (pH ~ 6.5). Image extracted from* [184] *(b) common acid-catalized hydrolizable moieties and mechanisms used for pH-sensitive structural breakdown.*

1.4.2.2.2.1.2. Redox-mediated drug delivery

As discussed above, the unique cancer cell metabolism yields a TME that is hypoxic, acidic and abundant in metabolic subproducts such as ROS. Site-specific TME delivery is thus possible by using moieties and materials sensitive to redox reactivity and degradation. Three common strategies of redox-mediated nanomedicine delivery are:

(i) **Carrier breakdown:** Common examples are inorganic materials containing transition metal oxides, such as manganese, iron or copper [185–191] as well as

calcium peroxides [192,193]. Nanomaterial doping with iron and manganese can be used to increase vehicle biodegradability in the TME [110]. In addition, the products of their degradation, oxygen and metal ions, may show therapeutic benefits. For instance, $Fe^{2+/3+}$ ions may promote immunogenic tumor ferroptosis [32], the Mn^{2+} and $Fe^{2+/3+}$ ions can work as a contrast agent for biodistribution monitoring (see below) [187,194] and oxygen may relieve TME hypoxia and revert key immunosuppressive TME traits (e.g. TAM repolarization) (Fig. 1.11, a) [192,193].

(ii) **Oxidation state modulation in organometallic compounds:** Changes in the oxidation state of the central metal ion can induce changes in the biological relevance of an organometallic drug. Well-known clinically relevant metal-organic can be activated/generated through redox processes. [195,196]. For example, this is the case of biologically inactive Pt(IV)-based metallodrugs which can undergo activation upon Pt(IV) to Pt(II) reduction by intracellular thiol-rich glutathione, ascorbate or iron-rich heme groups (Fig. 1.11, c) [197].

(iii) **Enzyme-initiated self-immolative substrates:** Self-immolative substrates are clinically relevant redox-responsive moieties used in covalent bioconjugation strategies. They are typically initiated by enzymatic bond cleaving, which followed by an elimination reaction liberating CO_2, breaks the covalent structure and liberates the drug unmodified. A well-known example is para-amino benzyl alcohol (PABC) linked to Cathepsin B or glucuronidase enzyme-sensitive initiating linkers (Fig. 1.11, b) [198,199].

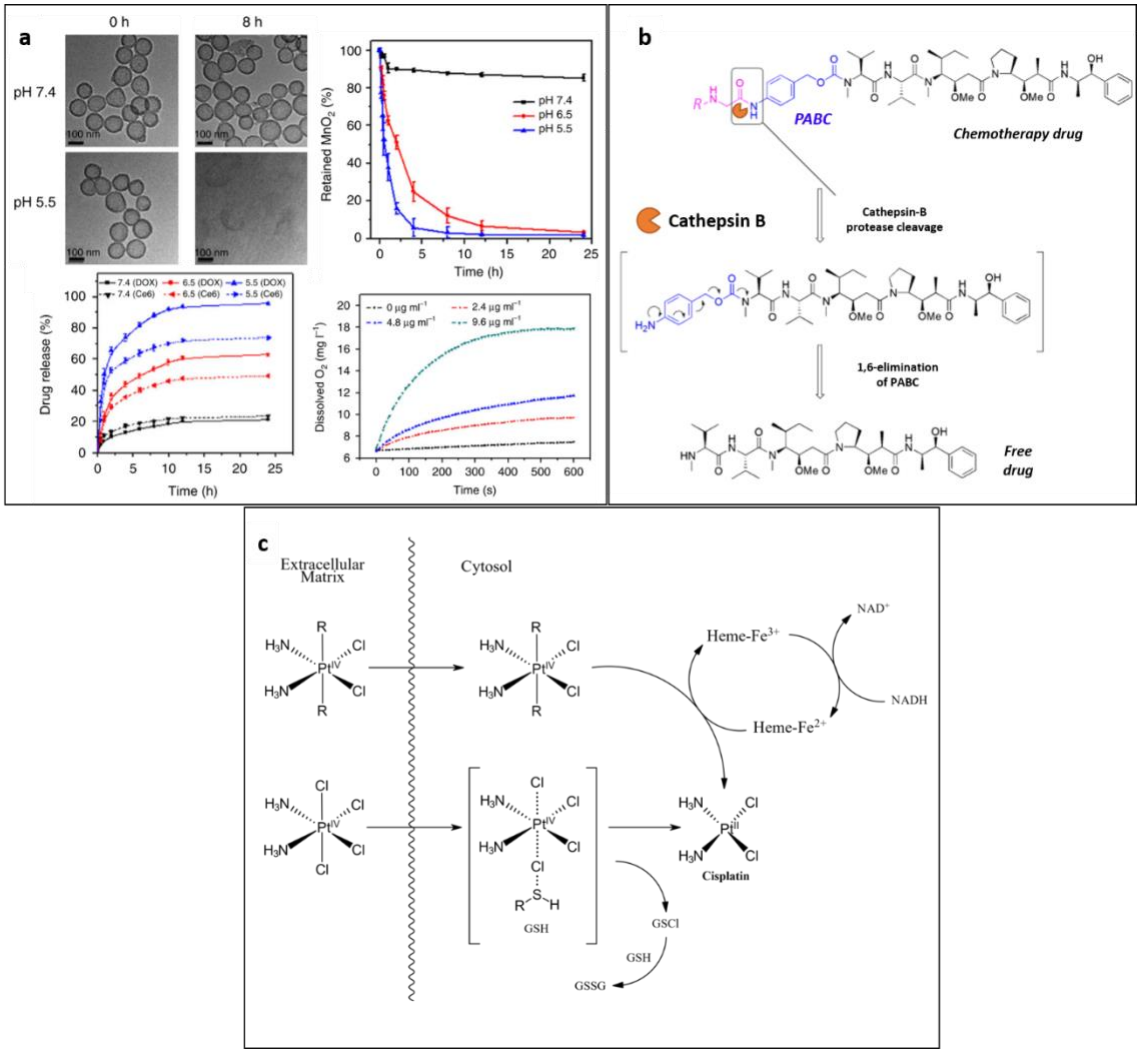

Figure 1.11. Redox-mediated drug release strategies. *(a) Redox-reactivity of hollow MnO_2 carriers can disassemble in the acidic and H_2O_2-rich TME triggering site-specific drug release and production of traceable Mn^{2+} ions and O_2 for hypoxia relief. Figure adapted from* [187]*. (b) PABC undergoes breakdown upon enzyme-initiated electron elimination thus releasing the captured drug. Figure adapted from* [200]*. (c) Two intracellular mechanisms of electronic reconfiguration for Pt(IV)-based metallodrugs yielding chemotherapy-active cisplatin (see Chapter 3).*

1.4.2.2.2.2. Exogenous-stimuli responsive drug delivery

1.4.2.2.2.2.1. Magnetic-responsive stimuli

Magnetic-responsive materials have proven beneficial for a wide variety of clinically-relevant therapeutic and diagnosis applications [201]. Among then, IONPs stand out for their excellent biocompatibility and tailorable properties [133,202]. Indeed, many synthetic

pathways have been devised to modulate IONP properties, including particle size, shape, surface area [203–208], phase change [209,210] or metal doping [211].

Two main strategies have been adopted for magnetic-responsive drug delivery:

(i) **Hyperthermic release:** Fast alternating magnetic spins generate heat resulting in increased local temperatures (hyperthermia). By modulating particle size, IONPs can acquire superparamagnetic behaviour (Fig. 1.12, a) [133]. Superparamagnetic iron oxide nanoparticles (SPIONs) require less energy inputs for spin inversion and thus show high heat generation capacity [212,213]. When an alternating magnetic field is applied, SPIONs embedded in the nanovehicle matrix can induce hyperthermia to trigger structural collapse and *on demand* drug release (Fig. 1.12, b) [214,215]. In addition, induction of magnetic hyperthermia as an anticancer therapy is known to trigger tumor ICD through DAMP and TAA release and MHC-I upregulation [216–221].

(ii) **Magnetic actuation:** Concentrating the therapeutic system into the tissue of interest is possible through magnetic navigation. Under an external magnetic field, therapeutic IONP nanovehicles can be directed and accumulated into the tissue of interest. These studies report an elevation in $CD8^+$ T-cell populations in tumor-draining lymph nodes [222] while decreasing systemic $CD8^+$ activation, which could become counterproductive for the therapy [223–226]. Similarly, ligand-presenting magnetic beads can be used to bind and isolate DC and $CD8^+$ T-cells [114,227,228] Finally, antigen-presenting magnetic beads can induce TCR clustering to enhance T-cell activation and expansion [83].

Magnetic fields can penetrate the target tissue, which allows for the treatment of both superficial and deep-seated tumors [229–231]. However, magnetic hyperthermia strategies are limited by the large concentrations of iron required and by the current impossibility of locally focusing the magnetic field at the targeted tissue [232,233].

1.4.2.2.2.2.2. Light-responsive stimuli

Photonic energy can be transformed into ROS and heat using a photosensitizer (PS). When a PS is exposed to light, it absorbs a photon which is promoted into an excited singlet state. This energy can be dissipated either by (i) thermal decay, (ii) emission of

fluorescence or (iii) intersystem crossing (ISC). ISC is a spin-forbidden process in which the excited singlet state S1 moves to a lower-energy excited triplet state T1. Release of energy from T1 state may induce singlet $^1O_2$ generation from molecular ground-state triplet $^3O_2$ (Fig. 1.11, c). ROS might be also generated after an electron is transferred from the photosensitizer to receptor molecules [234].

When the PS is loaded onto the endosome membrane, light-incidence can allow for on-demand endosomal drug escape through oxidative membrane damage (Fig. 1.12, d) [235–238]. Since the incidence of photoirradiation can be spatially concentrated, these therapies enable localized oxidative damage for tumor ICD and enhancement of DC maturation and TAM M1-activation [239–245]. However, the limited penetration depth of incident light limits these strategies to applications in superficial tumors only. Light-based strategies in the TME are also limited by lack of oxygen. Hence, they are typically coupled to redox-active O_2-generating nanodevices [193,246,247].

1.4.2.2.2.2.3. Ultrasound-responsive stimuli

Vibrational ultrasound (US) energy can be used to induce local increases in temperature and mechanical/cavitation effects for on-demand drug delivery. Vibrational energy can be transformed into ROS using sonodynamic synthetisers. These materials share their electronic properties and mechanisms of action with PSs (Fig. 1.12, c, e). Notable examples of sonodynamic synthetisers are organic porphyrins, [248,249] ZnO and TiO_2 nanoparticles [250,251] and quantum dots. [252]

Under incident US waves, temperature-sensitive structures can undergo on-demand structural collapse and liberate the cargo [253,254]. Also, mechanogenetics is a recently described therapeutic US-application that allows *on demand* mechanical modulation of signalling pathways and cell dynamics. In this context and for modulation of immune responses for anticancer application, Piezo1 is a Ca^{2+} ion channel and mechanical sensor that affects macrophage and T-cell immunity [255,256]. Incidence of vibrational ultrasound to Piezo1-targetting microbubbles has been shown to activate Piezo1 and favor T-cell anticancer killing effects (Fig. 1.12, f) [257]. US-based therapies can also cause tumor damage through temperature and mechanical strain. Ultrasound can be applied to increase blood flow and rearrange TME tumor vasculature for enhanced immune infiltration and

hypoxia relief [258]. US-mediated tumor killing can induce ICD and enable TAM M1-activation and DC maturation [253,259–262]. In comparison to heat-intensive hyperthermia or photo-thermal therapies, DAMP and TAA release can be triggered without generation of heat thus preventing protein denaturation [263]. However, ultrasound-based therapies suffer from limited tissue penetration due to wave scattering and intensity attenuation, particularly through air-filled organs such as the lungs and intestines [264].

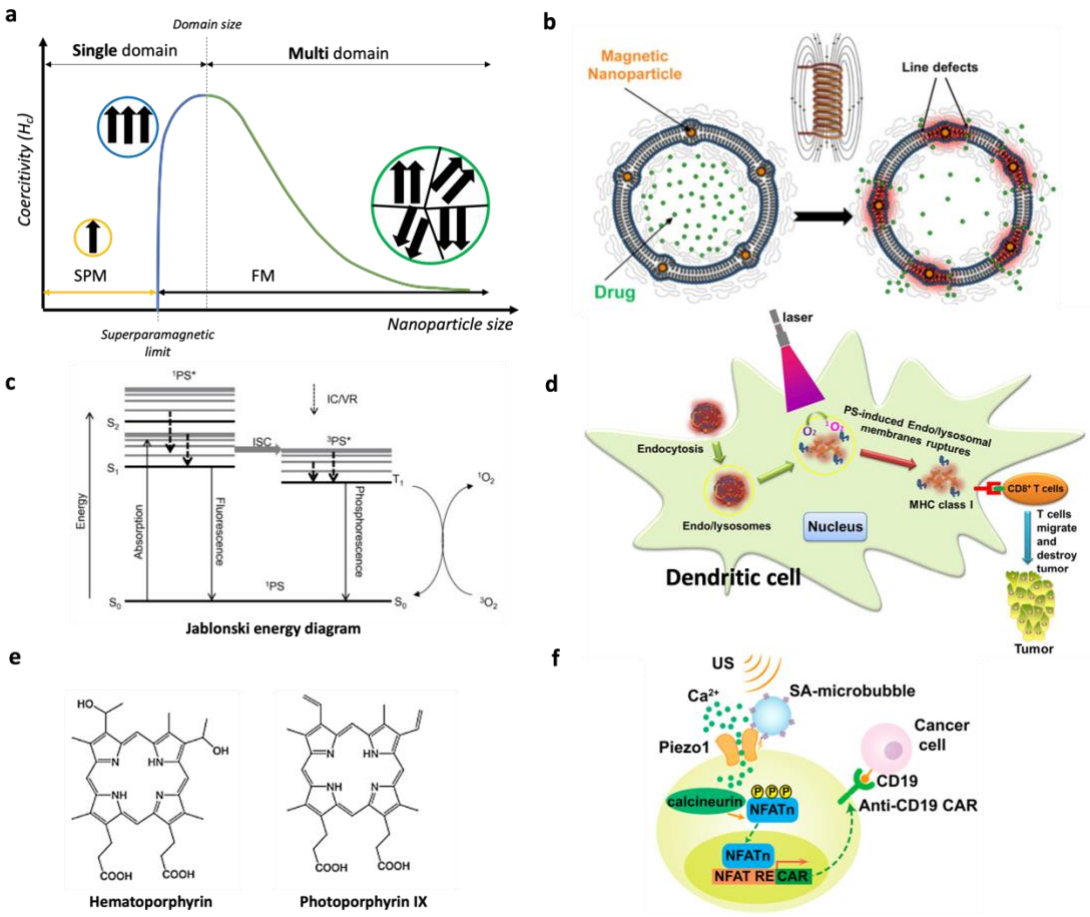

Figure 1.12. Exogenous stimuli-responsive strategies. *(a) Schematic representation of IONP superparamagnetic properties and their dependence with particle size. SPM, superparamagnetism, FM, ferromagnetism, Ms, magnetization saturation, Hc, magnetic coercivity. (b) Schematic representation of SPION-embedded liposomes for thermally controlled drug release. Figure taken from [215]. (c) Simplified Jablonski energy diagram for the generation of singlet oxygen after light or vibration energy absorption by photo- or sonosensitizers. Figure taken from [265]. (d) Endosome escape triggered upon PS induced ROS emission enhancing DC antigen cross-presentation and anticancer T-cell activation. Figure taken from [240] (e) Common porphyrin structures used as photo or sono-sensitizers. Figure adapted from [249]. (f) US-triggered mechanogenetic Piezo1 activation for enhanced T-cell anticancer action. Figure adapted from [257].*

1.4.2.3. Theranostics

Theranostics refers to the combination of therapeutics and diagnostics. The term describes molecular or nanosized systems that integrate therapeutic agents with imaging probes for *in vivo* therapy monitoring [266–268]. Theranostic vehicles enable the detection and treatment of the disease while visualizing the activity of the therapy (i.e. biodistribution, intracellular trafficking, drug release activation) in a non-invasive manner. Theranostics are useful to study the expression of relevant targetable markers before and after treatment, control off-target toxicities, determine alternative strategies for nonresponsive patients and accumulate information for further therapeutic improvement.

The imaging modalities commonly integrated in cancer nanomedicine carriers make use of:

a) **Magnetic Resonance Imaging (MRI)**: MRI is a diagnostic imaging modality that uses non-ionising -radiation, suitable for deep-tissue, high-resolution imaging. MRI is based on nuclear magnetic resonance and the magnetic properties and imaging of mainly hydrogen nuclei (protons) in the target tissue. Under a strong magnetic field, their nuclear spins align with the applied magnetic field. A radio-frequency pulse is then applied perpendicular to magnetic field, which causes the nuclei to resonate and alter their magnetic alignment. When the pulse is removed, the nuclei realign with the original magnetic field. This realignment phenomenon is referred to as “relaxation”. Relaxation releases energy in form of electromagnetic waves which can be recorded and reconstructed into a 3-dimentional MRI image [269–271]. Relaxation can be measured in two ways: T1 relaxation, which defines the time needed for longitudinal magnetization to recover (> 63% of ground state magnetization); and T2 relaxation, which defines the time needed for transverse magnetization to disappear. Image resolution is increased when the relaxation times of the water protons are shortened. Relaxation shortening can be achieved by increasing the strength of the incident magnetic field. However, this is a very costly approach. Instead, administration of contrast agents (CAs) can be used to decrease relaxation times of the protons surrounding the agent, leading to shaper and more precise images [272]. Broadly, CAs are divided

into: T1-weighted CAs, or positive contrast agents, when they shorten T1 relaxation times thus the enhanced areas appearing bright on T1-weighted images; or T2 CAs, or negative contrast agents, when they shorten T2 relaxation times thus appearing as darker areas in T2-weighted images. T1-CAs are usually highly paramagnetic agents consisting of Gd^{3+} and Mn^{2+}. T2-CAs are usually SPIONs.

b) **Nuclear imaging:** Nuclear imaging techniques are deep-tissue imaging modalities which detect high-energy photon (γ-ray) emission by radioactive tracers (radiotracers). The two main nuclear imaging techniques are Positron Emission Tomography (PET) and Single Photon Emission Computed Tomography (SPECT). SPECT detects γ-rays emitted from the radioactive decay of the radiotracer. Common SPECT radiotracers are technetium-99m (^{99m}Tc; $t_{1/2}$ = 6 h), iodine-123 (^{123}I; $t_{1/2}$ = 13 h) and gallium-67 (^{67}Ga; $t_{1/2}$ = 78 h). Instead, PET detects γ-rays emitted from an annihilated positron emitted by a proton-rich radiotracer. A positron (positive β-radiation) is emitted when a proton decays into a neutron in proton-rich isotopes. The emitted positron travels a short distance before it is annihilated by colliding with a surrounding electron. The collision produces the simultaneous emission of two anti-parallel high-energy γ-photons. The two γ-photons are recorded as a single coincident event, which produces images with higher resolution than SPECT. Common PET tracers like gallium-68 (^{68}Ga; $t_{1/2}$ = 68 min) or fluor-18 (^{18}F; $t_{1/2}$ = 110 min), which show relatively short half-lives and limit long-term experimentation [268,273,274]

c) **Optical imaging:** Optical imaging offers the highest spatial resolution of the three imaging modalities. However, its penetration depth is limited due to tissue light absorption and scattering. Hence, fluorescence imaging techniques are widely used for *in vitro* or *ex vivo* assays. When used for *in vivo* studies, it is limited to imaging centimetre-deep tissue. Optical imaging is mainly based on fluorophore-labeled tracers conjugated to targeting ligands, which allows the detection and quantification of different disease markers, as well as studying intracellular drug trafficking [275–278].

To compensate for each technique weaknesses and limitations, there is increasing interest in the design of multimodal systems that can be used for multimodal imaging applications. Again, owing to their highly biocompatible and tailorable features, IONPs

have shown unique features for the design of such multimodal theranostic vehicles for cancer therapy and diagnosis [202,279–281].

1.5. Justification and objectives of this research

Better understanding of the mechanisms involved in immunoediting, the immune response and development of novel technologies for site-specific drug delivery have enabled increasingly effective approaches for cancer therapy and diagnosis. The sections above provided an overview of the immunotherapeutic, nanomedicine and theranostic strategies that can be used to enhance clinical success. However, none of those strategies is free from limitations. There is a need for the development of combination cancer therapies and multimodal diagnostic strategies that can compensate for the weaknesses of each individual technique/therapy.

This thesis aims to harness the properties of IONP-based systems for cancer immunotherapy and combination therapy. A systematic nanoparticle engineering design rationale is established to integrate ICD-inducing redox reactivity, site-specific drug delivery and non-invasive imaging modalities for the development of generalizable theranostic platforms (Chapter II). The IONP redox activity is utilized to complement and enhance the scope and efficiency of platinum-based drugs for chemoimmunotherapy (Chapter III). ROS-mediated therapeutic mechanisms combined with potent TLRa adjuvants, antigen-presentation mechanisms and state-of-the-art ICB therapies are shown to result in complete tumor regression and long-memory acquisition *in vivo* (Chapter IV). Finally, specific customization of the vehicle is used to enable the delivery of potent ferroptosis inducers for cancer-specific cell death and the development of neoantigen-presenting nanovaccines for cancer (Chapter V).

The specific objectives of this work can be summarized as:

- The optimization of IONP-filled micelles (mIONPs) for cancer therapy by investigating:
    - The customization of intrinsic physicochemical features of the device (size, surface charge, stability, chemical reactivity).
    - The redox-active IONP core and the loading of TLRa adjuvants, DAMP-like danger signals and ferroptosis inducers to trigger cytotoxic immune cell activation and cancer-specific cell killing.

    - The loading and delivery of gold-standard chemotherapy drugs to complement and enhance their anticancer activity.
    - The incorporation of targeting ligands for tissue recognition and site-specific drug delivery.
    - The presentation of tumor neoantigens for the development of therapeutic nanovaccines for cancer.
- The demonstration of the efficacy of these mIONP systems as therapeutic agents in vitro in a panel of cancer of cell lines and *in vivo* in an aggressive and difficult to treat mouse melanoma model.

1.6. References

(1) Sung, H. et al. Global Cancer Statistics 2020: GLOBOCAN Estimates of Incidence and Mortality Worldwide for 36 Cancers in 185 Countries. *CA. Cancer J. Clin.* **2021**, *71* (3), 209–249. https://doi.org/10.3322/caac.21660.

(2) Sachet, M.; Liang, Y. Y.; Oehler, R. The Immune Response to Secondary Necrotic Cells. *Apoptosis* **2017**, *22* (10), 1189–1204. https://doi.org/10.1007/s10495-017-1413-z.

(3) Penn, I.; Starzl, T. E. Immunosuppression and Cancer. *Transplant. Proc.* **1973**, *5* (1), 943–947.

(4) Middleton, J. D.; Stover, D. G.; Hai, T. Chemotherapy-Exacerbated Breast Cancer Metastasis: A Paradox Explainable by Dysregulated Adaptive-Response. *Int. J. Mol. Sci.* **2018**, *19* (11). https://doi.org/10.3390/ijms19113333.

(5) Lee Ventola, C. *Cancer Immunotherapy, Part 2: Efficacy, Safety, and Other Clinical Considerations*; 2017; Vol. 42.

(6) Pardoll, D. M. The Blockade of Immune Checkpoints in Cancer Immunotherapy. *Nat. Rev. Cancer* **2012**, *12* (4), 252–264. https://doi.org/10.1038/nrc3239.

(7) Nam, J. et al. Cancer Nanomedicine for Combination Cancer Immunotherapy. *Nature Reviews Materials*. Nature Publishing Group June 26, 2019, pp 398–414. https://doi.org/10.1038/s41578-019-0108-1.

(8) Shi, Y.; Lammers, T. Combining Nanomedicine and Immunotherapy. *Acc. Chem. Res.* **2019**, *52* (6), 1543–1554. https://doi.org/10.1021/acs.accounts.9b00148.

(9) Schreiber, R. D.; Old, L. J.; Smyth, M. J. Cancer Immunoediting: Integrating Immunity's Roles in Cancer Suppression and Promotion. *Science (80-.).* **2011**, *331* (6024), 1565–1570. https://doi.org/10.1126/science.1203486.

(10) Cornel, A. M.; Mimpen, I. L.; Nierkens, S. MHC Class I Downregulation in Cancer: Underlying Mechanisms and Potential Targets for Cancer Immunotherapy. *Cancers (Basel).* **2020**, *12* (7), 1–33. https://doi.org/10.3390/cancers12071760.

(11) Pardoll, D. M. The Blockade of Immune Checkpoints in Cancer Immunotherapy. *Nat. Rev. Cancer* **2012**, *12* (4), 252–264. https://doi.org/10.1038/nrc3239.

(12) Jain, N.; Nguyen, H.; Chambers, C.; Kang, J. Dual Function of CTLA-4 in Regulatory T Cells and Conventional T Cells to Prevent Multiorgan Autoimmunity. *Proc. Natl. Acad. Sci. U. S. A.* **2010**, *107* (4), 1524–1528. https://doi.org/10.1073/pnas.0910341107.

(13) Hargadon, K. M.; Johnson, C. E.; Williams, C. J. Immune Checkpoint Blockade Therapy for Cancer: An Overview of FDA-Approved Immune Checkpoint Inhibitors. *Int. Immunopharmacol.* **2018**, *62*, 29–39.

https://doi.org/10.1016/j.intimp.2018.06.001.

(14) Vaupel, P.; Multhoff, G. Accomplices of the Hypoxic Tumor Microenvironment Compromising Antitumor Immunity: Adenosine, Lactate, Acidosis, Vascular Endothelial Growth Factor, Potassium Ions, and Phosphatidylserine. *Front. Immunol.* **2017**, *8* (DEC), 1887. https://doi.org/10.3389/fimmu.2017.01887.

(15) Gabrilovich, D. I. Myeloid-Derived Suppressor Cells. *Cancer Immunol. Res.* **2017**, *5* (1), 3–8. https://doi.org/10.1158/2326-6066.CIR-16-0297.

(16) Sica, A. et al. Macrophage Polarization in Tumour Progression. *Seminars in Cancer Biology*. 2008, pp 349–355. https://doi.org/10.1016/j.semcancer.2008.03.004.

(17) Quail, D. F.; Joyce, J. A. Microenvironmental Regulation of Tumor Progression and Metastasis. *Nat. Med.* **2013**, *19* (11), 1423–1437. https://doi.org/10.1038/nm.3394.

(18) Ratajczak, M. Z.; Bujko, K.; Mack, A.; Kucia, M.; Ratajczak, J. Cancer from the Perspective of Stem Cells and Misappropriated Tissue Regeneration Mechanisms. *Leukemia* **2018**, *32* (12), 2519–2526. https://doi.org/10.1038/s41375-018-0294-7.

(19) Dvorak, H. F. Tumors: Wounds That Do Not Heal-Redux. *Cancer Immunol. Res.* **2015**, *3* (1), 1–11. https://doi.org/10.1158/2326-6066.CIR-14-0209.

(20) Garrido, F.; Aptsiauri, N.; Doorduijn, E. M.; Garcia Lora, A. M.; van Hall, T. The Urgent Need to Recover MHC Class I in Cancers for Effective Immunotherapy. *Curr. Opin. Immunol.* **2016**, *39*, 44–51. https://doi.org/10.1016/j.coi.2015.12.007.

(21) Vinay, D. S. et al. Immune Evasion in Cancer: Mechanistic Basis and Therapeutic Strategies. *Semin. Cancer Biol.* **2015**, *35*, S185–S198. https://doi.org/10.1016/j.semcancer.2015.03.004.

(22) de Charette, M.; Marabelle, A.; Houot, R. Turning Tumour Cells into Antigen Presenting Cells: The next Step to Improve Cancer Immunotherapy? *Eur. J. Cancer* **2016**, *68*, 134–147. https://doi.org/10.1016/j.ejca.2016.09.010.

(23) Marabelle, A. et al. Erratum: Depleting Tumor-Specific Tregs at a Single Site Eradicates Disseminated Tumors (Journal of Clinical Investigation (2013) 123:11 (4980) DOI:10.1172/JCI73340). *J. Clin. Invest.* **2013**, *123* (11), 4980. https://doi.org/10.1172/jci73340.

(24) Galon, J.; Bruni, D. Approaches to Treat Immune Hot, Altered and Cold Tumours with Combination Immunotherapies. *Nat. Rev. Drug Discov.* **2019**, *18* (3), 197–218. https://doi.org/10.1038/s41573-018-0007-y.

(25) Kroemer, G.; Galluzzi, L.; Kepp, O.; Zitvogel, L. Immunogenic Cell Death in Cancer Therapy. *Annu. Rev. Immunol.* **2013**, *31* (1), 51–72.

https://doi.org/10.1146/annurev-immunol-032712-100008.

(26) Zhou, J. et al. Immunogenic Cell Death in Cancer Therapy: Present and Emerging Inducers. *J. Cell. Mol. Med.* **2019**, *23* (8), 4854–4865. https://doi.org/10.1111/jcmm.14356.

(27) Rodriguez-Ruiz, M. E.; Vitale, I.; Harrington, K. J.; Melero, I.; Galluzzi, L. Immunological Impact of Cell Death Signaling Driven by Radiation on the Tumor Microenvironment. *Nat. Immunol.* **2020**, *21* (2), 120–134. https://doi.org/10.1038/s41590-019-0561-4.

(28) Gorrini, C.; Harris, I. S.; Mak, T. W. Modulation of Oxidative Stress as an Anticancer Strategy. *Nat. Rev. Drug Discov.* **2013**, *12* (12), 931–947. https://doi.org/10.1038/nrd4002.

(29) Zou, Z.; Chang, H.; Li, H.; Wang, S. Induction of Reactive Oxygen Species: An Emerging Approach for Cancer Therapy. *Apoptosis* **2017**, *22* (11), 1321–1335. https://doi.org/10.1007/s10495-017-1424-9.

(30) Ayala, A.; Muñoz, M. F.; Argüelles, S. Lipid Peroxidation: Production, Metabolism, and Signaling Mechanisms of Malondialdehyde and 4-Hydroxy-2-Nonenal. *Oxid. Med. Cell. Longev.* **2014**, *2014*. https://doi.org/10.1155/2014/360438.

(31) Szatrowski, T. P.; Nathan, C. F. Production of Large Amounts of Hydrogen Peroxide by Human Tumor Cells. *Cancer Res.* **1991**, *51* (3), 794–798.

(32) Dixon, S. J. et al. Ferroptosis: An Iron-Dependent Form of Nonapoptotic Cell Death. *Cell* **2012**, *149* (5), 1060–1072. https://doi.org/10.1016/j.cell.2012.03.042.

(33) Ranji-Burachaloo, H.; Gurr, P. A.; Dunstan, D. E.; Qiao, G. G. Cancer Treatment through Nanoparticle-Facilitated Fenton Reaction. *ACS Nano* **2018**, *12* (12), 11819–11837. https://doi.org/10.1021/acsnano.8b07635.

(34) Liu, Y. et al. Topical Ferumoxytol Nanoparticles Disrupt Biofilms and Prevent Tooth Decay in Vivo via Intrinsic Catalytic Activity. *Nat. Commun.* **2018**, *9* (1), 2920. https://doi.org/10.1038/s41467-018-05342-x.

(35) Badgley, M. A. et al. Cysteine Depletion Induces Pancreatic Tumor Ferroptosis in Mice. *Science (80-.).* **2020**, *368* (6486), 85–89. https://doi.org/10.1126/science.aaw9872.

(36) Trachootham, D.; Alexandre, J.; Huang, P. Targeting Cancer Cells by ROS-Mediated Mechanisms: A Radical Therapeutic Approach? *Nat. Rev. Drug Discov.* **2009**, *8* (7), 579–591. https://doi.org/10.1038/nrd2803.

(37) Friedmann Angeli, J. P.; Krysko, D. V.; Conrad, M. Ferroptosis at the Crossroads of Cancer-Acquired Drug Resistance and Immune Evasion. *Nat. Rev. Cancer* **2019**, *19* (7), 405–414. https://doi.org/10.1038/s41568-019-0149-1.

(38) Li, J. et al. Ferroptosis: Past, Present and Future. *Cell Death Dis.* **2020**, *11* (2). https://doi.org/10.1038/s41419-020-2298-2.

(39) Hassannia, B.; Vandenabeele, P.; Vanden Berghe, T. Targeting Ferroptosis to Iron Out Cancer. *Cancer Cell* **2019**, *35* (6), 830–849. https://doi.org/10.1016/j.ccell.2019.04.002.

(40) Mou, Y. et al. Ferroptosis, a New Form of Cell Death: Opportunities and Challenges in Cancer. *J. Hematol. Oncol.* **2019**, *12* (1), 34. https://doi.org/10.1186/s13045-019-0720-y.

(41) Shan, X. et al. Ferroptosis-Driven Nanotherapeutics for Cancer Treatment. *J. Control. Release* **2020**, *319*, 322–332. https://doi.org/10.1016/j.jconrel.2020.01.008.

(42) Huo, M.; Wang, L.; Chen, Y.; Shi, J. Tumor-Selective Catalytic Nanomedicine by Nanocatalyst Delivery. *Nat. Commun.* **2017**, *8* (1), 357. https://doi.org/10.1038/s41467-017-00424-8.

(43) Lin, H.; Chen, Y.; Shi, J. Nanoparticle-Triggered: In Situ Catalytic Chemical Reactions for Tumour-Specific Therapy. *Chem. Soc. Rev.* **2018**, *47* (6), 1938–1958. https://doi.org/10.1039/c7cs00471k.

(44) Sarhan, M.; Von Mässenhausen, A.; Hugo, C.; Oberbauer, R.; Linkermann, A. Immunological Consequences of Kidney Cell Death Review-Paper. *Cell Death Dis.* **2018**, *9* (2). https://doi.org/10.1038/s41419-017-0057-9.

(45) Xie, Y. et al. Ferroptosis: Process and Function. *Cell Death Differ.* **2016**, *23* (3), 369–379. https://doi.org/10.1038/cdd.2015.158.

(46) Vernon, P. J.; Tang, D. Eat-Me: Autophagy, Phagocytosis, and Reactive Oxygen Species Signaling. *Antioxidants Redox Signal.* **2013**, *18* (6), 677–691. https://doi.org/10.1089/ars.2012.4810.

(47) Mittal, M.; Siddiqui, M. R.; Tran, K.; Reddy, S. P.; Malik, A. B. Reactive Oxygen Species in Inflammation and Tissue Injury. *Antioxidants Redox Signal.* **2014**, *20* (7), 1126–1167. https://doi.org/10.1089/ars.2012.5149.

(48) Garg, A. D.; Romano, E.; Rufo, N.; Agostinis, P. Immunogenic versus Tolerogenic Phagocytosis during Anticancer Therapy: Mechanisms and Clinical Translation. *Cell Death Differ.* **2016**, *23* (6), 938–951. https://doi.org/10.1038/cdd.2016.5.

(49) Feng, M. et al. Phagocytosis Checkpoints as New Targets for Cancer Immunotherapy. *Nat. Rev. Cancer* **2019**, *19* (10), 568–586. https://doi.org/10.1038/s41568-019-0183-z.

(50) Tan, H. Y. et al. The Reactive Oxygen Species in Macrophage Polarization: Reflecting Its Dual Role in Progression and Treatment of Human Diseases. *Oxid. Med. Cell. Longev.* **2016**, *2016*, 1–16. https://doi.org/10.1155/2016/2795090.

(51) Hernandez, C.; Huebener, P.; Schwabe, R. F. Damage-Associated Molecular Patterns in Cancer: A Double-Edged Sword. *Oncogene* **2016**, *35* (46), 5931–5941. https://doi.org/10.1038/onc.2016.104.

(52) Bedognetti, D. et al. Toward a Comprehensive View of Cancer Immune Responsiveness: A Synopsis from the SITC Workshop. *J. Immunother. Cancer* **2019**, *7* (1), 131. https://doi.org/10.1186/s40425-019-0602-4.

(53) Perica, K.; Varela, J. C.; Oelke, M.; Schneck, J. Adoptive T Cell Immunotherapy For Cancer. *Rambam Maimonides Med. J.* **2015**, *6* (1), e0004. https://doi.org/10.5041/rmmj.10179.

(54) Rosenberg, S. A.; Restifo, N. P.; Yang, J. C.; Morgan, R. A.; Dudley, M. E. Adoptive Cell Transfer: A Clinical Path to Effective Cancer Immunotherapy. *Nat. Rev. Cancer* **2008**, *8* (4), 299–308. https://doi.org/10.1038/nrc2355.

(55) Chen, Y. et al. Tumor-Associated Macrophages: An Accomplice in Solid Tumor Progression. *J. Biomed. Sci.* **2019**, *26* (1), 1–13. https://doi.org/10.1186/s12929-019-0568-z.

(56) Lian, G. et al. Colon Cancer Cell Secretes EGF to Promote M2 Polarization of TAM Through EGFR/PI3K/AKT/MTOR Pathway. *Technol. Cancer Res. Treat.* **2019**, *18*. https://doi.org/10.1177/1533033819849068.

(57) Zhang, F. et al. TGF-β Induces M2-like Macrophage Polarization via SNAILmediated Suppression of a pro-Inflammatory Phenotype. *Oncotarget* **2016**, *7* (32), 52294–52306. https://doi.org/10.18632/oncotarget.10561.

(58) Muliaditan, T. et al. Macrophages Are Exploited from an Innate Wound Healing Response to Facilitate Cancer Metastasis. *Nat. Commun.* **2018**, *9* (1), 2951. https://doi.org/10.1038/s41467-018-05346-7.

(59) Kohno, K. et al. Inflammatory M1-like Macrophages Polarized by NK-4 Undergo Enhanced Phenotypic Switching to an Anti-Inflammatory M2-like Phenotype upon Co-Culture with Apoptotic Cells. *J. Inflamm. (United Kingdom)* **2021**, *18* (1), 1–14. https://doi.org/10.1186/s12950-020-00267-z.

(60) Ngambenjawong, C.; Gustafson, H. H.; Pun, S. H. Progress in Tumor-Associated Macrophage (TAM)-Targeted Therapeutics. *Adv. Drug Deliv. Rev.* **2017**, *114*, 206–221. https://doi.org/10.1016/j.addr.2017.04.010.

(61) Zhou, Y. et al. Iron Overloaded Polarizes Macrophage to Proinflammation Phenotype through ROS/Acetyl-P53 Pathway. *Cancer Med.* **2018**, *7* (8), 4012–4022. https://doi.org/10.1002/cam4.1670.

(62) Liu, L. et al. ROS-Inducing Micelles Sensitize Tumor-Associated Macrophages to TLR3 Stimulation for Potent Immunotherapy. *Biomacromolecules* **2018**, *19* (6), 2146–2155. https://doi.org/10.1021/acs.biomac.8b00239.

(63) DiDomenico, J. et al. The Immune Checkpoint Protein PD-L1 Induces and

Maintains Regulatory T Cells in Glioblastoma. *Oncoimmunology* **2018**, *7* (7), e1448329. https://doi.org/10.1080/2162402X.2018.1448329.

(64) Diskin, B. et al. PD-L1 Engagement on T Cells Promotes Self-Tolerance and Suppression of Neighboring Macrophages and Effector T Cells in Cancer. *Nat. Immunol.* **2020**, *21* (4), 442–454. https://doi.org/10.1038/s41590-020-0620-x.

(65) Philips, G. K.; Atkins, M. Therapeutic Uses of Anti-PD-1 and Anti-PD-L1 Antibodies. *Int. Immunol.* **2015**, *27* (1), 39–46. https://doi.org/10.1093/intimm/dxu095.

(66) Kang, H. et al. Theranostic Nanosystems for Targeted Cancer Therapy. *Nano Today* **2018**, *23*, 59–72. https://doi.org/10.1016/j.nantod.2018.11.001.

(67) Aspeslagh, S. et al. Rationale for Anti-OX40 Cancer Immunotherapy. *Eur. J. Cancer* **2016**, *52*, 50–66. https://doi.org/10.1016/j.ejca.2015.08.021.

(68) Gong, J.; Chehrazi-Raffle, A.; Reddi, S.; Salgia, R. Development of PD-1 and PD-L1 Inhibitors as a Form of Cancer Immunotherapy: A Comprehensive Review of Registration Trials and Future Considerations. *J. Immunother. Cancer* **2018**, *6* (1), 8. https://doi.org/10.1186/s40425-018-0316-z.

(69) Messenheimer, D. J. et al. Timing of PD-1 Blockade Is Critical to Effective Combination Immunotherapy with Anti-OX40. *Clin. Cancer Res.* **2017**, *23* (20), 6165–6177. https://doi.org/10.1158/1078-0432.CCR-16-2677.

(70) Myers, G. Immune-Related Adverse Events of Immune Checkpoint Inhibitors: A Brief Review. *Curr. Oncol.* **2018**, *25* (5), 342–347. https://doi.org/10.3747/co.25.4235.

(71) Chuzi, S. et al. Clinical Features, Diagnostic Challenges, and Management Strategies in Checkpoint Inhibitor-Related Pneumonitis. *Cancer Manag. Res.* **2017**, *9*, 207–213. https://doi.org/10.2147/CMAR.S136818.

(72) Chae, Y. K. et al. Current Landscape and Future of Dual Anti-CTLA4 and PD-1/PD-L1 Blockade Immunotherapy in Cancer; Lessons Learned from Clinical Trials with Melanoma and Non-Small Cell Lung Cancer (NSCLC). *J. Immunother. Cancer* **2018**, *6* (1), 39. https://doi.org/10.1186/s40425-018-0349-3.

(73) Mandai, M. et al. Dual Faces of Ifnγ in Cancer Progression: A Role of Pd-L1 Induction in the Determination of Proand Antitumor Immunity. *Clin. Cancer Res.* **2016**, *22* (10), 2329–2334. https://doi.org/10.1158/1078-0432.CCR-16-0224.

(74) Jenkins, R. W.; Barbie, D. A.; Flaherty, K. T. Mechanisms of Resistance to Immune Checkpoint Inhibitors. *Br. J. Cancer* **2018**, *118* (1), 9–16. https://doi.org/10.1038/bjc.2017.434.

(75) Friedman, C. F.; Proverbs-Singh, T. A.; Postow, M. A. Treatment of the Immune-Related Adverse Effects of Immune Checkpoint Inhibitors: A Review.

JAMA Oncol. **2016**, *2* (10), 1346–1353. https://doi.org/10.1001/jamaoncol.2016.1051.

(76) Moslehi, J. J.; Salem, J. E.; Sosman, J. A.; Lebrun-Vignes, B.; Johnson, D. B. Increased Reporting of Fatal Immune Checkpoint Inhibitor-Associated Myocarditis. *Lancet* **2018**, *391* (10124), 933. https://doi.org/10.1016/S0140-6736(18)30533-6.

(77) Dingjan, I. et al. Lipid Peroxidation Causes Endosomal Antigen Release for Cross-Presentation. *Sci. Rep.* **2016**, *6* (1), 22064. https://doi.org/10.1038/srep22064.

(78) Peng, W. et al. PD-1 Blockade Enhances T-Cell Migration to Tumors by Elevating IFN-γ Inducible Chemokines. *Cancer Res.* **2012**, *72* (20), 5209–5218. https://doi.org/10.1158/0008-5472.CAN-12-1187.

(79) Chen, H. et al. Anti-CTLA-4 Therapy Results in Higher CD4 +ICOS Hi T Cell Frequency and IFN-γ Levels in Both Nonmalignant and Malignant Prostate Tissues. *Proc. Natl. Acad. Sci. U. S. A.* **2009**, *106* (8), 2729–2734. https://doi.org/10.1073/pnas.0813175106.

(80) Karachaliou, N. et al. Interferon Gamma, an Important Marker of Response to Immune Checkpoint Blockade in Non-Small Cell Lung Cancer and Melanoma Patients. *Ther. Adv. Med. Oncol.* **2018**, *10*, 1758834017749748. https://doi.org/10.1177/1758834017749748.

(81) Ammi, R. et al. Poly(I:C) as Cancer Vaccine Adjuvant: Knocking on the Door of Medical Breakthroughs. *Pharmacol. Ther.* **2015**, *146*, 120–131. https://doi.org/10.1016/j.pharmthera.2014.09.010.

(82) Ma, F.; Zhang, J.; Zhang, J.; Zhang, C. The TLR7 Agonists Imiquimod and Gardiquimod Improve DC-Based Immunotherapy for Melanoma in Mice. *Cell. Mol. Immunol.* **2010**, *7* (5), 381–388. https://doi.org/10.1038/cmi.2010.30.

(83) Perica, K. et al. Magnetic Field-Induced t Cell Receptor Clustering by Nanoparticles Enhances t Cell Activation and Stimulates Antitumor Activity. *ACS Nano* **2014**, *8* (3), 2252–2260. https://doi.org/10.1021/nn405520d.

(84) Shi, Y.; Lammers, T. Combining Nanomedicine and Immunotherapy. *Acc. Chem. Res.* **2019**, *52* (6), 1543–1554. https://doi.org/10.1021/acs.accounts.9b00148.

(85) van der Meel, R. et al. Smart Cancer Nanomedicine. *Nat. Nanotechnol.* **2019**, *14* (11), 1007–1017. https://doi.org/10.1038/s41565-019-0567-y.

(86) He, H.; Liu, L.; Morin, E. E.; Liu, M.; Schwendeman, A. Survey of Clinical Translation of Cancer Nanomedicines - Lessons Learned from Successes and Failures. *Acc. Chem. Res.* **2019**, *52* (9), 2673–2683. https://doi.org/10.1021/acs.accounts.9b00228.

(87) Hare, J. I. et al. Challenges and Strategies in Anti-Cancer Nanomedicine

Development: An Industry Perspective. *Adv. Drug Deliv. Rev.* **2017**, *108*, 25–38. https://doi.org/10.1016/j.addr.2016.04.025.

(88) Pati, R.; Shevtsov, M.; Sonawane, A. Nanoparticle Vaccines against Infectious Diseases. *Front. Immunol.* **2018**, *9* (OCT), 2224. https://doi.org/10.3389/fimmu.2018.02224.

(89) Chen, G.; Roy, I.; Yang, C.; Prasad, P. N. Nanochemistry and Nanomedicine for Nanoparticle-Based Diagnostics and Therapy. *Chem. Rev.* **2016**, *116* (5), 2826–2885. https://doi.org/10.1021/acs.chemrev.5b00148.

(90) Kauscher, U.; Holme, M. N.; Björnmalm, M.; Stevens, M. M. Physical Stimuli-Responsive Vesicles in Drug Delivery: Beyond Liposomes and Polymersomes. *Adv. Drug Deliv. Rev.* **2019**, *138*, 259–275. https://doi.org/10.1016/j.addr.2018.10.012.

(91) Zhou, Q.; Zhang, L.; Yang, T. H.; Wu, H. Stimuli-Responsive Polymeric Micelles for Drug Delivery and Cancer Therapy. *Int. J. Nanomedicine* **2018**, *13*, 2921–2942. https://doi.org/10.2147/IJN.S158696.

(92) Haghiralsadat, F. et al. Preparation of PEGylated Cationic Nanoliposome-SiRNA Complexes for Cancer Therapy. *Artif. Cells, Nanomedicine Biotechnol.* **2018**, *46* (sup1), 684–692. https://doi.org/10.1080/21691401.2018.1434533.

(93) Leriche, G. et al. Characterization of Drug Encapsulation and Retention in Archaea-Inspired Tetraether Liposomes. *Org. Biomol. Chem.* **2017**, *15* (10), 2157–2162. https://doi.org/10.1039/c6ob02832b.

(94) Suk, J. S.; Xu, Q.; Kim, N.; Hanes, J.; Ensign, L. M. PEGylation as a Strategy for Improving Nanoparticle-Based Drug and Gene Delivery. *Adv. Drug Deliv. Rev.* **2016**, *99*, 28–51. https://doi.org/10.1016/j.addr.2015.09.012.

(95) Parks, M. H. Fact Sheet for Recipients and Caregivers Emergency Use Authorization (Eua) Of. **2009**, 1–24.

(96) Wu, W.; Wu, Z.; Yu, T.; Jiang, C.; Kim, W. S. Recent Progress on Magnetic Iron Oxide Nanoparticles: Synthesis, Surface Functional Strategies and Biomedical Applications. *Sci. Technol. Adv. Mater.* **2015**, *16* (2), 023501. https://doi.org/10.1088/1468-6996/16/2/023501.

(97) Vallabani, N. V. S.; Singh, S. Recent Advances and Future Prospects of Iron Oxide Nanoparticles in Biomedicine and Diagnostics. *3 Biotech* **2018**, *8* (6), 279. https://doi.org/10.1007/s13205-018-1286-z.

(98) Almeida, J. P. M.; Figueroa, E. R.; Drezek, R. A. Gold Nanoparticle Mediated Cancer Immunotherapy. *Nanomedicine: Nanotechnology, Biology, and Medicine*. 2014, pp 503–514. https://doi.org/10.1016/j.nano.2013.09.011.

(99) Karlsson, H. L.; Cronholm, P.; Gustafsson, J.; Möller, L. Copper Oxide Nanoparticles Are Highly Toxic: A Comparison between Metal Oxide

Nanoparticles and Carbon Nanotubes. *Chem. Res. Toxicol.* **2008**, *21* (9), 1726–1732. https://doi.org/10.1021/tx800064j.

(100) De Jong, W. H.; Borm, P. J. A. Drug Delivery and Nanoparticles: Applications and Hazards. *Int. J. Nanomedicine* **2008**, *3* (2), 133–149. https://doi.org/10.2147/ijn.s596.

(101) Mao, B. H.; Chen, Z. Y.; Wang, Y. J.; Yan, S. J. Silver Nanoparticles Have Lethal and Sublethal Adverse Effects on Development and Longevity by Inducing ROS-Mediated Stress Responses. *Sci. Rep.* **2018**, *8* (1), 1–16. https://doi.org/10.1038/s41598-018-20728-z.

(102) Ruiz-De-Angulo, A.; Zabaleta, A.; Gómez-Vallejo, V.; Llop, J.; Mareque-Rivas, J. C. Microdosed Lipid-Coated 67Ga-Magnetite Enhances Antigen-Specific Immunity by Image Tracked Delivery of Antigen and Cpg to Lymph Nodes. *ACS Nano* **2016**, *10* (1), 1602–1618. https://doi.org/10.1021/acsnano.5b07253.

(103) Chakravarty, R. et al. Intrinsically Germanium-69-Labeled Iron Oxide Nanoparticles: Synthesis and in-Vivo Dual-Modality PET/MR Zimaging. *Adv. Mater.* **2014**, *26* (30), 5119–5123. https://doi.org/10.1002/adma.201401372.

(104) Sun, S. et al. Monodisperse MFe2O4 (M = Fe, Co, Mn) Nanoparticles. *J. Am. Chem. Soc.* **2004**, *126* (1), 273–279. https://doi.org/10.1021/ja0380852.

(105) Kim, J. et al. Continuous O2-Evolving MnFe2O4 Nanoparticle-Anchored Mesoporous Silica Nanoparticles for Efficient Photodynamic Therapy in Hypoxic Cancer. *J. Am. Chem. Soc.* **2017**, *139* (32), 10992–10995. https://doi.org/10.1021/jacs.7b05559.

(106) Joshi, A.; Naatz, H.; Faber, K.; Pokhrel, S.; Dringen, R. Iron-Doping of Copper Oxide Nanoparticles Lowers Their Toxic Potential on C6 Glioma Cells. *Neurochem. Res.* **2020**, *45* (4), 809–824. https://doi.org/10.1007/s11064-020-02954-y.

(107) Hu, Y.; Mignani, S.; Majoral, J. P.; Shen, M.; Shi, X. Construction of Iron Oxide Nanoparticle-Based Hybrid Platforms for Tumor Imaging and Therapy. *Chem. Soc. Rev.* **2018**, *47* (5), 1874–1900. https://doi.org/10.1039/c7cs00657h.

(108) Kondrashova, N. B. et al. Preparation and Properties of Iron Oxide Doped Mesoporous Silica Systems. *J. Inorg. Organomet. Polym. Mater.* **2020**, *30* (6), 2081–2088. https://doi.org/10.1007/s10904-019-01370-2.

(109) Alvarez-Berrios, M. P.; Sosa-Cintron, N.; Rodriguez-Lugo, M.; Juneja, R.; Vivero-Escoto, J. L. Hybrid Nanomaterials Based on Iron Oxide Nanoparticles and Mesoporous Silica Nanoparticles: Overcoming Challenges in Current Cancer Treatments. *J. Chem.* **2016**, *2016*. https://doi.org/10.1155/2016/2672740.

(110) Croissant, J. G.; Fatieiev, Y.; Khashab, N. M. Degradability and Clearance of Silicon, Organosilica, Silsesquioxane, Silica Mixed Oxide, and Mesoporous Silica Nanoparticles. *Adv. Mater.* **2017**, *29* (9).

https://doi.org/10.1002/adma.201604634.

(111) Li, L. et al. Biodistribution, Excretion, and Toxicity of Mesoporous Silica Nanoparticles after Oral Administration Depend on Their Shape. *Nanomedicine Nanotechnology, Biol. Med.* **2015**, *11* (8), 1915–1924. https://doi.org/10.1016/j.nano.2015.07.004.

(112) Guan, Q. et al. Mesoporous Polydopamine Carrying Sorafenib and SPIO Nanoparticles for MRI-Guided Ferroptosis Cancer Therapy. *J. Control. Release* **2020**, *320*, 392–403. https://doi.org/10.1016/j.jconrel.2020.01.048.

(113) Zhang, Y. et al. Aptamer-Anchored Di-Polymer Shell-Capped Mesoporous Carbon as a Drug Carrier for Bi-Trigger Targeted Drug Delivery. *J. Mater. Chem. B* **2017**, *5* (33), 6882–6889. https://doi.org/10.1039/c7tb01528c.

(114) Fadel, T. R. et al. A Carbon Nanotube-Polymer Composite for T-Cell Therapy. *Nat. Nanotechnol.* **2014**, *9* (8), 639–647. https://doi.org/10.1038/nnano.2014.154.

(115) Yang, G. et al. An Implantable Active-Targeting Micelle-in-Nanofiber Device for Efficient and Safe Cancer Therapy. *ACS Nano* **2015**, *9* (2), 1161–1174. https://doi.org/10.1021/nn504573u.

(116) Samadzadeh, S.; Babazadeh, M.; Zarghami, N.; Pilehvar-Soltanahmadi, Y.; Mousazadeh, H. An Implantable Smart Hyperthermia Nanofiber with Switchable, Controlled and Sustained Drug Release: Possible Application in Prevention of Cancer Local Recurrence. *Mater. Sci. Eng. C* **2021**, *118*, 111384. https://doi.org/10.1016/j.msec.2020.111384.

(117) Qiu, K. et al. Doxorubicin-Loaded Electrospun Poly(l-Lactic Acid)/Mesoporous Silica Nanoparticles Composite Nanofibers for Potential Postsurgical Cancer Treatment. *J. Mater. Chem. B* **2013**, *1* (36), 4601–4611. https://doi.org/10.1039/c3tb20636j.

(118) Wu, M. X.; Yang, Y. W. Metal–Organic Framework (MOF)-Based Drug/Cargo Delivery and Cancer Therapy. *Adv. Mater.* **2017**, *29* (23), 1–20. https://doi.org/10.1002/adma.201606134.

(119) Zheng, D. W. et al. Switching Apoptosis to Ferroptosis: Metal-Organic Network for High-Efficiency Anticancer Therapy. *Nano Lett.* **2017**, *17* (1), 284–291. https://doi.org/10.1021/acs.nanolett.6b04060.

(120) Horcajada, P. et al. Porous Metal-Organic-Framework Nanoscale Carriers as a Potential Platform for Drug Deliveryand Imaging. *Nat. Mater.* **2010**, *9* (2), 172–178. https://doi.org/10.1038/nmat2608.

(121) Sajid, M. Toxicity of Nanoscale Metal Organic Frameworks: A Perspective. *Environ. Sci. Pollut. Res.* **2016**, *23* (15), 14805–14807. https://doi.org/10.1007/s11356-016-7053-y.

(122) Cook, T. R.; Zheng, Y. R.; Stang, P. J. Metal-Organic Frameworks and Self-

Assembled Supramolecular Coordination Complexes: Comparing and Contrasting the Design, Synthesis, and Functionality of Metal-Organic Materials. *Chem. Rev.* **2013**, *113* (1), 734–777. https://doi.org/10.1021/cr3002824.

(123) Gao, Z. et al. Iron Oxide Nanocarrier-Mediated Combination Therapy of Cisplatin and Artemisinin for Combating Drug Resistance through Highly Increased Toxic Reactive Oxygen Species Generation. *ACS Appl. Bio Mater.* **2018**, *1* (2), 270–280. https://doi.org/10.1021/acsabm.8b00056.

(124) Ruiz-de-Angulo, A. et al. Chemically Programmed Vaccines: Iron Catalysis in Nanoparticles Enhances Combination Immunotherapy and Immunotherapy-Promoted Tumor Ferroptosis. *iScience* **2020**, *23* (9). https://doi.org/10.1016/j.isci.2020.101499.

(125) Nath, A. et al. Gold-manganese Oxide Nanocomposite Suppresses Hypoxia and Augments Pro-Inflammatory Cytokines in Tumor Associated Macrophages. *Int. Immunopharmacol.* **2018**, *57*, 157–164. https://doi.org/10.1016/j.intimp.2018.02.021.

(126) Islam, M. N. et al. Gold-Loaded Nanoporous Ferric Oxide Nanocubes for Electrocatalytic Detection of MicroRNA at Attomolar Level. *Biosens. Bioelectron.* **2018**, *101*, 275–281. https://doi.org/10.1016/j.bios.2017.09.027.

(127) Ju, Y. et al. Monodisperse Au-Fe2C Janus Nanoparticles: An Attractive Multifunctional Material for Triple-Modal Imaging-Guided Tumor Photothermal Therapy. *ACS Nano* **2017**, *11* (9), 9239–9248. https://doi.org/10.1021/acsnano.7b04461.

(128) Deng, Z. et al. One Stone Two Birds: Zr-Fc Metal-Organic Framework Nanosheet for Synergistic Photothermal and Chemodynamic Cancer Therapy. *ACS Appl. Mater. Interfaces* **2020**, *12* (18), 20321–20330. https://doi.org/10.1021/acsami.0c06648.

(129) Tagliamonte, M.; Petrizzo, A.; Tornesello, M. L.; Buonaguro, F. M.; Buonaguro, L. Antigen-Specific Vaccines for Cancer Treatment. *Hum. Vaccines Immunother.* **2014**, *10* (11), 3332–3346. https://doi.org/10.4161/21645515.2014.973317.

(130) Napolitani, G.; Rinaldi, A.; Bertoni, F.; Sallusto, F.; Antonio, L. Selected TLR Agonist Combinations Synergistically Trigger a TH1 Polarizing Program in Dendritic Cells. *Nat. Immunol.* **2005**, *6* (8), 769–776. https://doi.org/10.1038/ni1223.Selected.

(131) Dagenborg, V. J. et al. Neoadjuvant Chemotherapy Is Associated with a Transient Increase of Intratumoral T-Cell Density in Microsatellite Stable Colorectal Liver Metastases. *Cancer Biol. Ther.* **2020**, *21* (5), 432–440. https://doi.org/10.1080/15384047.2020.1721252.

(132) Bar-On, Y. M. et al. Protection of BNT162b2 Vaccine Booster against Covid-19 in Israel. *N. Engl. J. Med.* **2021**, *385* (15), 1393–1400. https://doi.org/10.1056/nejmoa2114255.

(133) Gupta, A. K.; Gupta, M. Synthesis and Surface Engineering of Iron Oxide Nanoparticles for Biomedical Applications. *Biomaterials* **2005**, *26* (18), 3995–4021. https://doi.org/10.1016/j.biomaterials.2004.10.012.

(134) Kim, D. K.; Chang, J. H.; Kang, Y. J. Ef?Cient Internalization of Peptide-Conjugated SPIONs in Dendritic Cells for Tumor Targeting. *J. Nanosci. Nanotechnol.* **2012**, *12* (7), 5191–5198. https://doi.org/10.1166/jnn.2012.6379.

(135) Ott, P. A. et al. An Immunogenic Personal Neoantigen Vaccine for Patients with Melanoma. *Nature* **2017**, *547* (7662), 217–221. https://doi.org/10.1038/nature22991.

(136) Sahin, U. et al. Personalized RNA Mutanome Vaccines Mobilize Poly-Specific Therapeutic Immunity against Cancer. *Nature* **2017**, *547* (7662), 222–226. https://doi.org/10.1038/nature23003.

(137) Min, Y. et al. Antigen-Capturing Nanoparticles Improve the Abscopal Effect and Cancer Immunotherapy. *Nat. Nanotechnol.* **2017**, *12* (9), 877–882. https://doi.org/10.1038/nnano.2017.113.

(138) Sun, Q.; Zhou, Z.; Qiu, N.; Shen, Y. Rational Design of Cancer Nanomedicine: Nanoproperty Integration and Synchronization. *Adv. Mater.* **2017**, *29* (14), 1–18. https://doi.org/10.1002/adma.201606628.

(139) Kim, D. K.; Dobson, J. Nanomedicine for Targeted Drug Delivery. *J. Mater. Chem.* **2009**, *19* (35), 6294–6307. https://doi.org/10.1039/b902711b.

(140) Shao, K. et al. Nanoparticle-Based Immunotherapy for Cancer. *ACS Nano*. 2015, pp 16–30. https://doi.org/10.1021/nn5062029.

(141) Shi, J.; Kantoff, P. W.; Wooster, R.; Farokhzad, O. C. Cancer Nanomedicine: Progress, Challenges and Opportunities. *Nat. Rev. Cancer* **2017**, *17* (1), 20–37. https://doi.org/10.1038/nrc.2016.108.

(142) Toy, R.; Peiris, P. M.; Ghaghada, K. B.; Karathanasis, E. Shaping Cancer Nanomedicine: The Effect of Particle Shape on the in Vivo Journey of Nanoparticles. *Nanomedicine* **2014**, *9* (1), 121–134. https://doi.org/10.2217/nnm.13.191.

(143) Kranz, L. M. et al. Systemic RNA Delivery to Dendritic Cells Exploits Antiviral Defence for Cancer Immunotherapy. *Nature* **2016**, *534* (7607), 396–401. https://doi.org/10.1038/nature18300.

(144) Wang, D.; Lippard, S. J. Cellular Processing of Platinum Anticancer Drugs. *Nat. Rev. Drug Discov.* **2005**, *4* (4), 307–320. https://doi.org/10.1038/nrd1691.

(145) Kaczanowska, S.; Joseph, A. M.; Davila, E. TLR Agonists: Our Best Frenemy in Cancer Immunotherapy . *J. Leukoc. Biol.* **2013**, *93* (6), 847–863. https://doi.org/10.1189/jlb.1012501.

(146) Chesson, C. B.; Zloza, A. Nanoparticles: Augmenting Tumor Antigen Presentation for Vaccine and Immunotherapy Treatments of Cancer. *Nanomedicine* **2017**, *12* (23), 2693–2706. https://doi.org/10.2217/nnm-2017-0254.

(147) Gasparini, G.; Bang, E. K.; Montenegro, J.; Matile, S. Cellular Uptake: Lessons from Supramolecular Organic Chemistry. *Chem. Commun.* **2015**, *51* (52), 10389–10402. https://doi.org/10.1039/c5cc03472h.

(148) Vaidyanathan, S.; Orr, B. G.; Banaszak Holl, M. M. Role of Cell Membrane-Vector Interactions in Successful Gene Delivery. *Acc. Chem. Res.* **2016**, *49* (8), 1486–1493. https://doi.org/10.1021/acs.accounts.6b00200.

(149) Boisguérin, P. et al. Delivery of Therapeutic Oligonucleotides with Cell Penetrating Peptides. *Adv. Drug Deliv. Rev.* **2015**, *87*, 52–67. https://doi.org/10.1016/j.addr.2015.02.008.

(150) Allolio, C.; Baxova, K.; Vazdar, M.; Jungwirth, P. Guanidinium Pairing Facilitates Membrane Translocation. *J. Phys. Chem. B* **2016**, *120* (1), 143–153. https://doi.org/10.1021/acs.jpcb.5b10404.

(151) Montenegro, J. et al. Conceptually New Entries into Cells. *Chimia (Aarau).* **2011**, *65* (11), 853–858. https://doi.org/10.2533/chimia.2011.853.

(152) Fuertes, A.; Juanes, M.; Granja, J. R.; Montenegro, J. Supramolecular Functional Assemblies: Dynamic Membrane Transporters and Peptide Nanotubular Composites. *Chem. Commun.* **2017**, *53* (56), 7861–7871. https://doi.org/10.1039/c7cc02997g.

(153) Priegue, J. M. et al. In Situ Functionalized Polymers for SiRNA Delivery. *Angew. Chemie - Int. Ed.* **2016**, *55* (26), 7492–7495. https://doi.org/10.1002/anie.201601441.

(154) Louzao, I.; García-Fandiño, R.; Montenegro, J. Hydrazone-Modulated Peptides for Efficient Gene Transfection. *J. Mater. Chem. B* **2017**, *5* (23), 4426–4434. https://doi.org/10.1039/c7tb00179g.

(155) Crisan, D. N. et al. Poly(Acryloyl Hydrazide), a Versatile Scaffold for the Preparation of Functional Polymers: Synthesis and Post-Polymerisation Modification. *Polym. Chem.* **2017**, *8* (31), 4576–4584. https://doi.org/10.1039/c7py00535k.

(156) Donahue, N. D.; Acar, H.; Wilhelm, S. Concepts of Nanoparticle Cellular Uptake, Intracellular Trafficking, and Kinetics in Nanomedicine. *Adv. Drug Deliv. Rev.* **2019**, *143*, 68–96. https://doi.org/10.1016/j.addr.2019.04.008.

(157) Smith, S. A.; Selby, L. I.; Johnston, A. P. R.; Such, G. K. The Endosomal Escape of Nanoparticles: Toward More Efficient Cellular Delivery. *Bioconjug. Chem.* **2019**, *30* (2), 263–272. https://doi.org/10.1021/acs.bioconjchem.8b00732.

(158) Varkouhi, A. K.; Scholte, M.; Storm, G.; Haisma, H. J. Endosomal Escape Pathways for Delivery of Biologicals. *J. Control. Release* **2011**, *151* (3), 220–228. https://doi.org/10.1016/j.jconrel.2010.11.004.

(159) Wilhelm, S. et al. Analysis of Nanoparticle Delivery to Tumours. *Nat. Rev. Mater.* **2016**, *1* (5), 16014. https://doi.org/10.1038/natrevmats.2016.14.

(160) Sengupta, S. Cancer Nanomedicine: Lessons for Immuno-Oncology. *Trends in Cancer* **2017**, *3* (8), 551–560. https://doi.org/10.1016/j.trecan.2017.06.006.

(161) Richards, D. A.; Maruani, A.; Chudasama, V. Antibody Fragments as Nanoparticle Targeting Ligands: A Step in the Right Direction. *Chem. Sci.* **2016**, *8* (1), 63–77. https://doi.org/10.1039/c6sc02403c.

(162) Zhong, Y.; Meng, F.; Deng, C.; Zhong, Z. Ligand-Directed Active Tumor-Targeting Polymeric Nanoparticles for Cancer Chemotherapy. *Biomacromolecules* **2014**, *15* (6), 1955–1969. https://doi.org/10.1021/bm5003009.

(163) Boutureira, O.; Bernardes, G. J. L. Advances in Chemical Protein Modification. *Chem. Rev.* **2015**, *115* (5), 2174–2195. https://doi.org/10.1021/cr500399p.

(164) Biju, V. Chemical Modifications and Bioconjugate Reactions of Nanomaterials for Sensing, Imaging, Drug Delivery and Therapy. *Chem. Soc. Rev.* **2014**, *43* (3), 744–764. https://doi.org/10.1039/c3cs60273g.

(165) Beck, A.; Goetsch, L.; Dumontet, C.; Corvaïa, N. Strategies and Challenges for the next Generation of Antibody-Drug Conjugates. *Nat. Rev. Drug Discov.* **2017**, *16* (5), 315–337. https://doi.org/10.1038/nrd.2016.268.

(166) Ravasco, J. M. J. M.; Faustino, H.; Trindade, A.; Gois, P. M. P. Bioconjugation with Maleimides: A Useful Tool for Chemical Biology. *Chem. - A Eur. J.* **2019**, *25* (1), 43–59. https://doi.org/10.1002/chem.201803174.

(167) Kölmel, D. K.; Kool, E. T. Oximes and Hydrazones in Bioconjugation: Mechanism and Catalysis. *Chem. Rev.* **2017**, *117* (15), 10358–10376. https://doi.org/10.1021/acs.chemrev.7b00090.

(168) Montenegro, J.; Fin, A.; Matile, S. Comprehensive Screening of Octopus Amphiphiles as DNA Activators in Lipid Bilayers: Implications on Transport, Sensing and Cellular Uptake. *Org. Biomol. Chem.* **2011**, *9* (8), 2641–2647. https://doi.org/10.1039/c0ob00948b.

(169) Shim, M. S.; Kwon, Y. J. Stimuli-Responsive Polymers and Nanomaterials for Gene Delivery and Imaging Applications. *Adv. Drug Deliv. Rev.* **2012**, *64* (11), 1046–1059. https://doi.org/10.1016/j.addr.2012.01.018.

(170) Qiao, Y. et al. Stimuli-Responsive Nanotherapeutics for Precision Drug Delivery and Cancer Therapy. *Wiley Interdiscip. Rev. Nanomedicine Nanobiotechnology* **2019**, *11* (1), 1–20. https://doi.org/10.1002/wnan.1527.

(171) Meng, F.; Zhong, Z.; Feijen, J. Stimuli-Responsive Polymersomes for Programmed Drug Delivery. *Biomacromolecules* **2009**, *10* (2), 197–209. https://doi.org/10.1021/bm801127d.

(172) Tannock, I. F.; Rotin, D. Acid PH in Tumors and Its Potential for Therapeutic Exploitation. *Cancer Res.* **1989**, *49* (16), 4373–4384. https://doi.org/2545340.

(173) Kim, J. O.; Kabanov, A. V.; Bronich, T. K. Polymer Micelles with Cross-Linked Polyanion Core for Delivery of a Cationic Drug Doxorubicin. *J. Control. Release* **2009**, *138* (3), 197–204. https://doi.org/10.1016/j.jconrel.2009.04.019.

(174) Roik, N. V.; Belyakova, L. A. Mesoporous Silica Nanoparticles Equipped with Surface Nanovalves for PH-Controlled Liberation of Doxorubicin. *Interface Focus* **2016**, *6* (6), 20160041. https://doi.org/10.1098/rsfs.2016.0041.

(175) Duo, Y. et al. DOX-Loaded PH-Sensitive Mesoporous Silica Nanoparticles Coated with PDA and PEG Induce pro-Death Autophagy in Breast Cancer. *RSC Adv.* **2017**, *7* (63), 39641–39650. https://doi.org/10.1039/c7ra05135b.

(176) Kamimura, M.; Furukawa, T.; Akiyama, S. I.; Nagasaki, Y. Enhanced Intracellular Drug Delivery of PH-Sensitive Doxorubicin/ Poly(Ethylene Glycol)-Block-Poly(4-Vinylbenzylphosphonate) Nanoparticles in Multi-Drug Resistant Human Epidermoid KB Carcinoma Cells. *Biomater. Sci.* **2013**, *1* (4), 361–367. https://doi.org/10.1039/c2bm00156j.

(177) Karimi, Z. et al. Pegylated and Amphiphilic Chitosan Coated Manganese Ferrite Nanoparticles for PH-Sensitive Delivery of Methotrexate: Synthesis and Characterization. *Mater. Sci. Eng. C* **2017**, *71*, 504–511. https://doi.org/10.1016/j.msec.2016.10.008.

(178) Cai, T.-T. et al. Utilization of H-Bond Interaction of Nucleobase Uralic with Antitumor Methotrexate to Design Drug Carrier with Ultrahigh Loading Efficiency and PH-Responsive Drug Release. *Regen. Biomater.* **2014**, *1* (1), 27–35. https://doi.org/10.1093/rb/rbu010.

(179) Liu, J. et al. PH-Sensitive Nano-Systems for Drug Delivery in Cancer Therapy. *Biotechnol. Adv.* **2014**, *32* (4), 693–710. https://doi.org/10.1016/j.biotechadv.2013.11.009.

(180) Pazo, M.; Fernández-Caro, H.; Priegue, J. M.; Lostalé-Seijo, I.; Montenegro, J. Tuning the Properties of Penetrating Peptides by Oxime Conjugation. *Synlett* **2017**, *28* (8), 924–928. https://doi.org/10.1055/s-0036-1588689.

(181) Tang, S. et al. Dual PH-Sensitive Micelles with Charge-Switch for Controlling Cellular Uptake and Drug Release to Treat Metastatic Breast Cancer. *Biomaterials* **2017**, *114*, 44–53. https://doi.org/10.1016/j.biomaterials.2016.06.005.

(182) Buss, J. L.; Ponka, P. Hydrolysis of Pyridoxal Isonicotinoyl Hydrazone and Its Analogs. *Biochim. Biophys. Acta - Gen. Subj.* **2003**, *1619* (2), 177–186.

https://doi.org/10.1016/S0304-4165(02)00478-6.

(183) Liederer, B. M.; Borchardt, R. T. Enzymes Involved in the Bioconversion of Ester-Based Prodrugs. *J. Pharm. Sci.* **2006**, *95* (6), 1177–1195. https://doi.org/10.1002/jps.20542.

(184) Li, H. J. et al. Smart Superstructures with Ultrahigh PH-Sensitivity for Targeting Acidic Tumor Microenvironment: Instantaneous Size Switching and Improved Tumor Penetration. *ACS Nano* **2016**, *10* (7), 6753–6761. https://doi.org/10.1021/acsnano.6b02326.

(185) Zhao, L. et al. Advanced Nanotechnology for Hypoxia-Associated Antitumor Therapy. *Nanoscale* **2020**, *12* (5), 2855–2874. https://doi.org/10.1039/c9nr09071a.

(186) Wang, Y.; Shang, W.; Niu, M.; Tian, J.; Xu, K. Hypoxia-Active Nanoparticles Used in Tumor Theranostic. *Int. J. Nanomedicine* **2019**, *14*, 3705–3722. https://doi.org/10.2147/IJN.S196959.

(187) Yang, G. et al. Hollow MnO2 as a Tumor-Microenvironment-Responsive Biodegradable Nano-Platform for Combination Therapy Favoring Antitumor Immune Responses. *Nat. Commun.* **2017**, *8* (1). https://doi.org/10.1038/s41467-017-01050-0.

(188) Bai, J.; Jia, X.; Zhen, W.; Cheng, W.; Jiang, X. A Facile Ion-Doping Strategy to Regulate Tumor Microenvironments for Enhanced Multimodal Tumor Theranostics. *J. Am. Chem. Soc.* **2018**, *140* (1), 106–109. https://doi.org/10.1021/jacs.7b11114.

(189) Wu, J.; Li, S.; Wei, H. Multifunctional Nanozymes: Enzyme-like Catalytic Activity Combined with Magnetism and Surface Plasmon Resonance. *Nanoscale Horizons* **2018**, *3* (4), 367–382. https://doi.org/10.1039/c8nh00070k.

(190) Kim, J. et al. Continuous O2-Evolving MnFe2O4 Nanoparticle-Anchored Mesoporous Silica Nanoparticles for Efficient Photodynamic Therapy in Hypoxic Cancer. *J. Am. Chem. Soc.* **2017**, *139* (32), 10992–10995. https://doi.org/10.1021/jacs.7b05559.

(191) Song, M.; Liu, T.; Shi, C.; Zhang, X.; Chen, X. Bioconjugated Manganese Dioxide Nanoparticles Enhance Chemotherapy Response by Priming Tumor-Associated Macrophages toward M1-like Phenotype and Attenuating Tumor Hypoxia. *ACS Nano* **2016**, *10* (1), 633–647. https://doi.org/10.1021/acsnano.5b06779.

(192) Huang, C. C. et al. An Implantable Depot That Can Generate Oxygen in Situ for Overcoming Hypoxia-Induced Resistance to Anticancer Drugs in Chemotherapy. *J. Am. Chem. Soc.* **2016**, *138* (16), 5222–5225. https://doi.org/10.1021/jacs.6b01784.

(193) He, C. et al. Enhancement of Cisplatin Efficacy by Lipid-CaO2 Nanocarrier-

Mediated Comprehensive Modulation of the Tumor Microenvironment. *Biomater. Sci.* **2019**, *7* (10), 4260–4272. https://doi.org/10.1039/c9bm00797k.

(194) Wang, Z. et al. A Bifunctional Nanomodulator for Boosting CpG-Mediated Cancer Immunotherapy. *Nanoscale* **2017**, *9* (37), 14236–14247. https://doi.org/10.1039/c7nr04396a.

(195) Wheate, N. J.; Walker, S.; Craig, G. E.; Oun, R. The Status of Platinum Anticancer Drugs in the Clinic and in Clinical Trials. *Dalton Trans.* **2010**, *39* (35), 8113–8127. https://doi.org/10.1039/c0dt00292e.

(196) Xiaoyong, W.; Zijian, G. Targeting and Delivery of Platinum-Based Anticancer Drugs. *Chem. Soc. Rev.* **2013**, *42* (1), 202–224. https://doi.org/10.1039/c2cs35259a.

(197) Medici, S. et al. Noble Metals in Medicine: Latest Advances. *Coord. Chem. Rev.* **2015**, *284*, 329–350. https://doi.org/10.1016/j.ccr.2014.08.002.

(198) Dubowchik, G. M. et al. Cathepsin B-Labile Dipeptide Linkers for Lysosomal Release of Doxorubicin from Internalizing Immunoconjugates: Model Studies of Enzymatic Drug Release and Antigen-Specific in Vitro Anticancer Activity. *Bioconjug. Chem.* **2002**, *13* (4), 855–869. https://doi.org/10.1021/bc025536j.

(199) Jeffrey, S. C.; De Brabander, J.; Miyamoto, J.; Senter, P. D. Expanded Utility of the β-Glucuronide Linker: ADCs That Deliver Phenolic Cytotoxic Agents. *ACS Med. Chem. Lett.* **2010**, *1* (6), 277–280. https://doi.org/10.1021/ml100039h.

(200) Jain, N.; Smith, S. W.; Ghone, S.; Tomczuk, B. Current ADC Linker Chemistry. *Pharm. Res.* **2015**, *32* (11), 3526–3540. https://doi.org/10.1007/s11095-015-1657-7.

(201) Ulbrich, K. et al. Targeted Drug Delivery with Polymers and Magnetic Nanoparticles: Covalent and Noncovalent Approaches, Release Control, and Clinical Studies. *Chem. Rev.* **2016**, *116* (9), 5338–5431. https://doi.org/10.1021/acs.chemrev.5b00589.

(202) Lee, N. et al. Iron Oxide Based Nanoparticles for Multimodal Imaging and Magnetoresponsive Therapy. *Chem. Rev.* **2015**, *115* (19), 10637–10689. https://doi.org/10.1021/acs.chemrev.5b00112.

(203) Wang, H. et al. Hexagonal Magnetite Nanoprisms: Preparation, Characterization and Cellular Uptake. *J. Mater. Chem. B* **2015**, *3* (23), 4647–4653. https://doi.org/10.1039/c5tb00340g.

(204) Guardia, P. et al. One Pot Synthesis of Monodisperse Water Soluble Iron Oxide Nanocrystals with High Values of the Specific Absorption Rate. *J. Mater. Chem. B* **2014**, *2* (28), 4426–4434. https://doi.org/10.1039/c4tb00061g.

(205) Alipour, A. et al. A New Class of Cubic SPIONs as a Dual-Mode T1 and T2 Contrast Agent for MRI. *Magn. Reson. Imaging* **2018**, *49*, 16–24.

https://doi.org/10.1016/j.mri.2017.09.013.

(206) Demortière, A. et al. Size-Dependent Properties of Magnetic Iron Oxide Nanocrystals. *Nanoscale* **2011**, *3* (1), 225–232. https://doi.org/10.1039/c0nr00521e.

(207) Tanaka, S. et al. A Review on Iron Oxide-Based Nanoarchitectures for Biomedical, Energy Storage, and Environmental Applications. *Small Methods* **2019**, *3* (5), 1800512. https://doi.org/10.1002/smtd.201800512.

(208) Zhu, N. et al. Surface Modification of Magnetic Iron Oxide Nanoparticles. *Nanomaterials* **2018**, *8* (10). https://doi.org/10.3390/nano8100810.

(209) Basti, H. et al. Catechol Derivatives-Coated Fe3O4 and γ-Fe2O3 Nanoparticles as Potential MRI Contrast Agents. *J. Colloid Interface Sci.* **2010**, *341* (2), 248–254. https://doi.org/10.1016/j.jcis.2009.09.043.

(210) Barrow, M. et al. SPIONs for Cell Labelling and Tracking Using MRI: Magnetite or Maghemite? *Biomater. Sci.* **2018**, *6* (1), 101–106. https://doi.org/10.1039/c7bm00515f.

(211) Bárcena, C. et al. Zinc Ferrite Nanoparticles as MRI Contrast Agents. *Chem. Commun.* **2008**, No. 19, 2224–2226. https://doi.org/10.1039/b801041b.

(212) Deatsch, A. E.; Evans, B. A. Heating Efficiency in Magnetic Nanoparticle Hyperthermia. *J. Magn. Magn. Mater.* **2014**, *354*, 163–172. https://doi.org/10.1016/j.jmmm.2013.11.006.

(213) Abenojar, E. C.; Wickramasinghe, S.; Bas-Concepcion, J.; Samia, A. C. S. Structural Effects on the Magnetic Hyperthermia Properties of Iron Oxide Nanoparticles. *Prog. Nat. Sci. Mater. Int.* **2016**, *26* (5), 440–448. https://doi.org/10.1016/j.pnsc.2016.09.004.

(214) Hoare, T. et al. Magnetically Triggered Nanocomposite Membranes: A Versatile Platform for Triggered Drug Release. *Nano Lett.* **2011**, *11* (3), 1395–1400. https://doi.org/10.1021/nl200494t.

(215) Shirmardi Shaghasemi, B.; Virk, M. M.; Reimhult, E. Optimization of Magneto-Thermally Controlled Release Kinetics by Tuning of Magnetoliposome Composition and Structure. *Sci. Rep.* **2017**, *7* (1). https://doi.org/10.1038/s41598-017-06980-9.

(216) Ito, A.; Shinkai, M.; Honda, H.; Kobayashi, T. Medical Application of Functionalized Magnetic Nanoparticles. *J. Biosci. Bioeng.* **2005**, *100* (1), 1–11. https://doi.org/10.1263/jbb.100.1.

(217) Ito, A. et al. Augmentation of MHC Class I Antigen Presentation via Heat Shock Protein Expression by Hyperthermia. *Cancer Immunol. Immunother.* **2001**, *50* (10), 515–522. https://doi.org/10.1007/s00262-001-0233-7.

(218) Tanaka, K. et al. Intratumoral Injection of Immature Dendritic Cells Enhances Antitumor Effect of Hyperthermia Using Magnetic Nanoparticles. *Int. J. Cancer* **2005**, *116* (4), 624–633. https://doi.org/10.1002/ijc.21061.

(219) Ito, A.; Honda, H.; Kobayashi, T. Cancer Immunotherapy Based on Intracellular Hyperthermia Using Magnetite Nanoparticles: A Novel Concept of "Heat-Controlled Necrosis" with Heat Shock Protein Expression. *Cancer Immunol. Immunother.* **2006**, *55* (3), 320–328. https://doi.org/10.1007/s00262-005-0049-y.

(220) Chatterjee, S.; Burns, T. F. Targeting Heat Shock Proteins in Cancer: A Promising Therapeutic Approach. *Int. J. Mol. Sci.* **2017**, *18* (9). https://doi.org/10.3390/ijms18091978.

(221) Chao, Y. et al. Iron Nanoparticles for Low-Power Local Magnetic Hyperthermia in Combination with Immune Checkpoint Blockade for Systemic Antitumor Therapy. *Nano Lett.* **2019**, *19* (7), 4287–4296. https://doi.org/10.1021/acs.nanolett.9b00579.

(222) Sanz-Ortega, L.; Portilla, Y.; Pérez-Yagüe, S.; Barber, D. F. Magnetic Targeting of Adoptively Transferred Tumour-Specific Nanoparticle-Loaded CD8+ T Cells Does Not Improve Their Tumour Infiltration in a Mouse Model of Cancer but Promotes the Retention of These Cells in Tumour-Draining Lymph Nodes. *J. Nanobiotechnology* **2019**, *17* (1). https://doi.org/10.1186/s12951-019-0520-0.

(223) Chiang, C. S. et al. Combination of Fucoidan-Based Magnetic Nanoparticles and Immunomodulators Enhances Tumour-Localized Immunotherapy. *Nat. Nanotechnol.* **2018**, *13* (8), 746–754. https://doi.org/10.1038/s41565-018-0146-7.

(224) Zhang, F. et al. Engineering Magnetosomes for Ferroptosis/Immunomodulation Synergism in Cancer. *ACS Nano* **2019**, *13* (5), 5662–5673. https://doi.org/10.1021/acsnano.9b00892.

(225) Seo, W. S. et al. FeCo/Graphitic-Shell Nanocrystals as Advanced Magnetic-Resonance-Imaging and near-Infrared Agents. *Nat. Mater.* **2006**, *5* (12), 971–976. https://doi.org/10.1038/nmat1775.

(226) Zhang, Q. et al. Biomimetic Magnetosomes as Versatile Artificial Antigen-Presenting Cells to Potentiate T-Cell-Based Anticancer Therapy. *ACS Nano* **2017**, *11* (11), 10724–10732. https://doi.org/10.1021/acsnano.7b04955.

(227) Jeong, J. et al. Synthesis of Multifunctional Fe3O4-CdSe/ZnS Nanoclusters Coated with Lipid a toward Dendritic Cell-Based Immunotherapy. *ACS Appl. Mater. Interfaces* **2014**, *6* (7), 5297–5307. https://doi.org/10.1021/am500661j.

(228) Takahashi, M. et al. Magnetic Separation of Melanoma-Specific Cytotoxic T Lymphocytes from a Vaccinated Melanoma Patient's Blood Using MHC/Peptide Complex-Conjugated Bacterial Magnetic Particles. *Bioconjug. Chem.* **2009**, *20* (2), 304–309. https://doi.org/10.1021/bc800398d.

(229) Hurwitz, M. D. Hyperthermia and Immunotherapy: Clinical Opportunities. *Int. J.*

Hyperth. **2019**, *36* (sup1), 4–9. https://doi.org/10.1080/02656736.2019.1653499.

(230) Xiao, Y.; Du, J. Superparamagnetic Nanoparticles for Biomedical Applications. *J. Mater. Chem. B* **2020**, *8* (3), 354–367. https://doi.org/10.1039/c9tb01955c.

(231) Das, P.; Colombo, M.; Prosperi, D. Recent Advances in Magnetic Fluid Hyperthermia for Cancer Therapy. *Colloids Surfaces B Biointerfaces* **2019**, *174*, 42–55. https://doi.org/10.1016/j.colsurfb.2018.10.051.

(232) Hergt, R.; Dutz, S. Magnetic Particle Hyperthermia-Biophysical Limitations of a Visionary Tumour Therapy. *J. Magn. Magn. Mater.* **2007**, *311* (1 SPEC. ISS.), 187–192. https://doi.org/10.1016/j.jmmm.2006.10.1156.

(233) Chang, D. et al. Biologically Targeted Magnetic Hyperthermia: Potential and Limitations. *Front. Pharmacol.* **2018**, *9* (AUG), 831. https://doi.org/10.3389/fphar.2018.00831.

(234) Josefsen, L. B.; Boyle, R. W. Photodynamic Therapy and the Development of Metal-Based Photosensitisers. *Met. Based. Drugs* **2008**, *2008*. https://doi.org/10.1155/2008/276109.

(235) Berg, K. et al. Photochemical Internalization: A Novel Technology for Delivery of Macromolecules into Cytosol. *Cancer Res.* **1999**, *59* (6), 1180–1183.

(236) Selbo, P. K. et al. Photochemical Internalisation, a Minimally Invasive Strategy for Light-Controlled Endosomal Escape of Cancer Stem Cell-Targeting Therapeutics. *Photochem. Photobiol. Sci.* **2015**, *14* (8), 1433–1450. https://doi.org/10.1039/c5pp00027k.

(237) De Pinillos Bayona, A. M.; Moore, C. M.; Loizidou, M.; MacRobert, A. J.; Woodhams, J. H. Enhancing the Efficacy of Cytotoxic Agents for Cancer Therapy Using Photochemical Internalisation. *Int. J. Cancer* **2016**, *138* (5), 1049–1057. https://doi.org/10.1002/ijc.29510.

(238) Wang, J. T. W.; Berg, K.; Høgset, A.; Bown, S. G.; MacRobert, A. J. Photophysical and Photobiological Properties of a Sulfonated Chlorin Photosensitiser TPCS2a for Photochemical Internalisation (PCI). *Photochem. Photobiol. Sci.* **2013**, *12* (3), 519–526. https://doi.org/10.1039/c2pp25328c.

(239) Waeckerle-Men, Y. et al. Photochemical Targeting of Antigens to the Cytosol for Stimulation of MHC Class-I-Restricted T-Cell Responses. *Eur. J. Pharm. Biopharm.* **2013**, *85* (1), 34–41. https://doi.org/10.1016/j.ejpb.2013.02.002.

(240) Zhang, C. et al. A Light Responsive Nanoparticle-Based Delivery System Using Pheophorbide A Graft Polyethylenimine for Dendritic Cell-Based Cancer Immunotherapy. *Mol. Pharm.* **2017**, *14* (5), 1760–1770. https://doi.org/10.1021/acs.molpharmaceut.7b00015.

(241) Håkerud, M. et al. Intradermal Photosensitisation Facilitates Stimulation of MHC Class-I Restricted CD8 T-Cell Responses of Co-Administered Antigen. *J.*

Control. Release **2014**, *174* (1), 143–150. https://doi.org/10.1016/j.jconrel.2013.11.017.

(242) Håkerud, M. et al. Photosensitisation Facilitates Cross-Priming of Adjuvant-Free Protein Vaccines and Stimulation of Tumour-Suppressing CD8 T Cells. *J. Control. Release* **2015**, *198*, 10–17. https://doi.org/10.1016/j.jconrel.2014.11.032.

(243) Hjálmsdóttir, Á. et al. Cytosolic Delivery of Liposomal Vaccines by Means of the Concomitant Photosensitization of Phagosomes. *Mol. Pharm.* **2016**, *13* (2), 320–329. https://doi.org/10.1021/acs.molpharmaceut.5b00394.

(244) Bruno, C. et al. Photosensitizer and Light Pave the Way for Cytosolic Targeting and Generation of Cytosolic CD8 T Cells Using PLGA Vaccine Particles. *J. Immunol.* **2015**, *195* (1), 166–173. https://doi.org/10.4049/jimmunol.1500431.

(245) Shi, C. et al. Reprogramming Tumor-Associated Macrophages by Nanoparticle-Based Reactive Oxygen Species Photogeneration. *Nano Lett.* **2018**, *18* (11), 7330–7342. https://doi.org/10.1021/acs.nanolett.8b03568.

(246) Liang, S. et al. Core-Shell Structured Upconversion Nanocrystal-Dendrimer Composite as a Carrier for Mitochondria Targeting and Catalase Enhanced Anti-Cancer Photodynamic Therapy. *Biomaterials* **2020**, *240*, 119850. https://doi.org/10.1016/j.biomaterials.2020.119850.

(247) Wang, D. et al. Photo-Enhanced Singlet Oxygen Generation of Prussian Blue-Based Nanocatalyst for Augmented Photodynamic Therapy. *iScience* **2018**, *9*, 14–26. https://doi.org/10.1016/j.isci.2018.10.005.

(248) Wan, G. Y. et al. Recent Advances of Sonodynamic Therapy in Cancer Treatment. *Cancer Biol. Med.* **2016**, *13* (3), 325–338. https://doi.org/10.20892/j.issn.2095-3941.2016.0068.

(249) Rengeng, L.; Qianyu, Z.; Yuehong, L.; Zhongzhong, P.; Libo, L. Sonodynamic Therapy, a Treatment Developing from Photodynamic Therapy. *Photodiagnosis Photodyn. Ther.* **2017**, *19*, 159–166. https://doi.org/10.1016/j.pdpdt.2017.06.003.

(250) You, D. G. et al. ROS-Generating TiO2 Nanoparticles for Non-Invasive Sonodynamic Therapy of Cancer. *Sci. Rep.* **2016**, *6*. https://doi.org/10.1038/srep23200.

(251) Bogdan, J.; Pławińska-Czarnak, J.; Zarzyńska, J. Nanoparticles of Titanium and Zinc Oxides as Novel Agents in Tumor Treatment: A Review. *Nanoscale Res. Lett.* **2017**, *12* (1). https://doi.org/10.1186/s11671-017-2007-y.

(252) Deepagan, V. G. et al. Long-Circulating Au-TiO2 Nanocomposite as a Sonosensitizer for ROS-Mediated Eradication of Cancer. *Nano Lett.* **2016**, *16* (10), 6257–6264. https://doi.org/10.1021/acs.nanolett.6b02547.

(253) Unga, J.; Hashida, M. Ultrasound Induced Cancer Immunotherapy. *Adv. Drug Deliv. Rev.* **2014**, *72*, 144–153. https://doi.org/10.1016/j.addr.2014.03.004.

(254) Wang, X. et al. Enhanced Drug Delivery Using Sonoactivatable Liposomes with Membrane-Embedded Porphyrins. *J. Control. Release* **2018**, *286*, 358–368. https://doi.org/10.1016/j.jconrel.2018.07.048.

(255) Solis, A. G. et al. Mechanosensation of Cyclical Force by PIEZO1 Is Essential for Innate Immunity. *Nature* **2019**, *573* (7772), 69–74. https://doi.org/10.1038/s41586-019-1485-8.

(256) Liu, C. S. C. et al. Cutting Edge: Piezo1 Mechanosensors Optimize Human T Cell Activation. *J. Immunol.* **2018**, *200* (4), 1255–1260. https://doi.org/10.4049/jimmunol.1701118.

(257) Pan, Y. et al. Mechanogenetics for the Remote and Noninvasive Control of Cancer Immunotherapy. *Proc. Natl. Acad. Sci. U. S. A.* **2018**, *115* (5), 992–997. https://doi.org/10.1073/pnas.1714900115.

(258) Song, X.; Feng, L.; Liang, C.; Yang, K.; Liu, Z. Ultrasound Triggered Tumor Oxygenation with Oxygen-Shuttle Nanoperfluorocarbon to Overcome Hypoxia-Associated Resistance in Cancer Therapies. *Nano Lett.* **2016**, *16* (10), 6145–6153. https://doi.org/10.1021/acs.nanolett.6b02365.

(259) Wang, S. et al. 5-Aminolevulinic Acid-Mediated Sonodynamic Therapy Reverses Macrophage and Dendritic Cell Passivity in Murine Melanoma Xenografts. *Ultrasound Med. Biol.* **2014**, *40* (9), 2125–2133. https://doi.org/10.1016/j.ultrasmedbio.2014.05.007.

(260) Yang, B.; Chen, Y.; Shi, J. Reactive Oxygen Species (ROS)-Based Nanomedicine. *Chemical Reviews*. American Chemical Society April 24, 2019, pp 4881–4985. https://doi.org/10.1021/acs.chemrev.8b00626.

(261) Cirincione, R. et al. High-Intensity Focused Ultrasound– and Radiation Therapy–Induced Immuno-Modulation: Comparison and Potential Opportunities. *Ultrasound Med. Biol.* **2017**, *43* (2), 398–411. https://doi.org/10.1016/j.ultrasmedbio.2016.09.020.

(262) Un, K. et al. Development of an Ultrasound-Responsive and Mannose-Modified Gene Carrier for DNA Vaccine Therapy. *Biomaterials* **2010**, *31* (30), 7813–7826. https://doi.org/10.1016/j.biomaterials.2010.06.058.

(263) van den Bijgaart, R. J. E. et al. Thermal and Mechanical High-Intensity Focused Ultrasound: Perspectives on Tumor Ablation, Immune Effects and Combination Strategies. *Cancer Immunol. Immunother.* **2017**, *66* (2), 247–258. https://doi.org/10.1007/s00262-016-1891-9.

(264) Jung, S. E.; Cho, S. H.; Jang, J. H.; Han, J. Y. High-Intensity Focused Ultrasound Ablation in Hepatic and Pancreatic Cancer: Complications. *Abdom. Imaging* **2011**, *36* (2), 185–195. https://doi.org/10.1007/s00261-010-9628-2.

(265) Imran, M.; Ramzan, M.; Qureshi, A. K.; Azhar Khan, M.; Tariq, M. Emerging Applications of Porphyrins and Metalloporphyrins in Biomedicine and

Diagnostic Magnetic Resonance Imaging. *Biosensors* **2018**, *8* (4), 1–17. https://doi.org/10.3390/bios8040095.

(266) Ou, Y. C.; Wen, X.; Bardhan, R. Cancer Immunoimaging with Smart Nanoparticles. *Trends Biotechnol.* **2020**, *38* (4), 388–403. https://doi.org/10.1016/j.tibtech.2019.11.001.

(267) Chen, H.; Zhang, W.; Zhu, G.; Xie, J.; Chen, X. Rethinking Cancer Nanotheranostics. *Nat. Rev. Mater.* **2017**, *2* (7), 17024. https://doi.org/10.1038/natrevmats.2017.24.

(268) Yordanova, A. et al. Theranostics in Nuclear Medicine Practice. *Onco. Targets. Ther.* **2017**, *10*, 4821–4828. https://doi.org/10.2147/OTT.S140671.

(269) Jeong, Y.; Hwang, H. S.; Na, K. Theranostics and Contrast Agents for Magnetic Resonance Imaging. *Biomater. Res.* **2018**, *22* (1), 1–13. https://doi.org/10.1186/s40824-018-0130-1.

(270) Gobbo, O. L.; Sjaastad, K.; Radomski, M. W.; Volkov, Y.; Prina-Mello, A. Magnetic Nanoparticles in Cancer Theranostics. *Theranostics* **2015**, *5* (11), 1249–1263. https://doi.org/10.7150/thno.11544.

(271) Berger, A. Magnetic Resonance Imaging. *Bmj* **2002**, *324* (7328), 35. https://doi.org/10.1136/bmj.324.7328.35.

(272) Chen, Y. et al. Design and Synthesis of Magnetic Nanoparticles for Biomedical Diagnostics. *Quant. Imaging Med. Surg.* **2018**, *8* (9), 957–970. https://doi.org/10.21037/qims.2018.10.07.

(273) Phelps, M. E. Positron Emission Tomography Provides Molecular Imaging of Biological Processes. *Proc. Natl. Acad. Sci. U. S. A.* **2000**, *97* (16), 9226–9233. https://doi.org/10.1073/pnas.97.16.9226.

(274) Pimlott, S. L.; Sutherland, A. Molecular Tracers for the PET and SPECT Imaging of Disease. *Chem. Soc. Rev.* **2011**, *40* (1), 149–162. https://doi.org/10.1039/b922628c.

(275) Heinzmann, K.; Carter, L. M.; Lewis, J. S.; Aboagye, E. O. Multiplexed Imaging for Diagnosis and Therapy. *Nat. Biomed. Eng.* **2017**, *1* (9), 697–713. https://doi.org/10.1038/s41551-017-0131-8.

(276) Moek, K. L. et al. Theranostics Using Antibodies Antibody-Related Therapeutics. *J. Nucl. Med.* **2017**, *58* (Suppl 2), 83S-90S. https://doi.org/10.2967/jnumed.116.186940.

(277) Chang, Z. M. et al. Shape Engineering Boosts Magnetic Mesoporous Silica Nanoparticle-Based Isolation and Detection of Circulating Tumor Cells. *ACS Appl. Mater. Interfaces* **2018**, *10* (13), 10656–10663. https://doi.org/10.1021/acsami.7b19325.

(278) Liu, C. et al. Capture and Separation of Circulating Tumor Cells Using Functionalized Magnetic Nanocomposites with Simultaneous in Situ Chemotherapy. *Nanotechnology* **2019**, *30* (28), 285706. https://doi.org/10.1088/1361-6528/ab0e25.

(279) Yu, Y.; Sun, D. Superparamagnetic Iron Oxide Nanoparticle "theranostics" for Multimodality Tumor Imaging, Gene Delivery, Targeted Drug and Prodrug Delivery. *Expert Rev. Clin. Pharmacol.* **2010**, *3* (1), 117–130. https://doi.org/10.1586/ecp.09.39.

(280) Fan, W.; Yung, B.; Huang, P.; Chen, X. Nanotechnology for Multimodal Synergistic Cancer Therapy. *Chem. Rev.* **2017**, *117* (22), 13566–13638. https://doi.org/10.1021/acs.chemrev.7b00258.

(281) Xie, J. et al. PET/NIRF/MRI Triple Functional Iron Oxide Nanoparticles. *Biomaterials* **2010**, *31* (11), 3016–3022. https://doi.org/10.1016/j.biomaterials.2010.01.010.

Chapter 2 :

Customization of theranostic and redox-active magnetite-based nanovehicles for cancer therapy

2.1. Introduction

Cancer nanomedicine has emerged as a promising approach for the development of new tools against cancer. The engineering of devices that can safely deliver therapeutic agents into the tissue of interest can help to make cancer treatments safer and more effective and precise. However, the complexity and uniqueness of each patient's disease limits the development of generalizable, "off-the-shelf" cancer therapies. Cancer nanomedicine therapies have to refine their design principles to better suit the specificities and uniqueness of each patient's cancer. To this end, a chemistry and material science perspective has been used to fine-tune the efficacy of nanodevices for personalized cancer treatments. Effective drug delivery can be achieved through (i) the modulation of nanodevice physicochemical properties such as size, charge, device stability; (ii) surface decoration with biofunctional ligands that target the tissue of interest; (iii) loading of synergistic therapeutic drug cocktails (iv) incorporation of stimuli-responsive moieties that trigger site-specific drug delivery; and (v) incorporation of imaging features that enable to non-invasively track the delivery of the drugs and monitor the efficacy of the therapy. The growing successes of immunotherapy established that it is also key to incorporate bioactive features that can stimulate the immune system to kill cancer cells. This chapter, sets the design principles and approaches used in this thesis for the development of highly customizable nanodevices for personalized cancer therapy. The devices are based on iron oxide nanoparticles (IONPs), a material that offers a unique combination of anticancer chemical reactivity and non-invasive imaging features.

2.1.1. IONP-based nanomedicine for cancer therapy and diagnosis

Nanomedicine for cancer entails the development of nanosized structures and materials to enable innovative and more precise means of diagnosis, patient stratification and treatment [1]. A key nanomedicine asset is the enhanced control that it offers over the delivery of therapeutic drugs and diagnostic imaging probes. Cancer develops in a patient and cancer type-specific fashion, which limits the development of universally applicable therapies. To better suit the particularities of each patient, modern oncology therapy development can use an extensive range of nanomedicine systems [2]. Among them, recent research has highlighted the unique material-specific features that IONPs offer for cancer therapy and diagnosis [34].

IONPs are inorganic nanomaterials offering excellent biocompatibility, functional features and tuneability [5]. Indeed, iron is the most abundant transition metal in the human body and it plays crucial functions for tissue oxygenation and immune cell proliferation and maturation. Also, the major endogenous iron storage protein is ferritin, which contains iron in the form of IONPs (a combination of ferrihydrite, maghemite and magnetite structures) [6]. Under physiological conditions, IONPs can be metabolized and degraded in a way that it is impossible for other materials (i.e. gold nanoparticles, mesoporous silica particles or polymeric meshes) [7]. IONP degradation products are also much safer than those of other biodegradable inorganic particles (i.e. copper, titanium or zinc oxides)[8]. Most notably, it has been the intriguing oxidative, magnetic and imaging active properties of IONPs that establishes the basis for their utility in different cancer diagnosis, therapy and theranostic strategies.

2.1.1.1. IONP redox properties for cancer therapy

Iron ions can catalyse the generation of reactive oxygen species (ROS) like hydroxyl and peroxyl radicals from H_2O_2. These reactions are enabled under acidic conditions and are referred to as Fenton chemistry. Under these conditions, iron is considered to "mimic" the natural enzyme peroxidase [9,10]. Iron-based compounds may also catalyse generation of O_2 from H_2O_2 at neutral and basic pH, thus "mimicking" the natural enzyme catalase [11]. Only a few other elements such as copper or cobalt are capable of Fenton-like chemistry [12], but their therapeutic application has been limited due to safety concerns [8]. Redox reactions enabled by iron-containing compounds can be summarized as follows:

$$Fe^{2+} + H_2O_2 \xrightarrow[(pH<7)]{Peroxidase-like} Fe^{3+} + \cdot OH + OH^- \qquad (1)$$

$$Fe^{3+} + H_2O_2 \xrightarrow[(pH<7)]{Peroxidase-like} Fe^{2+} + \cdot OOH + H^+ \qquad (2)$$

$$H_2O_2 \xrightarrow[(pH\geq 7)]{Catalase-like} O_2 + 2H_2O \qquad (3)$$

Fenton chemistry can also occur on the IONP surface. The reaction is favored by coordinated Fe^{2+} ions and oxygen vacancies [13]. Nanoparticles capable of enzymatic-like

activity are generally identified as nanozymes. In the case of catalytic IONPs, they have been referred as IONzymes [14].

Two characteristic features of the tumor microenvironment (TME) are its acidic pH (pH ~ 6.5) and high levels of H_2O_2 [15,16]. They both represent very favorable conditions for exploiting therapeutically Fenton chemistry. Hence, IONzyme-mediated ROS generation can be triggered in the TME in a site-specific fashion. Another key characteristic of the TME is its rich density in pro-tumoral immune cells. These cells serve as a barrier to stop anticancer immune system attacks and promote wound healing-like mechanisms for cancer growth and tumor tissue repair [17,18]. In such environment, therapy-induced ROS can function as a messaging signal to transform pro-tumoral immune cells into anticancer immune cells [19,20]. Pro-tumoral M2-like tumor-associated macrophages (TAMs), which are ubiquitous in the TME, can be activated (polarized) towards an anticancer cytotoxic M1-like phenotype (Fig. 2.1) [21,22]. M1-like macrophages display increased cytotoxic phagocytotic activity and can function as cancer cell scavengers [23]. The immunostimulatory signals that M1-like macrophages elicit can also facilitate the recruitment and infiltration of other anticancer immune cells into the TME [24]. Therapy-induced ROS can also potentiate the antitumor features of other cancer therapy and immunotherapy drugs. A promising pathway for M2-to-M1 macrophage polarization is via the administration of Toll-like receptors (TLR) agonists (TLRa) [25]. These compounds stimulate the immune system as they are recognized as “danger signals”. ROS generation has been reported to synergise with TLRa immunostimulatory features, facilitating anticancer immune cell maturation and infiltration into the TME [26–29].

Elevated local ROS levels induce oxidative stress and cell damage. Accumulation of irreversible oxidative damage is also important to trigger ferroptosis, a recently described ROS- and iron-mediated cell death mechanism [30]. It has been shown that cancer cells are especially susceptible to this cell death mechanism given their already high intracellular ROS levels (Fig. 1.4; see Chapter I) [31]. A cancer cell undergoing ferroptosis might release messaging signals like ROS and damage-associated molecular patterns (DAMPs), which can work as a stimulatory “danger signal” for the immune system. It may also release tumor-associated antigens (TAAs) and tumor-specific antigens (TSAs), which are molecular structures only- or overexpressed by the tumor cells. TAA and TSA release can be assimilated by the immune system to identify and kill cancer cells, thus working

as an *in situ* vaccine [32]. Ferroptosis is thus considered a promising new way to induce anticancer immunostimulatory cell death (ICD). All in all, this mechanism holds enormous interest as a safer cytotoxic pathway alternative to classic chemotherapies [4, 31, 41,33–40].

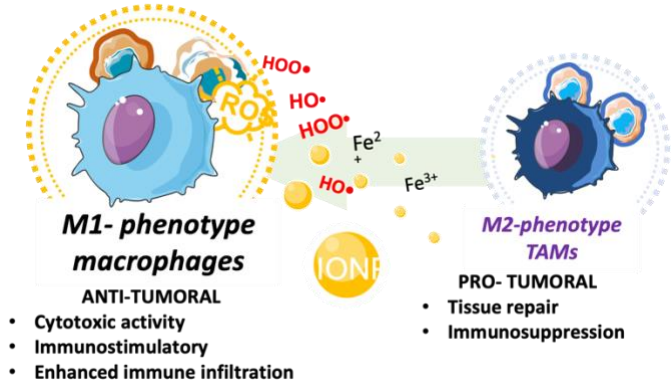

Figure 2.1. IONP peroxidase-like features enable ROS-mediated cancer therapies. *Schematic representation of cytotoxic M2-to-M1 macrophage activation.*

2.1.1.2. IONP magnetic properties for cancer therapy

IONP magnetic features have been extensively applied in anticancer therapy. Cytotoxic T-cells are activated ($CD8^+$) when TAAs or TSAs is presented to them by antigen-presenting cells (APCs). The presentation occurs through the T-cell receptor (TCR) expressed on the T-cell membrane. Through this process, T-cells acquire a target, the antigen, to direct their cytotoxic action. Antigen-presenting magnetic beads can bind to TCRs to artificially induce T-cell activation. Upon the incidence of a magnetic field, the beads induce TCR clustering which has been reported to enhance T-cell activation and expansion [42–44]. A magnetic field can also be used to concentrate IONP-containing vehicles into the tissue of interest through magnetic navigation (Fig. 2.2, a) [45–47]. Finally, IONPs show size-dependent superparamagnetic behaviour [48]. Superparamagnetic iron oxide nanoparticles (SPIONs) are of great interest for their application in magnetic hyperthermia therapies (MHTs). In these therapies, an alternating magnetic field is applied for the SPIONs to produce heat. Local high temperatures induce tumor cell killing and have been reported to release DAMPs and TAAs for immune cell recruitment and ICD (Fig. 2.2, b) [49–54].

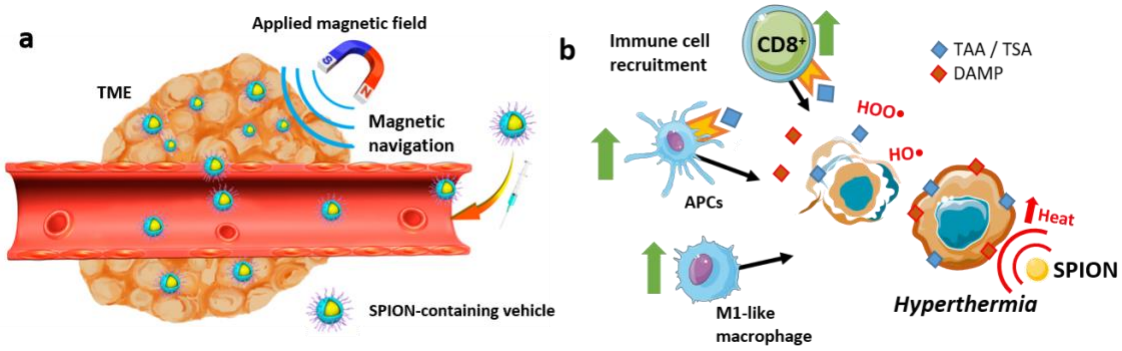

Figure 2.2. IONP (super)paramagnetic features can be applied in cancer therapy*. Schematic representation of magnetically navigated SPION-containing vehicles into the TME. Image adapted from [55]; (b) Schematic representation of SPION-enabled MHT inducing cancer cell death and immunostimulatory DAMP, TAA, TSA release for cytotoxic immune cell activation and recruitment.*

2.1.1.3. IONP imaging properties for cancer diagnosis

SPIONs are widely used as diagnostic probes for magnetic resonance imaging (MRI). This imaging modality is used in the clinic for non-invasive deep-tissue visualization and disease diagnosis (Fig. 2.3, a). SPION-loaded vehicles can be visualized by MRI and can thus be used also to monitor treatment biodistribution [56,57, 66–69,58–65]. If the particles are functionalized with targeting ligands (these are molecular structures that can selectively bind to specific cell surface receptors), MRI can be used as a diagnostic tool for predictive tumor markers and studies of immune [70–78] and tumor [3,79–81] cellular dynamics.

The MRI-active imaging properties of IONPs can be complemented with positron emission tomography (PET) or photon emission computerized tomography-computerized tomography (SPECT). PET and SPECT are non-invasive nuclear imaging modalities that commonly use radioactive ^{67}Ga, ^{68}Ga or ^{18}F as tracers (radiotracers). Typically, the incorporation of chelating agents is required for the radiolabelling of nanomedicine vehicles. However, previous studies from our group showed that magnetite structures can accommodate gallium radiotracers given their comparable size to iron ions [82]. Thus, the intrinsic SPION characteristics readily enable the chelate-free design of multimodal diagnostic vehicles monitorable by MRI, SPECT (^{67}Ga) and PET (^{68}Ga) (Fig. 2.3, b-d).

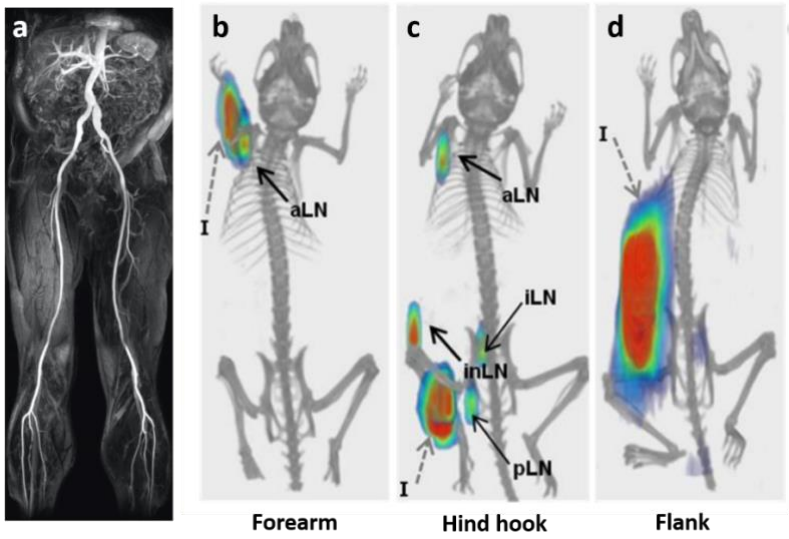

Figure 2.3. SPIONs serve as efficient diagnostic agents. *(a) High-resolution MRI image of the human abdominal aorta and bilateral lower extremity obtained after administration of Ferumoxytol, a clinically approved IONP-based MRI active agent. Image (a) extracted from* [83]*; (b-d) SPECT images of* [67]*Ga-doped SPION-based vehicles allowing for the study of treatment biodistribution depending injection site. Images taken 3 h post injection. SPION-based vehicles were injected in the (b) left forearm, (c) hind hook and (d) flank in mice. I, injection site, aLN, axillary lymph node, inLN, inguinal lymph node, iLN, iliac lymph node, pLN, popliteal lymph node; Images (b-d) extracted from* [82].

2.1.2. Functionalization of IONP-based theranostic devices for cancer therapy

Success in anticancer nanomedicine is an interdisciplinary effort. A biological and medical perspective can assess the therapeutic benefits and toxic side-effects of a drug delivery construct. However, a chemistry and material science perspective is needed to allow efficient drug loading, targeting-ligand incorporation and device imaging features. In the discussion above, the intrinsic IONP characteristics have been shown to offer key features for the design of multimodal therapeutic and diagnostic (theranostic) vehicles [84,85]. However, careful particle functionalization is fundamental to enable and optimize their biomedical applications.

Previous research from our group showed that IONP-filled immunostimulatory nanovehicles provide more safety and efficacy in decreasing tumor growth than gold-standard platinum-based chemotherapies. Their [67]Ga-doped SPION structure could be monitored by MRI/SPECT to accumulate in the tumor as well as in crucial immune cell-

rich tissues (such as lymph nodes and spleen). Careful particle functionalization enabled site-specific delivery of potent immunomodulatory drug cocktails and effective antigen presentation, yielding complete tumor elimination and long term immune protection for mice *in vivo* [82,86,87].

The sections that follow will study how chemistry can be used to further customize, adapt and optimize theranostic IONP-based devices for cancer therapy. In this chapter, the devices will be assembled to: (i) optimize their stability in aqueous suspension, (ii) display IONP-mediated peroxidase-like reactivity, (iii) load bioactive compounds in inner hydrophobic sites, (iv) capture immunomodulatory TLR agonists through electrostatic self-assembly, and (iv) incorporate directing ligands for active targeting using reversible covalent surface decoration (via hydrazone and thiosuccinimide bonds; see Chapter I). Fenton chemistry-mediated IONP degradation is aimed at being site-specifically catalysed in acid environments like the TME and intracellular endolysosomal compartments [16]. Structural breakdown of the device is expected to induce drug release and reveal "stealth" immunostimulatory structures (Fig 2.4). Amongst the therapeutic nanodevices designed in this work, three key functional levels can be distinguished:

1. **Core**: The devices of this work share a common IONP core. The solid inorganic particle will provide a stable foundation for the construction of the therapeutic device. Their peroxidase-like redox reactivity and theranostic features will be exploited in future chapters to unite and enhance various anticancer strategies.
2. **Inner Framework:** The IONP core requires aqueous stabilization for systemic *in vivo* delivery of the multimodal therapy. Aqueous stabilization will be critical to produce a first functional layer, or "inner framework", which can be customized to control and optimise hydrodynamic size, particle charge and device stability. The inner framework, dense in hydrophobic sites, will also enable the loading of small amphiphilic bioactive compounds.
3. **Outer Framework**: Outward exposure of electrostatic charges and chemically reactive moieties will enable surface particle functionalization. The device outermost layer will be customized to (i) capture immunomodulatory drug cocktails through electrostatic self-assembly, and (ii) to incorporate targeting ligands through covalent click-chemistry conjugation strategies. In further chapters, it will also serve for the

delivery and presentation of chemotherapy compounds (Chapter III) and tumor antigens (Chapter IV and Chapter V).

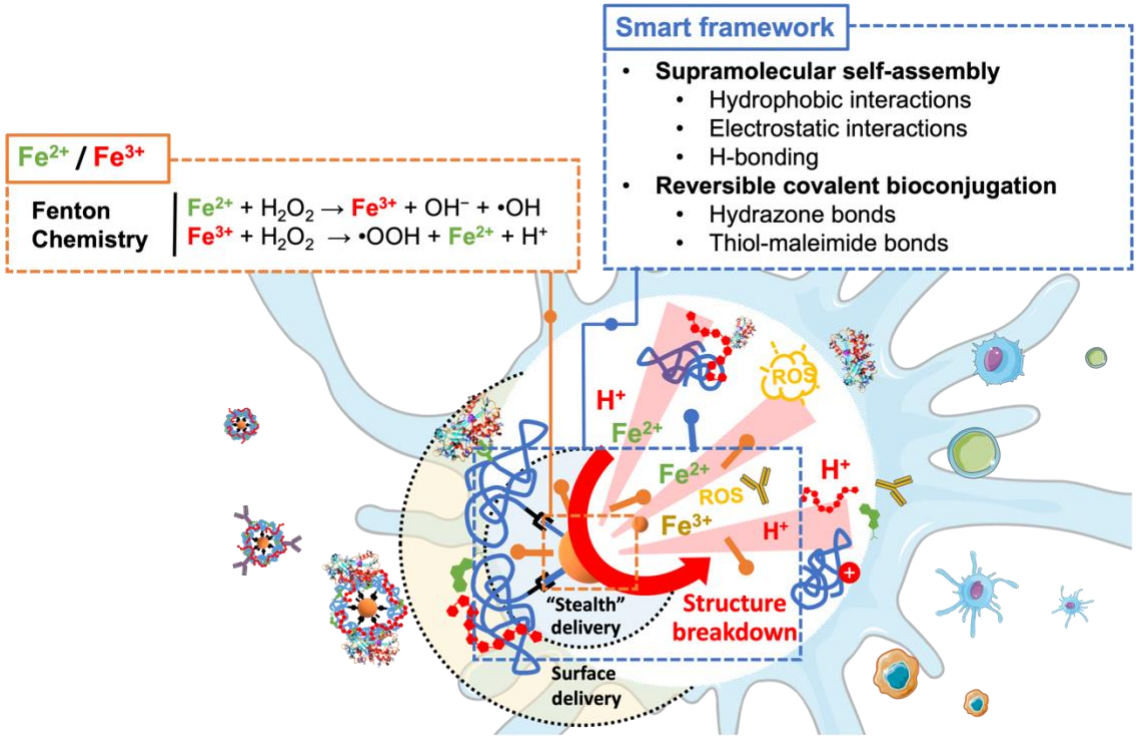

Figure 2.4. Multilevel customizable scaffolds for personalizable anticancer therapies. *Schematic representation of IONP-based nanodevice chemical features and framework design facilitating metabolization in the cell, structural breakdown and drug release.*

2.2. Results and Discussion

2.2.1. IONP core: synthesis and characterization

A wide variety of IONP synthetic routes have been designed to attain control over size, shape, crystallographic phase and metal doping [48,88,89]. Among them, methods of controlled thermal decomposition of metalorganic complexes provide higher particle growth control and reproducibility [90].

Upon heating to 200 °C, mixtures of iron (III) acetylacetonate with the reducing agent oleyamine and oleic acid, yield the *in-situ* formation of iron oleates (II) and (III). Increasing the heating to 300 °C initiates cluster growth (Fig. 2.5, a) [91]. The presence of oleic acid, oleylamine and 1,2-hexandiol offer kinetic control over particle growth. Hence, particle size can be fine-tuned by varying their concentrations in the mix [92]. After simple purification steps, oleic acid-coated iron oxide nanoparticle spheres of 7 nm and low polydispersity could be obtained with excellent reproducibility (Fig. 2.5, a). High-resolution X-ray photoelectron spectroscopy (XPS) confirmed the elemental Fe_3O_4 composition of the IONP particles used in this work (Fig. 2.5, b-c) (see Materials and Methods). The Fe 2p region confirmed the presence of multiplet peaks (~725 eV and ~710 eV) assigned to Fe-O bonds and absence of the ~707 eV peak assigned to metal Fe-Fe bonds (Fig. 2.5, b) [93]. Fe 3p region (60 - 50 eV) confirmed the elemental Fe^{3+}/Fe^{2+} ratio of ~1:2 expected for Fe_3O_4 magnetite structures by calculating the areas of each peak (Fig. 2.5, c) [94].

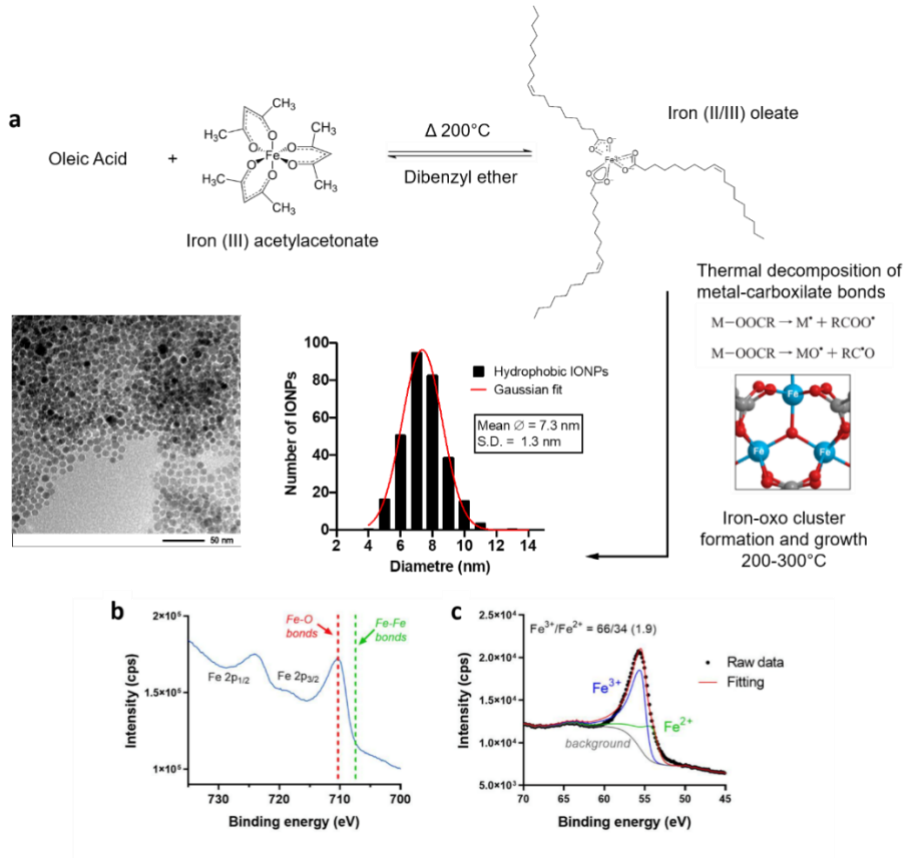

Figure 2.5. IONP synthesis using thermal decomposition methods and characterization. *(a) Reaction scheme and representative example of particle size frequency distribution as imaged by Transmission Electron Microscopy (TEM). (b-c) XPS measurements were carried out on (b) Fe 2p and (c) Fe 3p regions to confirm the elemental Fe_3O_4 composition of our IONPs. XPS measurements (b-c) were kindly performed by Dr. A Ruiz-de-Angulo (CIC BioGUNE, Spain* [95].

2.2.2. Inner framework functionalization

2.2.2.1. mIONP stabilization

Systemic nanodevice administration requires aqueous stabilization. However, the oleic acid-coated IONPs are hydrophobic. Supramolecular self-assembly represents as an ideal strategy to drive aqueous suspension of the hydrophobic IONP core. Amphiphilic molecules can be interdigitated among oleic acid chains to yield aqueous suspensions of IONP-filled micelles (mIONPs).

Amphiphile polyethylene glycol (PEG) phospholipids (PEG-PLs) are a ubiquitous resource for aqueous nanoparticle stabilization. Owing to their versatility and

biocompatibility, PEG-based polymers are present in many FDA-approved formulations for cancer therapy. They are commercially available in a variety of lengths and chemical terminations, each conferring a specific set of physicochemical properties such as surface charge, hydrodynamic size or chemical reactivity [96,97].

Hydrophobic IONP and amphiphilic PEG-PL self-assembly followed previously stablished methods of thin-film formation [82]. IONPs and PEG-PLs were solubilized and mixed in $CHCl_3$. Complete solvent evaporation resulted in the deposition of a thin dry-film. Its hydration yielded aqueous suspensions of PEGylated mIONPs. Aggregates and IONP-empty micelles could be removed by centrifugation (see Materials and Methods). mIONP hydrodynamic size, charge and chemical reactivity depended on PEG-PL selection. In the chapters of this work, numerous PEGylated mIONP formulations will be developed and evaluated. Different IONP- to-PL ratios were used to optimize suspension formation for each kind of PEG-phospholipid. The most common formulation used carboxylic acid (-COOH) terminated PEG-PL chains. Typically, 1 mg of IONP was mixed with 2 mg of PEG(2000 kDa)-carboxylic acid, leading to <40 nm IONP-filled micelles that will be referred to as mIONP-COOH (Fig. 2.6).

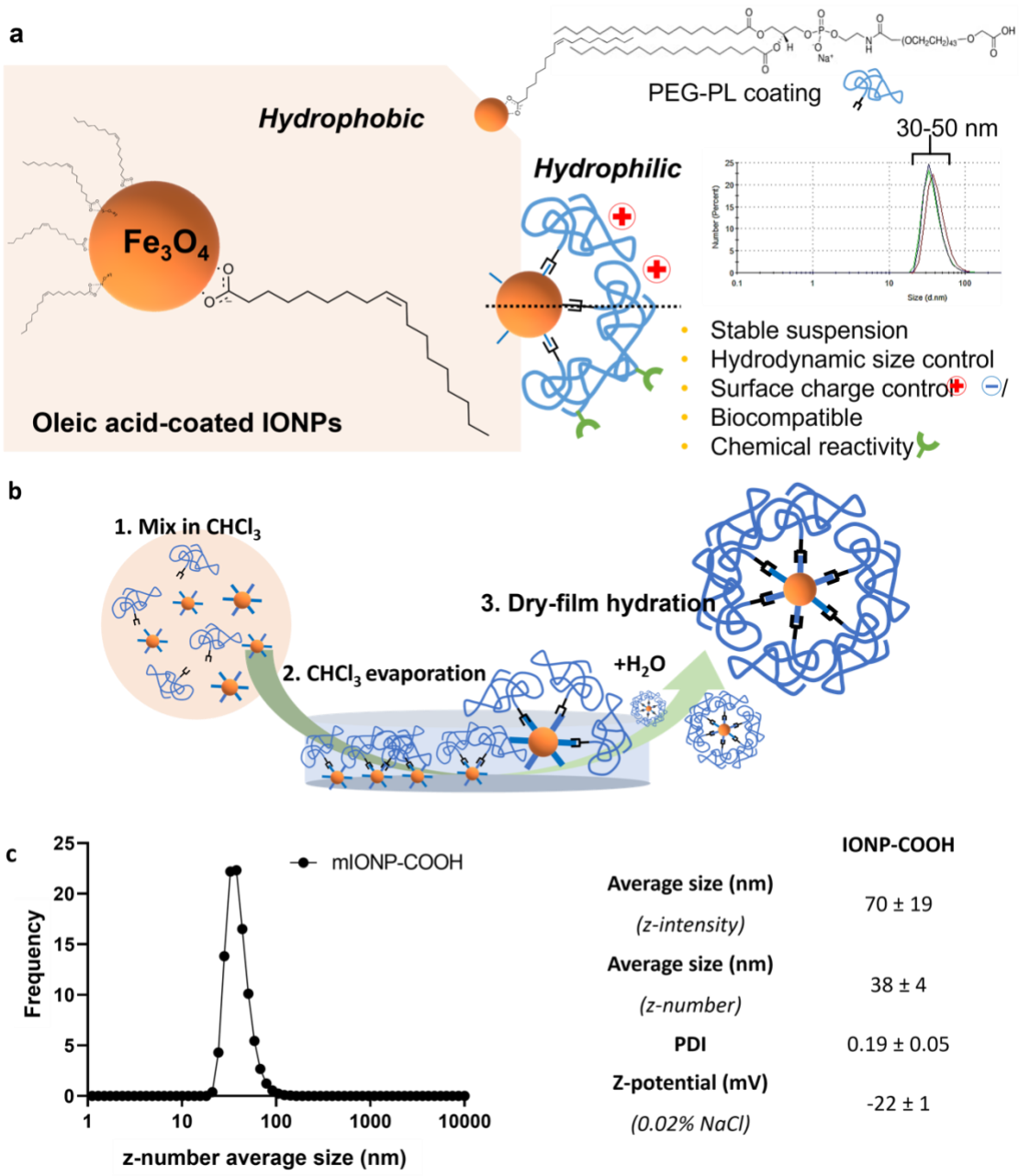

Figure 2.6. Aqueous self-assembly stabilization of IONP-filled PEGylated micelles (mIONP). *(a) PEG-PL coating of hydrophobic IONPs is necessary to yield stable hydrophilic suspensions and can be used to modulate key physicochemical properties of the resulting particle. (b) Schematic representation of dry-film hydration methods for the obtention of IONP-filled micelles. (c) Representative nanoparticle size distribution as percentage (%) of events by z-number from mIONP-COOH suspensions and physicochemical characterization summary. Representative values as mean ± SEM for different mIONP suspensions for at least three independent experiments as characterized by Dynamic Light Scattering (DLS).*

2.2.2.2. mIONP catalytic activity

Peroxidase-like activity from aqueous stabilized mIONPs could be studied using colorimetric methods. 3,3′,5,5′-tetramethylbenzidine (TMB) is a well-known peroxidase substrate which through oxygen radical-mediated oxidation forms a blue TMB_{OX} complex (ε_{652} = 3.9 × 10^4 M^{-1} cm^{-1}). As a confirmation, o-phenylenediamine (OPD), which turns yellow upon oxidation (ε_{418} = 1.67 × 10^4 M^{-1} cm^{-1}) yielding 2,3-diaminophenazine (DAP), was also used as peroxidase substrate (Fig. 2.7) (see Materials and Methods).

mIONPs demonstrated pH-dependent catalytic activity peaking at acidic conditions equivalent to those found in intracellular endolysosomal compartments (pH=4.5). Peroxidase-like catalysis decreased when rising pH, becoming negligible at normal physiological conditions (pH = 7.5) (Fig. 2.7, b). Negligible catalytic activity arising from free iron ions leached under acidic pH (accumulated after a 40-minute incubation at pH = 4.5) confirmed that the observed catalytic activity occurs on the particle surface (Fig. 2.7, b).

Catalytic mIONP performance could be evaluated at room temperature in steady-state Michaelis–Menten terms of catalytic rate (k_{cat}), maximal rate (V_{max}), Michaelis constant (K_M), and catalytic efficiency (k_{cat}/K_M). By varying the concentration of H_2O_2 and TMB (Fig. 2.6, c-d), we obtained values of K_M (H_2O_2) = 338 µM, K_M (TMB) = 351 µM, V_{max} = 6.59 × 10^{-8} M^{-1} s^{-1} and K_{cat} = 3.9 s^{-1} (Fig. 2.7, d-e). These values are indicative of a strong catalytic performance. The mIONPs show a H_2O_2 affinity that is ten-fold stronger than that of horseradish peroxidase (HRP), for which the K_M at similar conditions is 3.7 mM [11]. This value is relevant for anticancer therapeutic purposes as it accounts for the levels of H_2O_2 required for our mIONPs to be catalytically active. It is known that cancer cells continuously produce elevated levels of H_2O_2, much higher than non-cancerous cells [98] and it is reasonable to expect this production to be further increased upon immune stimulation. H_2O_2 steady-state levels in human blood can reach a range of 30 – 50 µM during inflammation [14].

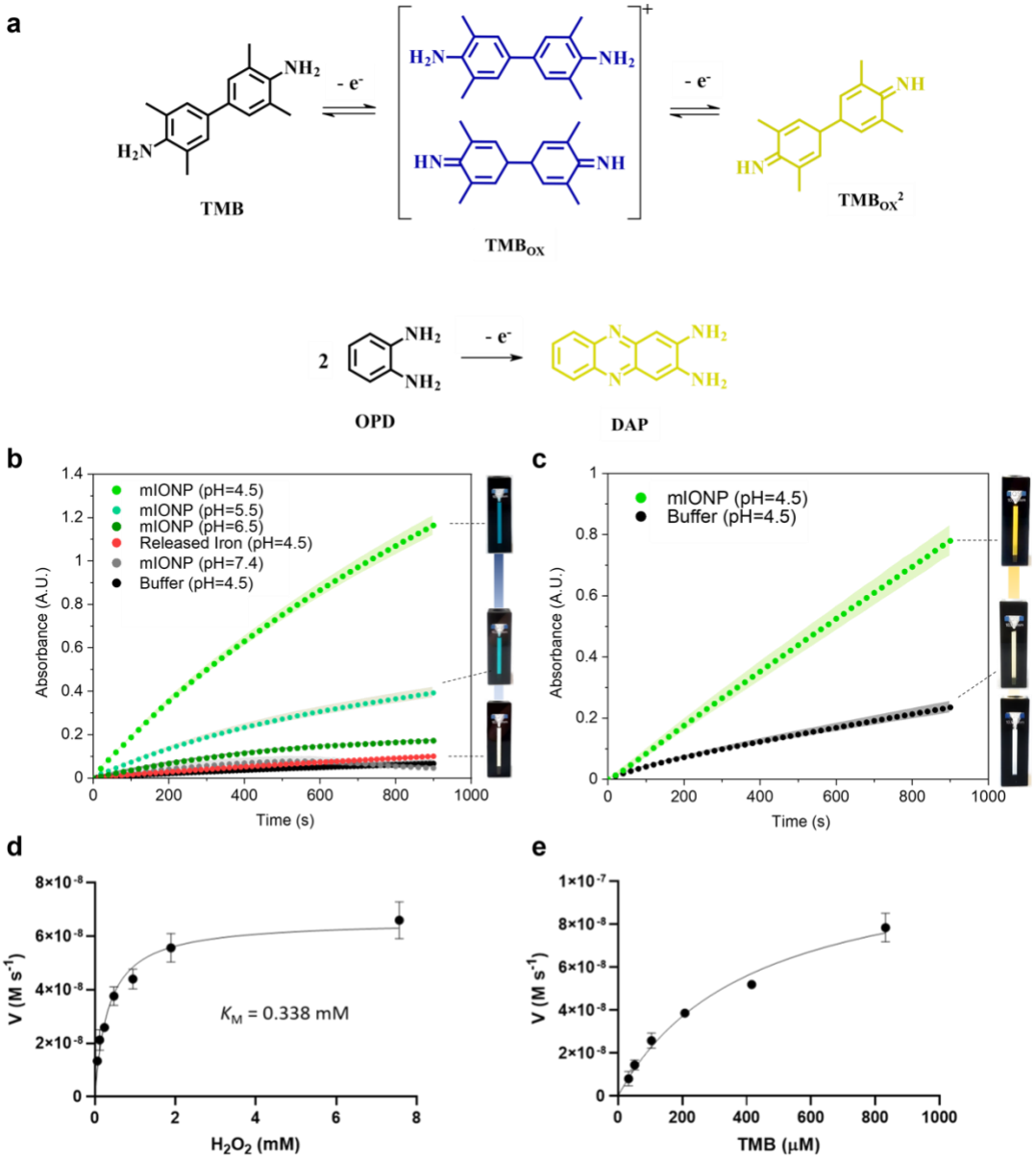

Figure 2.7. mIONPs display strong pH-dependent peroxidase-like catalytic properties. *(a) Reaction schemes of TMB and OPD oxidation. (b-c) Time course curves assessing the catalytic activity of mIONPs at different pH values and released free iron cations for the oxidation of (b) TMB ([TMB] = 830 µM) and (c) OPD ([OPD] = 3 mM). Concentrations of [Fe] = 150 µM for mIONPs and [H_2O_2] = 30 mM were used. c, d) Michaelis-Menten kinetics plots for TMB oxidation at varying concentrations of (c) H_2O_2 and (d) TMB. The reactions were monitored at room temperature using 10 mm pathlength quartz cuvettes. Results are shown as mean ± SEM from three independent experiments.*

2.2.2.3. Bioactive compound loading

The mIONP amphiphilic coating forms a hydrophobic inner framework layer. This feature is already of interest to cancer immunotherapies, as hydrophobicity can be recognized by the immune system as a stimulatory "danger signal" [99]. In addition, hydrophobic interactions in this region can be used to load amphiphilic bioactive compounds.

In this work, the amphiphilic bioactive compound of choice was linoleic acid. Linoleic acid is an essential fatty acid that can be obtained from vegetable oils, nuts and seeds. This polyunsaturated lipid has been shown to induce membrane lipid peroxidation and enhance numerous processes involved in ICD and ferroptosis [100]. Hence, linoleic acid has attracted interest for cancer therapy [101]. Two methods were used for the loading of the compound: (i) dry-film hydration methods and (ii) solvent exchange methods.

2.2.2.3.1. Formation of linoleic acid-rich mIONPs by dry film hydration methods

Formation of PEG-stabilized linoleic acid-rich IONP-filled micelles (mIONP-PEG-Lin) followed previously described processes of thin dry-film hydration. In this case, the dry-film would be enriched with increasing amounts of linoleic acid following linoleic acid addition to the IONP and PEG-PL mix in $CHCl_3$. It was found that increasing the proportion of linoleic acid in the mIONP coating yields bigger particles and suspensions that were more prone to aggregation (Fig. 2.8). Formulations in which the molar percentage of linoleic acid was higher than 50% led to mIONP with low stability. Indeed, it was expected that the presence of linoleic acid chains would form less compact particle coatings, a feature that could be beneficial to expose the immunostimulatory hydrophobic portions and facilitate targeted delivery of the linoleic acid to membrane of cancer cells

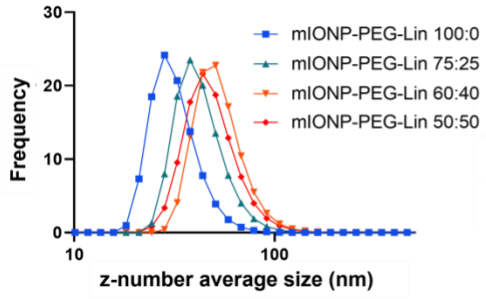

PEG-PL:Lin *(molar ratio)*	Z-average (nm) *(z-intensity)*	PDI	Average size (nm) *(z-number)*
100:0	56 ± 2	0.14 ± 0.01	32 ± 1
75:25	95 ± 5	0.19 ± 0.02	43 ± 2
60:40	92 ± 1	0.16 ± 0.02	53 ± 4
50:50	96 ± 1	0.19 ± 0.01	48 ± 7

Figure 2.8. Increasing linoleic acid loading leads to bigger mIONP particles. *Nanoparticle size distribution as percentage (%) of events by z-number from IONP-PEG-Lin suspensions and physicochemical characterization summary after 7 days in phosphate saline buffer (PBS). Larger proportions of linoleic acid in the mix led to the formation of larger particles. Representative values as mean ± SEM for at least three independent experiments as characterized by DLS.*

2.2.2.3.1.1. Linoleic acid-loading: Confirmatory tests

Two colorimetric TMB-based methods could be used to confirm linoleic acid loading in mIONP suspensions (see Materials and Methods):

- **Method A**: As it has been discussed above, IONPs are able to catalyse the formation of ROS from H_2O_2 and thus oxidise TMB. However, H_2O_2 and ROS can also oxidise unsaturated lipids [102]. Hence, linoleic acid content in the sample could be expected to compete with TMB for the oxidative ROS agent. In this case an increase in the linoleic acid content of our mIONPs would result in a drop in the rate of IONP-catalysed TMB oxidation by H_2O_2. Indeed, we observe a decrease in in the kinetic parameters associated with TMB oxidation for mIONP-Lin-PEG (50:50) compared to mIONP-COOH (Fig. 2.9, a).
- **Method B:** Ag^+ ion in solution is an oxidant strong enough to induce quick oxidation of TMB (Fig. 2.9, b, Negative Control). However, unsaturated fatty chains can chelate Ag^+ ions and sequestrate them , thus limiting their oxidative action [103]. Therefore, we reasoned that an increase in the linoleic acid content of the mIONPs would be reflected in decrease of the rate and extent of Ag^+-TMB oxidation. Indeed, the studies showed this expected trend in Ag^+-TMB oxidation: Negative Control (absence of particle) > mIONP-COOH > mIONP-Lin-PEG (50:50) (Fig. 2.9, b).

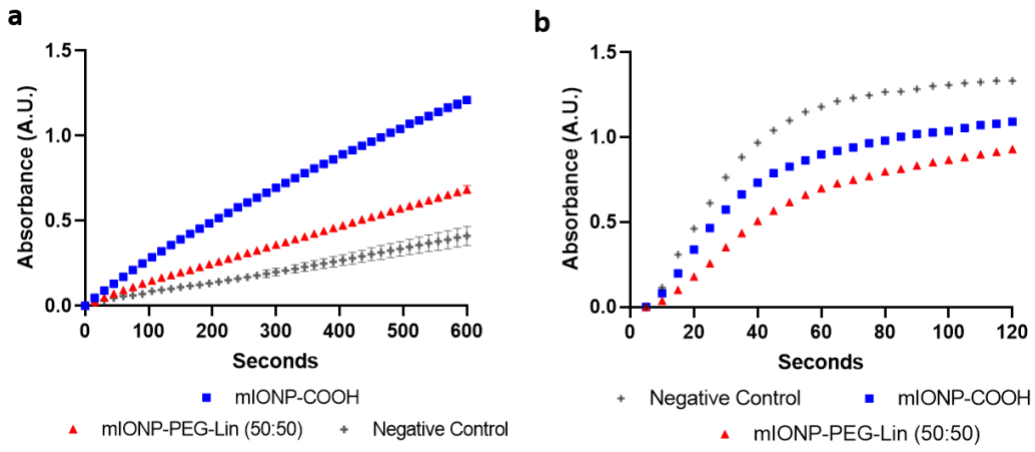

Figure 2.9. Colorimetric confirmation of linoleic acid content in stabilized mIONP-PEG-Lin particles. *Time course curves assessing the catalytic activity of mIONP-COOH and mIONP-PEG-Lin for the oxidation of 3,3',5,5'-tetramethylbenzidine (TMB) at (a) [TMB] = 840 uM and [H_2O_2] = 10 mM; and (b) [TMB] = 300 uM and [Ag+] = 175 uM; Concentrations were [Fe] = 150 µM for both mIONPs and mIONP-PEG-Lin. Negative control means absence of particle. pH was controlled with sodium acetate (0.1M) buffer (pH=4.5). The reactions were monitored at room temperature using 10 mm pathlength quartz cuvettes.*

2.2.2.3.2. Formation of linoleic acid-coated IONPs by a phase-transfer strategy

Linoleic acid-only coated IONP-filled micelles (IONP-Lin) were obtained using a phase-transfer strategy. (Fig. 2.10, a). Hydrophobic IONPs were dispersed in linoleic acid and deposited on top of a concentrated sodium linoleate solution. Under very gentle stirring, linoleic acid chains rearranged to coat the IONP-oleic particles in the interphase. Linoleic acid-coated IONP-filled micelles, c. 10nm hydrophilic nanoparticles, transferred into the aqueous phase (Fig. 2.10, b). The product was purified through centrifugation and spin-filter cycles to discard big aggregates and empty linoleic micelles (see Materials and Methods).

Avoiding the use of PEG-PLs has its advantages, as the polymer has been reported to limit cellular uptake [104]. Although, these IONP-Lin systems were stable in deionized water, in PBS it led to uncontrolled particle aggregation.

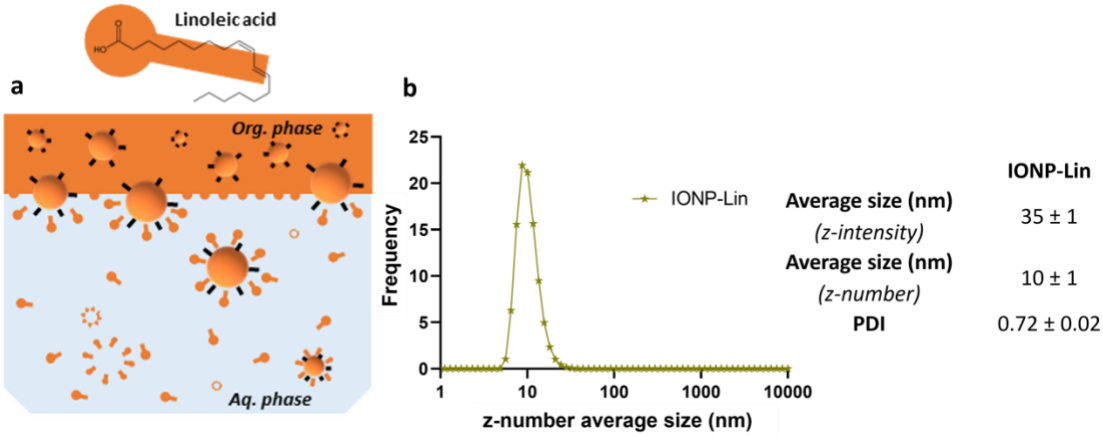

Figure 2.10. Solvent exchange methods enable the formation of linoleic acid-only coated IONPs. *(a) Schematic representation of solvent-exchange methods for the obtention of IONP-Lin micelles. (b) Nanoparticle size distribution as percentage (%) of events by z-number from IONP-Lin suspensions and physicochemical characterization summary. Representative values as mean ± SEM for at least three independent experiments as characterized by DLS.*

2.2.2.4. Optimizing mIONP stabilization

2.2.2.4.1. Assessing structural matching during amphiphilic self-assembly

In an attempt to demonstrate the versatility and potential to further tune the stability and properties of the mIONP, these were combined with some custom made amphiphiles. Structural matching between IONP surface oleic acid chains and these amphiphiles was expected to govern the mIONP self-assembly. Hence, four amphiphilic compounds were synthetized as candidates to study and optimize mIONP formation. These molecules shared a common hydrophilic peptide backbone (P1) (Fig. 2.11, a) kindly provided by our collaborators (see Materials and Methods). The P1 is rich in positively charged arginine-moieties, which were expected to stabilize mIONP suspensions through interparticle electrostatic repulsion [105]. However, the molecules were designed to differ in terms of the structure of their hydrophobic units (Fig. 2.11, b). The peptide was engineered to allow covalent attachment to the hydrophobic structures through click-chemistry via hydrazone adduct formation, with the adduct formed through the reaction of the aldehyde groups with the P1 hydrazine moieties (2.11, a).

Following previously stablished methods, hydrazine-rich peptides P1 were conjugated to: cyclohexane-carboxaldehyde (T1), benzaldehyde (T3), dodecanal (T20) and oleic

aldehyde (T25) [105]. The reaction yielded four different P1-Tx amphiphilic candidates for mIONP self-assembly (Fig. 2.11, b). The candidates were used immediately after their synthesis to minimize stability issues. P1-Tx-coated mIONPs (P1-Tx-IONP) assembly used an adapted version of previously described methods of dry film formation. P1-Tx and hydrophobic IONPs were solubilized in $CHCl_3$ in a 2:1 mass ratio. However, this time, the $CHCl_3$ solvent was not left to evaporate overnight, but instead it was made to evaporate quickly under a gentle nitrogen flow at room temperature. Once the $CHCl_3$ was evaporated, Milli-Q water was added to form the aqueous suspension of P1-Tx-IONPs (see Materials and Methods).

Combinations of hydrophobic IONPs with P1-T1 and P1-T3, which contained shorter cyclic chains of low structural matching to oleic acid, resulted in IONP-filled micelles of high polydispersity and instability. Instead, P1-T20/25-IONP, which contained longer hydrophobic chains of higher structural matching to oleic acid, led to stable < 200nm micelle suspensions (Fig, 2.11, b-d). Among these two, P1-T25-IONP showed preferential formation of particles of < 100nm (Fig, 2.11, d).

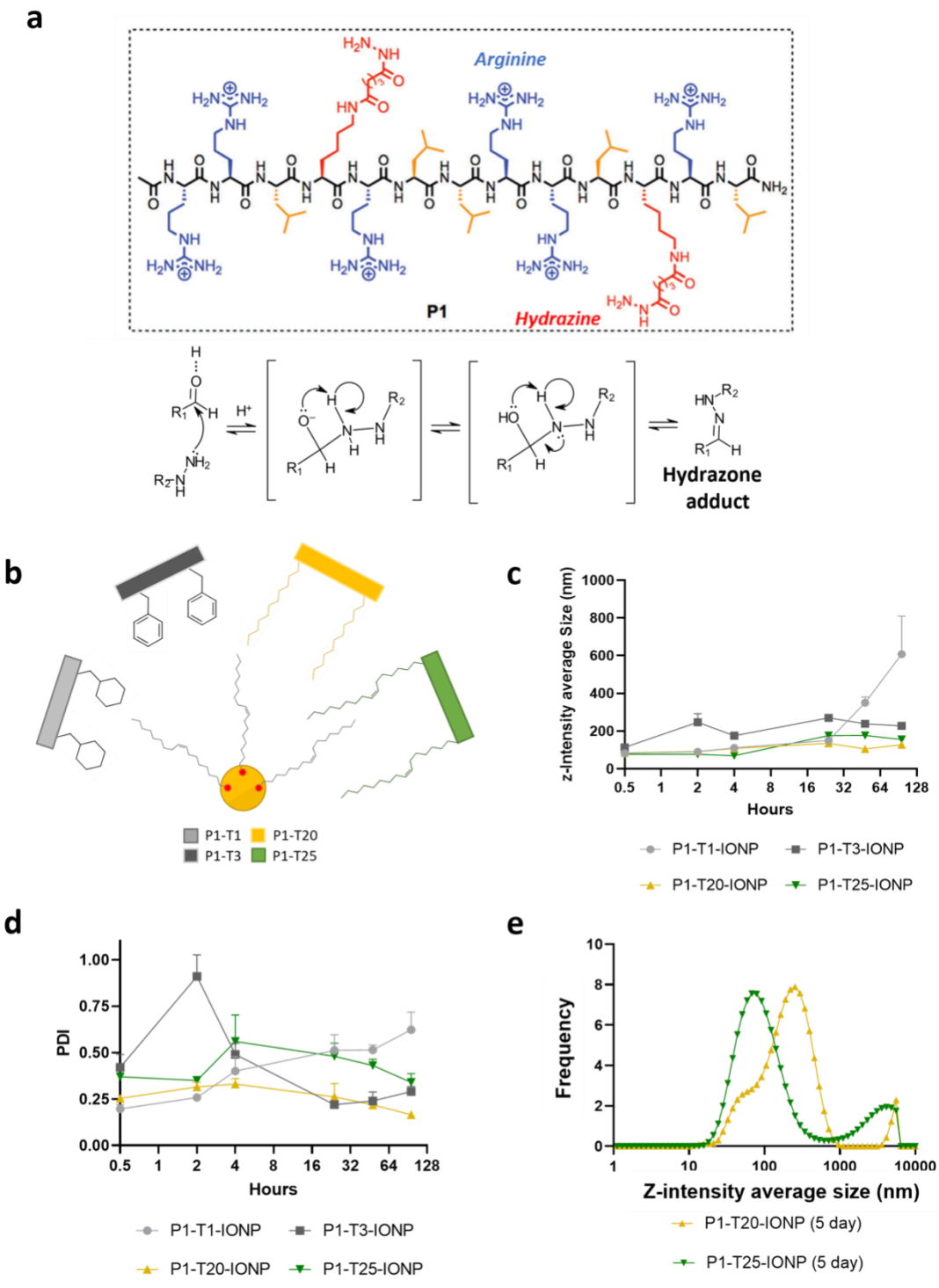

Figure 2.11. Structural matching governs mIONP self-assembly. *(a) Structure of the peptide backbone P1 and hydrazone adduct reaction scheme (a) Schematic representation of the interaction between oleic-acid coated IONPs with peptide (T1) decorated with cyclohexane-carboxaldehyde (P1-T1), benzaldehyde (P1-T3), dodecanal (P1-T20) and oleic aldehyde (P1-T25). (b) Size and (c) PDI monitoring of P1-T1-IONP (light grey line, circle), P1-T3-IONP (dark grey line, square), P1-T20-IONP (gold line,*

triangle) and P1-T25-IONP (green line, inverted triangle). (d) Frequency particle size distribution by Z-Intensity of P1-T20-IONP and P1-T25-IONP. Suspensions incubated in Milli-Q water at room temperature and characterized by DLS. Image (a) adapted from [105].

2.2.2.4.2. Assessing PEGylation and solid IONP core stabilizing contributions

P1-T20-IONP and P1-T25-IONP systems were unstable when suspended in PBS buffer (Fig. 2.12, b). This could be due to interactions of the phosphate ions with P1 arginine moieties through electrostatic and hydrogen bonds, thus attenuating interparticle electrostatic repulsion.

As discussed above, PEG chains are polymeric chains used as nanoparticle stabilizers. They form bulky meshes that prevent particle coalescence through steric hindrance. Here, PEG-PLs were also expected to stabilize the vehicle through increased coating cohesion, as phosphate moieties in the PEG-PL structure could also interact with P1 arginines through electrostatic and hydrogen bonds (Fig. 2.12, a).

To test this hypothesis, PEGylated P1-Tx-IONP assembly followed methods of particle formation described in the section above (2.2.2.4.1.). Now, PEG-PL chains were added into the $CHCl_3$ mix at a mass ratio of 1:2:1 (IONP: P1-Tx : PEG-PL) (see Materials and Methods). PEGylation of P1-T25-IONPs yielded particle suspensions that proved stable in PBS until the end of experimentation (10 days). Although PEGylation could also stabilize IONP-free micelles, the oleic acid-coated IONP core was also needed to ensure long-term stability (Fig. 2.12, b-c). Thus, these results highlight the stabilizing contributions of both PEG-PLs and the solid particle core in mIONP formation.

PEG-PL with different chemical terminations could be interchanged without harming the product. PEG(2000 kDa)-PLs terminated in either maleimide (-MAL) or methoxy (-OMe) moieties could be used to form stable, < 30 nm particle suspensions of low polydispersity. The two vehicles differed in surface charge (Fig 2.12. d) and in chemical reactivity (see section 2.2.3.2.1), which will be key for downstream surface particle functionalization strategies.

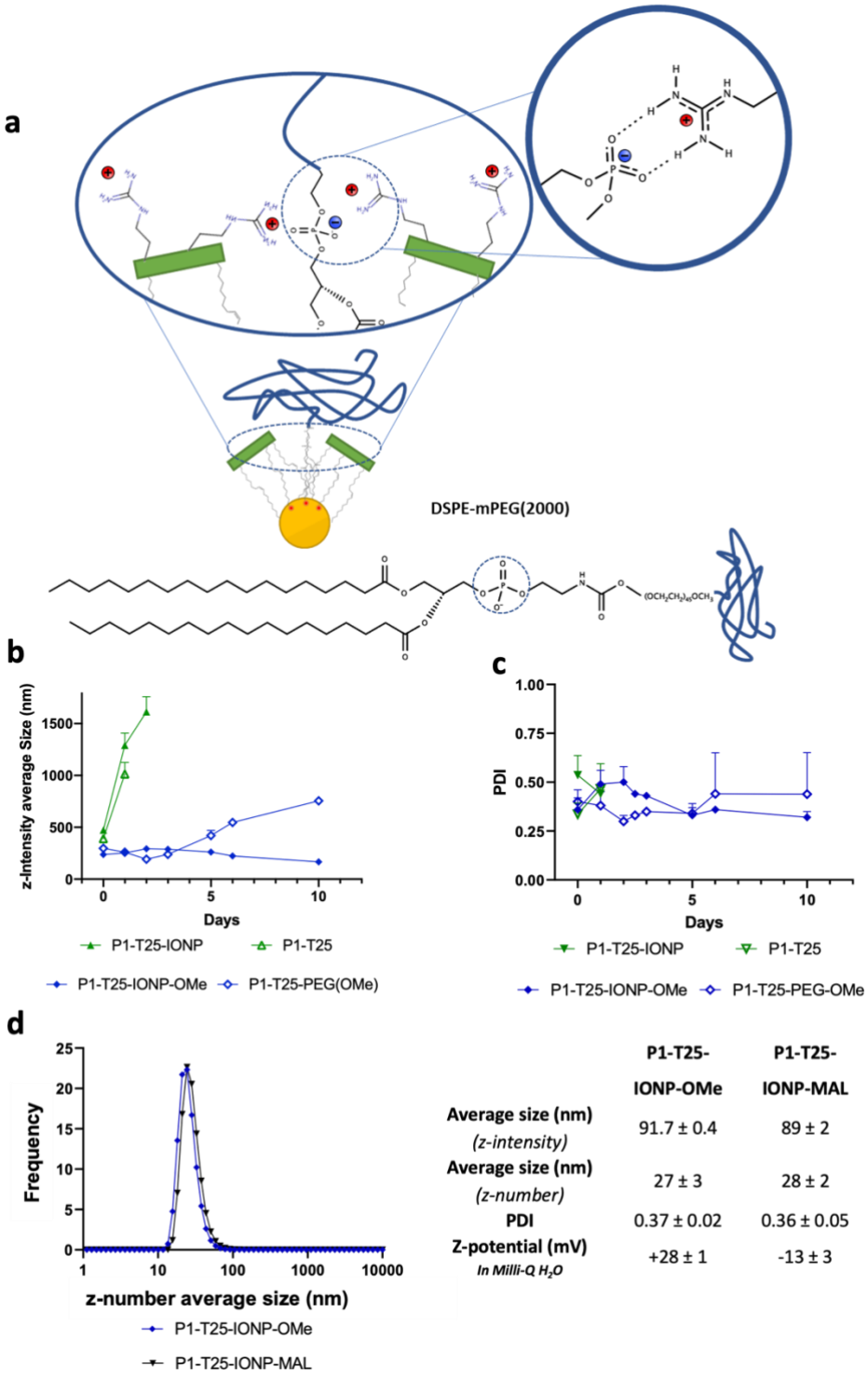

	P1-T25-IONP-OMe	P1-T25-IONP-MAL
Average size (nm) *(z-intensity)*	91.7 ± 0.4	89 ± 2
Average size (nm) *(z-number)*	27 ± 3	28 ± 2
PDI	0.37 ± 0.02	0.36 ± 0.05
Z-potential (mV) *In Milli-Q H_2O*	+28 ± 1	-13 ± 3

Figure 2.12. PEGylation and solid IONP core confer strong mIONP stabilizing contributions *(a) Schematic representation of the proposed structural changes resulting of PEGylation. (b) size and (c) PDI monitoring of P1-T25-IONP (green line, full triangle), IONP-free P1-T25 (green line, empty circle), P1-T25-IONP-OMe (blue line, full diamond) and IONP-free P1-T25-PEG(OMe) (blue line, empty diamond). Suspensions incubated in PBS at room temperature and characterized by DLS.*

Nanoparticle size distribution as percentage (%) of events by z-number from (a) P1-T25-IONP-OMe, (b) P1-T25-IONP-MAL suspensions and (c) physicochemical characterization summary. Representative values as mean ± SEM for different mIONP suspensions for at least three independent measurements as characterized by DLS.

2.2.3. Outer framework functionalization

2.2.3.1. TLRa capture through electrostatic self-assembly

As previously discussed, TLR agonists are used in cancer immunotherapies to stimulate anticancer immunity. TLRa serve as "danger signals", or adjuvants, which support the development of strongly immunostimulatory systems for vaccine development and anticancer applications. A variety of nanomedicine devices have been used to deliver TLRa adjuvants into the TME. These strategies demonstrated capacity of inducing *in situ* protumoral-to-antitumoral immune cell activation for cancer immunotherapy [25,27]. However, TLRa adjuvant administration alone can suffer from limited therapeutic efficiency [106]. Recent research has shown that ROS release can sensitize immune cells to TLRa-mediated activation and potentiate their effects [29]. Hence, TLRa delivery using IONzyme-based vehicles offers promising strategies for the development of more potent immunotherapies [26,95].

Previous research from our group showed that electrostatic self-assembly offers an efficient and straight forward strategy for mIONP-mediated TLRa delivery [82,86]. In previous sections, variations in the mIONP assembly process were shown to yield mIONPs solutions with distinguishable particle size, stability and surface charge. P1-T25-IONP-OMe particles showed positive surface charges owing to the arginine-rich P1 backbone [105]. P1-T25-IONP-OMe could then be used load negatively charged TLRa adjuvants like polyinosinic:polycytidylic acid (poly(I:C) or pIC). Poly(I:C) is a clinically relevant TLRa adjuvant proposed as one of the "twelve immunotherapy drugs that can cure cancer" [107]. The compound shows a negatively charged phosphate-rich structure in the form of a double-strand (Fig. 2.13, a). In addition, poly(I:C) activates the TLR3 found in intracellular endolysosomal compartments. Previous research from our group observed that mIONPs are trafficked through such compartments [82], thus making them ideal for poly(I:C) delivery. pH-catalysed Fenton chemistry-mediated IONP disassembly (typical endolysosome pH ~ 3-5 [16]) may further facilitate site-specific delivery of the compound.

A range poly(I:C) concentrations were mixed with P1-T25-IONP-OMe vehicles and left overnight to self-assemble at room temperature. An ultra-centrifugation cycle was applied to remove non-bound poly(I:C) remaining in the supernatant. The IONP pellet formed could be resuspended in aqueous media and evaluated (see Materials and Methods). UV-vis assessment confirmed pIC capture (absorbance peak at 260 nm) (Fig. 2.13, b) by the mIONP. Their self-assembly yielded particle suspensions that proved stable (Fig. 2.13, a). Increasing amounts of poly(I:C) (0 – 500 µg/mL) led to a progressive decrease in particle surface charge (z-potential) (Fig. 2.13, c). Finally, TEM imaging confirmed absence of aggregates in pIC-loaded P1-T25-IONP-OMe samples (Fig. 2.13, d).

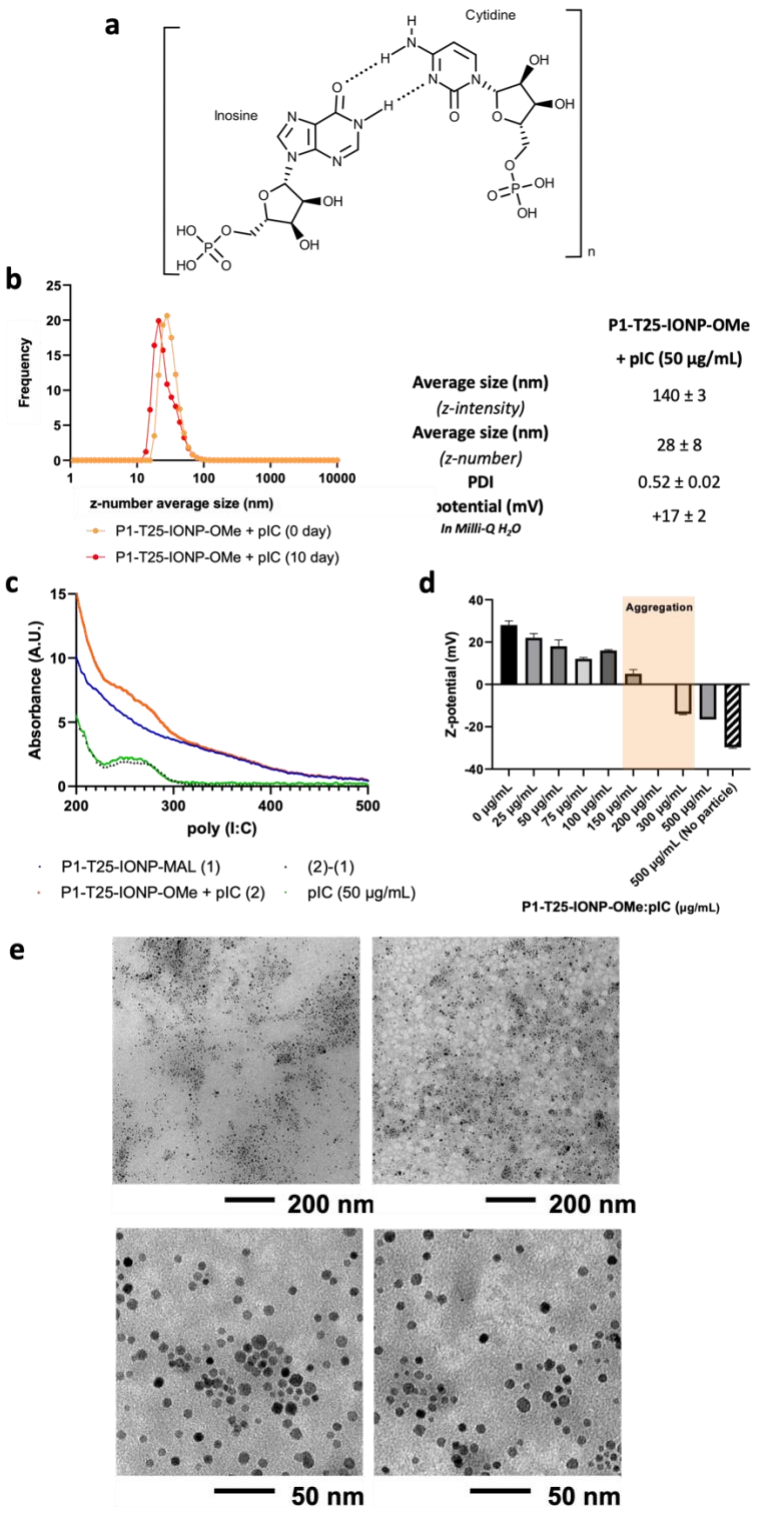

Figure 2.13. mIONP surface charge enables stable TLRa electrostatic self-assembly. *(a) Poly(I:C) (pIC) chemical structure. Nanoparticle (b) size distribution as percentage (%) of events by z-number from P1-T25-IONP-OMe ([Fe] = 600 µM) + pIC (50 µg/mL) at day 0 and day 10 and physicochemical characterization summary; (c) Absorbance spectra comparison between P1-T25-IONP-OMe and P1-T25-IONP-OMe + pIC after*

purification, indicating effective capture of pIC; (d) Z-potential from P1-T25-IONP-OMe + pIC (0-500 µg/mL) combinations; (e) TEM images of the construct. Representative values as mean ± SD for at least three independent measurements as characterized by DLS.

2.2.3.2. Targeting ligand decoration through maleimide-thiol adducts

Several studies have stablished the limited scope of passive targeting, where only an approximate 1% of the dose accumulates in the tumor site [108]. As previously described (see Chapter I), literature has devised many active targeting drug strategies to better control payload delivery [97109,110]. Among them, the incorporation of active targeting ligands offers intriguing means for controlled therapy delivery by selectively recognizing and binding to specific cell receptors.

In this section, we study the surface decoration of our mIONP systems with antibodies acting as targeting ligands. These are biological bodies (MW ~ 150 kDA) that stand out for their high binding specificity [111,112].

2.2.3.2.1. **ICB antibody-surface particle decoration**

Thiosuccinimide adduct formation has proven a useful bioconjugation pathway and indeed was adopted in many clinically approved compounds [124–127].Reduced thiols react with maleimide groups through Michael addition to form thiosuccinimide adducts (Fig. 2.14, a). The reaction is quick and quantitative under mild conditions (neutral pH, saline buffer, room temperature), which avoid biomolecule degradation and loss of biological activity [124]. However, reactive available thiols may be scarce in the antibody surface. Hence, surface thiolation using 2-Iminothiolane (Traut's reagent) is an attractive strategy to turn surface lysine amine residues into reactive thiols (Fig. 2.14, b) [128]. The reaction also occurs at mild conditions avoiding concerns over structural integrity of the modified antibody [129].

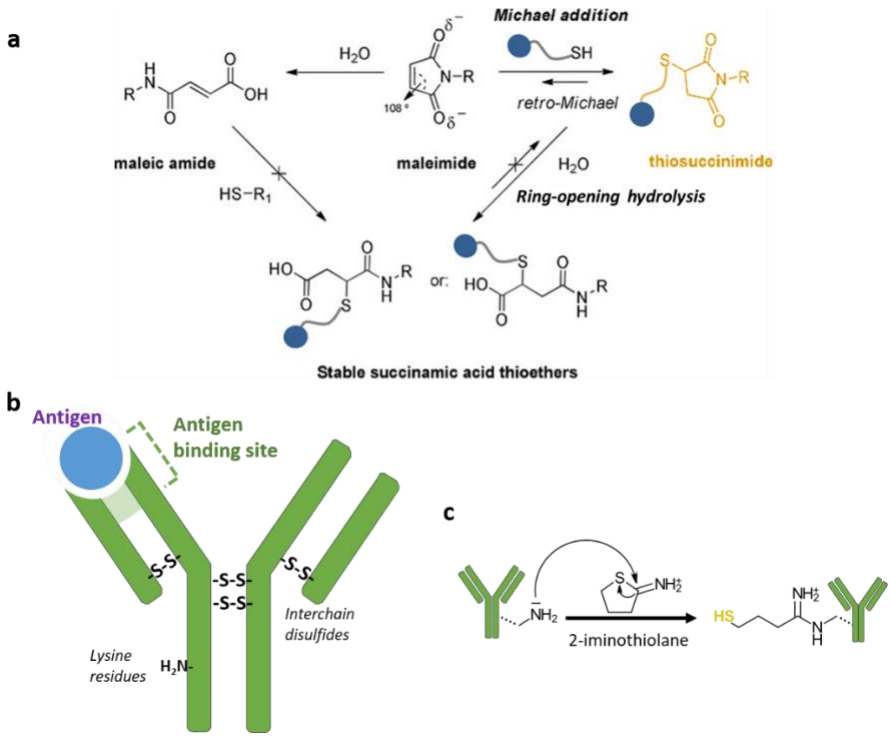

Figure 2.14. Thiol-maleimide "click-chemistry" bioconjugation and antibody thiolation strategies scheme*. (a) Michael addition between nucleophilic thiol and π-conjugated maleimide double bond yields thiosuccinimide. Further hydrolyzation of the ring prevents retro-Michael reactions. Early maleimide hydrolyzation will prevent thiol conjugation. Figure adapted from* [124]*. (b) Schematic representation of antibody structure and (c) surface thiolation strategies through lysine modification.*

The discovery of programmed death ligand type-1 (PD-L1) was a breakthrough for cancer immunotherapy. PD-L1 overexpression is a relevant mechanism used by cancer cells to induce immune cell deactivation [113]. As previously described (see Chapter I), PD-L1 functions as an immune checkpoint yielding the deactivation of cytotoxic $CD8^+$ T-cells, downregulation of important immune stimulatory signalling, stabilization of M2-like macrophage phenotypes and, overall, reinforcing the immunosuppressive character of the TME [114,115]. Hence, we devise that mIONP decoration with an anti-PD-L1 (aPD-L1) antibody could simultaneously provide: (i) therapeutic effects via immune checkpoint blockade immunotherapy [116] (ii) PD-L1 detection and patient discrimination through non-invasive imaging techniques (only 20% of cancer patients express PD-L1) [117–120] and (iii) active targeted drug/vaccine delivery.

IONP were coated with MAL-terminated PEG(2000 kDa)-PLs using the methods of dry-film hydration described in sections above (Fig. 2.6, a-b; See Materials and Methods).

Typically, 1 mg of IONP were mixed with 2.5 mg of PEG-PL-MAL yielding IONP suspensions that will be referred to as mIONP-MAL (Fig. 2.15). Following previously stablished methods and manufacturer instructions, antibody and 2-Iminothiolane were mixed at 1:10 molar ratio and left to react for one hour at room temperature in PBS [112]. Then, 2-Iminothiolane excess was removed through spin-filtration (using 100 kDa pore size filters) to avoid interferences with maleimide-thiol conjugation. To prevent early thiol degradation, antibody thiolation was only performed when ready to use. mIONP-Mal suspensions were combined with thiolated antibodies in a 1:9 molar ratio (IONP : Antibody) and left to react overnight at room temperature. Free aPDL1 and reagent excess was removed by spin-filtration, yielding 50 nm aPDL1-coated mIONP (mIONP-aPDL1) suspensions of low polydispersity (Fig. 2.15, a) (see Materials and Methods). mIONP-aPDL1 suspensions would remain stable until end of experimentation (one week; Data not shown).

The amount of antibody in these systems was quantified using bicinchoninic acid assays (BCA) (see Materials and Methods). BCA tests are well-stablished methods for total protein quantification by UV-Vis spectroscopy. The test uses copper Cu^{2+} ions that are reduced to Cu^{+} in proportion to the amount of protein in solution. Proteins contain multiple moieties (i.e. cysteine, cystine, tryptophan or the peptide bond) that can induce induce Cu^{2+} to Cu^{+} reduction [130]. Two molecules of bicinchoninic acid will chelate free Cu^{+} yielding a blue organometallic complex (absorbance peak at 562 nm) that is quantifiable by UV-Vis spectroscopy (Fig. 2.15, b) [131]. BCA tests indicated that mIONP-aPDL1 particles retained an average 24 ± 7 % of the aPDL1 added (Fig. 2.15, c). The amount captured was equivalent to 4 mols of aPDL1 antibodies decorating each IONP. Negligible amounts of aPDL1 were retained by similarly sized and charged non-reactive IONP-COOH particles thus confirming that antibody binding was due to covalent thiosuccinimide bonds (Fig. 2.15, c).

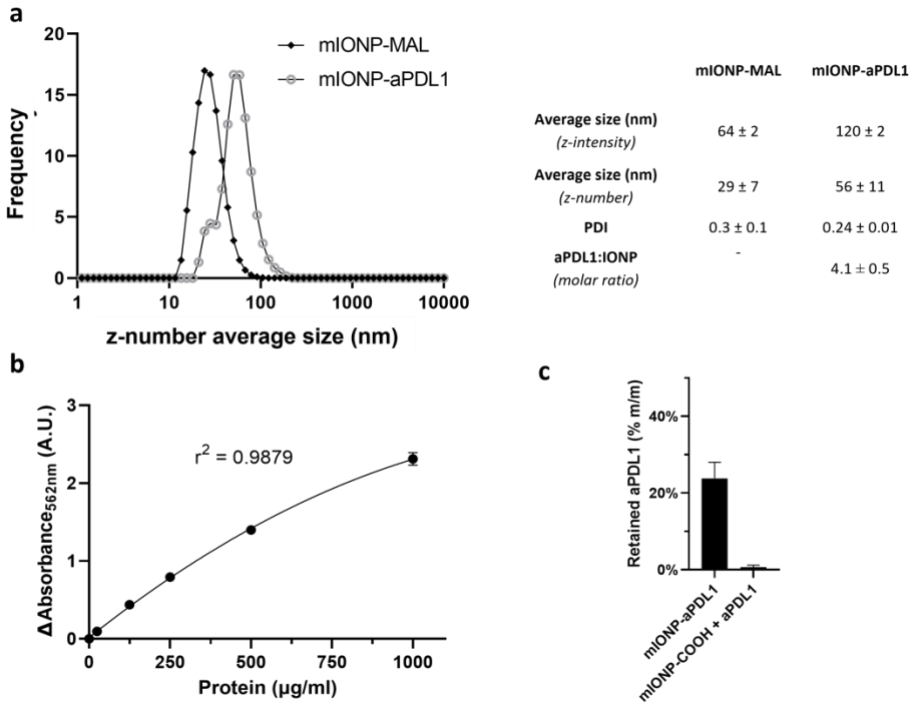

	mIONP-MAL	mIONP-aPDL1
Average size (nm) *(z-intensity)*	64 ± 2	120 ± 2
Average size (nm) *(z-number)*	29 ± 7	56 ± 11
PDI	0.3 ± 0.1	0.24 ± 0.01
aPDL1:IONP *(molar ratio)*	-	4.1 ± 0.5

Figure 2.15. Maleimide-thiol bioconjugation enables aPDL1 decoration of IONP-filled micelles *(a) Nanoparticle size distribution as percentage (%) of events by z-number from mIONP-MAL and mIONP-aPDL1 suspensions, physicochemical characterization and aPD-L1 retention summary as characterized by DLS. (b) BCA fit curve for protein quantification and (c) initial aPDL1 retained (% m/m) after purification steps in comparison with non-reactive mIONP-COOH vehicles. Representative values as mean ± SEM for at least three independent experiments.*

2.2.3.2.1.2. Antibody binding activity after particle decoration

Commercial enzyme-linked immunosorbent assays (ELISAs) were used to evaluate mIONP-aPDL1 binding activity to PD-L1 (Fig, 2.15, a-c) (see Materials and Methods). ELISA tests are well-stablished methods for analyte quantification by UV-Vis spectroscopy. Routine ELISA tests use a surface coated with analyte capturing biomolecules (typically antibodies) which bind to the analyte in solution. The immobilized analyte is then labeled with another analyte-binding antibody that is typically linked to a peroxidase enzyme. The peroxidase enzyme catalyses the oxidation of TMB, which yields the blue coloured charge transfer complex TMB_{OX} as described above. Final HCl excess addition will yield complete $TMB_{OX}{}^2$ oxidation, which shows a characteristic yellow colour (absorbance peak at 450 nm). The intensity of the yellow

colour is thus proportional to the amount of analyte in the sample, which can then be quantified (Fig. 2.16, c).

Free PD-L1 (80 pg/mL) in solution displayed a positive bright yellow colour by ELISA (Fig. 2.16, a). Instead, when mIONP-aPDL1 suspensions were added into a solution of free PD-L1, the antibody was captured by the IONP-based formulation (Fig. 2.16, c) and removed from solution during well wash cycles, resulting in baselevel absorbance values by ELISA (Fig, 2.16, a-b). In comparison, minimal non-specific antibody removal from solution was observed when PD-L1 was incubated with mIONP-MAL. These results confirmed that mIONP-aPDL1 suspensions retained PD-L1-specific binding activity after conjugation.

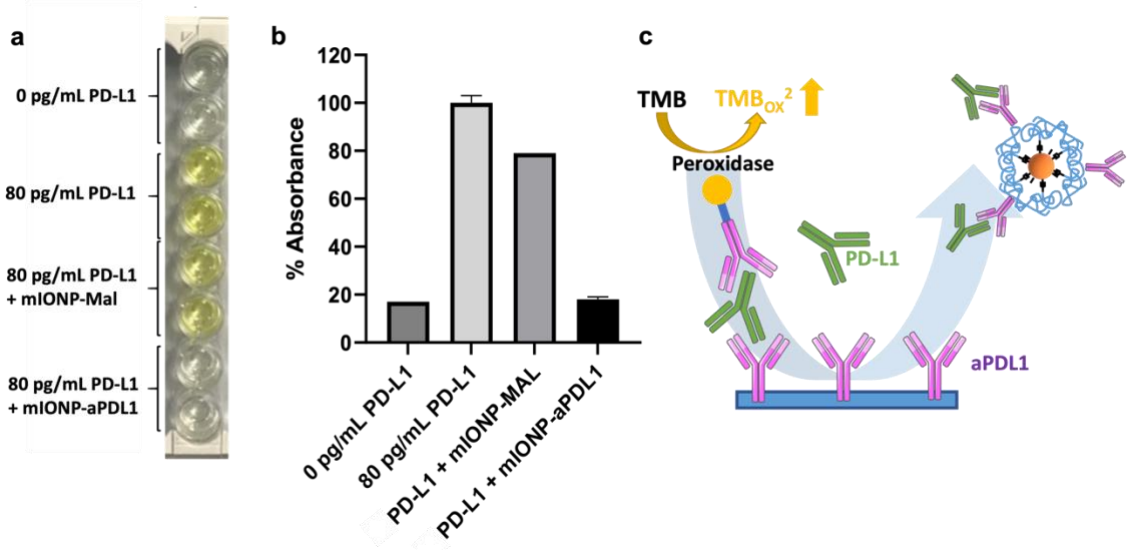

Figure 2.16. mIONP-aPDL1 retains antibody binding activity. *PD-L1 concentration was measured by ELISA test kit following PD-L1 incubation with mIONP-MAL and mIONP-aPDL1 for 1 hour at room temperature. (a) ELISA kit picture after HCl excess solution addition; (b) variation in absorbance signal (λ= 450 nm) relative to positive control (80 pg PD-L1/mL); (c) Schematic representation of the indirect ELISA assay method used. Concentrations used were [Fe] = 0.5 mM for both mIONPs and [aPDL1] = 40 ug/mL for mIONP-aPDL1. Representative values as an ± SEM for two independent experiments.*

2.2.3.2.1.3. mIONP-aPDL1 active targeting features *in vitro*

Finally, we assessed activity of mIONP-aPDL1 treatments in *in vitro* cell cultures. Their properties were evaluated using murine melanoma B16-F10(OVA) cells, which show

high PD-L1 expression (See Chapter 4) and murine macrophages RAW 264.7 cells, which may express PD-L1 only after M2-like activation [132]. Melanoma and macrophage cells were co-cultured together in the same compartment (Fig. 2.17, a). The TME is rich in different immune cell types [133], among which macrophages represent a predominant population [134]. Hence, these heterogeneous cell co-cultures can offer interesting indications on the dynamics of treatment action in the TME.

Cell viability per each cell type was measured by Flow Cytometry. After treatment, cells were collected and labeled with fluorescent Zombie NIR™ dye. This is an amine-reactive dye that permeates through cells with compromized membranes (typical of dead cells) and accumulates inside the amine-rich cytosol [135]. Hence, from differences in fluorescent intensity we can distinguish living and dead cell populations (Fig. 2.17, b; y-axis). Collected cells were also labeled with fluorescent antibodies targeting F4/80, which is a membrane protein expressed only in macrophage cells [136]. Hence, from differences in fluorescent intensity we can distinguish the two cell types (Fig. 2.17, b; x-axis) (see Materials and Methods).

In comparison to non-decorated mIONP treatments, mIONP-aPDL1 triggered an increase in cancer cell death with no detrimental effect towards macrophages (Fig, 2.17, c-d). Research developed in this thesis has proven that increased IONzyme uptake by melanoma cells can induce oxidative stress and cancer-specific ferroptosis [95]. In turn, increased cancer cell ferroptosis can trigger anticancer macrophage activation. These results were not reproduced by free aPDL1 and mIONP co-administration. Hence, the increase in melanoma-specific cancer death here reported is indicative of increased IONzyme delivery through effective PD-L1^{+} targeting by IONP-aPDL1 vehicles.

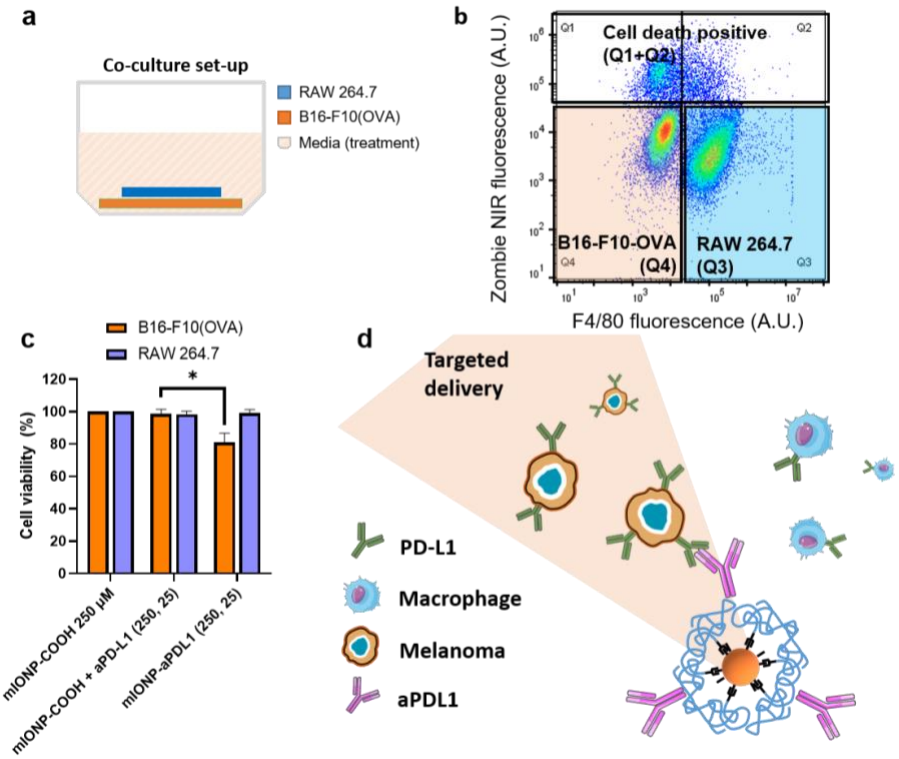

Figure 2.17. mIONP-aPDL1 selectively reduce cancer cell viability. *B16-F10(OVA) and RAW 264.7 cell viability in direct cell-to-cell co-cultures measured by flow cytometry following 24 h treatment. (a) Schematic representation of the immune-cancer co-culture assay set-up. (b) flow cytometry gating strategy for cell death (y-axis) and cell-type (x-axis) discrimination. (c) Cell viability per cell type after 24-hour treatment with mIONP, mIONP + free aPDL1 or mIONP-aPDL1. Concentrations were [Fe] = 250 µM and [aPDL1] = 25 µg/mL. (d) Proposed schematic representation of PD-L1 targeting strategy. Results are shown normalized to non-decorated mIONP-COOH control. Representative values as mean ± SEM for three independent experiments.*

2.3. Conclusions

The multilevel customizable features of redox-active IONP-based devices were here characterized and optimized. Variations in the mIONP assembly process provided control over distinguishable device properties (i.e. size, charge, stability, chemical reactivity, bioactive molecule loading and particle surface functionalization) key for downstream anticancer applications. The constructs were assembled and evaluated demonstrating:

- IONPs functioning as the core of our devices can be synthetized with high reproducibly and size-control. The mIONPs display peroxidase-like properties. Their high affinity for H_2O_2, an abundant subproduct of the accelerated cancerous metabolism, makes them ideal for site-specific redox stress-inducing therapies in the TME. Their catalytic behaviour proved negligible in standard physiologic conditions found outside the acidic tumor site and intracellular endolysosomal compartments.
- The oleic acid coating of the IONP core provides anchoring sites for amphiphilic self-assembly and aqueous stabilization. Self-assembly dynamics are governed by structural matching between interlaced amphiphilic compounds. The solid IONP core and surface PEGylation contribute to mIONP stabilization through increased steric hindrance and particle-micelle cohesion.
- Inner hydrophobicity resulting from mIONP self-assembly can be utilized for bioactive compound loading. Through the pH-mediated Fenton reactivity demonstrated by the IONP, the formulation is expected to undergo structural disassembly in acidotic biological compartments of interest like the TME, which represents an intriguing feature to trigger site-specific drug delivery and reveal "stealth" bioactive and immunostimulatory properties of the vehicle.
- Functionalization of the mIONP outmost layer can be optimized for:
    - Electrostatic self-assembly with immunostimulatory TLRa adjuvant molecules. Modulation of the particle surface charge could be suited to load other clinically relevant immunostimulatory compounds.
    - Targeting ligand decoration through stable covalent bonding. Functionalization of surface particle coating with thiol-maleimide "click chemistry" allowed the incorporation of clinically PD-L1 immune check

blockade inhibitors. mIONP-aPDL1s retained antibody binding activity and triggered cancer-specific cell death in complex macrophage-melanoma co-cultures. It is envisioned that these results open the door for potential applications in: (i) PD-L1 detection and diagnosis, (ii) ICB therapy strategies and (iii) active targeting.

The multilevel customization rationale stablished here will enable the “programming” of IONP-based vehicles towards the reinforcement of non-redundant anticancer therapies in the chapters that follow.

2.4. References

(1) van der Meel, R. et al. Smart Cancer Nanomedicine. *Nat. Nanotechnol.* **2019**, *14* (11), 1007–1017. https://doi.org/10.1038/s41565-019-0567-y.

(2) Fan, W.; Yung, B.; Huang, P.; Chen, X. Nanotechnology for Multimodal Synergistic Cancer Therapy. *Chem. Rev.* **2017**, *117* (22), 13566–13638. https://doi.org/10.1021/acs.chemrev.7b00258.

(3) Gobbo, O. L.; Sjaastad, K.; Radomski, M. W.; Volkov, Y.; Prina-Mello, A. Magnetic Nanoparticles in Cancer Theranostics. *Theranostics* **2015**, *5* (11), 1249–1263. https://doi.org/10.7150/thno.11544.

(4) Hassannia, B.; Vandenabeele, P.; Vanden Berghe, T. Targeting Ferroptosis to Iron Out Cancer. *Cancer Cell* **2019**, *35* (6), 830–849. https://doi.org/10.1016/j.ccell.2019.04.002.

(5) Saeed, M.; Ren, W.; Wu, A. Therapeutic Applications of Iron Oxide Based Nanoparticles in Cancer: Basic Concepts and Recent Advances. *Biomater. Sci.* **2018**, *6* (4), 708–725. https://doi.org/10.1039/c7bm00999b.

(6) Gálvez, N. et al. Comparative Structural and Chemical Studies of Ferritin Cores with Gradual Removal of Their Iron Contents. *J. Am. Chem. Soc.* **2008**, *130* (25), 8062–8068. https://doi.org/10.1021/ja800492z.

(7) Zhu, M. et al. Physicochemical Properties Determine Nanomaterial Cellular Uptake, Transport, and Fate. *Acc. Chem. Res.* **2013**, *46* (3), 622–631. https://doi.org/10.1021/ar300031y.

(8) Karlsson, H. L.; Cronholm, P.; Gustafsson, J.; Möller, L. Copper Oxide Nanoparticles Are Highly Toxic: A Comparison between Metal Oxide Nanoparticles and Carbon Nanotubes. *Chem. Res. Toxicol.* **2008**, *21* (9), 1726–1732. https://doi.org/10.1021/tx800064j.

(9) Gao, L. et al. Intrinsic Peroxidase-like Activity of Ferromagnetic Nanoparticles. *Nat. Nanotechnol.* **2007**, *2* (9), 577–583. https://doi.org/10.1038/nnano.2007.260.

(10) Chaudhari, K. N.; Chaudhari, N. K.; Yu, J. S. Peroxidase Mimic Activity of Hematite Iron Oxides (α-Fe 2O 3) with Different Nanostructures. *Catal. Sci. Technol.* **2012**, *2* (1), 119–124. https://doi.org/10.1039/c1cy00124h.

(11) Gao, L.; Fan, K.; Yan, X. Iron Oxide Nanozyme: A Multifunctional Enzyme Mimetic for Biomedical Applications. *Theranostics* **2017**, *7* (13), 3207–3227. https://doi.org/10.7150/thno.19738.

(12) Strlič, M.; Kolar, J.; Šelih, V. S.; Kočar, D.; Pihlar, B. A Comparative Study of Several Transition Metals in Fenton-like Reaction Systems at Circum-Neutral PH. *Acta Chim. Slov.* **2003**, *50* (4), 619–632.

(13) Jian, W.; Wang, S. P.; Zhang, H. X.; Bai, F. Q. Disentangling the Role of

Oxygen Vacancies on the Surface of Fe3O4 and γ-Fe2O3. *Inorg. Chem. Front.* **2019**, *6* (10), 2660–2666. https://doi.org/10.1039/c9qi00351g.

(14) Gao, L.; Fan, K.; Yan, X. Iron Oxide Nanozyme: A Multifunctional Enzyme Mimetic for Biomedical Applications. *Theranostics* **2017**, *7* (13), 3207–3227. https://doi.org/10.7150/thno.19738.

(15) Vaupel, P.; Multhoff, G. Accomplices of the Hypoxic Tumor Microenvironment Compromising Antitumor Immunity: Adenosine, Lactate, Acidosis, Vascular Endothelial Growth Factor, Potassium Ions, and Phosphatidylserine. *Front. Immunol.* **2017**, *8* (DEC), 1887. https://doi.org/10.3389/fimmu.2017.01887.

(16) Tannock, I. F.; Rotin, D. Acid PH in Tumors and Its Potential for Therapeutic Exploitation. *Cancer Res.* **1989**, *49* (16), 4373–4384. https://doi.org/2545340.

(17) Ratajczak, M. Z.; Bujko, K.; Mack, A.; Kucia, M.; Ratajczak, J. Cancer from the Perspective of Stem Cells and Misappropriated Tissue Regeneration Mechanisms. *Leukemia* **2018**, *32* (12), 2519–2526. https://doi.org/10.1038/s41375-018-0294-7.

(18) Dvorak, H. F. Tumors: Wounds That Do Not Heal-Redux. *Cancer Immunol. Res.* **2015**, *3* (1), 1–11. https://doi.org/10.1158/2326-6066.CIR-14-0209.

(19) Vernon, P. J.; Tang, D. Eat-Me: Autophagy, Phagocytosis, and Reactive Oxygen Species Signaling. *Antioxidants Redox Signal.* **2013**, *18* (6), 677–691. https://doi.org/10.1089/ars.2012.4810.

(20) Mittal, M.; Siddiqui, M. R.; Tran, K.; Reddy, S. P.; Malik, A. B. Reactive Oxygen Species in Inflammation and Tissue Injury. *Antioxidants Redox Signal.* **2014**, *20* (7), 1126–1167. https://doi.org/10.1089/ars.2012.5149.

(21) Zhou, J. et al. Immunogenic Cell Death in Cancer Therapy: Present and Emerging Inducers. *J. Cell. Mol. Med.* **2019**, *23* (8), 4854–4865. https://doi.org/10.1111/jcmm.14356.

(22) Garg, A. D.; Romano, E.; Rufo, N.; Agostinis, P. Immunogenic versus Tolerogenic Phagocytosis during Anticancer Therapy: Mechanisms and Clinical Translation. *Cell Death Differ.* **2016**, *23* (6), 938–951. https://doi.org/10.1038/cdd.2016.5.

(23) Feng, M. et al. Phagocytosis Checkpoints as New Targets for Cancer Immunotherapy. *Nat. Rev. Cancer* **2019**, *19* (10), 568–586. https://doi.org/10.1038/s41568-019-0183-z.

(24) Kohno, K. et al. Inflammatory M1-like Macrophages Polarized by NK-4 Undergo Enhanced Phenotypic Switching to an Anti-Inflammatory M2-like Phenotype upon Co-Culture with Apoptotic Cells. *J. Inflamm. (United Kingdom)* **2021**, *18* (1), 1–14. https://doi.org/10.1186/s12950-020-00267-z.

(25) Napolitani, G.; Rinaldi, A.; Bertoni, F.; Sallusto, F.; Antonio, L. Selected TLR

Agonist Combinations Synergistically Trigger a TH1 Polarizing Program in Dendritic Cells. *Nat. Immunol.* **2005**, *6* (8), 769–776. https://doi.org/10.1038/ni1223.Selected.

(26) Mulens-Arias, V.; Rojas, J. M.; Pérez-Yagüe, S.; Morales, M. P.; Barber, D. F. Polyethylenimine-Coated SPIONs Trigger Macrophage Activation through TLR-4 Signaling and ROS Production and Modulate Podosome Dynamics. *Biomaterials* **2015**, *52* (1), 494–506. https://doi.org/10.1016/j.biomaterials.2015.02.068.

(27) West, A. P. et al. TLR Signalling Augments Macrophage Bactericidal Activity through Mitochondrial ROS. *Nature* **2011**, *472* (7344), 476–480. https://doi.org/10.1038/nature09973.

(28) Zhao, J. et al. Anti-Tumor Macrophages Activated by Ferumoxytol Combined or Surface-Functionalized with the TLR3 Agonist Poly (I: C) Promote Melanoma Regression. *Theranostics* **2018**, *8* (22), 6307–6321. https://doi.org/10.7150/thno.29746.

(29) Liu, L. et al. ROS-Inducing Micelles Sensitize Tumor-Associated Macrophages to TLR3 Stimulation for Potent Immunotherapy. *Biomacromolecules* **2018**, *19* (6), 2146–2155. https://doi.org/10.1021/acs.biomac.8b00239.

(30) Dixon, S. J. et al. Ferroptosis: An Iron-Dependent Form of Nonapoptotic Cell Death. *Cell* **2012**, *149* (5), 1060–1072. https://doi.org/10.1016/j.cell.2012.03.042.

(31) Gorrini, C.; Harris, I. S.; Mak, T. W. Modulation of Oxidative Stress as an Anticancer Strategy. *Nat. Rev. Drug Discov.* **2013**, *12* (12), 931–947. https://doi.org/10.1038/nrd4002.

(32) Ranji-Burachaloo, H.; Gurr, P. A.; Dunstan, D. E.; Qiao, G. G. Cancer Treatment through Nanoparticle-Facilitated Fenton Reaction. *ACS Nano* **2018**, *12* (12), 11819–11837. https://doi.org/10.1021/acsnano.8b07635.

(33) Trachootham, D.; Alexandre, J.; Huang, P. Targeting Cancer Cells by ROS-Mediated Mechanisms: A Radical Therapeutic Approach? *Nat. Rev. Drug Discov.* **2009**, *8* (7), 579–591. https://doi.org/10.1038/nrd2803.

(34) Friedmann Angeli, J. P.; Krysko, D. V.; Conrad, M. Ferroptosis at the Crossroads of Cancer-Acquired Drug Resistance and Immune Evasion. *Nat. Rev. Cancer* **2019**, *19* (7), 405–414. https://doi.org/10.1038/s41568-019-0149-1.

(35) Li, J. et al. Ferroptosis: Past, Present and Future. *Cell Death Dis.* **2020**, *11* (2). https://doi.org/10.1038/s41419-020-2298-2.

(36) Mou, Y. et al. Ferroptosis, a New Form of Cell Death: Opportunities and Challenges in Cancer. *J. Hematol. Oncol.* **2019**, *12* (1), 34. https://doi.org/10.1186/s13045-019-0720-y.

(37) Shan, X. et al. Ferroptosis-Driven Nanotherapeutics for Cancer Treatment. *J.*

Control. Release **2020**, *319*, 322–332. https://doi.org/10.1016/j.jconrel.2020.01.008.

(38) Huo, M.; Wang, L.; Chen, Y.; Shi, J. Tumor-Selective Catalytic Nanomedicine by Nanocatalyst Delivery. *Nat. Commun.* **2017**, *8* (1), 357. https://doi.org/10.1038/s41467-017-00424-8.

(39) Lin, H.; Chen, Y.; Shi, J. Nanoparticle-Triggered: In Situ Catalytic Chemical Reactions for Tumour-Specific Therapy. *Chem. Soc. Rev.* **2018**, *47* (6), 1938–1958. https://doi.org/10.1039/c7cs00471k.

(40) Liu, Y. et al. Topical Ferumoxytol Nanoparticles Disrupt Biofilms and Prevent Tooth Decay in Vivo via Intrinsic Catalytic Activity. *Nat. Commun.* **2018**, *9* (1), 2920. https://doi.org/10.1038/s41467-018-05342-x.

(41) Badgley, M. A. et al. Cysteine Depletion Induces Pancreatic Tumor Ferroptosis in Mice. *Science (80-.).* **2020**, *368* (6486), 85–89. https://doi.org/10.1126/science.aaw9872.

(42) Perica, K. et al. Magnetic Field-Induced t Cell Receptor Clustering by Nanoparticles Enhances t Cell Activation and Stimulates Antitumor Activity. *ACS Nano* **2014**, *8* (3), 2252–2260. https://doi.org/10.1021/nn405520d.

(43) Kumar, R. et al. Increased Sensitivity of Antigen-Experienced T Cells through the Enrichment of Oligomeric T Cell Receptor Complexes. *Immunity* **2011**, *35* (3), 375–387. https://doi.org/10.1016/j.immuni.2011.08.010.

(44) Fahmy, T. M.; Bieler, J. G.; Edidin, M.; Schneck, J. P. Increased TCR Avidity after T Cell Activation: A Mechanism for Sensing Low-Density Antigen. *Immunity* **2001**, *14* (2), 135–143. https://doi.org/10.1016/s1074-7613(01)00096-6.

(45) Sanz-Ortega, L.; Portilla, Y.; Pérez-Yagüe, S.; Barber, D. F. Magnetic Targeting of Adoptively Transferred Tumour-Specific Nanoparticle-Loaded CD8+ T Cells Does Not Improve Their Tumour Infiltration in a Mouse Model of Cancer but Promotes the Retention of These Cells in Tumour-Draining Lymph Nodes. *J. Nanobiotechnology* **2019**, *17* (1). https://doi.org/10.1186/s12951-019-0520-0.

(46) Chiang, C. S. et al. Combination of Fucoidan-Based Magnetic Nanoparticles and Immunomodulators Enhances Tumour-Localized Immunotherapy. *Nat. Nanotechnol.* **2018**, *13* (8), 746–754. https://doi.org/10.1038/s41565-018-0146-7.

(47) Zhang, F. et al. Engineering Magnetosomes for Ferroptosis/Immunomodulation Synergism in Cancer. *ACS Nano* **2019**, *13* (5), 5662–5673. https://doi.org/10.1021/acsnano.9b00892.

(48) Gupta, A. K.; Gupta, M. Synthesis and Surface Engineering of Iron Oxide Nanoparticles for Biomedical Applications. *Biomaterials* **2005**, *26* (18), 3995–4021. https://doi.org/10.1016/j.biomaterials.2004.10.012.

(49) Ito, A.; Shinkai, M.; Honda, H.; Kobayashi, T. Medical Application of Functionalized Magnetic Nanoparticles. *J. Biosci. Bioeng.* **2005**, *100* (1), 1–11. https://doi.org/10.1263/jbb.100.1.

(50) Ito, A. et al. Augmentation of MHC Class I Antigen Presentation via Heat Shock Protein Expression by Hyperthermia. *Cancer Immunol. Immunother.* **2001**, *50* (10), 515–522. https://doi.org/10.1007/s00262-001-0233-7.

(51) Tanaka, K. et al. Intratumoral Injection of Immature Dendritic Cells Enhances Antitumor Effect of Hyperthermia Using Magnetic Nanoparticles. *Int. J. Cancer* **2005**, *116* (4), 624–633. https://doi.org/10.1002/ijc.21061.

(52) Ito, A.; Honda, H.; Kobayashi, T. Cancer Immunotherapy Based on Intracellular Hyperthermia Using Magnetite Nanoparticles: A Novel Concept of "Heat-Controlled Necrosis" with Heat Shock Protein Expression. *Cancer Immunol. Immunother.* **2006**, *55* (3), 320–328. https://doi.org/10.1007/s00262-005-0049-y.

(53) Chatterjee, S.; Burns, T. F. Targeting Heat Shock Proteins in Cancer: A Promising Therapeutic Approach. *Int. J. Mol. Sci.* **2017**, *18* (9). https://doi.org/10.3390/ijms18091978.

(54) Chao, Y. et al. Iron Nanoparticles for Low-Power Local Magnetic Hyperthermia in Combination with Immune Checkpoint Blockade for Systemic Antitumor Therapy. *Nano Lett.* **2019**, *19* (7), 4287–4296. https://doi.org/10.1021/acs.nanolett.9b00579.

(55) Yu, J. et al. Magnetic Reactive Oxygen Species Nanoreactor for Switchable Magnetic Resonance Imaging Guided Cancer Therapy Based on PH-Sensitive Fe5C2@Fe3O4 Nanoparticles. *ACS Nano* **2019**, *13* (9), 10002–10014. https://doi.org/10.1021/acsnano.9b01740.

(56) Peng, X. H. et al. Targeted Magnetic Iron Oxide Nanoparticles for Tumor Imaging and Therapy. *Int. J. Nanomedicine* **2008**, *3* (3), 311–321. https://doi.org/10.2147/ijn.s2824.

(57) Aluicio-Sarduy, E. et al. PET Radiometals for Antibody Labeling. *J. Label. Compd. Radiopharm.* **2018**, *61* (9), 636–651. https://doi.org/10.1002/jlcr.3607.

(58) Huang, Z. et al. Application and Development of Superparamagnetic Nanoparticles in Sample Pretreatment and Immunochromatographic Assay. *TrAC - Trends in Analytical Chemistry*. Elsevier May 1, 2019, pp 151–170. https://doi.org/10.1016/j.trac.2019.03.004.

(59) Thakor, A. S. et al. Clinically Approved Nanoparticle Imaging Agents. *J. Nucl. Med.* **2016**, *57* (12), 1833–1837. https://doi.org/10.2967/jnumed.116.181362.

(60) Vallabani, N. V. S.; Singh, S. Recent Advances and Future Prospects of Iron Oxide Nanoparticles in Biomedicine and Diagnostics. *3 Biotech* **2018**, *8* (6), 279. https://doi.org/10.1007/s13205-018-1286-z.

(61) Revia, R. A.; Zhang, M. Magnetite Nanoparticles for Cancer Diagnosis, Treatment, and Treatment Monitoring: Recent Advances. *Materials Today*. NIH Public Access April 2016, pp 157–168. https://doi.org/10.1016/j.mattod.2015.08.022.

(62) Xie, J.; Lee, S.; Chen, X. Nanoparticle-Based Theranostic Agents. *Adv. Drug Deliv. Rev.* **2010**, *62* (11), 1064–1079. https://doi.org/10.1016/j.addr.2010.07.009.

(63) Cardoso, V. F. et al. Advances in Magnetic Nanoparticles for Biomedical Applications. *Adv. Healthc. Mater.* **2018**, *7* (5), 1–35. https://doi.org/10.1002/adhm.201700845.

(64) Hu, Y.; Mignani, S.; Majoral, J. P.; Shen, M.; Shi, X. Construction of Iron Oxide Nanoparticle-Based Hybrid Platforms for Tumor Imaging and Therapy. *Chem. Soc. Rev.* **2018**, *47* (5), 1874–1900. https://doi.org/10.1039/c7cs00657h.

(65) Janib, S. M.; Moses, A. S.; MacKay, J. A. Imaging and Drug Delivery Using Theranostic Nanoparticles. *Adv. Drug Deliv. Rev.* **2010**, *62* (11), 1052–1063. https://doi.org/10.1016/j.addr.2010.08.004.

(66) Song, J. et al. Self-Assembled Responsive Bilayered Vesicles with Adjustable Oxidative Stress for Enhanced Cancer Imaging and Therapy. *J. Am. Chem. Soc.* **2020**, *141* (20), 8158–8170. https://doi.org/10.1021/jacs.8b13902.

(67) Mottaghitalab, F.; Farokhi, M.; Fatahi, Y.; Atyabi, F.; Dinarvand, R. New Insights into Designing Hybrid Nanoparticles for Lung Cancer: Diagnosis and Treatment. *J. Control. Release* **2019**, *295*, 250–267. https://doi.org/10.1016/j.jconrel.2019.01.009.

(68) Lee, N. et al. Iron Oxide Based Nanoparticles for Multimodal Imaging and Magnetoresponsive Therapy. *Chem. Rev.* **2015**, *115* (19), 10637–10689. https://doi.org/10.1021/acs.chemrev.5b00112.

(69) Bakhtiary, Z. et al. Targeted Superparamagnetic Iron Oxide Nanoparticles for Early Detection of Cancer: Possibilities and Challenges. *Nanomedicine Nanotechnology, Biol. Med.* **2016**, *12* (2), 287–307. https://doi.org/10.1016/j.nano.2015.10.019.

(70) Smirnov, P. et al. In Vivo Cellular Imaging of Lymphocyte Trafficking by MRI: A Tumor Model Approach to Cell-Based Anticancer Therapy. *Magn. Reson. Med.* **2006**, *56* (3), 498–508. https://doi.org/10.1002/mrm.20996.

(71) Tremblay, M. L. et al. Using MRI Cell Tracking to Monitor Immune Cell Recruitment in Response to a Peptide-Based Cancer Vaccine. *Magn. Reson. Med.* **2018**, *80* (1), 304–316. https://doi.org/10.1002/mrm.27018.

(72) Karimian-Jazi, K. et al. Monitoring Innate Immune Cell Dynamics in the Glioma Microenvironment by Magnetic Resonance Imaging and Multiphoton Microscopy (MR-MPM). *Theranostics* **2020**, *10* (4), 1873–1883.

https://doi.org/10.7150/thno.38659.

(73) Verdijk, P. et al. Sensitivity of Magnetic Resonance Imaging of Dendritic Cells for in Vivo Tracking of Cellular Cancer Vaccines. *Int. J. Cancer* **2007**, *120* (5), 978–984. https://doi.org/10.1002/ijc.22385.

(74) Zhang, X. et al. Cellular Magnetic Resonance Imaging of Monocyte-Derived Dendritic Cell Migration from Healthy Donors and Cancer Patients as Assessed in a Scid Mouse Model. *Cytotherapy* **2011**, *13* (10), 1234–1248. https://doi.org/10.3109/14653249.2011.605349.

(75) Tavaré, R. et al. Monitoring of in Vivo Function of Superparamagnetic Iron Oxide Labelled Murine Dendritic Cells during Anti-Tumour Vaccination. *PLoS One* **2011**, *6* (5). https://doi.org/10.1371/journal.pone.0019662.

(76) Crisci, E. et al. In Vivo Tracking and Immunological Properties of Pulsed Porcine Monocyte-Derived Dendritic Cells. *Mol. Immunol.* **2015**, *63* (2), 343–354. https://doi.org/10.1016/j.molimm.2014.08.006.

(77) de chickera, S. et al. Cellular MRI as a Suitable, Sensitive Non-Invasive Modality for Correlating in Vivo Migratory Efficiencies of Different Dendritic Cell Populations with Subsequent Immunological Outcomes. *Int. Immunol.* **2012**, *24* (1), 29–41. https://doi.org/10.1093/intimm/dxr095.

(78) Zhang, Z. et al. Antigen-Loaded Dendritic Cell Migration: MR Imaging in a Pancreatic Carcinoma Model. *Radiology* **2015**, *274* (1), 192–200. https://doi.org/10.1148/radiol.14132172.

(79) Oppitz, M. et al. Magnetic Resonance Imaging of Iron-Oxide Labeled SK-Mel 28 Human Melanoma Cells in the Chick Embryo Using a Clinical Whole Body MRI Scanner. *Magn. Reson. Mater. Physics, Biol. Med.* **2007**, *20* (1), 1–9. https://doi.org/10.1007/s10334-006-0062-y.

(80) Mamani, J. B. et al. In Vivo Magnetic Resonance Imaging Tracking of C6 Glioma Cells Labeled with Superparamagnetic Iron Oxide Nanoparticles. *Einstein (Sao Paulo).* **2012**, *10* (2), 164–170. https://doi.org/10.1590/S1679-45082012000200009.

(81) Sundstrøm, T. et al. Automated Tracking of Nanoparticle-Labeled Melanoma Cells Improves the Predictive Power of a Brain Metastasis Model. *Cancer Res.* **2013**, *73* (8), 2445–2456. https://doi.org/10.1158/0008-5472.CAN-12-3514.

(82) Ruiz-De-Angulo, A.; Zabaleta, A.; Gómez-Vallejo, V.; Llop, J.; Mareque-Rivas, J. C. Microdosed Lipid-Coated 67Ga-Magnetite Enhances Antigen-Specific Immunity by Image Tracked Delivery of Antigen and Cpg to Lymph Nodes. *ACS Nano* **2016**, *10* (1), 1602–1618. https://doi.org/10.1021/acsnano.5b07253.

(83) Lehrman, E. D.; Plotnik, A. N.; Hope, T.; Saloner, D. Ferumoxytol-Enhanced MRI in the Peripheral Vasculature. *Clin. Radiol.* **2019**, *74* (1), 37–50. https://doi.org/10.1016/j.crad.2018.02.021.

(84) Chakravarty, R. et al. Intrinsically Germanium-69-Labeled Iron Oxide Nanoparticles: Synthesis and in-Vivo Dual-Modality PET/MR Zimaging. *Adv. Mater.* **2014**, *26* (30), 5119–5123. https://doi.org/10.1002/adma.201401372.

(85) Maldonado, C. R.; Salassa, L.; Gomez-Blanco, N.; Mareque-Rivas, J. C. Nano-Functionalization of Metal Complexes for Molecular Imaging and Anticancer Therapy. *Coord. Chem. Rev.* **2013**, *257* (19–20), 2668–2688. https://doi.org/10.1016/j.ccr.2013.04.014.

(86) Bocanegra Gondan, A. I. et al. Effective Cancer Immunotherapy in Mice by PolyIC-Imiquimod Complexes and Engineered Magnetic Nanoparticles. *Biomaterials* **2018**, *170*, 95–115. https://doi.org/10.1016/j.biomaterials.2018.04.003.

(87) Cobaleda-Siles, M. et al. An Iron Oxide Nanocarrier for DsRNA to Target Lymph Nodes and Strongly Activate Cells of the Immune System. *Small* **2014**, *10* (24), 5054–5067. https://doi.org/10.1002/smll.201401353.

(88) Tanaka, S. et al. A Review on Iron Oxide-Based Nanoarchitectures for Biomedical, Energy Storage, and Environmental Applications. *Small Methods* **2019**, *3* (5), 1800512. https://doi.org/10.1002/smtd.201800512.

(89) Zhu, N. et al. Surface Modification of Magnetic Iron Oxide Nanoparticles. *Nanomaterials* **2018**, *8* (10). https://doi.org/10.3390/nano8100810.

(90) Lassenberger, A. et al. Monodisperse Iron Oxide Nanoparticles by Thermal Decomposition: Elucidating Particle Formation by Second-Resolved in Situ Small-Angle X-Ray Scattering. *Chem. Mater.* **2017**, *29* (10), 4511–4522. https://doi.org/10.1021/acs.chemmater.7b01207.

(91) Sun, S. et al. Monodisperse MFe2O4 (M = Fe, Co, Mn) Nanoparticles. *J. Am. Chem. Soc.* **2004**, *126* (1), 273–279. https://doi.org/10.1021/ja0380852.

(92) Moya, C.; Batlle, X.; Labarta, A. The Effect of Oleic Acid on the Synthesis of Fe3-XO4 Nanoparticles over a Wide Size Range. *Phys. Chem. Chem. Phys.* **2015**, *17* (41), 27373–27379. https://doi.org/10.1039/c5cp03395k.

(93) Biesinger, M. C. et al. Resolving Surface Chemical States in XPS Analysis of First Row Transition Metals, Oxides and Hydroxides: Cr, Mn, Fe, Co and Ni. *Appl. Surf. Sci.* **2011**, *257* (7), 2717–2730. https://doi.org/10.1016/j.apsusc.2010.10.051.

(94) Yamashita, T.; Hayes, P. Analysis of XPS Spectra of Fe 2+ and Fe 3+ Ions in Oxide Materials. *Appl. Surf. Sci.* **2008**, *254* (8), 2441–2449. https://doi.org/10.1016/j.apsusc.2007.09.063.

(95) Ruiz-de-Angulo, A. et al. Chemically Programmed Vaccines: Iron Catalysis in Nanoparticles Enhances Combination Immunotherapy and Immunotherapy-Promoted Tumor Ferroptosis. *iScience* **2020**, *23* (9). https://doi.org/10.1016/j.isci.2020.101499.

(96) Shi, J.; Kantoff, P. W.; Wooster, R.; Farokhzad, O. C. Cancer Nanomedicine: Progress, Challenges and Opportunities. *Nat. Rev. Cancer* **2017**, *17* (1), 20–37. https://doi.org/10.1038/nrc.2016.108.

(97) Rosenblum, D.; Joshi, N.; Tao, W.; Karp, J. M.; Peer, D. Progress and Challenges towards Targeted Delivery of Cancer Therapeutics. *Nat. Commun.* **2018**, *9* (1), 1410. https://doi.org/10.1038/s41467-018-03705-y.

(98) Szatrowski, T. P.; Nathan, C. F. Production of Large Amounts of Hydrogen Peroxide by Human Tumor Cells. *Cancer Res.* **1991**, *51* (3), 794–798.

(99) Seong, S. Y.; Matzinger, P. Hydrophobicity: An Ancient Damage-Associated Molecular Pattern That Initiates Innate Immune Responses. *Nature Reviews Immunology*. Nature Publishing Group 2004, pp 469–478. https://doi.org/10.1038/nri1372.

(100) Zhou, Z. et al. Activatable Singlet Oxygen Generation from Lipid Hydroperoxide Nanoparticles for Cancer Therapy. *Angew. Chemie - Int. Ed.* **2017**, *56* (23), 6492–6496. https://doi.org/10.1002/anie.201701181.

(101) Jóźwiak, M.; Filipowska, A.; Fiorino, F.; Struga, M. Anticancer Activities of Fatty Acids and Their Heterocyclic Derivatives. *Eur. J. Pharmacol.* **2020**, *871* (August 2019). https://doi.org/10.1016/j.ejphar.2020.172937.

(102) Girotti, A. W.; Korytowski, W. Nitric Oxide Inhibition of Chain Lipid Peroxidation Initiated by Photodynamic Action in Membrane Environments. *Cell Biochem. Biophys.* **2020**, *78* (2), 149–156. https://doi.org/10.1007/s12013-020-00909-2.

(103) Zhang, F.; Wang, X.; Jie, X.; Wei, W. Test Paper for Colorimetric Inspection of Fatty Acids and Edible Oils. *Sensors (Switzerland)* **2018**, *18* (10), 3252. https://doi.org/10.3390/s18103252.

(104) Verhoef, J. J. F.; Anchordoquy, T. J. Questioning the Use of PEGylation for Drug Delivery. *Drug Deliv. Transl. Res.* **2013**, *3* (6), 499–503. https://doi.org/10.1007/s13346-013-0176-5.

(105) Louzao, I.; García-Fandiño, R.; Montenegro, J. Hydrazone-Modulated Peptides for Efficient Gene Transfection. *J. Mater. Chem. B* **2017**, *5* (23), 4426–4434. https://doi.org/10.1039/c7tb00179g.

(106) Kaczanowska, S.; Joseph, A. M.; Davila, E. TLR Agonists: Our Best Frenemy in Cancer Immunotherapy . *J. Leukoc. Biol.* **2013**, *93* (6), 847–863. https://doi.org/10.1189/jlb.1012501.

(107) Mac Cheever, M. A. Twelve Immunotherapy Drugs That Could Cure Cancers. *Immunol. Rev.* **2008**, *222* (1), 357–368. https://doi.org/10.1111/j.1600-065X.2008.00604.x.

(108) Wilhelm, S. et al. Analysis of Nanoparticle Delivery to Tumours. *Nat. Rev.*

Mater. **2016**, *1* (5), 16014. https://doi.org/10.1038/natrevmats.2016.14.

(109) Richards, D. A.; Maruani, A.; Chudasama, V. Antibody Fragments as Nanoparticle Targeting Ligands: A Step in the Right Direction. *Chem. Sci.* **2016**, *8* (1), 63–77. https://doi.org/10.1039/c6sc02403c.

(110) Zhong, Y.; Meng, F.; Deng, C.; Zhong, Z. Ligand-Directed Active Tumor-Targeting Polymeric Nanoparticles for Cancer Chemotherapy. *Biomacromolecules* **2014**, *15* (6), 1955–1969. https://doi.org/10.1021/bm5003009.

(111) Teicher, B. A.; Chari, R. V. J. Antibody Conjugate Therapeutics: Challenges and Potential. *Clin. Cancer Res.* **2011**, *17* (20), 6389–6397. https://doi.org/10.1158/1078-0432.CCR-11-1417.

(112) Manjappa, A. S. et al. Antibody Derivatization and Conjugation Strategies: Application in Preparation of Stealth Immunoliposome to Target Chemotherapeutics to Tumor. *J. Control. Release* **2011**, *150* (1), 2–22. https://doi.org/10.1016/j.jconrel.2010.11.002.

(113) DiDomenico, J. et al. The Immune Checkpoint Protein PD-L1 Induces and Maintains Regulatory T Cells in Glioblastoma. *Oncoimmunology* **2018**, *7* (7), e1448329. https://doi.org/10.1080/2162402X.2018.1448329.

(114) Diskin, B. et al. PD-L1 Engagement on T Cells Promotes Self-Tolerance and Suppression of Neighboring Macrophages and Effector T Cells in Cancer. *Nat. Immunol.* **2020**, *21* (4), 442–454. https://doi.org/10.1038/s41590-020-0620-x.

(115) Philips, G. K.; Atkins, M. Therapeutic Uses of Anti-PD-1 and Anti-PD-L1 Antibodies. *Int. Immunol.* **2015**, *27* (1), 39–46. https://doi.org/10.1093/intimm/dxu095.

(116) Xu, S. et al. PD-L1 Monoclonal Antibody-Conjugated Nanoparticles Enhance Drug Delivery Level and Chemotherapy Efficacy in Gastric Cancer Cells. *Int. J. Nanomedicine* **2019**, *14* (14), 17–32. https://doi.org/10.2147/IJN.S175340.

(117) Pang, Y. et al. Personalized Detection of Circling Exosomal PD-L1 Based on Fe3O4@TiO2 Isolation and SERS Immunoassay. *Biosens. Bioelectron.* **2020**, *148*, 111800. https://doi.org/10.1016/j.bios.2019.111800.

(118) Feng, E.; Zheng, T.; He, X.; Chen, J.; Tian, Y. A Novel Ternary Heterostructure with Dramatic SERS Activity for Evaluation of PD-L1 Expression at the Single-Cell Level. *Sci. Adv.* **2018**, *4* (11), eaau3494. https://doi.org/10.1126/sciadv.aau3494.

(119) Goto, M. et al. Analytical Performance of a New Automated Chemiluminescent Magnetic Immunoassays for Soluble PD-1, PD-L1, and CTLA-4 in Human Plasma. *Sci. Rep.* **2019**, *9* (1), 10144. https://doi.org/10.1038/s41598-019-46548-3.

(120) Meir, R. et al. Fast Image-Guided Stratification Using Anti-Programmed Death Ligand 1 Gold Nanoparticles for Cancer Immunotherapy. *ACS Nano* **2017**, *11* (11), 11127–11134. https://doi.org/10.1021/acsnano.7b05299.

(121) Boutureira, O.; Bernardes, G. J. L. Advances in Chemical Protein Modification. *Chem. Rev.* **2015**, *115* (5), 2174–2195. https://doi.org/10.1021/cr500399p.

(122) Biju, V. Chemical Modifications and Bioconjugate Reactions of Nanomaterials for Sensing, Imaging, Drug Delivery and Therapy. *Chem. Soc. Rev.* **2014**, *43* (3), 744–764. https://doi.org/10.1039/c3cs60273g.

(123) Beck, A.; Goetsch, L.; Dumontet, C.; Corvaïa, N. Strategies and Challenges for the next Generation of Antibody-Drug Conjugates. *Nat. Rev. Drug Discov.* **2017**, *16* (5), 315–337. https://doi.org/10.1038/nrd.2016.268.

(124) Ravasco, J. M. J. M.; Faustino, H.; Trindade, A.; Gois, P. M. P. Bioconjugation with Maleimides: A Useful Tool for Chemical Biology. *Chem. - A Eur. J.* **2019**, *25* (1), 43–59. https://doi.org/10.1002/chem.201803174.

(125) Boutureira, O.; Bernardes, G. J. L. Advances in Chemical Protein Modification. *Chem. Rev.* **2015**, *115* (5), 2174–2195. https://doi.org/10.1021/cr500399p.

(126) Lu, J.; Jiang, F.; Lu, A.; Zhang, G. Linkers Having a Crucial Role in Antibody–Drug Conjugates. *Int. J. Mol. Sci.* **2016**, *17* (4), 852–3411. https://doi.org/10.3390/ijms17040561.

(127) Lyon, R. P. et al. Self-Hydrolyzing Maleimides Improve the Stability and Pharmacological Properties of Antibody-Drug Conjugates. *Nat. Biotechnol.* **2014**, *32* (10), 1059–1062. https://doi.org/10.1038/nbt.2968.

(128) Jain, N.; Smith, S. W.; Ghone, S.; Tomczuk, B. Current ADC Linker Chemistry. *Pharm. Res.* **2015**, *32* (11), 3526–3540. https://doi.org/10.1007/s11095-015-1657-7.

(129) Junutula, J. R. et al. Site-Specific Conjugation of a Cytotoxic Drug to an Antibody Improves the Therapeutic Index. *Nat. Biotechnol.* **2008**, *26* (8), 925–932. https://doi.org/10.1038/nbt.1480.

(130) Wiechelman, K. J.; Braun, R. D.; Fitzpatrick, J. D. Investigation of the Bicinchoninic Acid Protein Assay: Identification of the Groups Responsible for Color Formation. *Anal. Biochem.* **1988**, *175* (1), 231–237. https://doi.org/10.1016/0003-2697(88)90383-1.

(131) Walker, J. M. The Bicinchoninic Acid (BCA) Assay for Protein Quantitation. **2009**, 11–15. https://doi.org/10.1007/978-1-59745-198-7_3.

(132) Loke, P.; Allison, J. P. *PD-L1 and PD-L2 Are Differentially Regulated by Th1 and Th2 Cells*; 2003; Vol. 100. https://doi.org/10.1073/pnas.0931259100.

(133) Quail, D. F.; Joyce, J. A. Microenvironmental Regulation of Tumor Progression

and Metastasis. *Nat. Med.* **2013**, *19* (11), 1423–1437. https://doi.org/10.1038/nm.3394.

(134) Sica, A. et al. Macrophage Polarization in Tumour Progression. *Seminars in Cancer Biology*. 2008, pp 349–355. https://doi.org/10.1016/j.semcancer.2008.03.004.

(135) Perfetto, S. P. et al. Amine-Reactive Dyes for Dead Cell Discrimination in Fixed Samples. *Curr. Protoc. Cytom.* **2010**, *CHAPTER* (SUPPL. 53), Unit. https://doi.org/10.1002/0471142956.cy0934s53.

(136) Khazen, W. et al. Expression of Macrophage-Selective Markers in Human and Rodent Adipocytes. *FEBS Lett.* **2005**, *579* (25), 5631–5634. https://doi.org/10.1016/j.febslet.2005.09.032.

Chapter 3 . **IONP-enabled platinum (IV) chemotherapy enhancement and cancer-specific ferroptosis for cancer chemoimmunotherapy**

3.1. Introduction

Platinum-based drugs serve as the first front of action for many anticancer therapies. Cisplatin was the first Pt (II)-based drug approved against testicular and ovarian cancer in 1978. Since then, the drug has taken part in more than three thousand anticancer clinical trials, with ca. 25 % of them reaching advanced clinical phases III and IV [1]. Today, cisplatin and some of its derivates are listed in WHO's list of Essential Medicines [2]. However, the clinical use of these drugs is limited by severe side effects and drug resistance. In the past decade, a major shift in platinum-based drug design has occurred with the development of kinetically inert Pt(IV) drugs and prodrugs [3]. Although some of these Pt(IV) complexes have undergone clinical trials, there are currently no clinically approved platinum(IV) agents. Recent research shows that oxidative stress-inducing therapies offer new routes of overcoming some of the limitations of chemotherapy. Ferroptosis, a newly defined reactive oxygen species (ROS)- and iron-mediated mechanism of programmed cell death, offers a potentially safer and more effective alternative means of triggering cancer cell death and immunogenic cell death (ICD). Studies have also reported chemotherapy enhancement through the action of redox-active iron oxide nanoparticle (IONP)-mediated drug delivery. In this chapter, mIONPs loaded with Pt(IV) chemotherapy prodrugs (mIONP-Pt) are investigated as new systems for enhanced cancer chemotherapy and immunotherapy (chemoimmunotherapy). ROS generation, the Fenton reaction and peroxidase-like activity triggered by the mIONPs combined with nanoparticle (NP)-assisted lymphatic delivery are used in this system to improve the cancer-specific sensitivity towards oxidative damage, ferroptosis and treating *metastatic* and therapy-resistant cancer. Indeed, the results show that mIONP-Pt(IV) systems achieve significantly enhanced suppression of melanoma tumor growth compared to cisplatin-based chemotherapy and chemoimmunotherapy

3.1.1. Platinum-based cancer therapy

Cisplatin is a small platinum-based metallodrug with the formula *cis*-$[Pt(NH_3)_2Cl_2]$. It enters the cell via two pathways: i) passive diffusion, and ii) active transport mechanisms mediated by membrane proteins such as copper transporters [4]. Upon entering the cell, the low intracellular chloride ion concentration ensures a chloride ligand is replaced by a water molecule, a reaction which under these conditions has a half-life of approximately

two hours [5]. Cisplatin becomes then an "activated" compound with high binding reactivity towards nucleophilic N7-guanine purine bases in DNA (Fig. 3.1). Ligand exchange and binding is favored by neighbouring N7-guanines that can replace both cisplatin chloride ligands, yielding cross-linked DNA structures. In accordance with hard-soft acid-base theory, the soft platinum(II) metal centre will form also stable complexes with other ligands and biomolecules presenting soft donor atoms, such as sulphur in reduced glutathione (see Chapter I, Fig. 1.1, c) [6,7]. Cisplatin-derived Pt (II) metallodrugs target DNA in the nucleus, where they cause a plethora of lesions that arrest the cell cycle and induce apoptosis (Fig. 3.1) [7]. The action of platinum drugs has also been linked to the induction of oxidative damage through elevation of H_2O_2 and reactive oxygen species (ROS) levels [8]. Moreover, platinum drug-mediated cancer cell death may elicit immunogenic cell death via presentation and secretion of damage-associated molecular patterns (DAMPs), inducing dendritic cell phagocytic and tumor antigen recognition and T cell activation [9–11].

Cisplatin uptake is higher for nutrient-avid cancer cells. Its DNA binding capacity is also most active in rapidly dividing cancer cells. However, the diffusive and highly reactive character of the drug is known to lead to severe off-target toxicities. Only the higher chloride concentration in blood plasma prevents early aquation of cisplatin [12]. The side effects in platinum-based treatments include severe neurotoxicity or nephrotoxicity, myelosuppression or gastro-intestinal toxicity [13–16].

Development of chemoresistance is a common concern that correlates with development of immunosuppressive mechanisms and tumor relapse [6,7,16]. Cancers are highly dynamic systems able to adapt and evolve in response to the therapy to develop mechanisms of protection. Two major cisplatin drug resistance mechanisms are (i) modulation of intracellular drug accumulation and (ii) increased antioxidant glutathione (GSH) expression (Fig. 3.1). Cisplatin-resistant cells have been shown to downregulate relevant uptake transmembrane transporters (like Copper Transporter 1) and upregulate secretion transporters (like Transmembrane Protein 205). As a result, the drug spends less time in the cytosol and is removed before it can be activated. In turn, elevated levels of free reactive thiols in GSH can deactivate cisplatin by binding to it, and thus ejecting it out of the cell. GSH overexpression will also protect the cell from oxidative damage induced by the therapy [17].

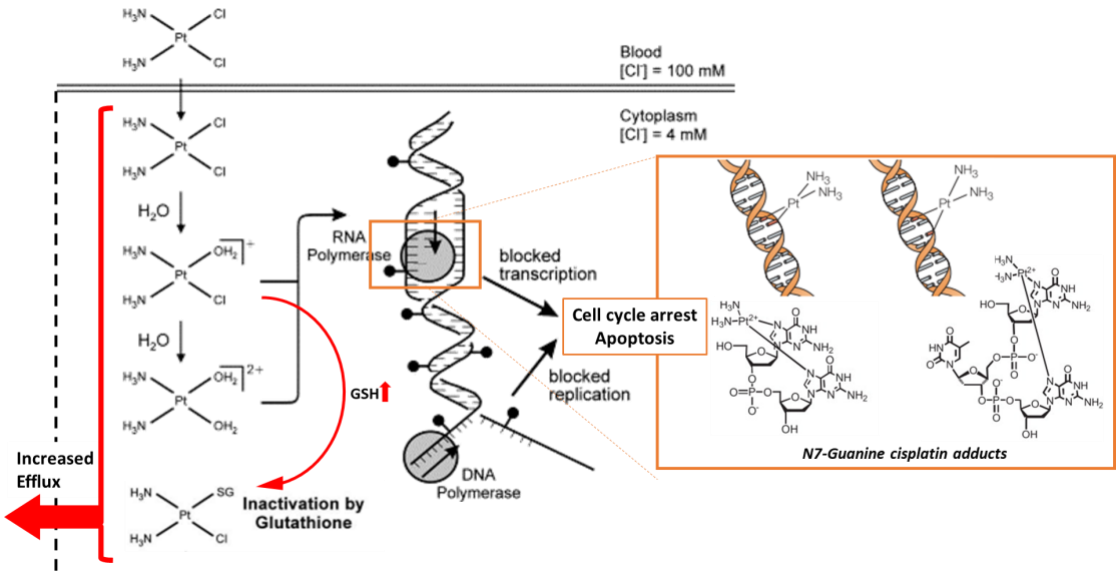

Figure 3.1. Cisplatin mechanisms of action and chemoresistance acquisition. *Cisplatin is activated upon entering the lower chloride concentration of the cytosol. The compound acquires high DNA binding reactivity resulting in inhibition of DNA replication and transcription, cell cycle arrest and/or apoptosis. GSH overexpression and increased drug efflux might lead to chemoresistance acquisition. Image adapted from* [17], [18] *and* [19].

3.1.1.1. Chemistry approaches for mitigating off-target toxicity

Cisplatin side effects can be reduced by preventing early aquation [20,21]. Customization of the platinum coordination sphere and oxidation state can modulate drug bioactivity and fine-tune desirable biological properties by providing a means to control redox stability, specific targeting, lipophilicity, orthogonal bioactivity and improved cellular uptake, among others. For example, other Pt(II) drugs such as carboplatin and oxaliplatin use chelating ligands to confer greater water stability and modulate DNA binding [6, 12,22,23].

More recently, metallodrug candidates used kinetically inert Pt(IV) as metal centre. Pt(IV)-based prodrugs remain biologically inactive until reduced to their Pt(II) analogue (see Chapter I, Fig. 1.11, c). Reduction of these prodrugs is facilitated by high intracellular GSH, iron-heme and NADH concentrations [24,25]. The reduction potential of the Pt(IV) centre is modulated by the nature of the ligands used [26]. Photoirradiation can also be used to trigger on-demand Pt(IV) reduction [27]. Satraplatin once led to hope for an orally-administered Pt(IV)-based chemotherapy. However, Phase III clinical trials in 2009 showed that although the compound was better tolerated, it failed to improve patient survival rates [28]. New generations of Pt(IV)-based compounds have shown promising

results but still remain in early clinical phases [29,30]. Finally, other chemotherapy metallodrugs have exchanged their metal centre for ruthenium, gold, silver, copper or iron [31]. However, platinum compounds remain as the only chemotherapeutic metallodrugs available in the clinic with arsenic trioxides standing as the only exception [32].

3.1.1.2. Ferroptosis as a complementary cell killing mechanism for chemotherapy and metastasis control

Oxidative stress-inducing therapies offer intriguing routes for chemotherapy enhancement [33]. Depletion of antioxidant protection can overcome mechanisms of cancer cell chemoresistance and induce sensitization towards ROS- and iron-mediated cell death mechanisms (ferroptosis) (Fig. 3.2, a) [34–36]. Indeed, cancer cell susceptibility to oxidative damage has been used as a predictive tool for chemotherapy success [37].

IONPs have gathered enormous interest for their oxidative stress-inducing features. IONPs can exploit intrinsic tumor microenvironment (TME) features such as its acidity (pH ~6.5) and high concentration of H_2O_2 for the site-specific ROS generation through Fenton chemistry. Increased ROS generation can induce antioxidant GSH depletion and cancer sensitization to ferroptosis [38]. IONP oxidative features mimic those of peroxidases, thus acquiring the label of "IONzymes". IONzyme administration has been shown to re-sensitise cisplatin-resistant cancer cells through ROS-mediated antioxidant depletion for various malignancy types [39–42]. IONPs have been shown to enhance also other clinically relevant chemotherapy drugs like Doxorubicin, Artesunate [43] and Sorafenib [44] (Fig. 3.2, b).

However, these IONPs are typically designed and optimized for intravenous administration of the therapy, which greatly limits the ability to target melanoma cells in lymph fluid and in the tumor draining lymph nodes (TDLNs). This is an important design limitation. The lymph nodes (LNs) provide a microenvironment distinct from the primary tissue [45] and differences in oxidative stress in lymph fluid compared to in blood plasma have been shown to promote the survival of metastasizing melanoma cells and their resistance to ferroptosis (Fig. 3.2, c) [46]. Although cancer metastasis can occur through the blood, it is a highly inefficient process in which few cancer cells survive [47]. Indeed,

epithelial cancers are known to metastasize to draining LNs mainly via lymphatic vessels [48] and, in melanoma, regional lymph node metastasis is one of the most important predictors of distant metastasis and death [49]. Many studies have provided clear demonstration of the principle and therapeutic benefit of LN targeting using lymphatic draining NPs to improve cancer immunotherapy [50–53]. However, little or no attention has been devoted to lymphatic delivery of platinum based chemotherapy [54,55] and nanomaterials for ferroptosis/ROS-mediated therapy. The biological mechanisms that allow tumor cells to survive and grow exploiting the lymphatic system are not well-known, but recent evidence points to the unique therapeutic potential of targeting their enhanced ability to withstand oxidative stress [56].

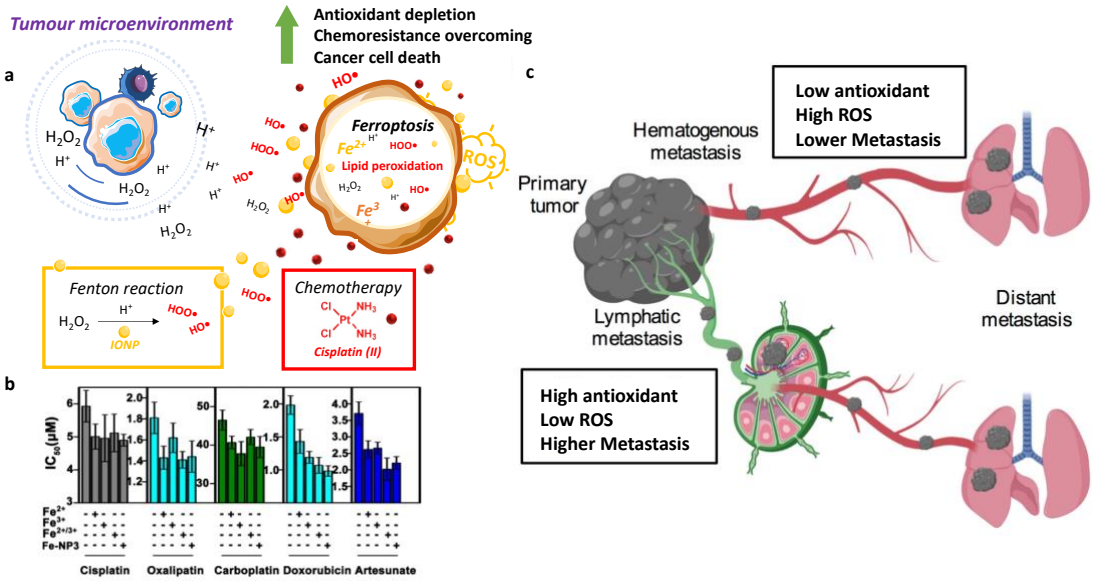

Figure 3.2. Ferroptosis for chemotherapy and metastasis control *(a) Schematic representation of chemotherapy and complementary ferroptosis action; (b) IC_{50} variation for different chemotherapeutic drugs (cisplatin, oxaliplatin, carboplatin, doxorubicin and artesunate) after cell pre-treatment with iron salts (Fe^{2+}, Fe^{3+} or both) or iron nanoparticles (Fe-NP3); (c) Schematic representation of antioxidant lymph metastases protection. Image (b) was adapted from [41]; Image (c) was adapted from [46].*

3.1.1.3. Macrophages, chemoimmunotherapy and nanomedicine

Increasing studies are now showing that chemotherapy benefits are in part due to its ability to stimulate immunity. Cancer chemoimmunotherapy, the combination of chemotherapy and immunotherapy, is an emerging promising approach to combat the disease [57].

Cancer cell growth establishes an intricate network of dynamic signalling pathways to protect itself from recognition and attack by the immune system [58]. The TME is home to various types of deactivated, protumoral immune cells. In some cancers, tumor associated macrophages (TAMs) account for over 50% of the cells within the site [59]. TAMs present a M2-like phenotype that has been shown to aid tumor growth and metastasis, and are key drivers of immunosuppression in the TME [60]. Killing or reprogramming of TAMs in the TME is thus a key new target in cancer immunotherapy (Fig. 3.3, a). In particular, the shift of tumor-promoting M2 TAMs toward tumor-suppressive M1-type macrophages is desirable ("TAM reprogramming"), and can be triggered by pro-inflammatory TLR signalling, DAMPs and ROS [61,62]. M1-like macrophages display increased cytotoxic phagocytotic activity, promote tumor identification as a target by the immune system, induce the release of immunostimulatory signals and increase cytotoxic ROS levels for anticancer ICD [60,63,64]. Moreover, by displaying high phagocytotic activity and mobility, and ability to sense chemotactic cues and home to tumors with high efficiency, several recent studies have established a new paradigm for using macrophages as "Trojan horses" for drug and therapeutic NP delivery (Fig. 3.3, b-c). These cells have been shown to internalize the drug or therapeutic NP, carry it through biological barriers, infiltrate the TME and release it deep into the tissue [65,66].

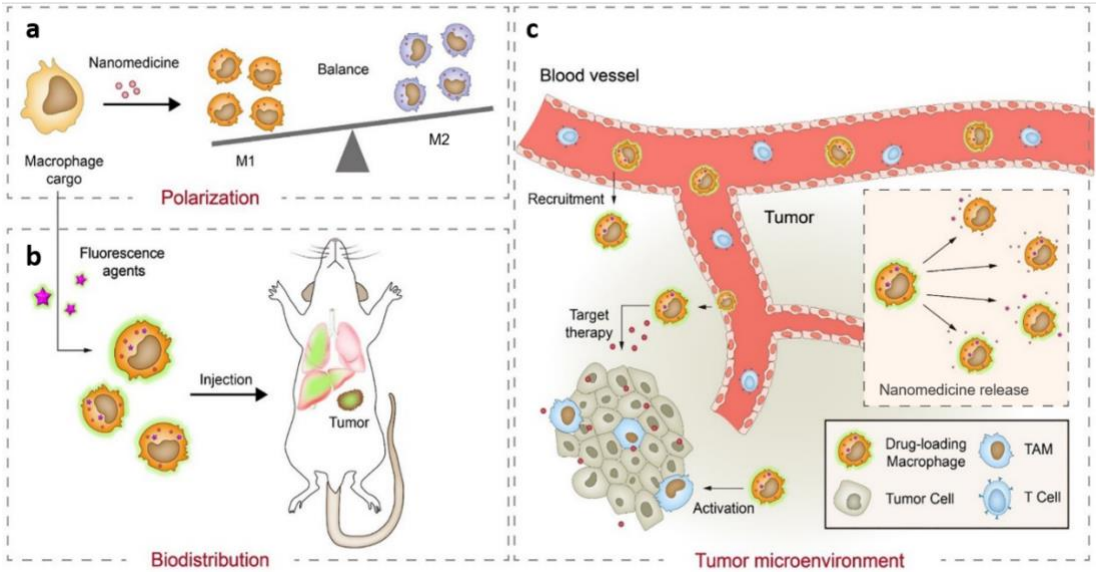

Figure 3.3. M2-to-M1 polarization and macrophage-mediated drug biodistribution strategies. *(a) Schematic representation of macrophage phenotype balance for cancer immunotherapy. (b) loading of theranostic agents for biodistribution visualization and (c) deep-tissue drug release into the TME. Figure adapted from* [66].

Nanomedicine has become an important area of research for cancer chemotherapy enhancement. The development of nanomaterials that incorporate and carry anticancer drugs has offered a plethora of approaches for safer, targeted therapy. Through properly tailored carriers, therapeutic agents can be concentrated in the disease-affected tissue to prevent off-target degradation and toxicities [67]. Nanomedicine also allowed the design of multidrug delivery systems to establish synergies among different cancer therapy strategies and compensate for each other weaknesses [68].

A wide range of platinum-loaded NP systems have been developed aiming to improve drug accumulation in the tumor by intravenous administration relying on the enhanced permeability and retention (EPR) effect. Although this approach can work in some instances, it has major limitations and has led to major clinical failures in cancer nanomedicine [69,70]. In the specific case of melanoma, none of these systems have been demonstrated to provide improved *in vivo* treatments compared to the clinically used Pt(II)-based chemotherapy. Therefore, new strategies to enhance and expand the activity and delivery of platinum-based treatments in melanoma and other therapy-resistant cancers are necessary.

Therapy-induced antioxidant depletion combined with NP-directed lymphatic delivery could offer unique opportunities to control both primary tumor growth and cancer metastasis. Previous research in our group developed platinum (IV)-loaded IONP-filled micelles suspensions (IONP-Pt(IV) or mIONP-Pt) (Fig. 3.4, a), which reported increased intracellular platinum accumulation, enhanced cytotoxicity rates in various human cancer cell lines and synergies with potent immunostimulatory drugs to enhance immune cell activation [71]. This chapter investigates the oxidative features of the mIONPs and different ways in which the mINOP-Pt system can contribute to their ability to provide enhanced suppression of melanoma tumor growth compared to cisplatin-based chemotherapy and chemoimmunotherapy (Fig. 3.4, b). It also develops an active targeting strategy exploiting insertion of *glyco-amphiphiles*.

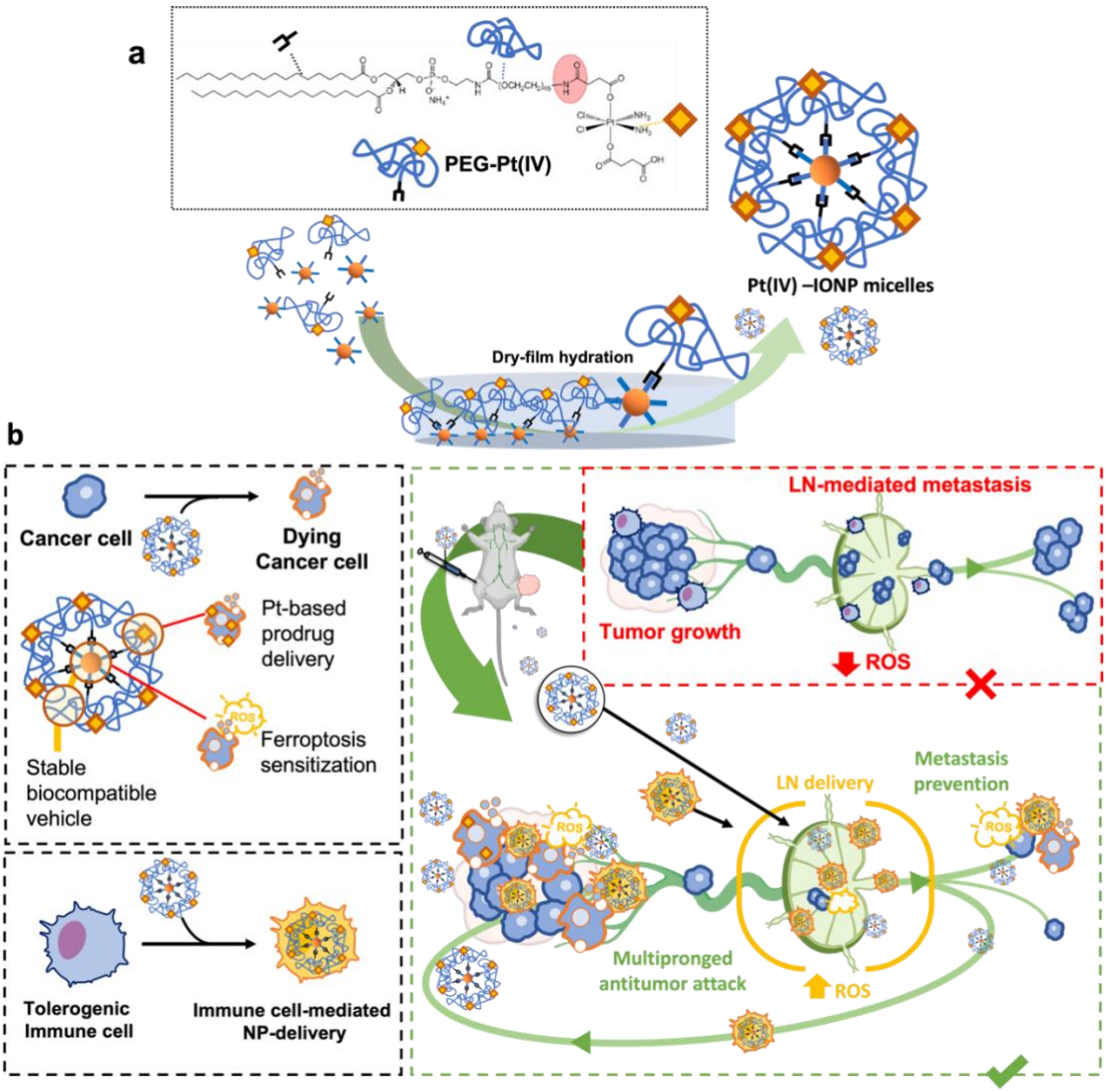

Figure 3.4. Pt(IV)-decorated IONPs synthesis and opportunities for therapy. *(a) Chemical structure of Pt-PEG and dry-film mIONP-Pt self-assembly methods reproduced in this work* [71]*. (b) mIONP-Pt(IV)-mediated platinum-based pro-drug delivery and sensitization to ferroptosis, combined with NP-directed lymphatic delivery, provide unique opportunities to induce suppression of tumor growth and metastasis.*

3.2. Results and discussion

3.2.1. Pt(IV) prodrug-loaded mIONP synthesis and physicochemical characterization

Adopting the Pt(IV) prodrug approach, the inert Pt(IV) prodrug *cis,cis,trans*-[$Pt(NH_3)_2Cl_2(O_2CCH_2CH_2CO_2H)_2$] (kindly synthetized by our colleagues; see Materials and Methods) was functionalized for delivery using water soluble IONPs micelles. Methods of self-assembly of amphiphiles and thin dry-film formation (see Chapter 2) were used to obtain aqueous suspensions of Pt(IV)-decorated IONPs (mIONP-Pt(IV)) (Fig. 3.5, a). Typically, 1 mg of IONPs would be combined with 2.5 mg of Pt(IV)-modified PEGylated phospholipid (PEG-PL-functionalized Pt(IV) prodrug). Excess reagents, particle aggregates and IONP-free micelles resulting from the process were removed by several cycles of centrifugation and ultracentrifugation (see Materials and Methods). The synthesis of the PEG-PL-functionalized Pt(IV) prodrug followed well-established methods of covalent amide coupling between the symmetric dicarboxylic-presenting Pt(IV) prodrugs (PtSym) and amine-terminated PEG-PLs [71] (see Materials and Methods).

mIONP-Pt formation yielded nanoparticles with a size of 30 nm and low polydispersity (Fig. 3.5, e). TEM imaging confirmed absence of aggregates (Fig. 3.5, f-g). Platinum loading in the nanoparticle could be quantified using a previously optimized colorimetric method (see Materials and Methods). In this method, ortho-phenylenediamine (OPD) reacts with Pt(II)-complexes by substituting labile cis-chloro ligands, yielding Pt-OPD. The compound presents a strong absorbance peak at 706 nm monitorable by UV-Vis spectroscopy. OPD is a also strong reducing agent so the method can be used to quantify also cisplatin liberated from Pt(IV) prodrug reduction (Fig. 3.5, a-d) [72], as the PEG-PL-functionalized Pt(IV) prodrug is designed to yield the Pt(II) cisplatin complex upon reduction in the cell [73]. mIONP systems were unable to capture free cisplatin drug, thus confirming that the Pt detected in purified mIONP-Pt is covalently conjugated (Fig. 3.5, b). However, Pt(IV) prodrug reduction to cisplatin is not completely quantitative (81 ± 2% yield; N=3) (Fig. S3.1). This is consistent with recent research, which has indicated that Pt(IV) prodrug reduction results in the formation of different complexes and that the assumption of clean axial ligand loss needs to be reassessed [74].

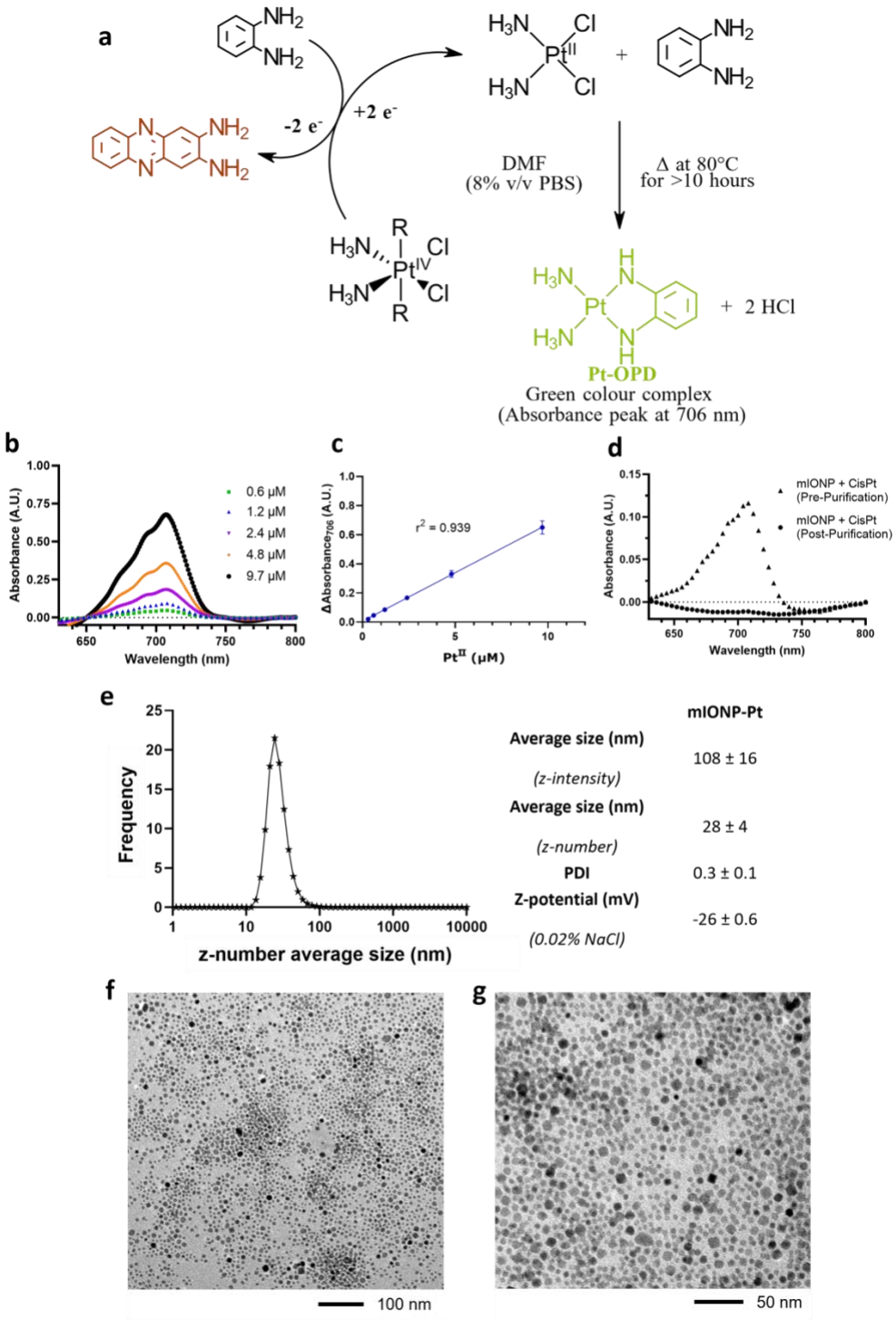

Figure 3.5. Pt(IV) mIONP decoration is confirmed by colorimetric methods. *(a) OPD-mediated Pt(IV) reduction and formation of green colour Pt(II)-OPD complex. (b) Pt-OPD absorbance peaks at increasing Pt(II) concentrations and (c) linear fit. (d) Pt-OPD absorbance peaks confirming that mIONPs do not capture free Pt(II) cisplatin drug. (e) Nanoparticle size distribution as percentage (%) of events by z-number from mIONP-Pt suspensions as evaluated by Dynamic Light Scattering (DLS) and physicochemical characterization summary. Values as mean ± SEM from at least three independent*

experiments. (f-g) Representative mIONP-Pt imaging by Transmission Electron Microscopy (TEM).

The peroxidase-like activity of mIONP-Pt was assayed by the colorimetric reaction of H_2O_2 with the peroxidase substrate 3,3′,5,5′-tetramethylbenzidine (TMB) as described previously (see Materials and Methods). The catalytic studies were studied at physiological temperature (37°C). UV-vis absorption time course curves and the kinetic parameters obtained by Lineweaver–Burk plots and fitting the catalytic reaction curves to the Michaelis–Menten equation were indicative of high catalytic activity: K_M (H_2O_2) = 127 µM, V_{max} = 3.8 × 10^{-8} M^{-1} s^{-1} and k_{cat} = 2.3 s^{-1} (Fig. 3.6). Notably, the apparent K_M (H_2O_2) value for mIONP-Pt is indicative of these nanozymes having 10-fold higher affinity for the H_2O_2 substrate than natural peroxidases like horseradish peroxidase (HRP) [75]. Also, Pt(IV) to Pt(II) reduction is expected to be contributing to the overall oxidative reactivity demonstrated by the formulation.

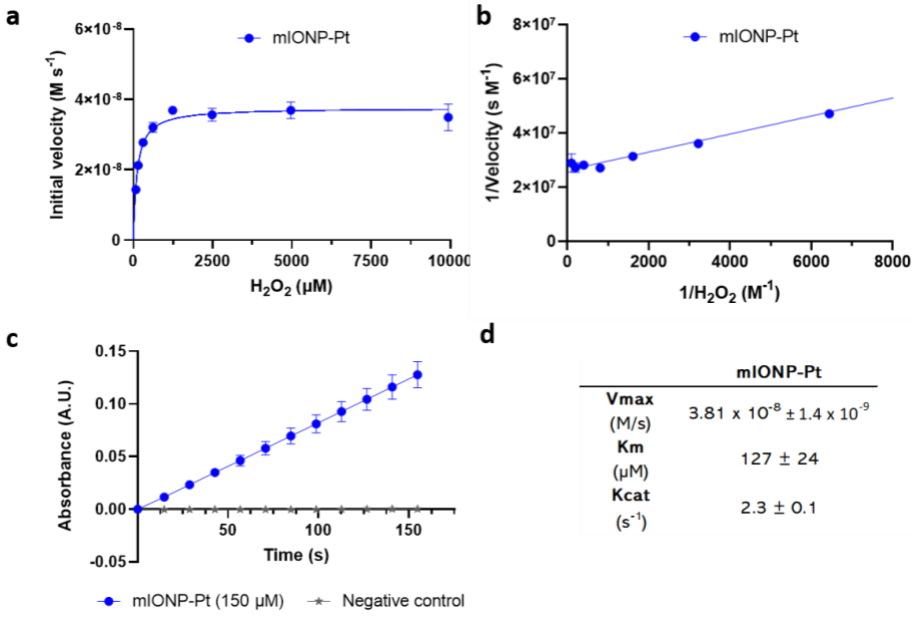

Figure 3.6. mIONP-Pt display strong catalytic oxidative activity*. TMB oxidation ([TMB] = 830 µM) at 37 °C in sodium acetate (0.1M) buffer (pH = 4.5) using increasing concentrations of H_2O_2 (0 - 10 mM) as (a) Michaelis-Menten or (b) Lineweaver-burk data fit. (c) TMB oxidation rate comparison between mIONP-Pt and absence of particle using 10 mM H_2O_2. (d) Kinetic evaluation data summary. Data shown as average ± SEM (N=3).*

3.2.2. mIONP-Pt biological activity evaluation

3.2.2.1. Effects on melanoma cell viability

B16-F10(OVA) murine melanoma cells were treated for 24 h with mIONP-Pt to evaluate its cancer cell killing features. Equivalent concentrations of Pt(II)-drug cisplatin and Pt(IV)-prodrug Ptsym were used as controls, as well as similarly sized and charged, Pt-free mIONP-COOH (synthesis and characterization described in Chapter 2). After the 24-h treatment, non-internalized therapies were removed, and cells were then incubated for additional 24 h. Cell viability was evaluated by colorimetric 3-(4,5-dimethylthiazol-2-yl)-2,5-diphenyltetrazolium bromide (MTT) assays [76].

The results show that Pt-free mIONP-COOH and Pt(IV) prodrug Ptsym induce low toxicity in the melanoma cells (Fig. 3.7). However, at the same concentrations mIONP-Pt(IV) and Pt(II) drug cisplatin (including cisplatin combinations with mIONP-COOH) reduced the melanoma cell viability to below 60%. As previously discussed, Pt(IV) prodrugs require intracellular reduction to Pt(II) to become active and cytotoxic. The higher mIONP-Pt(IV) cytotoxicity in comparison to free PtSym and mIONP + Ptsym is clearly indicative of significantly improved intracellular Pt(IV) prodrug delivery and activation. Indeed, mIONP-Pt(IV) cytotoxic activity is comparable to that of cisplatin.

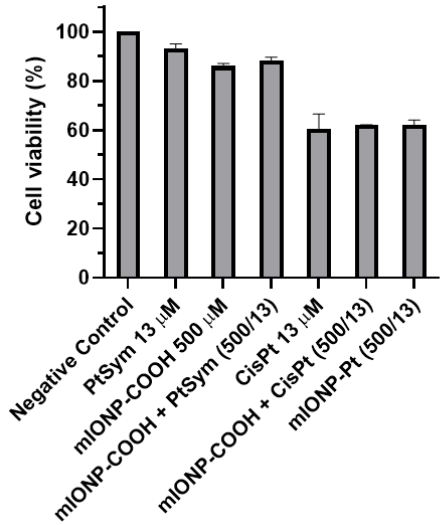

Figure 3.7. mIONP-Pt(IV) effects on melanoma. *mIONP, mIONP-Pt ([Fe] =500 μM) and equivalent doses of Pt(II)-drug cisplatin and Pt(IV)-prodrug Ptsym ([Pt] = 13 μM) were loaded into B16-F10(OVA) for a 24-hour pre-treatment. Non-internalized*

treatments were removed, and cells were incubated for an additional 24 hours before assessing cell viability. Cell viability was assayed by MTT assay. Cell viability is shown relative to negative control as (a) absence of both H_2O_2 and pre-treatment to show absolute cell viability variation; and (b) absence of H_2O_2 per pre-treatment to show variations in oxidative sensitivity. Data is shown as average ± SEM (N=3).

3.2.2.2. IONzyme effects on cisplatin re-sensitization

Fenton chemistry ROS production has been shown to re-sensitize cisplatin resistant cancer cells. IONzyme loading into cancer cells can deplete antioxidant GSH concentrations, thus decreasing the threshold of redox stress that cells can sustain before inducing ferroptosis. The lowering of this threshold can then translate into enhanced cancer cell killing [39–41].

To test this hypothesis, the melanoma cells were treated for 6 h with mIONPs. Non-internalized particles were removed, and cells were then treated for 72 h with increasing concentrations of cisplatin. The results showed that IONP-pre-treatment does not increase cisplatin cytotoxicity in the melanoma cells (Fig. 3.8). Indeed, biochemical pathways and cellular mechanisms involved in ROS-mediated chemotherapy enhancement are known to be strongly dependent on cancer cell type, as well as drug dosage and timing [77]. Melanoma cells, and in particular the B16-F10-derived cells used in this work, are known for their aggressive growth and strong chemotherapy resistance [78,79]. The non-responsiveness to cisplatin chemotherapy highlights the previously discussed limitations of these therapies, and the pressing need to study alternative, complementary mechanisms of cancer cell death.

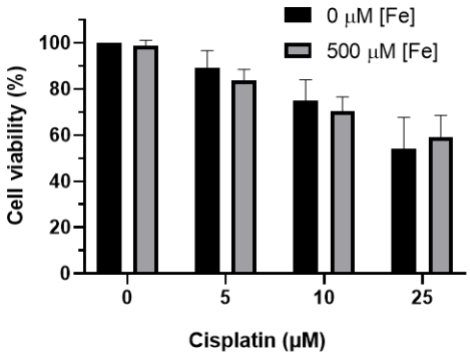

Figure 3.8. mIONP pre-treatment does not re-sensitize B16-F10(OVA) melanoma cells to cisplatin. *mIONPs ([Fe] =500 μM) are loaded into B16-F10(OVA) cells during a 6h*

pre-treatment. Various concentrations of cisplatin (0-100 µM) are then administered for a 72h treatment. Cell viability was assayed by MTT assay. Data shown as average ± SEM (N=3).

3.2.2.3. mIONP-Pt effects on melanoma membrane lipid peroxidation

Accumulation of lipid hydroperoxides in the cell membrane is indicative of unbalanced redox stress [80,81], and one of the most critical indicators of ferroptosis [36]. Cisplatin induced lipid peroxidation is known to be involved in its nephrotoxicity [80], but some evidence suggests it can induce similar oxidative damage to tumor cells [81]. To study the possible contribution of peroxidase-like activity and ferroptosis in the cancer cell killing effects of IONP-Pt(IV), we measured lipid peroxidation in the melanoma cells. Membrane lipid peroxidation was studied using Liperfluo™. After treatment, the dye is loaded into the cell membrane and selectively reacts with hydroperoxides yielding the fluorescent oxidated Liperfluo-Ox product (Fig. 3.9, a). Flow cytometry was used to study the accumulation of hydroperoxide lipids in the cell membrane (see Materials and Methods). Cell treatment with cumene hydroperoxide (100 µM) was used as a known source of membrane peroxidation and thus as positive control [83]. The melanoma cells showed signs of lipid peroxidation upon IONzyme administration, confirming the generation of biologically relevant increases in ROS production. Notably, treatment with mIONP-Pt increased the levels of lipid peroxidation (Fig. 3.9, b). These effects are consistent with previous studies which reported antioxidant GSH depletion upon intracellular Pt(IV)-to-Pt(II) reduction, thus increasing ROS-mediated damage [82].

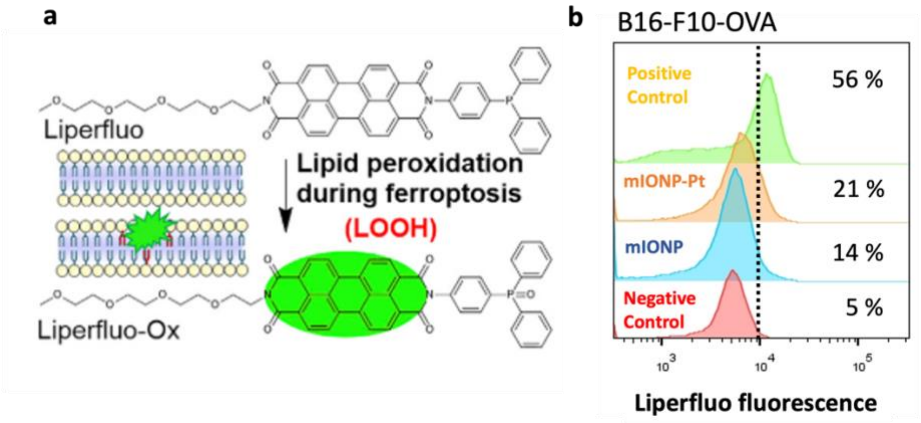

Figure 3.9. mIONP-Pt induce lipid peroxidation in melanoma cells. *(a) Schematic representation of Liperfluo oxidation and fluorescence activation with membrane*

hydroperoxide lipids; (b) Lipid peroxidation levels as measured by fluorescent positive cell populations (%) using Liperfluo. Concentrations were [Fe] = 500 µM for mIONPs and [Pt] = 10 µM for Pt-containing therapies after a 24-hour treatment. Cumene hydroperoxide (100 µM) for a 1-hour treatment was used as positive control. Image (a) extracted from [83].

3.2.2.4. mIONP-Pt effects on melanoma cell viability in H_2O_2-rich environments

The metabolic reprogramming in the TME is characterized by nutrient deficiency and accumulation of specific metabolic subproducts such as lactate and H_2O_2 [84]. The production of ROS is elevated in the TME and it is reasonable to expect further increases in ROS levels resulting from a pro-inflammatory response to chemoimmunotherapy treatments. The H_2O_2-dependant oxidative features of the IONzyme are thus expected to be increased in the tumor tissue, leading to increased accumulation of lipid hydroperoxides and ferroptosis [36].

Hence, we investigated the effect of exogenously applied H_2O_2 on melanoma cell survival. As shown in Fig. 3.10, a treatment with 50 and 75 µM H_2O_2 for 24 h resulted in ca. 20% cell death. These are physiologically relevant H_2O_2 concentrations, as H_2O_2 can reach 30 – 50 µM during inflammation [85]. We sought to identify if the H_2O_2-induced cancer cell death could be enhanced by the IONP and platinum-based treatments. For this, melanoma cells were first exposed to the treatments for 24 h, the non-internalized drugs were removed, and the cells were exposed to H_2O_2 for another 24 h. The mIONP-delivered Pt(IV) prodrug induced higher levels of melanoma cell death than mIONP treatment (Fig 3.10, a). Moreover, when the data was normalized to absence of H_2O_2 treatment, it showed that the mINOP and platinum-based treatments enhanced the H_2O_2-induced cell death (Fig 3.10, b). It is evident from the results that the combined effects of the mINOP and Pt(IV) prodrug delivery ultimately result in a combination of redox-triggered effects that enhance melanoma cell death.

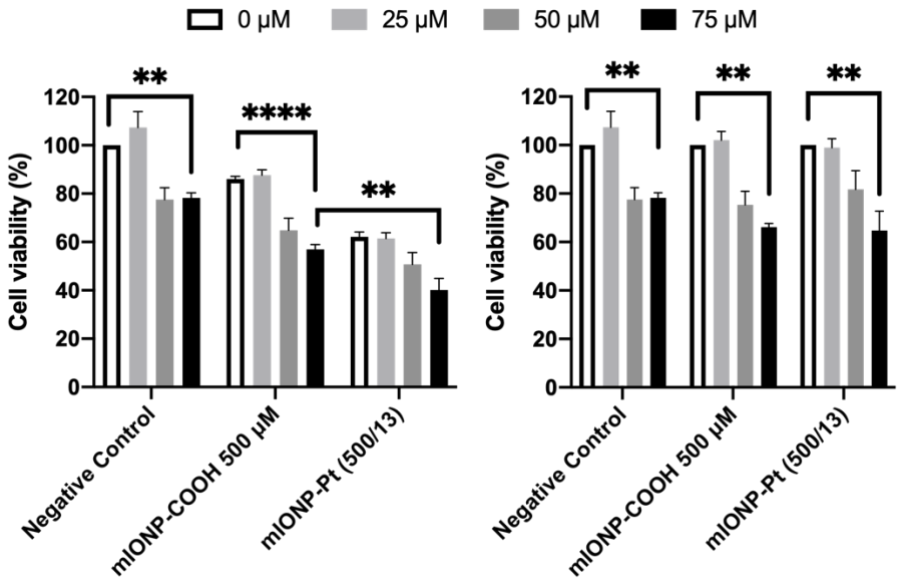

Figure 3.10. Melanoma cell viability in the presence of exogenously added H_2O_2. *Equivalent doses of mIONP and mIONP-Pt ([Fe] =500 µM) were used for pre-treatment of the melanoma cells for 24 h. Then, increasing concentrations of H_2O_2 (0, 25. 50 and 75 µM) were added for a 24-h incubation. Cell viability was assayed by MTT assay. Cell viability is shown as (a) relative to absence of both H_2O_2 and pre-treatment to show absolute cell viability variation; and (b) relative to absence of H_2O_2 per each pre-treatment to show variations in redox stress sensitivity. Data is shown as average ± SEM (N=3). Data is shown as mean ± SEM (n = 3). *P < 0.05, **P < 0.01, ***P < 0.005, ****P < 0.001 using two-way ANOVA test.*

3.2.2.5. mIONP-Pt effects on melanoma cell viability in combination with Vitamin C

Recent research showed that concentrations (0.3-20 mM) of sodium ascorbate (deprotonated ascorbic acid, Vitamin C) can show beneficial antitumor effects and synergies with chemotherapy. Sodium ascorbate can react with ROS in the TME, yielding ascorbate radical species to trigger enhanced ROS generation, oxidative damage and cancer cell ferroptosis [86–90]. In addition, ascorbate is a well-known reducing agent to intracellularly convert the Pt(IV) prodrugs into the corresponding Pt(II) drugs [3].

A screening of ascorbic acid (AA) concentrations (0-40 mM) revealed that short 1 h treatments were enough to trigger strong cytotoxicity in the melanoma cells (Fig. 3.11, a). AA cytotoxicity towards the melanoma cells was then evaluated following IONP and Ptsym therapy pre-treatments. The cells were treated with IONP-COOH, mIONP-Pt or Pt(IV) prodrugs for 24 h. Non-internalized drugs were removed, and the cells were then

treated with 5 mM AA for 1 h. Excess AA was then removed, and the cells were incubated for an additional 24 h before assessing cell viability by MTT. The results showed that cancer cell killing was enhanced according to the following trend: Pt(IV) prodrug < mIONP < mIONP-Pt (Fig. 3.11, b). Consistent with the results from the previous sections, the enhanced mIONP-Pt cytotoxic activity can be explained by the oxidative IONzyme activity, facilitated Pt(IV) intracellular accumulation and facilitated Pt(IV)-to-Pt(II) intracellular activation.

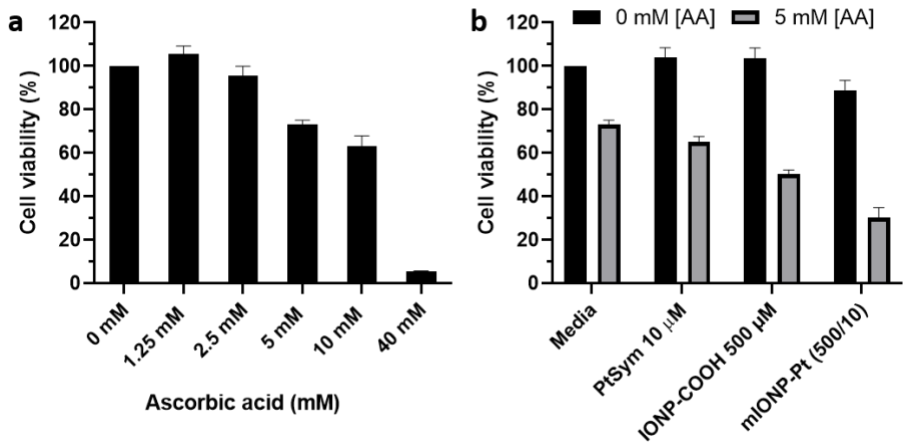

Figure 3.21. Effects of AA on mIONP-Pt treated melanoma cells. *mIONP, mIONP-Pt ([Fe] =500 μM) and equivalent doses of Pt-drug ([Pt] = 10 μM) were loaded into B16-F10(OVA) for a 24-hour pre-treatment. Indicated concentrations of ascorbic acid (AA) were then added for 1-h. Excess AA was removed, and cells were incubated for an additional 24 h before assessing cell viability. Cell viability was assayed by MTT assay. Data is shown as mean ± SD (n = 1)*

3.2.2.6. Effects on macrophage viability and polarization

Macrophages account for a large proportion (ca. 50%) of the TME, where exhibiting a predominantly M2 functionality they are the main drivers of immunosuppression in the TME [91]. Thus, induction of cytotoxic effects on M2-polarized macrophages could be important to improve the therapeutic efficiency of administered drugs [92]. On the other hand, effective antitumor immunotherapy can be achieved by reprogramming TAMs from the M2 protumoral phenotype toward the M1 antitumoral phenotype [93,94]. Macrophages also offer considerable potential if they can act as "drug depots" of therapeutic NPs [65,66,95]. However, the drug delivery role of macrophages requires attaining a high drug loading without compromising macrophage cell viability and functions.

Hence, we studied the effects of mIONP-Pt(IV) on macrophage viability and repolarization and for the cytotoxic effects on M1- and M2-polarized macrophages.

To study the cytotoxicity, RAW 264.7 macrophages were incubated with mIONPs or mIONP-Pt for 24 h and the cell viability was determined by MTT assays. As expected, the mIONP-Pt are significantly more cytotoxic to macrophages than mIONPs (Fig. 3.12).

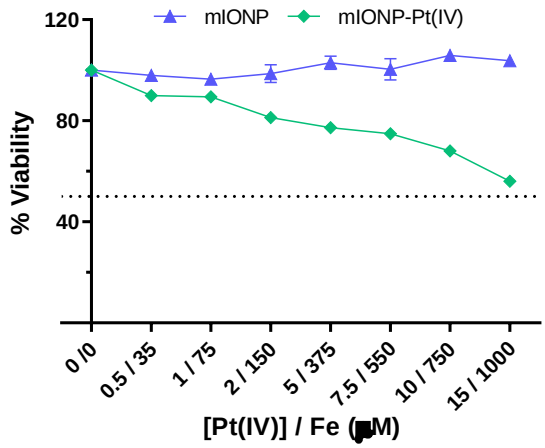

Figure 3.12. mIONP-Pt(IV) effects on RAW264.7 macrophage viability. *RAW264.7 macrophages were treated with the indicated concentrations of mIONP-COOH or mIONP-Pt for 24 h. Cell viability was assayed by MTT assay. Data shown as average ± SEM (N=3).*

To study the effect of mIONP-Pt on macrophage repolarization, bone marrow derived macrophages were polarized towards M1-like phenotype (stimulated with IFN-γ) [96] and M2 type (IL4) [62]. Stimulation with macrophage colony-stimulating factor (M-CSF) induces M2d phenotypes, which are considered to be a distinctive macrophage phenotype of immunosuppressive TAMs [97,98]. Following mIONP-Pt treatment, macrophage viability and surface marker expression typical of anticancer immunity (CD80/86 and MHCII) [96], pro-tumoral immunity (CD11c, CD206) [99] or immune suppression checkpoints PDL1/2 [13100] were analysed by Flow cytometry (Fig. 3.13).

The results show that 24 h macrophage incubation with mIONP-Pt (150 μM and 500 μM [Fe]) does not induce phenotype-selective cell killing or repolarization. We observed no significant differences among surface markers analysed (Fig. 3.13, a-g). For all macrophage populations, cell viability remained above 75% (Fig. 3.13, h). Overall, these

results are indicative of macrophage cell tolerance towards mIONP-Pt treatments at these concentrations.

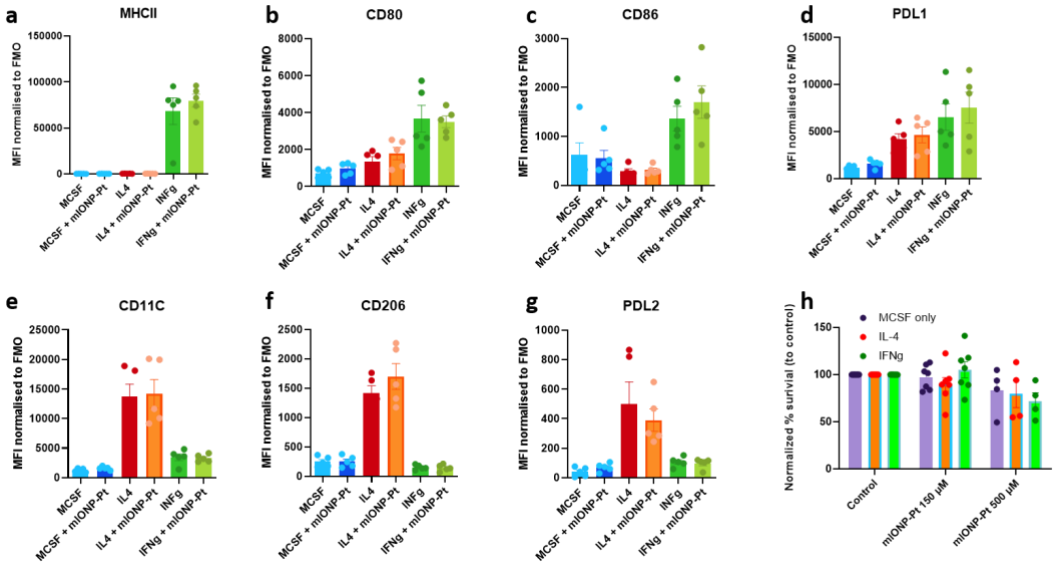

Figure 3.13. mIONP-Pt effects on polarized macrophages. *Flow cytometry fluorescent marker expression quantification of (a) MHC-II, (b) CD-80, (c) CD-86, (d) PD-L1, (e) CD11c, (f) CD-206, (g) PD-L2 and (h) macrophage cell viability after mIONP-Pt treatment ([Fe] =500 and 150 µM; [Pt] = 13 and 4 µM). In blue bars, M2d macrophages; In red bars, M2a macrophages; in green bars, M1 macrophages. Data shown as average ± SEM (N>4). Using our custom-synthetized treatments described above, these studies were kindly performed by Arnold, J. group in King's College London (UK).*

3.2.2.7. Effects in macrophage-melanoma cell co-cultures

Following previously described methods B16-F10(OVA) murine melanoma and RAW264.7 murine macrophage cells were co-cultured under direct cell-to-cell contact. Since macrophages are a dominant immune cell population in the TME, these co-cultures offer a closer resemblance to the TME reality than cell monoculture studies. Cell viability per cell type after treatment was evaluated using Flow cytometry (see Materials and Methods).

In these studies, administration of cisplatin (10-100 µM) lead to high macrophage killing, an effect that relates to the known systemic toxicity of the drug [13–16], which in turn appears to increase melanoma cell viability (Fig. 3.14, a). The free Pt(IV) prodrug administration did not lead to noticeable anticancer effects. Of all the treatments, although it was still

accompanied by a decreased macrophage viability, only mIONP-Pt triggered a significant decrease in melanoma cell viability in comparison to cisplatin. The enhancement seen in comparison with free Pt-drugs can be understood from the combination of enhanced intracellular Pt(IV)-to-Pt(II) prodrug activation, cancer cell sensitization to ferroptosis and lower immunocompromising effects. Indeed, Liperfluo assays confirmed higher lipid hydroperoxide accumulation in melanoma cells than in macrophages after the treatments (Fig. 3.14, b). These results are consistent with recent studies showing that unlike cancer cells, macrophages are quite resistant to oxidative damage [101]. Overall, these studies support the potential offered by mIONPs as anticancer-selective oxidative stress-inducing therapies.

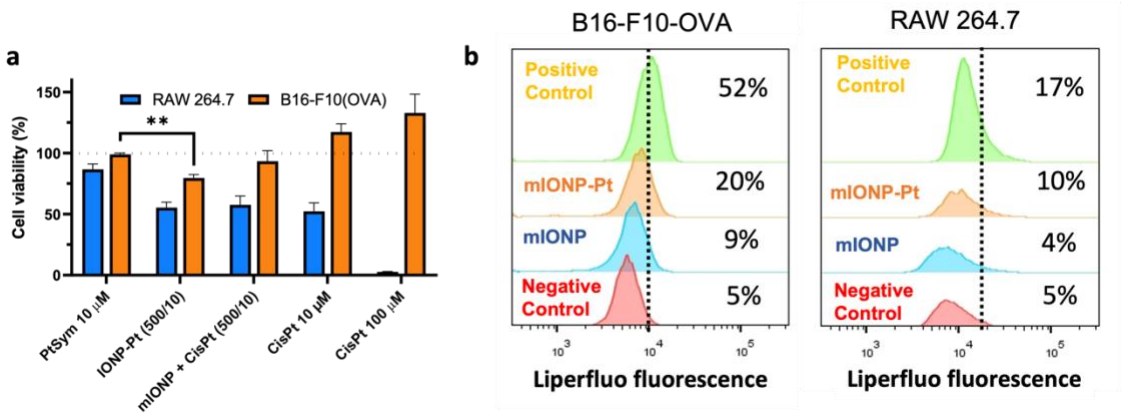

Figure 3.14. mIONP-Pt effects in melanoma-macrophage co-cultures. *B16-F10(OVA) melanoma cells and RAW 264.7 macrophages were seeded in direct cell-to-cell contact co-culture. (a) Following 24 h treatment Flow Cytometry was used to measure cell viability. Data are shown as mean ± SEM (n = 3). (b) Lipid peroxidation as measured by fluorescent positive cell populations (%) using Liperfluo. Cumene hydroperoxide (100 μM) for a 1-hour treatment was used as positive control. *P < 0.05, **P < 0.01 using two-tailed t-test.*

3.2.2.8. Active targeting strategies for mIONP-Pt administration

Glucose receptors (GLUTs) are transmembrane proteins that recognize and facilitate sugar transport into the cytosol. Malignant cells upregulate GLUT expression as a survival mechanism against TME nutrient deficiency. Indeed, GLUT overexpression is common among many cancer types and can be used as prognosis tool for disease survival

[102]. Their expression is also higher in metastases than in primary tumors [103]. Hence, surface functionalization of nanocarriers with glucose and other carbohydrates has been used to improve cancer cell targeting and uptake [104105]. For example, glucose-conjugated Pt(II) drugs have displayed enhanced cytotoxicity and therapeutic index for various cancer cell lines [106]. Also, glucose-decorated nanoparticles enhanced doxorubicin [107] and paclitaxel [108] chemotherapies providing improved *in vivo* drug biodistribution.

To incorporate glucose moieties on the mIONP-Pt, 1,3,5-triazine-cored dimaltoside amphiphiles were used (Malt-T9; Fig. 3.15, a; compounds kindly provided by our colleagues, See Materials and Methods). These glucose-presenting compounds offered various features of interest: (i) their amphiphilic structure was expected to be compatible with previously described methods of mIONP self-assembly and stabilization; (ii) the triazine moiety has been reported to induce DNA strand intercalation and cross-linking leading to cancer cell cycle arrest and apoptosis, the efficiency of which has been demonstrated by various triazine-derivates reaching advanced clinical trials and approval [109–111]; (iii) finally, these compounds have been designed as scaffolds for membrane protein extraction and stabilization [112,113]. Hence, it is reasonable to hypothesize that these compounds could provide favorable targeting of both cancer cells and immune cells, *in situ* cancer DAMP and TAA capture and delivery to immune cells [114].

Previously discussed methods of self-assembly of amphiphilic molecules and dry-film hydration were used to obtain water soluble and stable maltose- and Pt(IV)-decorated IONPs (mIONP-Pt-Malt). Typically, 1 mg of IONPs would be combined with 1.6 mg of Pt-PEG and 0.3 mg Malt-T9 (65:35, Pt-PEG:malt-T9 molar ratio). mIONP-Pt-Malt formation yielded nanoparticles of approximately 50 nm and low polydispersity (Fig. 3.15, c).

As discussed above, murine melanoma and macrophage cells were co-cultured under direct cell-to-cell contact. Cell viability per cell type after treatment was evaluated using Flow cytometry (see Materials and Methods*).*

The results show that mIONP-Pt-Malt systems achieved better anticancer cytotoxic discrimination than any of the controls (Fig. 3.15, b). A decrease in melanoma viability was observed while enabling increased macrophage viability in comparison to mIONP-

Pt treatments. mIONP-Pt-Malt also counteracted the cancer cell growth induced by control Pt-less mIONP-Malt administration. Indeed, in here glucose acts as a double-edged sword as the tumor is wired to boost its growth upon glucose administration as a mechanism to survive TME nutrient-deficiency [115,116]. Enhanced mIONP-Pt uptake through active GLUT targeting is the proposed driver of therapy enhancement (Fig 3.16, a). The capacity for mIONP-Pt-Malt to capture and present DAMPs and TAAs to immune cells remains to be studied.

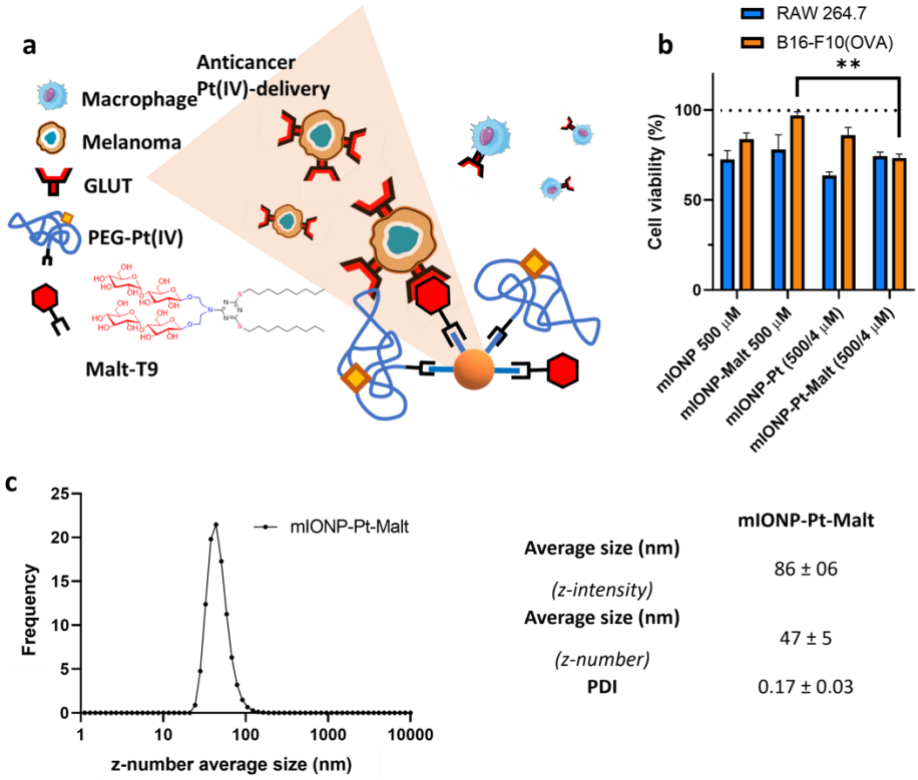

Figure 3.3. mIONP-Pt-Malt effects in complex melanoma-macrophage co-cultures. *(a) Amphiphilic Glu-T9 structure used in this work and proposed schematic representation of GLUT targeting strategy. (b) B16-F10(OVA) melanoma cells and RAW 264.7 macrophages were seeded in direct cell-to-cell contact co-culture. Following 24 h treatment, Flow Cytometry was used to measure cell viability. (c) Nanoparticle size distribution as percentage (%) of events by z-number from mIONP-Pt-MAlt suspensions as evaluated by DLS and physicochemical characterization summary. Data is shown as mean ± SEM (n = 3). *P < 0.05, **P < 0.01 using two-way ANOVA test.*

3.2.2.9. Therapy evaluation in vivo

The results obtained in this chapter allow us to better understand previous *in vivo* studies of our group. These were performed by Dr. Ane Ruiz-de-Angulo and in collaboration with Dr. Jordi Llop's research group at CIC biomaGUNE (Spain). These studies evaluated:

- **mIONP-Pt *in vivo* biodistribution:** As discussed in previous chapters, the magnetite core of our mIONPs can be doped with ^{67}Ga radiotracers to monitor by non-invasive MRI and PET/SPECT *in vivo* its trafficking and biodistribution to reach the tumor and tumor draining lymph nodes (see Chapter 2) [117].
- ***In vivo* therapeutic efficacy of mIONP-Pt against therapy-resistant and aggressive melanoma:** Chemotherapy in the clinic is often administered after primary treatment (typically surgery or radiotherapy) to limit cancer remission. The approach has shown clear benefits for various cancer cell malignancies [118,119] and its success depends on establishing controlled short timings between primary treatment and chemotherapy administration [119,120]. A single, low dose mIONP-Pt administration at the time of tumor implantation was used to evaluate the capacity of this system to prevent tumor establishment.
- **mIONP-Pt therapeutic efficacy against established melanoma tumors:** Chemotherapy is also used as primary treatment or as a means to reduce tumor sizes prior to surgery [121]. Preoperative chemotherapies allow for less invasive, organ-preserving surgical operations to limit major wound complications [122,123]. Low dose mIONP-Pt administration against established melanoma tumors is used to evaluate the capacity of this system to decrease tumor size and growth rates.

3.2.2.9.1. mIONP-Pt biodistribution

Following previously established methods, the IONP core was radiolabeled with ^{67}Ga ions to enable non-invasive SPECT imaging of therapy biodistribution [117]. The process is based on magnetite doping given the comparable size of Ga(III) and Fe(III) to ions [117]. The radiocation $[^{67}Ga][Ga(H_2O)_6]Cl_3$ (aq.) obtained on-site in reacted with mIONPs at 70 °C for 30 min. Following purification by ultracentrifugation, IONP ^{67}Ga-doping reports very good yield (Fig. 3.16, a). The ^{67}Ga-doped mIONP-Pts showed excellent

stability, as less than 10% of the bound ^{67}Ga is released over 48 h even when challenged with 10^6-fold molar excess of DOTA chelator (Fig. 3.16, b).

For SPECT/CT imaging B16–F10(OVA) melanoma cells were implanted in the left flank of C57BL/6 mice, and after tumor establishment, and ^{67}Ga-doped mIONP-Pt was injected in the peritumoral region. The results show that IONP-Pt(IV) selectively accumulates in LNs and tumor (Fig. 3.16, c-f). This biodistribution is consistent and confirms the lymphatic drainage from the tumor implantation site (Fig. 3.16, c). Particles clear from the injection site and accumulate at the tumor draining LNs (TDLNs) after 3, 24 and 48 h post-injection. IONP-Pt(IV) residing at LNs distant from the injection site is also seen. The results demonstrate that micellar IONP-Pt(IV) are sufficiently small and stealth to be quickly taken up into lymphatic vessels and transit to the draining LN after injection. Peritumoral lymphatics are responsible for providing access to cancer cells during metastasis. Here, the IONP-Pt(IV) system is able to use the peritumoral lymphatics to target the tumor tissue and TDLN without direct intratumoral injection.

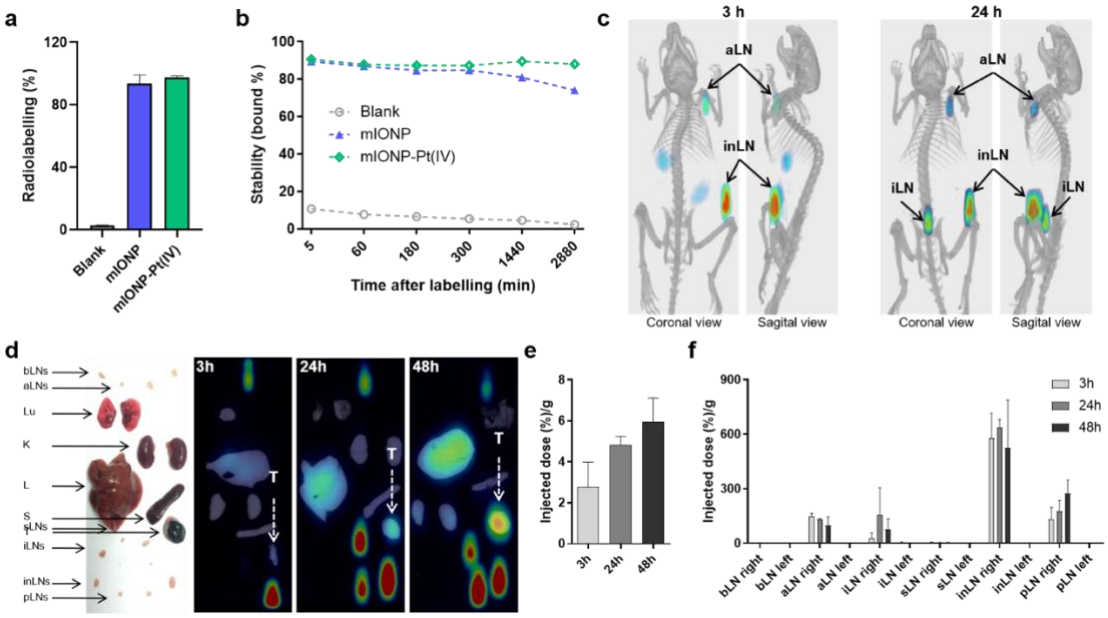

Figure 3.16. mIONP-Pt micelles biodistribution in vivo. *(a) Radiolabelling yield in PBS buffer and (b) stability in the presence of the chelator DOTA (10^6 molar DOTAP excess) of mIONP-Pt(IV) and mIONP micelles. Biodistribution studies of the mIONP-Pt were carried out in tumor bearing mice injected peritumorally with mIONP-Pt (23 μg of magnetite). (c) In vivo SPECT/CT images were taken 3 and 24 h after injection. Ex vivo biodistribution analysis after 3, 24 and 48 h: (d) photograph and SPECT/CT images of harvested organs at determined time points; biodistribution expressed as percentage of*

injected dose per gram of tissue (%)/g of (e) tumor and (f) lymph nodes over time. Data are presented as mean ± SEM of two mice. T, tumor; bLN, brachial LN; aLN, axillary LN; Lu, lungs; L, liver; S, spleen; K, kidneys; iLN, iliac LN; sLN, sciatic LN; inLN, inguinal LN; pLN, popliteal LN. These studies were performed by our collaborators in the research institutes of CIC biomaGUNE, in Donostia (Spain).

3.2.2.9.2. mIONP-Pt and melanoma co-injection

To evaluate whether Pt(IV) delivery by IONPs is beneficial compared to administration of cisplatin and IONP alone or combined with IONP and can control tumor establishment, we implanted the B16-F10-OVA melanoma cells with administration of a single low dose (0.55 mg Pt/kg) of cisplatin, Pt(IV) prodrug, mIONP, mIONP-Pt and mIONP + cisplatin. The results show that mIONP-Pt administration greatly decreased tumor growth and increased median survival for mice in comparison to Pt-free mIONP and Pt(IV) prodrug administration. The Pt(IV)-loaded mIONPs also reported stronger preventive effects against tumor stablishment than benchmark cisplatin. (Fig. 3.17). 15 days after challenge, tumor volumes upon mIONP-Pt administration remained unnoticeable in most mice (Fig. 3.17, c).

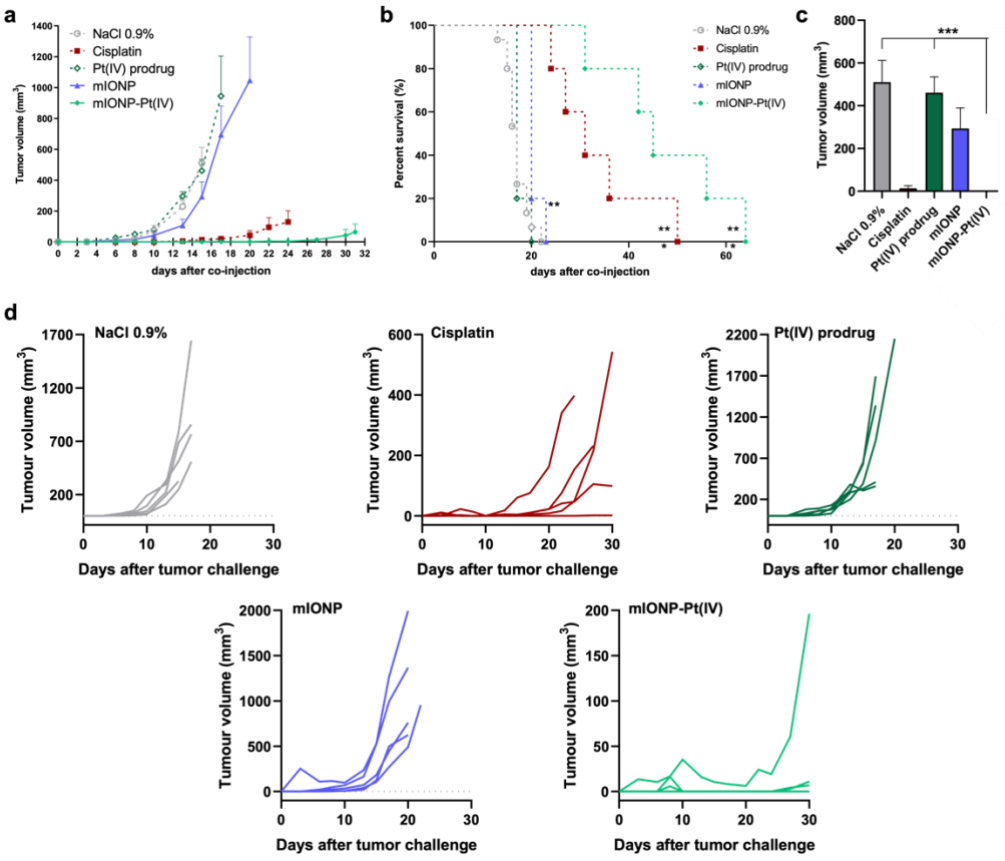

Figure 3.4. Pt(IV)-IONPs effects on co-injected melanoma cells. *C57BL/6J female mice were subcutaneously co-injected with the different treatments (12 mg Fe/kg, 0.55 mg Pt(IV)/kg) mixed with 3 x 10^5 B16-F10 cells in the back of the animal. a) Average tumor growth curves and b) Kaplan-Meier survival curves. c) Comparison of tumor volume of different experimental groups at day 15 after tumor challenge. d) Individual tumor growth curves for each experimental group. The data show mean ± SEM from a representative experiment. **p < 0.01, ***p < 0.001 by b) log rank (Mantel-Cox) test against NaCl 0.9% group, and one-way c) ANOVA followed by Tukey's test. Figure based on data from A. Garaikoetxea (PhD Thesis)* [124]*. These studies were performed by our collaborators in the research institutes of CIC biomaGUNE, in Donostia (Spain).*

3.2.2.9.3. mIONP-Pt effects on established melanoma tumors

To evaluate the therapeutic effects against established melanoma tumors, mIONP-Pt was administered on days 7, 10 and 13 after melanoma injection. Subcutaneous mIONP-Pt administration was used as means to enable LN-draining NP trafficking (Fig. 3.16) [125,126]. Cisplatin, Pt(IV) prodrug and parent mIONP were administered likewise to compare the therapeutic efficacy of the different iron and platinum-based systems.

Therapeutic mIONP-Pt administration was shown to decrease tumor growth rates and increase median survival times in comparison to controls. During and immediately after administration, mIONP-Pt were the only treatment to consistently contain the growth of small ~100 mm^3 tumor volumes (Fig. 3.18, d). A week after the end of therapy administration, tumor volumes upon mIONP-Pt administration remained the smallest among the different treatments (Fig. 3.18, c).

These *in vivo* results show that mIONP-Pt systems are able to achieve significantly enhanced suppression of melanoma tumor growth compared to cisplatin-based chemotherapy

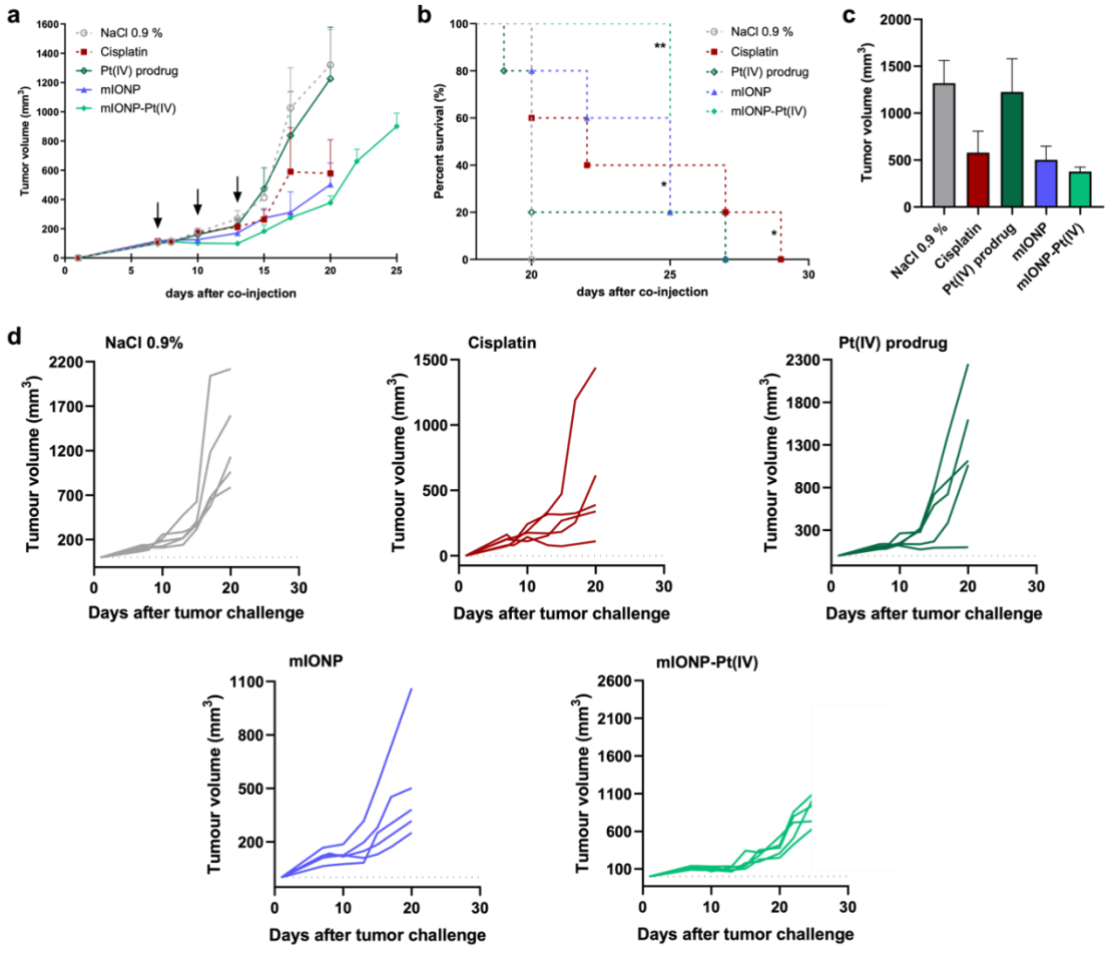

Figure 3.5. Pt(IV)-IONPs effects after therapeutic subcutaneous administration *C57BL/6J female mice were challenged with 3 x 10^5 B16-F10 cells in the back and on days 7, 10 and 13 mice were treated with the different formulations (4.6 mg Fe/kg, 0.24 mg Pt(IV)/kg of animal) subcutaneously in the peritumoral region. (a) Average tumor growth curves and (b) Kaplan-Meier survival curves. (c) Comparison of tumor volume of*

*different experimental groups at day 20 after tumor challenge. (d) Individual tumor growth curves for each experimental group until date of first mouse sacrifice within each group. The data show mean ± SEM from a representative experiment. *p < 0.05, **p < 0.01 by log rank (Mantel-Cox) test against NaCl 0.9% group (b). These studies were performed by our collaborators in the research institutes of CIC biomaGUNE, in Donostia (Spain).*

3.3. Conclusions

In this chapter, Pt(IV) prodrug-loaded mIONP-Pt systems were successfully formed, characterized and evaluated for their peroxidase activity and effects on melanoma cells and macrophages. Overall, these studies showed:

- mIONP-Pt devices could be self-assembled following previously established methods of dry-film hydration. The process yielded stable nanosized particle suspensions of low polydispersity. Pt(IV) prodrugs were demonstrated to be stably attached through covalent bonds onto the nanoparticle-filled micelles.
- mIONP-Pt displayed strong peroxidase-like activity. The particles showed an affinity towards H_2O_2 substrate over 10-times greater than HRP. Therapy-mediated ROS generation yielded increased lipid hydroperoxide accumulation in melanoma cell membranes, which is one of the key characteristics of ferroptotic cell death.
- mIONP-Pt successfully integrated features for induction of redox stress and ferroptosis with cisplatin-based cytotoxicity to provide enhanced melanoma cell killing.
- mIONP-Pt did not induce macrophage repolarization or phenotype-specific cell killing under the experimental conditions used. Still, macrophage tolerance to treatment suggests that immunotherapy strategies of cytotoxic macrophage activation and immune cell-mediated drug delivery cannot be ruled out.
- In melanoma-macrophage co-cultures, mIONP-Pt were the only treatment to increase melanoma cytotoxicity in comparison to cisplatin. Instead, Pt(II) drug treatments induced toxicity in macrophages only, which resulted in enhanced melanoma cell survival.
- Maltose-rich amphiphiles could be incorporated by the same methods of dry-film hydration to create mIONP-Pt-Malt systems. Our results are indicative of the potential of these amphiphiles to provide a slight improvement to cancer-specific cell killing via GLUT targeting strategies.

The findings reported in this chapter expanded the understanding of previous *in vitro* and *in vivo* data of our group. mIONP-Pt accumulation in the TME enabled a more potent and targeted anticancer activity through enhanced Pt(IV) prodrug activation and cancer-

specific redox damage, and improved drug delivery The observed IONP-mediated trafficking into lymph nodes via subcutaneous administration is ideal for sensitizing metastasizing melanoma cells towards oxidative damage, and overcome the resistance/protection lymph provides to cancer cell ferroptosis.

3.4. Supporting Information

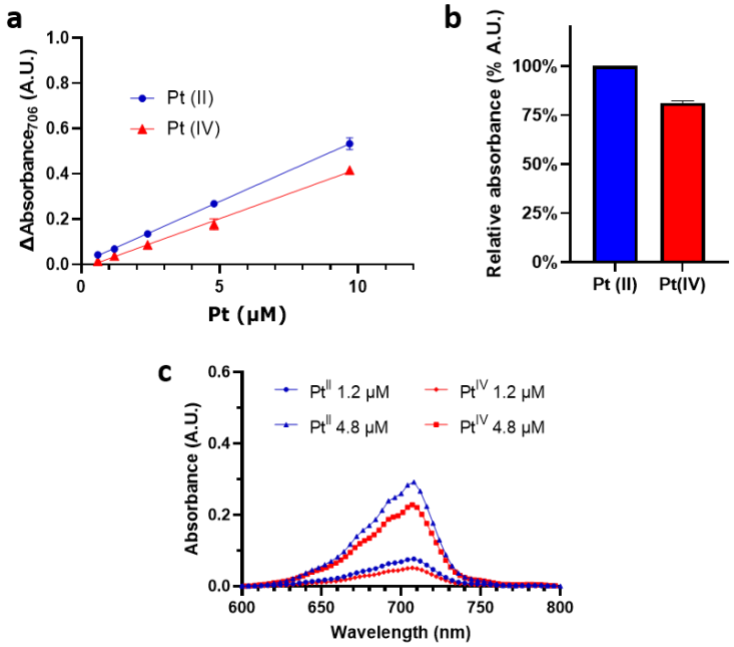

Figure S3.1. Comparative studies for Pt(IV) and Pt(II) quantification methods. *Pt-OPD absorbance peaks at increasing Pt(II) and Pt(IV) concentrations as a comparative (a) linear fit, (b) relative Pt(IV) absorbance to Pt(II) and (c) observable Uv-Vis peaks.*

3.5. References

(1) Wheate, N. J.; Walker, S.; Craig, G. E.; Oun, R. The Status of Platinum Anticancer Drugs in the Clinic and in Clinical Trials. *Dalt. Trans.* **2010**, *39* (35), 8113–8127. https://doi.org/10.1039/c0dt00292e.

(2) Van Boeckel, T. P. et al. *Global Antibiotic Consumption 2000 to 2010: An Analysis of National Pharmaceutical Sales Data*; 2014; Vol. 14. https://doi.org/10.1016/S1473-3099(14)70780-7.

(3) Johnstone, T. C.; Suntharalingam, K.; Lippard, S. J. The Next Generation of Platinum Drugs: Targeted Pt(II) Agents, Nanoparticle Delivery, and Pt(IV) Prodrugs. *Chem. Rev.* **2016**, *116* (5), 3436–3486. https://doi.org/10.1021/acs.chemrev.5b00597.

(4) Basu, A.; Krishnamurthy, S. Cellular Responses to Cisplatin-Induced DNA Damage. *J. Nucleic Acids* **2010**, *2010*, 16. https://doi.org/10.4061/2010/201367.

(5) Rosenberg, B. Platinum Complex-DNA Interactions and Anticancer Activity. *Biochimie* **1978**, *60* (9), 859–867. https://doi.org/10.1016/S0300-9084(78)80570-7.

(6) Oun, R.; Moussa, Y. E.; Wheate, N. J. The Side Effects of Platinum-Based Chemotherapy Drugs: A Review for Chemists. *Dalt. Trans.* **2018**, *47* (19), 6645–6653. https://doi.org/10.1039/c8dt00838h.

(7) Rocha, C. R. R.; Silva, M. M.; Quinet, A.; Cabral-Neto, J. B.; Menck, C. F. M. DNA Repair Pathways and Cisplatin Resistance: An Intimate Relationship. *Clinics* **2018**, *73* (suppl 1), e478s. https://doi.org/10.6061/clinics/2018/e478s.

(8) Nerush, A. S.; Shchukina, K. M.; Balalaeva, I. V.; Orlova, A. G. Hydrogen Peroxide in the Reactions of Cancer Cells to Cisplatin. *Biochim. Biophys. Acta - Gen. Subj.* **2019**, *1863* (4), 692–702. https://doi.org/10.1016/j.bbagen.2019.01.013.

(9) Englinger, B. et al. Metal Drugs and the Anticancer Immune Response. *Chem. Rev.* **2019**, *119* (2), 1519–1624. https://doi.org/10.1021/acs.chemrev.8b00396.

(10) Liang, Y.; Lü, W.; Zhang, X.; Lü, B. Tumor-Infiltrating CD8+ and FOXP3+ Lymphocytes before and after Neoadjuvant Chemotherapy in Cervical Cancer. *Diagn. Pathol.* **2018**, *13* (1), 93. https://doi.org/10.1186/s13000-018-0770-4.

(11) Guo, J. et al. Ferroptosis: A Novel Anti-Tumor Action for Cisplatin. *Cancer Res. Treat.* **2018**, *50* (2), 445–460. https://doi.org/10.4143/crt.2016.572.

(12) Pavelka, M.; Lucas, M. F. A.; Russo, N. On the Hydrolysis Mechanism of the Second-Generation Anticancer Drug Carboplatin. *Chem. - A Eur. J.* **2007**, *13* (36), 10108–10116. https://doi.org/10.1002/chem.200700887.

(13) Sachet, M.; Liang, Y. Y.; Oehler, R. The Immune Response to Secondary

Necrotic Cells. *Apoptosis* **2017**, *22* (10), 1189–1204. https://doi.org/10.1007/s10495-017-1413-z.

(14) Penn, I.; Starzl, T. E. Immunosuppression and Cancer. *Transplant. Proc.* **1973**, *5* (1), 943–947.

(15) Middleton, J. D.; Stover, D. G.; Hai, T. Chemotherapy-Exacerbated Breast Cancer Metastasis: A Paradox Explainable by Dysregulated Adaptive-Response. *Int. J. Mol. Sci.* **2018**, *19* (11). https://doi.org/10.3390/ijms19113333.

(16) Baghdadi, M. et al. Chemotherapy-Induced IL34 Enhances Immunosuppression by Tumor-Associated Macrophages and Mediates Survival of Chemoresistant Lung Cancer Cells. *Cancer Res.* **2016**, *76* (20), 6030–6042. https://doi.org/10.1158/0008-5472.CAN-16-1170.

(17) Kartalou, M.; Essigmann, J. M. Mechanisms of Resistance to Cisplatin. *Mutat. Res. - Fundam. Mol. Mech. Mutagen.* **2001**, *478* (1–2), 23–43. https://doi.org/10.1016/S0027-5107(01)00141-5.

(18) Wang, D.; Lippard, S. J. Cellular Processing of Platinum Anticancer Drugs. *Nat. Rev. Drug Discov.* **2005**, *4* (4), 307–320. https://doi.org/10.1038/nrd1691.

(19) Fujikawa, Y.; Kawanishi, M.; Kuraoka, I.; Yagi, T. Frequencies of Mutagenic Translesion DNA Synthesis over Cisplatin-Guanine Intra-Strand Crosslinks in LacZ Plasmids Propagated in Human Cells. *Mutat. Res. - Genet. Toxicol. Environ. Mutagen.* **2014**, *770*, 23–28. https://doi.org/10.1016/j.mrgentox.2014.05.006.

(20) Wheate, N. J.; Walker, S.; Craig, G. E.; Oun, R. The Status of Platinum Anticancer Drugs in the Clinic and in Clinical Trials. *Dalt. Trans.* **2010**, *39* (35), 8113–8127. https://doi.org/10.1039/c0dt00292e.

(21) Xiaoyong, W.; Zijian, G. Targeting and Delivery of Platinum-Based Anticancer Drugs. *Chem. Soc. Rev.* **2013**, *42* (1), 202–224. https://doi.org/10.1039/c2cs35259a.

(22) Di Pasqua, A. J.; Kerwood, D. J.; Shi, Y.; Goodisman, J.; Dabrowiak, J. C. Stability of Carboplatin and Oxaliplatin in Their Infusion Solutions Is Due to Self-Association. *Dalt. Trans.* **2011**, *40* (18), 4821–4825. https://doi.org/10.1039/c0dt01758b.

(23) Anthony, E. J. et al. Metallodrugs Are Unique: Opportunities and Challenges of Discovery and Development. *Chem. Sci.* **2020**, *11* (48), 12888–12917. https://doi.org/10.1039/d0sc04082g.

(24) Jungwirth, U. et al. Anticancer Activity of Metal Complexes: Involvement of Redox Processes. *Antioxidants Redox Signal.* **2011**, *15* (4), 1085–1127. https://doi.org/10.1089/ars.2010.3663.

(25) Carr, J. L.; Tingle, M. D.; McKeage, M. J. Satraplatin Activation by

Haemoglobin, Cytochrome C and Liver Microsomes in Vitro. *Cancer Chemother. Pharmacol.* **2006**, *57* (4), 483–490. https://doi.org/10.1007/s00280-005-0069-5.

(26) Petrović, B.; Jovanović, S.; Puchta, R.; van Eldik, R. Mechanistic Insight on the Chemistry of Potential Pt Antitumor Agents as Revealed by Collaborative Research Performed in Kragujevac and Erlangen. *Inorganica Chim. Acta* **2019**, *495*. https://doi.org/10.1016/j.ica.2019.06.004.

(27) Medici, S. et al. Noble Metals in Medicine: Latest Advances. *Coord. Chem. Rev.* **2015**, *284*, 329–350. https://doi.org/10.1016/j.ccr.2014.08.002.

(28) Sternberg, C. N. et al. Multinational, Double-Blind, Phase III Study of Prednisone and Either Satraplatin or Placebo in Patients with Castrate-Refractory Prostate Cancer Progressing after Prior Chemotherapy: The SPARC Trial. *J. Clin. Oncol.* **2009**, *27* (32), 5431–5438. https://doi.org/10.1200/JCO.2008.20.1228.

(29) Gibson, D. Platinum(IV) Anticancer Prodrugs-Hypotheses and Facts. *Dalt. Trans.* **2016**, *45* (33), 12983–12991. https://doi.org/10.1039/c6dt01414c.

(30) Wang, Z.; Deng, Z.; Zhu, G. Emerging Platinum(Iv) Prodrugs to Combat Cisplatin Resistance: From Isolated Cancer Cells to Tumor Microenvironment. *Dalton Transactions*. Royal Society of Chemistry February 19, 2019, pp 2536–2544. https://doi.org/10.1039/c8dt03923b.

(31) Ndagi, U.; Mhlongo, N.; Soliman, M. E. Metal Complexes in Cancer Therapy – An Update from Drug Design Perspective. *Drug Des. Devel. Ther.* **2017**, *11*, 599–616. https://doi.org/10.2147/DDDT.S119488.

(32) Dilda, P. J.; Hogg, P. J. Arsenical-Based Cancer Drugs. *Cancer Treat. Rev.* **2007**, *33* (6), 542–564. https://doi.org/10.1016/j.ctrv.2007.05.001.

(33) Filippova, M. et al. Cellular Levels of Oxidative Stress Affect the Response of Cervical Cancer Cells to Chemotherapeutic Agents. *Biomed Res. Int.* **2014**, *2014*. https://doi.org/10.1155/2014/574659.

(34) Lu, B. et al. The Role of Ferroptosis in Cancer Development and Treatment Response. *Front. Pharmacol.* **2018**, *8* (JAN), 992. https://doi.org/10.3389/fphar.2017.00992.

(35) Roh, J. L.; Kim, E. H.; Jang, H. J.; Park, J. Y.; Shin, D. Induction of Ferroptotic Cell Death for Overcoming Cisplatin Resistance of Head and Neck Cancer. *Cancer Lett.* **2016**, *381* (1), 96–103. https://doi.org/10.1016/j.canlet.2016.07.035.

(36) Dixon, S. J. et al. Ferroptosis: An Iron-Dependent Form of Nonapoptotic Cell Death. *Cell* **2012**, *149* (5), 1060–1072. https://doi.org/10.1016/j.cell.2012.03.042.

(37) Sun, C. et al. A Reactive Oxygen Species Scoring System Predicts Cisplatin Sensitivity and Prognosis in Ovarian Cancer Patients. *BMC Cancer* **2019**, *19* (1).

https://doi.org/10.1186/s12885-019-6288-7.

(38) Cheng, J. et al. Manganese-Deposited Iron Oxide Promotes Tumor-Responsive Ferroptosis That Synergizes the Apoptosis of Cisplatin. *Theranostics* **2021**, *11* (11), 5418–5429. https://doi.org/10.7150/thno.53346.

(39) Gokduman, K. Sensitization of Cisplatin-Resistant Ovarian Cancer Cells by Magnetite Iron Oxide Nanoparticles: An in Vitro Study. *Nanomedicine* **2019**, *14* (24), 3177–3191. https://doi.org/10.2217/nnm-2019-0126.

(40) Shen, Z. et al. Fenton-Reaction-Acceleratable Magnetic Nanoparticles for Ferroptosis Therapy of Orthotopic Brain Tumors. *ACS Nano* **2018**, *12* (11), 11355–11365. https://doi.org/10.1021/acsnano.8b06201.

(41) Ma, P. et al. Enhanced Cisplatin Chemotherapy by Iron Oxide Nanocarrier-Mediated Generation of Highly Toxic Reactive Oxygen Species. *Nano Lett.* **2017**, *17* (2), 928–937. https://doi.org/10.1021/acs.nanolett.6b04269.

(42) Gao, Z. et al. Iron Oxide Nanocarrier-Mediated Combination Therapy of Cisplatin and Artemisinin for Combating Drug Resistance through Highly Increased Toxic Reactive Oxygen Species Generation. *ACS Appl. Bio Mater.* **2018**, *1* (2), 270–280. https://doi.org/10.1021/acsabm.8b00056.

(43) Bao, W. et al. Nanolongan with Multiple On-Demand Conversions for Ferroptosis-Apoptosis Combined Anticancer Therapy. *ACS Nano* **2019**, *13* (1), 260–273. https://doi.org/10.1021/acsnano.8b05602.

(44) Guan, Q. et al. Mesoporous Polydopamine Carrying Sorafenib and SPIO Nanoparticles for MRI-Guided Ferroptosis Cancer Therapy. *J. Control. Release* **2020**, *320*, 392–403. https://doi.org/10.1016/j.jconrel.2020.01.048.

(45) Pereira, E. R.; Jones, D.; Jung, K.; Padera, T. P. The Lymph Node Microenvironment and Its Role in the Progression of Metastatic Cancer. *Semin. Cell Dev. Biol.* **2015**, *38*, 98–105. https://doi.org/10.1016/j.semcdb.2015.01.008.

(46) Ubellacker, J. M. et al. Lymph Protects Metastasizing Melanoma Cells from Ferroptosis. *Nature* **2020**, *585* (7823), 113–118. https://doi.org/10.1038/s41586-020-2623-z.

(47) Vanharanta, S.; Massagué, J. Origins of Metastatic Traits. *Cancer Cell* **2013**, *24* (4), 410–421. https://doi.org/10.1016/j.ccr.2013.09.007.

(48) Alitalo, A.; Detmar, M. Interaction of Tumor Cells and Lymphatic Vessels in Cancer Progression. *Oncogene* **2012**, *31* (42), 4499–4508. https://doi.org/10.1038/onc.2011.602.

(49) Morton, D. L. et al. Final Trial Report of Sentinel-Node Biopsy versus Nodal Observation in Melanoma. *N. Engl. J. Med.* **2014**, *370* (7), 599–609. https://doi.org/10.1056/nejmoa1310460.

(50) Thomas, S. N.; Vokali, E.; Lund, A. W.; Hubbell, J. A.; Swartz, M. A. Targeting the Tumor-Draining Lymph Node with Adjuvanted Nanoparticles Reshapes the Anti-Tumor Immune Response. *Biomaterials* **2014**, *35* (2), 814–824. https://doi.org/10.1016/j.biomaterials.2013.10.003.

(51) Liu, H. et al. Structure-Based Programming of Lymph-Node Targeting in Molecular Vaccines. *Nature* **2014**, *507* (7493), 519–522. https://doi.org/10.1038/nature12978.

(52) Kuai, R.; Ochyl, L. J.; Bahjat, K. S.; Schwendeman, A.; Moon, J. J. Designer Vaccine Nanodiscs for Personalized Cancer Immunotherapy. *Nat. Mater.* **2017**, *16* (4), 489–498. https://doi.org/10.1038/NMAT4822.

(53) Schudel, A.; Francis, D. M.; Thomas, S. N. Material Design for Lymph Node Drug Delivery. *Nature Reviews Materials*. Nature Publishing Group June 2019, pp 415–428. https://doi.org/10.1038/s41578-019-0110-7.

(54) Kato, S.; Mori, S.; Kodama, T. A Novel Treatment Method for Lymph Node Metastasis Using a Lymphatic Drug Delivery System with Nano/Microbubbles and Ultrasound. *J. Cancer* **2015**, *6* (12), 1282–1294. https://doi.org/10.7150/jca.13028.

(55) Cai, S.; Xie, Y.; Davies, N. M.; Cohen, M. S.; Forrest, M. L. Pharmacokinetics and Disposition of a Localized Lymphatic Polymeric Hyaluronan Conjugate of Cisplatin in Rodents. *J. Pharm. Sci.* **2010**, *99* (6), 2664–2671. https://doi.org/10.1002/jps.22016.

(56) Piskounova, E. et al. Oxidative Stress Inhibits Distant Metastasis by Human Melanoma Cells. *Nature* **2015**, *527* (7577), 186–191. https://doi.org/10.1038/nature15726.

(57) Emens, L. A. Chemoimmunotherapy. *Cancer J.* **2010**, *16* (4), 295–303. https://doi.org/10.1097/PPO.0b013e3181eb5066.

(58) Galon, J.; Bruni, D. Approaches to Treat Immune Hot, Altered and Cold Tumours with Combination Immunotherapies. *Nat. Rev. Drug Discov.* **2019**, *18* (3), 197–218. https://doi.org/10.1038/s41573-018-0007-y.

(59) Qiu, S. Q. et al. Tumor-Associated Macrophages in Breast Cancer: Innocent Bystander or Important Player? *Cancer Treat. Rev.* **2018**, *70*, 178–189. https://doi.org/10.1016/j.ctrv.2018.08.010.

(60) Sica, A. et al. Macrophage Polarization in Tumour Progression. *Seminars in Cancer Biology*. 2008, pp 349–355. https://doi.org/10.1016/j.semcancer.2008.03.004.

(61) Kaczanowska, S.; Joseph, A. M.; Davila, E. TLR Agonists: Our Best Frenemy in Cancer Immunotherapy . *J. Leukoc. Biol.* **2013**, *93* (6), 847–863. https://doi.org/10.1189/jlb.1012501.

(62) Mantovani, A. et al. The Chemokine System in Diverse Forms of Macrophage Activation and Polarization. *Trends Immunol.* **2004**, *25* (12), 677–686. https://doi.org/10.1016/j.it.2004.09.015.

(63) Kohno, K. et al. Inflammatory M1-like Macrophages Polarized by NK-4 Undergo Enhanced Phenotypic Switching to an Anti-Inflammatory M2-like Phenotype upon Co-Culture with Apoptotic Cells. *J. Inflamm. (United Kingdom)* **2021**, *18* (1), 1–14. https://doi.org/10.1186/s12950-020-00267-z.

(64) Vernon, P. J.; Tang, D. Eat-Me: Autophagy, Phagocytosis, and Reactive Oxygen Species Signaling. *Antioxidants Redox Signal.* **2013**, *18* (6), 677–691. https://doi.org/10.1089/ars.2012.4810.

(65) Liang, T. et al. Recent Advances in Macrophage-Mediated Drug Delivery Systems. *Int. J. Nanomedicine* **2021**, *16*, 2703–2714. https://doi.org/10.2147/IJN.S298159.

(66) Qi, Y.; Yan, X.; Xia, T.; Liu, S. Use of Macrophage as a Trojan Horse for Cancer Nanotheranostics. *Mater. Des.* **2021**, *198*, 109388. https://doi.org/10.1016/j.matdes.2020.109388.

(67) Kim, D. K.; Dobson, J. Nanomedicine for Targeted Drug Delivery. *J. Mater. Chem.* **2009**, *19* (35), 6294–6307. https://doi.org/10.1039/b902711b.

(68) Chen, G.; Roy, I.; Yang, C.; Prasad, P. N. Nanochemistry and Nanomedicine for Nanoparticle-Based Diagnostics and Therapy. *Chem. Rev.* **2016**, *116* (5), 2826–2885. https://doi.org/10.1021/acs.chemrev.5b00148.

(69) Danhier, F. To Exploit the Tumor Microenvironment: Since the EPR Effect Fails in the Clinic, What Is the Future of Nanomedicine? *J. Control. Release* **2016**, *244* (Pt A), 108–121. https://doi.org/10.1016/j.jconrel.2016.11.015.

(70) He, H.; Liu, L.; Morin, E. E.; Liu, M.; Schwendeman, A. Survey of Clinical Translation of Cancer Nanomedicines - Lessons Learned from Successes and Failures. *Acc. Chem. Res.* **2019**, *52* (9), 2673–2683. https://doi.org/10.1021/acs.accounts.9b00228.

(71) Hernández-Gil, J. et al. An Iron Oxide Nanocarrier Loaded with a Pt(IV) Prodrug and Immunostimulatory DsRNA for Combining Complementary Cancer Killing Effects. *Adv. Healthc. Mater.* **2015**, *4* (7), 1034–1042. https://doi.org/10.1002/adhm.201500080.

(72) Golla, E. D.; Ayres, G. H. Spectrophotometric Determination of Platinum with O-Phenylenediamine. *Talanta* **1973**, *20* (2), 199–210. https://doi.org/10.1016/0039-9140(73)80267-X.

(73) Garaikoetxea Arguinzoniz, A.; Gómez Blanco, N.; Ansorena Legarra, P.; Mareque-Rivas, J. C. Enhanced Cancer Cell Killing of a Pt(Iv) Prodrug Promoted by Outer-Sphere Coordination with Polyethyleneimines. *Dalt. Trans.* **2015**, *44* (16), 7135–7138. https://doi.org/10.1039/c5dt00175g.

(74) Nemirovski, A. et al. New Reduction Pathways for Ctc-[PtCl2(CH3CO 2)2(NH3)(Am)] Anticancer Prodrugs. *Chem. Commun.* **2010**, *46* (11), 1842–1844. https://doi.org/10.1039/b925721g.

(75) Gao, L.; Fan, K.; Yan, X. Iron Oxide Nanozyme: A Multifunctional Enzyme Mimetic for Biomedical Applications. *Theranostics* **2017**, *7* (13), 3207–3227. https://doi.org/10.7150/thno.19738.

(76) Van Meerloo, J.; Kaspers, G. J. L.; Cloos, J. Cell Sensitivity Assays: The MTT Assay. *Methods Mol. Biol.* **2011**, *731*, 237–245. https://doi.org/10.1007/978-1-61779-80-5_20.

(77) Mirzaei, S. et al. Elucidating Role of Reactive Oxygen Species (Ros) in Cisplatin Chemotherapy: A Focus on Molecular Pathways and Possible Therapeutic Strategies. *Molecules* **2021**, *26* (8), 2382. https://doi.org/10.3390/molecules26082382.

(78) Danciu, C. et al. Behaviour of Four Different B16 Murine Melanoma Cell Sublines: C57BL/6J Skin. *Int. J. Exp. Pathol.* **2015**, *96* (2), 73–80. https://doi.org/10.1111/iep.12114.

(79) Xu, D. et al. NK and CD8+ T Cell-Mediated Eradication of Poorly Immunogenic B16-F10 Melanoma by the Combined Action of IL-12 Gene Therapy and 4-1BB Costimulation. *Int. J. Cancer* **2004**, *109* (4), 499–506. https://doi.org/10.1002/ijc.11696.

(80) Cisplatin-induced, lipid peroxidation and decrease of; gluconeogenesis, in rat kidney cortex: D.; effects, of antioxidants and radical scavengers; Hannemann, J.; Baumann, K. Cisplatin-Induced Lipid Peroxidation and Decrease of Gluconeogenesis in Rat Kidney Cortex: Different Effects of Antioxidants and Radical Scavengers. *Toxicology* **1988**, *51* (2–3), 119–132. https://doi.org/10.1016/0300-483X(88)90143-6.

(81) Barrera, G. Oxidative Stress and Lipid Peroxidation Products in Cancer Progression and Therapy. *ISRN Oncol.* **2012**, *2012*, 1–21. https://doi.org/10.5402/2012/137289.

(82) Ling, X. et al. Glutathione-Responsive Prodrug Nanoparticles for Effective Drug Delivery and Cancer Therapy. *ACS Nano* **2019**, *13* (1), 357–370. https://doi.org/10.1021/acsnano.8b06400.

(83) Ruiz-de-Angulo, A. et al. Chemically Programmed Vaccines: Iron Catalysis in Nanoparticles Enhances Combination Immunotherapy and Immunotherapy-Promoted Tumor Ferroptosis. *iScience* **2020**, *23* (9). https://doi.org/10.1016/j.isci.2020.101499.

(84) Vaupel, P.; Multhoff, G. Accomplices of the Hypoxic Tumor Microenvironment Compromising Antitumor Immunity: Adenosine, Lactate, Acidosis, Vascular Endothelial Growth Factor, Potassium Ions, and Phosphatidylserine. *Front. Immunol.* **2017**, *8* (DEC), 1887. https://doi.org/10.3389/fimmu.2017.01887.

(85) Gao, L.; Fan, K.; Yan, X. Iron Oxide Nanozyme: A Multifunctional Enzyme Mimetic for Biomedical Applications. *Theranostics* **2017**, *7* (13), 3207–3227. https://doi.org/10.7150/thno.19738.

(86) Serrano, O. K. et al. Antitumor Effect of Pharmacologic Ascorbate in the B16 Murine Melanoma Model. *Free Radic. Biol. Med.* **2015**, *87*, 193–203. https://doi.org/10.1016/j.freeradbiomed.2015.06.032.

(87) Kajarabille, N.; Latunde-Dada, G. O. Programmed Cell-Death by Ferroptosis: Antioxidants as Mitigators. *Int. J. Mol. Sci.* **2019**, *20* (19). https://doi.org/10.3390/ijms20194968.

(88) Wang, X. et al. Vitamin C Induces Ferroptosis in Anaplastic Thyroid Cancer Cells by Ferritinophagy Activation. *Biochem. Biophys. Res. Commun.* **2021**, *551*, 46–53. https://doi.org/10.1016/j.bbrc.2021.02.126.

(89) Chen, Q. et al. Pharamacologic Ascorbic Acid Concentrations Selectively Kill Cancer Cells: Action as a pro-Drug to Deliver Hydrogen Peroxide to Tissuse. *Proc. Natl. Acad. Sci. U. S. A.* **2005**, *102* (38), 13604–13609. https://doi.org/10.1073/pnas.0506390102.

(90) Pal, S.; Jana, N. R. Pharmacologic Vitamin C-Based Cell Therapy via Iron Oxide Nanoparticle-Induced Intracellular Fenton Reaction. *ACS Appl. Nano Mater.* **2020**, *3* (2), 1683–1692. https://doi.org/10.1021/acsanm.9b02405.

(91) Lopez-Yrigoyen, M.; Cassetta, L.; Pollard, J. W. Macrophage Targeting in Cancer. *Ann. N. Y. Acad. Sci.* **2021**, *1499* (1), 18–41. https://doi.org/10.1111/nyas.14377.

(92) Cieslewicz, M. et al. Targeted Delièery of Proapoptotic Peptides to Tumor-Associated Macrophages Improèes Surèièal. *Proc. Natl. Acad. Sci. U. S. A.* **2013**, *110* (40), 15919–15924. https://doi.org/10.1073/pnas.1312197110.

(93) Wang, Y. et al. Polymeric Nanoparticles Enable Reversing Macrophage in Tumor Microenvironment for Immunotherapy. *Biomaterials* **2017**, *112*, 153–163. https://doi.org/10.1016/j.biomaterials.2016.09.034.

(94) Rodell, C. B. et al. TLR7/8-Agonist-Loaded Nanoparticles Promote the Polarization of Tumour-Associated Macrophages to Enhance Cancer Immunotherapy. *Nat. Biomed. Eng.* **2018**, *2* (8), 578–588. https://doi.org/10.1038/s41551-018-0236-8.

(95) Miller, M. A. et al. Tumour-Associated Macrophages Act as a Slow-Release Reservoir of Nano-Therapeutic Pt(IV) pro-Drug. *Nat. Commun.* **2015**, *6*. https://doi.org/10.1038/ncomms9692.

(96) Martinez, F. O.; Gordon, S. The M1 and M2 Paradigm of Macrophage Activation: Time for Reassessment. *F1000Prime Rep.* **2014**, *6*. https://doi.org/10.12703/P6-13.

(97) Chen, Y. et al. Tumor-Associated Macrophages: An Accomplice in Solid Tumor Progression. *J. Biomed. Sci.* **2019**, *26* (1), 1–13. https://doi.org/10.1186/s12929-019-0568-z.

(98) Jeannin, P.; Paolini, L.; Adam, C.; Delneste, Y. The Roles of CSFs on the Functional Polarization of Tumor-Associated Macrophages. *FEBS J.* **2018**, *285* (4), 680–699. https://doi.org/10.1111/febs.14343.

(99) Arnold, I. C. et al. CD11c+ Monocyte/Macrophages Promote Chronic Helicobacter Hepaticus-Induced Intestinal Inflammation through the Production of IL-23. *Mucosal Immunol.* **2016**, *9* (2), 352–363. https://doi.org/10.1038/mi.2015.65.

(100) Loke, P.; Allison, J. P. *PD-L1 and PD-L2 Are Differentially Regulated by Th1 and Th2 Cells*; 2003; Vol. 100. https://doi.org/10.1073/pnas.0931259100.

(101) Tan, H. Y. et al. The Reactive Oxygen Species in Macrophage Polarization: Reflecting Its Dual Role in Progression and Treatment of Human Diseases. *Oxid. Med. Cell. Longev.* **2016**, *2016*, 1–16. https://doi.org/10.1155/2016/2795090.

(102) Tian, S. B. et al. The Prognostic Value of AGR2 Expression in Solid Tumours: A Systematic Review and Meta-Analysis. *Sci. Rep.* **2017**, *7* (1), 43356–43367. https://doi.org/10.1038/s41598-017-15757-z.

(103) Koch, A. et al. Glucose Transporter Isoform 1 Expression Enhances Metastasis of Malignant Melanoma Cells. *Oncotarget* **2015**, *6* (32), 32748–32760. https://doi.org/10.18632/oncotarget.4977.

(104) Zhao, Z.; Ukidve, A.; Kim, J.; Mitragotri, S. Targeting Strategies for Tissue-Specific Drug Delivery. *Cell* **2020**, *181* (1), 151–167. https://doi.org/10.1016/j.cell.2020.02.001.

(105) Calvaresi, E. C.; Hergenrother, P. J. Glucose Conjugation for the Specific Targeting and Treatment of Cancer. *Chem. Sci.* **2013**, *4* (6), 2319–2333. https://doi.org/10.1039/c3sc22205e.

(106) Liu, P. et al. Highly Water-Soluble Platinum(Ii) Complexes as GLUT Substrates for Targeted Therapy: Improved Anticancer Efficacy and Transporter-Mediated Cytotoxic Properties. *Chem. Commun.* **2013**, *49* (24), 2421–2423. https://doi.org/10.1039/c3cc38589b.

(107) Mazumder, A. et al. Glucose Targeted Therapy against Liver Hepatocellular Carcinoma: In Vivo Study. *J. Drug Deliv. Sci. Technol.* **2019**, *49*, 502–512. https://doi.org/10.1016/j.jddst.2018.12.036.

(108) Jiang, X. et al. Nanoparticles of 2-Deoxy-d-Glucose Functionalized Poly(Ethylene Glycol)-Co-Poly(Trimethylene Carbonate) for Dual-Targeted Drug Delivery in Glioma Treatment. *Biomaterials* **2014**, *35* (1), 518–529. https://doi.org/10.1016/j.biomaterials.2013.09.094.

(109) Ghani, L. et al. 1,3,5-Triazine-Cored Maltoside Amphiphiles for Membrane Protein Extraction and Stabilization. *J. Am. Chem. Soc.* **2019**, *141* (50), 19677–19687. https://doi.org/10.1021/jacs.9b07883.

(110) Moreno, L. M.; Quiroga, J.; Abonia, R.; Ramírez-Prada, J.; Insuasty, B. Synthesis of New 1,3,5-Triazine-Based 2-Pyrazolines as Potential Anticancer Agents. *Molecules* **2018**, *23* (8). https://doi.org/10.3390/molecules23081956.

(111) Kim, E. S. Enasidenib: First Global Approval. *Drugs* **2017**, *77* (15), 1705–1711. https://doi.org/10.1007/s40265-017-0813-2.

(112) Das, M. et al. Diastereomeric Cyclopentane-Based Maltosides (CPMs) as Tools for Membrane Protein Study. *J. Am. Chem. Soc.* **2020**, *142* (51), 21382–21392. https://doi.org/10.1021/jacs.0c09629.

(113) Das, M. et al. Trehalose-Cored Amphiphiles for Membrane Protein Stabilization: Importance of the Detergent Micelle Size in GPCR Stability. *Org. Biomol. Chem.* **2019**, *17* (12), 3249–3257. https://doi.org/10.1039/c8ob03153c.

(114) Min, Y. et al. Antigen-Capturing Nanoparticles Improve the Abscopal Effect and Cancer Immunotherapy. *Nat. Nanotechnol.* **2017**, *12* (9), 877–882. https://doi.org/10.1038/nnano.2017.113.

(115) Liberti, M. V.; Locasale, J. W. The Warburg Effect: How Does It Benefit Cancer Cells? *Trends Biochem. Sci.* **2016**, *41* (3), 211–218. https://doi.org/10.1016/j.tibs.2015.12.001.

(116) Han, J. et al. Glucose Promotes Cell Proliferation, Glucose Uptake and Invasion in Endometrial Cancer Cells via AMPK/MTOR/S6 and MAPK Signaling. *Gynecol. Oncol.* **2015**, *138* (3), 668–675. https://doi.org/10.1016/j.ygyno.2015.06.036.

(117) Ruiz-De-Angulo, A.; Zabaleta, A.; Gómez-Vallejo, V.; Llop, J.; Mareque-Rivas, J. C. Microdosed Lipid-Coated 67Ga-Magnetite Enhances Antigen-Specific Immunity by Image Tracked Delivery of Antigen and Cpg to Lymph Nodes. *ACS Nano* **2016**, *10* (1), 1602–1618. https://doi.org/10.1021/acsnano.5b07253.

(118) Petrelli, F. et al. Timing of Adjuvant Chemotherapy and Survival in Colorectal, Gastric, and Pancreatic Cancer. A Systematic Review and Meta-Analysis. *Cancers (Basel).* **2019**, *11* (4), 550. https://doi.org/10.3390/cancers11040550.

(119) Zhan, Q. H.; Fu, J. Q.; Fu, F. M.; Zhang, J.; Wang, C. Survival and Time to Initiation of Adjuvant Chemotherapy among Breast Cancer Patients: A Systematic Review and Meta-Analysis. *Oncotarget* **2018**, *9* (2), 2739–2751. https://doi.org/10.18632/oncotarget.23086.

(120) Nakanishi, K. et al. Delay in Initiation of Postoperative Adjuvant Chemotherapy with S-1 Monotherapy and Prognosis for Gastric Cancer Patients: Analysis of a Multi-Institutional Dataset. *Gastric Cancer* **2019**, *22* (6), 1215–1225. https://doi.org/10.1007/s10120-019-00961-9.

(121) Burdett, S. Preoperative Chemotherapy for Non-Small-Cell Lung Cancer: A Systematic Review and Meta-Analysis of Individual Participant Data. *Lancet* **2014**, *383* (9928), 1561–1571. https://doi.org/10.1016/S0140-6736(13)62159-5.

(122) Van der Hage, J. A. et al. Preoperative Chemotherapy in Primary Operable Breast Cancer: Results from the European Organization for Research and Treatment of Cancer Trial 10902. *J. Clin. Oncol.* **2001**, *19* (22), 4224–4237. https://doi.org/10.1200/JCO.2001.19.22.4224.

(123) Wanebo, H. J. et al. Preoperative Chemoradiation Coupled with Aggressive Resection as Needed Ensures near Total Control in Advanced Head and Neck Cancer. *Am. J. Surg.* **1997**, *174* (5), 518–522. https://doi.org/10.1016/S0002-9610(97)00167-0.

(124) Thesis, P.; Garaikoetxea, A.; Supervisor, A.; Carlos, P. J.; Rivas, M. Nanoparticle-Based Delivery and Activation of Platinum (IV) Prodrugs and DsRNA for Cancer Chemotherapy AMAIA GARAIKOETXEA ARGUINZONIZ (Cc by-Nc 4.0). **2017**, *2017* (IV).

(125) Jewell, C. M.; Bustamante Lopẽz, S. C.; Irvine, D. J. In Situ Engineering of the Lymph Node Microenvironment via Intranodal Injection of Adjuvant-Releasing Polymer Particles. *Proc. Natl. Acad. Sci. U. S. A.* **2011**, *108* (38), 15745–15750. https://doi.org/10.1073/pnas.1105200108.

(126) Reddy, S. T. et al. Exploiting Lymphatic Transport and Complement Activation in Nanoparticle Vaccines. *Nat. Biotechnol.* **2007**, *25* (10), 1159–1164. https://doi.org/10.1038/nbt1332.

Chapter 4 . **Chemically programmed nanovaccines exploiting IONP-based redox catalytic activity for effective cancer combination immunotherapy**

4.1. Introduction

Cancer immunotherapies have yielded impressive results in clinical trials, opening a new era in cancer treatment. However, only some tumor types and a minority of patients respond to the current immunotherapy treatments. Hence, new strategies are required to potentiate immunotherapy. Ferroptosis is a newly described mechanism of iron-mediated oxidative cell death that connects with crucial pathways of immunogenic cancer cell death and immunotherapies that stimulate the immune system against cancer cells. In this chapter, we report the engineering of a therapeutic platform based on iron oxide-loaded nanovaccines (IONVs). The IONVs were "chemically programmed" to exploit the characteristics of the TME and enable multi-pronged tumor attacks. IONV's antitumor effects arise from: (i) cancer cell sensitization towards ferroptosis; (ii) macrophage repolarization towards tumor-suppressing M1 phenotypes and enhanced ROS generation; (iii) optimization of tumor-antigen processing and cross-presentation; (iv) monitorable therapy biodistribution and delivery; and (v) synergy with state-of-the-art immunostimulatory antibodies. Altogether, these results demonstrate the feasibility of using IONVs as generalizable platforms for the enhancement of cancer immunotherapy.

4.1.1. IONPs as an anticancer immunity boost in the TME

The tumor microenvironment (TME) evolves to establish a complex network of intercellular dynamics that support cancer growth and stabilization (see Chapter I) [1]. The site contains a tolerogenic mix of exhausted and regulatory T-cells (Tregs), myeloid-derived suppressor cells (MDSCs) and tumor associated macrophages (TAMs) [2]. The site also shows characteristic metabolic alterations such as hypoxia, low pH, nutrient deprivation, and high levels of ROS and H_2O_2. The combination of these features yields a TME that is difficult to infiltrate by active anticancer immune reactions [3].

Redox stress-inducing therapies can rewire the TME to make it permeable or more susceptible to antitumor immune responses. Cancer cell ferroptosis is a recently described mechanism of programmed cell death in which cells can undergo immunogenic cell death (ICD) triggered by irreversible accumulation of oxidative damage [4]. The pathway has been shown to enhance non-redundant means of immune cell recruitment and activation, including by inducing the release of damage-associated molecular patterns (DAMPs),

reactive oxygen species (ROS) and tumor-associated antigens (TAAs) [5]. ICD can induce TAM reprogramming (or repolarization) from pro-tumoral (M2-like) phenotypes to anticancer (M1-like) phenotypes [6–12]. M1-like macrophages display increased cytotoxic activity and induce the release of immunostimulatory signals like tumor necrosis factor-α (TNF-α), interferon-γ (IFN-γ) and an additional increase in cytotoxic ROS levels [13–16]. M1 macrophage recruitment in the TME can be achieved *in situ* as TAMs constitute a predominant part of the cells in the tumor site [17,18]. Also, ICD can enhance cancer cell identification by the immune system through facilitated TAA cross-presentation in antigen presenting cells (APCs) like macrophages or dendritic cells (DCs) (see Chapter I) [19].

The acidity of the TME and its large H_2O_2 availability represent very favorable conditions for ROS generation by catalytic iron-mediated Fenton chemistry reactions [20,21]. Elevations in local iron concentration have also been reported to facilitate ROS-mediated M2-to-M1 macrophage polarization [6,22] and increased expression of co-stimulatory receptors CD80 and CD86 for cytotoxic T-cell activation [23,24] (Fig. 4.1, d-e). Ferumoxytol is an example of a clinically approved IONP formulation reported to favor immune stimulation through M1 macrophage polarization (Fig. 4.1, a-c).

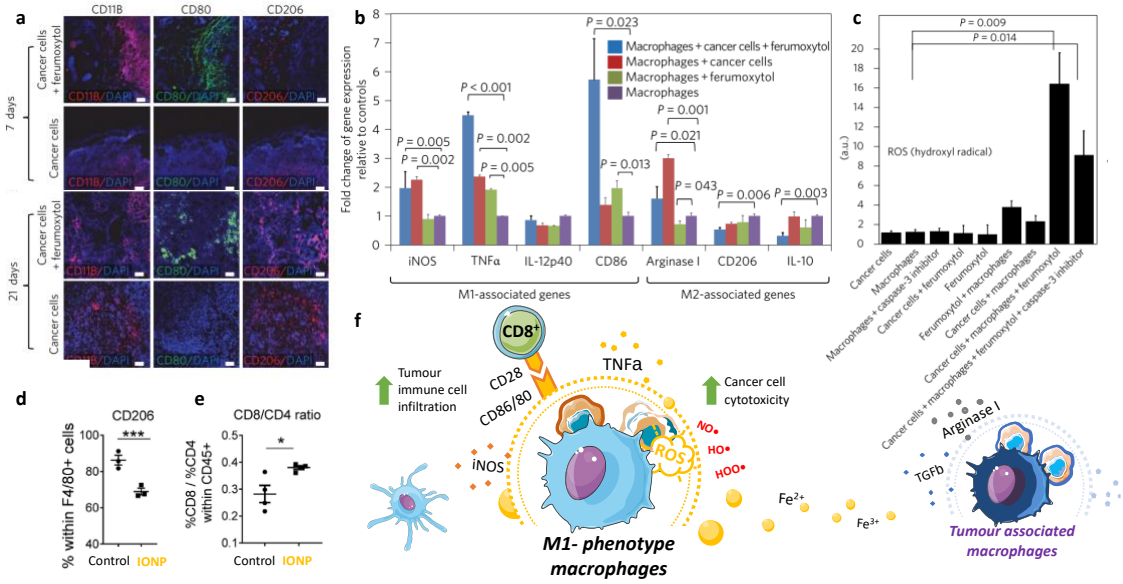

Figure 4.1. Oxidative Fenton chemistry induces TAM cytotoxic polarization *(a) Tumor immunofluorescence staining for CD11B, CD80 and CD206 as extracted after 7-day and 21-day ferumoxytol treatment in vivo; (b) In vitro mono or co-culture of cancer cells and*

macrophages showing signs of M2-to-M1 macrophage activation upon feromuxytol treatment; (c) colorimetric detection of hydrogen radical released in the aforementioned cultures upon treatment; tumor cell populations extracted after 15-day IONP in vivo treatment showing signs of (d) CD206 expression decrease and (e) increased cytotoxic $CD8^+$ T-cell infiltration; (f) Schematic representation of M2-to-M1 macrophage phenotype change. (a-c) images were adapted from [22]; (d-e) images were adapted from [23].

IONPs have been reported to synergize with various immunostimulatory compounds to enhance DC activation, $CD8^+$ T-cell activation and anticancer cytokine signalling [25–27]. Lipid peroxidation is also suspected to enhance TAA cross-presentation and immune memory acquisition through endosome escape mechanisms (Fig. 4.2, a; see Chapter I) [19]. In addition, state-of-the-art immune checkpoint blockade (ICB) therapies offer complementary means for tumor sensitization to oxidative damage and ferroptosis (Fig. 4.2, b). ICB therapies aim to "block" immunosuppressive "checkpoints", like Programmed Death Ligand-1 (PD-L1), that are highly expressed on the surface of cancer cells and immunosuppressive cell populations. PD-L1 binds to Programmed Death Ligand-1 (PD-1) expressed in active T-cells to deactivate them. [28] The blockade of the PD-1/PD-L1 interaction prevents T-cell deactivation thus "releasing the breaks" of the antitumor immune action. The activated T-cells secrete IFN-γ, which depletes cancer cell uptake of relevant precursors (cystine) required for the production of intracellular protecting antioxidants (glutathione; GSH) provide sensitization to tumor cell ferroptosis, and therefore, a new approach for improving immunotherapy [28–32].

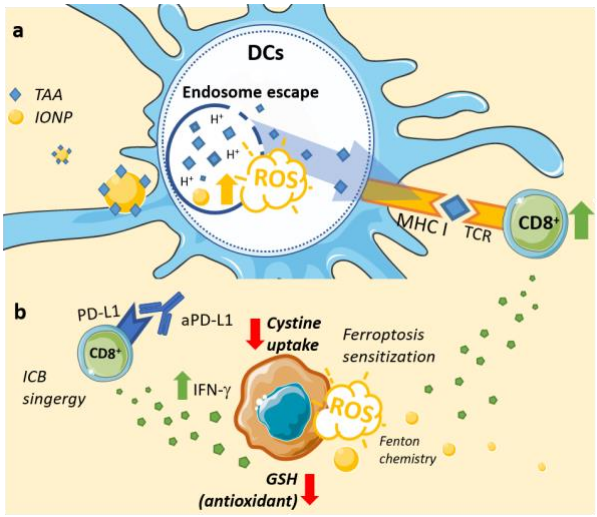

Figure 4.2. Oxidative Fenton chemistry induces anticancer immunity boost. *(a) Schematic representation of antigen cross-presentation enhancement via ROS-enabled endosome escape and (b) ferroptosis sensitization from ICB therapy via effector T-cell IFN-γ release.*

4.1.2. Chemically programmed nanovaccines for cancer combination immunotherapy

This chapter reports the engineering of immunostimulatory IONP-filled micelles (mIONPs) and IONVs to exploit site-specific TME biochemical properties for therapeutic H_2O_2 and ROS "self-generation". H_2O_2 production is induced through immunostimulatory properties and M1-macrophage polarization is converted into highly toxic ROS through IONP-enabled Fenton chemistry. This coupled reactivity is used to drive and concentrate complementary or synergistic antitumor mechanisms in the TME. The IONVs design provide: (i) non-invasive Magnetic Resonance Imaging (MRI) and Single Photon Emission Computed Tomography (SPECT) monitorable imaging and therapy delivery to the tumor and tumor draining lymph nodes; (ii) immunostimulatory drug delivery; (iii) a redox-active iron oxide core that can drive M2-to-M1 macrophage polarization and cancer cell ferroptosis sensitization; and (iv) improved tumor antigen cross-presentation by pH responsive hydrazone-mediated bioconjugation (Fig. 4.3). Combination of IONVs with state-of-the-art antibody-mediated immunotherapies resulted in complete eradication of established tumors *in vivo* and acquisition of long-lived protective antitumor immunity against tumor rechallenge.

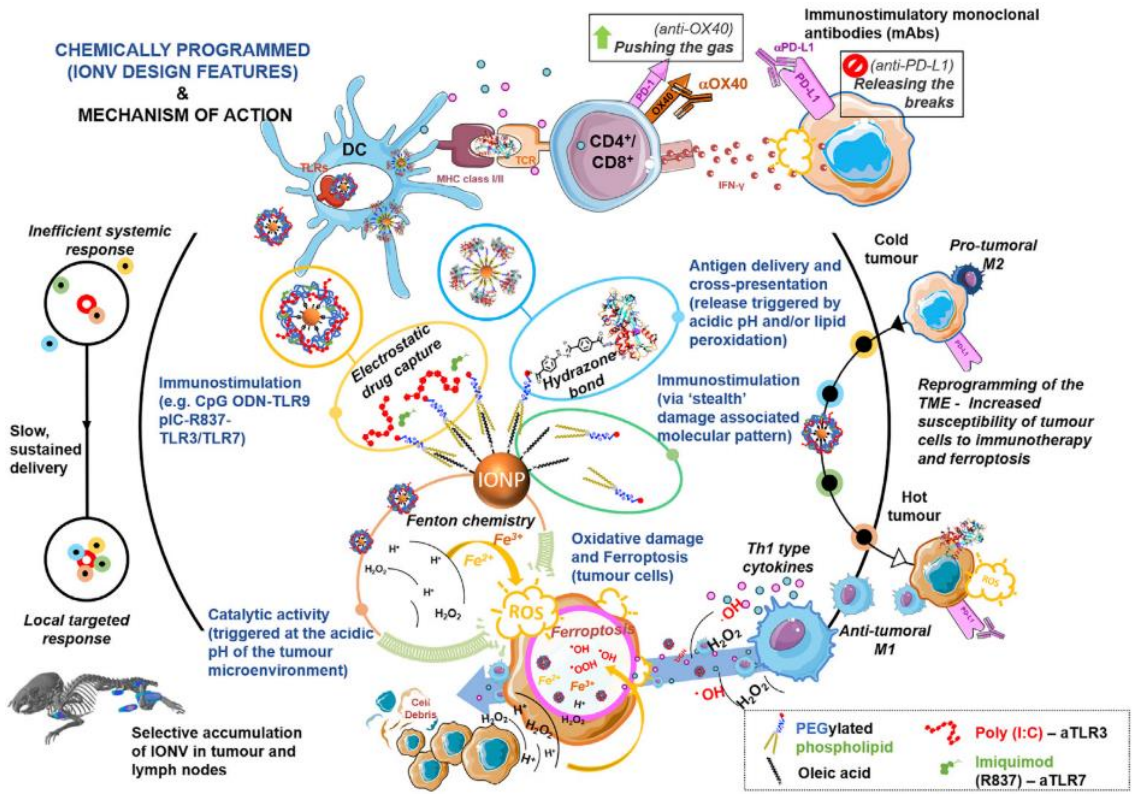

Figure 4.3. Summary of IONV features and mechanisms of action. *Therapeutic IONVs are made of chemically programmed multi-functional elements to activate and reprogram immune cells and cancer cells for effective combination therapy and cancer-specific ferroptosis. Image extracted from* [33].

4.2. Results and discussion

4.2.1. mIONP synthesis and physicochemical characterization

Methods of self-assembly of amphiphiles and thin dry-film formation (see Chapter 2) were used to obtain stable mIONP suspensions with defined and controllable size and surface charge. In this chapter, we form mIONPs that are coated with:

- 2000 kDa polyethylene glycol (PEG) phospholipids (PEG-PL) terminated in carboxylic acid (-COOH). The process yielded the previously characterized negatively charged mIONP-COOH particles (see Chapter 2).
- 2000 kDa methoxy-terminated PEG-PLs (PEG-OMe) with 1,2-dioleoyl-3-trimethylammonium-propane (DOTAP). Typically, 1 mg of hydrophobic IONP would be mixed with 2 mg of PEG-OMe and 1 mg of DOTAP. The process yielded the positively charged nanoparticles we refer to as mIONP-TAP (Fig. 4.4).

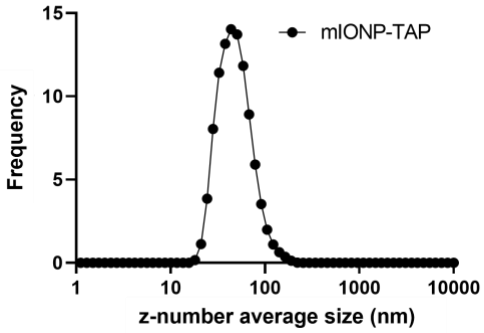

	mIONP-TAP
Average size (nm) *(z-intensity)*	143 ± 12
Average size (nm) *(z-number)*	52 ± 15
PDI	0.26 ± 0.03
Z-potential (mV) *(3.4 µM NaCl)*	+8 ± 1

Figure 4.4. Physicochemical mIONP-TAP characterization. *Nanoparticle size distribution as percentage (%) of events by z-number (b) mIONP-TAP suspensions and physicochemical characterization summary. Representative values as mean ± SEM for different mIONP suspensions for at least three independent experiments as characterized by Dynamic Light Scattering.*

4.2.1.1. Evaluation of redox IONP catalytic activity

Previously described methods based on 3,3′,5,5′-tetramethylbenzidine (TMB) and o-phenylenediamine (OPD) oxidation assays were used to evaluate the peroxidase-like catalytic features of the mIONPs (see Materials and Methods). As discussed in previous chapters, mIONP catalytic activity was shown to be pH-dependent, peaking at pH=4.5,

which is within the acidic pH of intracellular endolysosome compartments (see Chapter 2). The results also showed mIONP displayed stronger peroxidase-like catalytic properties than commercially-available ferumoxytol (Fig. 4.5, a,b). Substitution of mIONP for polyethylenimine-coated gold nanoparticles (Au@PEI) sharply decreased the oxidative activity.

Catalytic performance was evaluated at physiological temperature 37 °C in terms of catalytic rate (k_{cat}), maximal rate (V_{max}), Michaelis constant (K_M), and catalytic efficiency (k_{cat}/K_M) (see Materials and Methods). By varying the concentration of H_2O_2 we obtained values of K_M (H_2O_2) = 305 µM, V_{max} = 6.45 × 10^{-8} M^{-1} s^{-1} and k_{cat} = 1.9 s^{-1}. K_M(H_2O_2) is a relevant indicator as it accounts for the concentration of substrate needed for the catalyst to reach half of its maximum activity. Cancer cells continuously produce elevated levels of H_2O_2, much higher than non-cancerous cells [34]. Furthermore, it is reasonable to expect this production to be increased upon cell stimulation with TLR ligands. Human blood can reach a range of 30 – 50 µM H_2O_2 during inflammation [21].

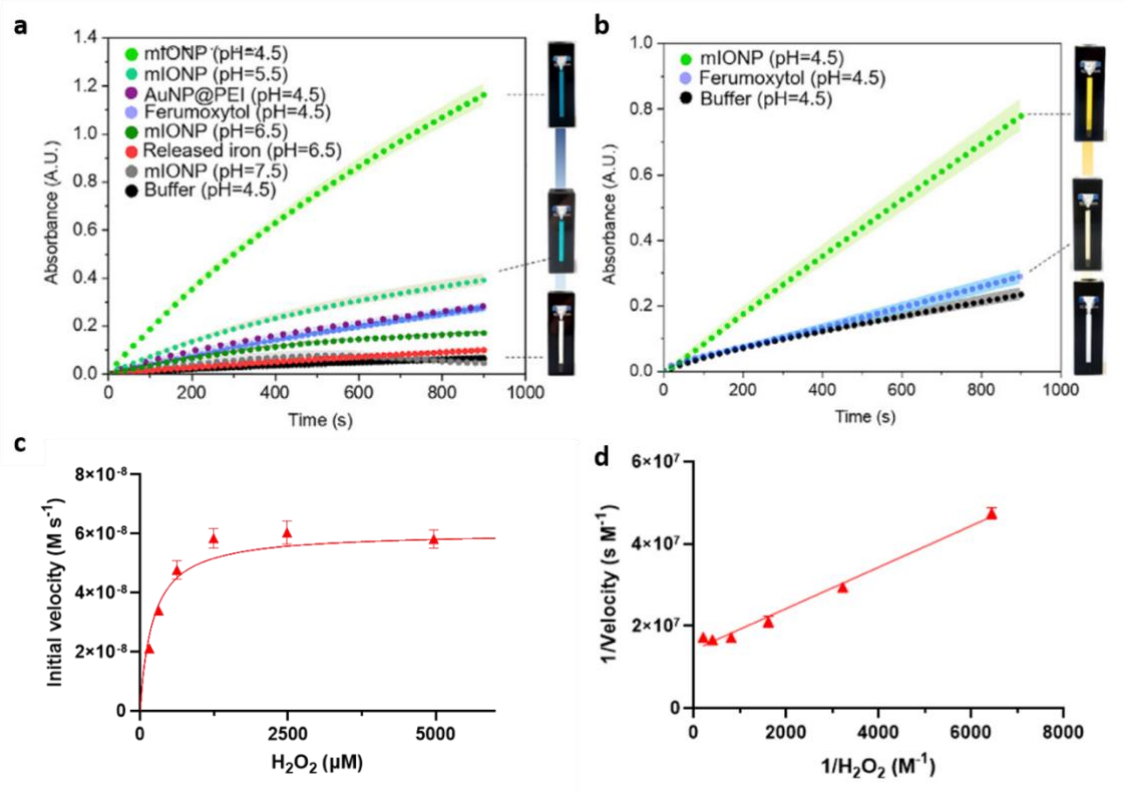

Figure 4.5. Characterization of mIONP peroxidase-like catalytic properties. *Time course curves assessing the catalytic activity of mIONPs at different pH values, AuNP@PEI, ferumoxytol and released free iron cations for the oxidation of (a) TMB ([TMB] = 830 µM) and (b) OPD ([OPD] = 3 mM). Concentrations of [Fe] = 150 µM for mIONPs, 550 µM for ferumoxytol and [H_2O_2] = 30 mM were used. (c) Michaelis-Menten and (d) Lineweaver-Burk kinetics plots for TMB oxidation at varying concentrations of H_2O_2. (a-b) comparative kinetic studies were monitored at room temperature using 10 mm pathlength quartz cuvettes. (c-d) steady-state kinetics were monitored at 37°C. Results are shown as mean ± SEM from three independent experiments.*

4.2.2. Immunomodulatory drug delivery strategies

As previously discussed, ROS generation can enhance various processes of anticancer immunity. In addition, mIONPs have an inner hydrophobic core, which is a well-known molecular feature recognized by the immune system as a immunostimulatory DAMP/"danger signal" (see below) [35]. However, oxidative stress is a double-edged sword that can also lead to counterproductive states of chronic inflammation and pro-tumoral tissue repair [36,37]. Hence, targeted delivery of immunostimulatory molecules is required to activate cytotoxic anticancer responses without systemic toxicity. Research has also

been focused on screening potent anticancer immunostimulatory drugs and evaluating their synergistic combination for immunotherapy [38]. Co-administration of polyinosinic:polycytidylic acid (poly(I:C) or pIC) and imiquimod (R837) was identified as one of the most powerful combinations of immunostimulatory TLR agonist for anticancer applications [39]. Poly(I:C) and R837 are synergistic TLR agonists (TLRa) for TLR3 and TLR7, which are TLRs that co-localize in intracellular endolysosomal compartments [40,41]. Previous research from our group demonstrated that the mIONP-based systems are trafficked into these compartments and co-localise with the TLR receptors [42], making them ideal vehicles for TLR3/7 drug delivery [43].

4.2.2.1. Poly(I:C) capture

Poly (I:C) is a synthetic analogue of viral dsRNA recognized by TLR3 localized in endolysosome compartments of immune cells such as DC, T cells or macrophages [38]. Activation of TLR3 by poly I:C in DCs culminates in the production of proinflammatory cytokines (IFNγ, TNFa and IL-6) as well as increased membrane expression of co-stimulatory CD80/86 and cytokine receptor CCR7 to orchestrate innate and adaptive immunity. Previous research from our group had observed that DC stimulation was greatly enhanced through mIONP + pIC combination [25]. pIC has also been shown to induce cell proliferation inhibition and apoptosis in some cancer cells [40].

Poly (I:C) structure contains repetitive negatively charged phosphate moieties (Fig. 2.13, a; See Chapter 2). These moieties can be captured by the positively charged surface of mIONP-TAP. Various concentrations of pIC (0- 500 µg/mL) were combined with mIONP-TAP ([IONP] = 0.5 µM) and left overnight to self-assembly. After removing excess pIC by ultracentrifuge (see Materials and Methods), the results showed that mIONP-TAP could efficiently capture and retain up to 500 µg/mL of pIC (Fig. 4.6). The obtained mIONP-TAP-pIC (from here on mIONP-pIC) system proved stable for at least seven days in PBS. Only a slight degree of aggregation could be observed when mIONP-TAP were combined with pIC concentrations above 200 µg/mL (Fig. 4.6, a-c). Poly(I:C) capture was confirmed by UV-Vis analysis (poly IC shows absorption peaks at 245 and 267 nm) (Fig 4.6, d-e) and quantitatively determined upon its hydrolyzation at basic pH (0.1 M NaOH; absorption peaks of hydrolysed pIC shift to 260 nm) (Fig. 4.6, f-i) (see Materials and Methods).

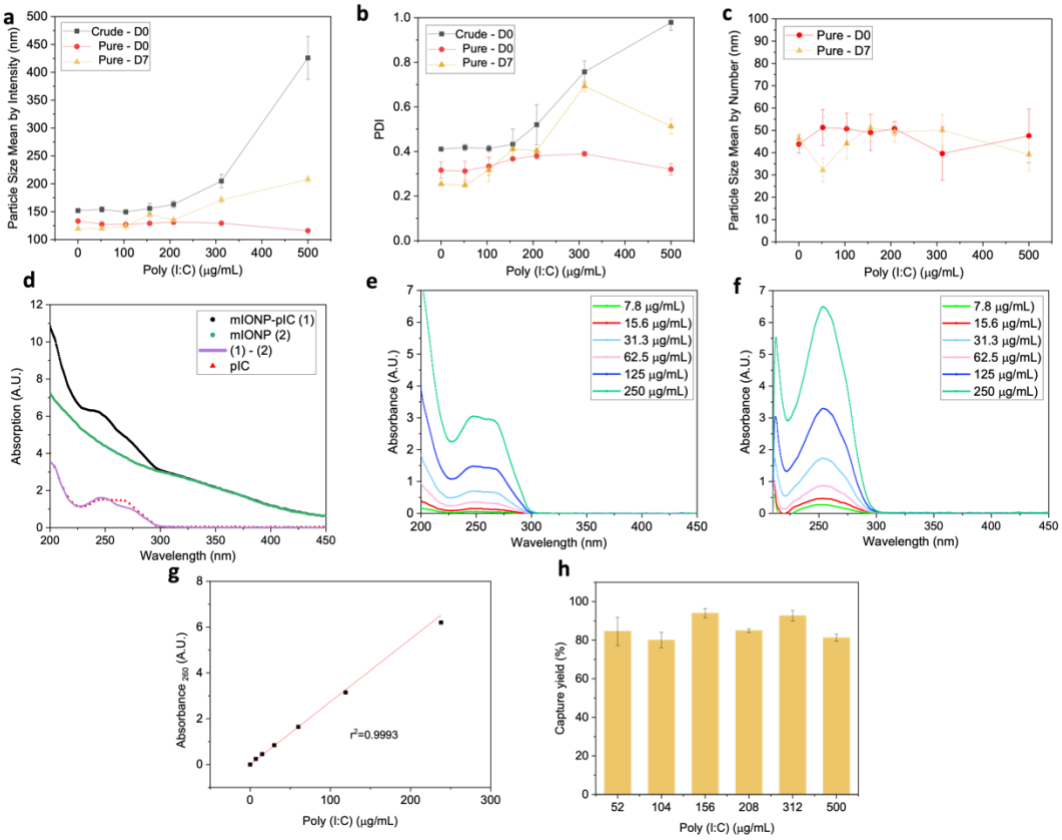

Figure 4.6. mIONP-pIC self-assembly characterization. *Hydrodynamic size characterization by DLS of IONP-TAP functionalized with increasing amounts of pIC (mIONP-pIC); crude product just after synthesis (Crude) and after purification (Pure) at days 0 (D0) and 7 (D7) stored at 4°C in PBS: (a) particle size mean by intensity and (b) polydispersity index (PDI); (c) particle size mean by number after purification. (d) Absorbance spectra comparison between mIONP-DOTAP and mIONP-pIC after purification, indicating the effective capture of pIC. (e) Typical pIC absorption spectra. (f) pIC absorption peaks after digestion in basic environment (λ = 260 nm) and (h) linear regression made to determine the (i) pIC capture yield in the mIONPs surface (%).*

4.2.2.2. Imiquimod capture

Imiquimod is a small synthetic derivative of imidazoquinoxaline (Fig 4.7, a). It functions as an agonist of TLR7 localized in endolysosome compartments of immune cells such as DC, T-cells or macrophages. Activation of TLR7 by R837 results in the production of potentiators of cytotoxic immunity like IFN-γ as well as increased immune cell proliferation and membrane expression of co-stimulatory CD80/86 [44]. Combinatory pIC-

R837 treatments have been shown to drive strong immunostimulatory profiles [41]. Previous research from our group had observed that immunostimulation was further enhanced through mIONP- delivery of pIC + R837 combination [43]. Imiquimod has also been shown to induce apoptosis in some cancer cells [45] and to sensitize cancer cells to oxidative damage [46].

Base-to-base interactions and hydrogen bonding is proposed to mediate R837 intercalation into pIC chains [43]. mIONP-pIC ([IONP] = 0.5 µM) and excess R837 concentrations (250 µg/mL) were left overnight to self-assemble. After removing non-retained R837 by ultracentrifuge (see Materials and Methods), the product obtained, mIONP-pIC-R837, displayed complete stability after 14 days of storage in PBS (Fig. 4.7, a-c). The system displayed low polydispersity like mIONP-TAP and mIONP-pIC systems. R837 shows an absorbance peak at 320 nm that allows for quantitative analysis by UV-Vis (Fig. 4.7, d-f). Owing to the weaker nature of pIC-R837 interactions and the limited number of interaction sites, capture yield by mIONP-pIC proved relatively low (Fig. 4.7, h). However, as we show in our *in vitro* cellular tests (see below), very little R837 amounts are required for mIONP-pIC-R837 to drive powerful anticancer immune responses.

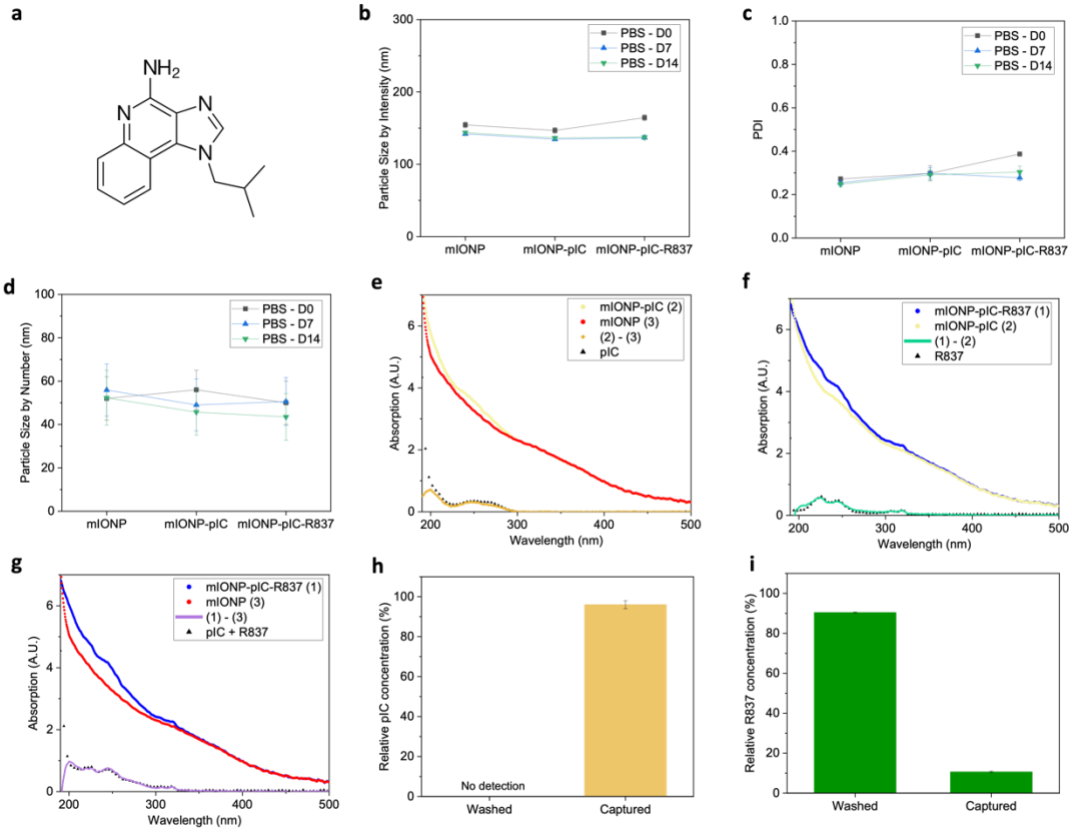

Figure 4.7. mIONP-PIC-R837 self-assembly characterization. *(a) Chemical structure of imiquimod (R837). (b-d) Hydrodynamic size characterization by DLS of mIONP-DOTAP micelles functionalized with pIC and R837 (mIONP-pIC-R837), after synthesis and purification at days 0 (D0), 7 (D7) and 14 (D14) in PBS at 4°C: (b) particle size mean by intensity, (c) PDI, and (d) particle size mean by number. Data are presented as an average of three readouts. Absorbance spectra comparison between (e) mIONP-DOTAP and mIONP-pIC, (f) mIONP-pIC-R837 and mIONP-pIC, and (g) and mIONP-pIC-R837 and mIONP after purification, indicating effective capture of both pIC and R837. Final capture yield (%) of (h) pIC (measured upon basic digestion) and (i) R837 (measured at λ = 320 nm prior to digestion).*

4.2.3. mIONP biological activity evaluation

4.2.3.1. Effects on tumor cell intracellular redox balance

Cystine is a key precursor for intracellular antioxidant GSH production. The molecule enters the cell through cysteine-glutamate antiporter (Fig. 4.8, a). GSH functions as the substrate of the enzyme glutathione peroxidase-4 (GPX4), which catalyses intracellular reduction and detoxification of H_2O_2 and ROS (Fig. 4.8, a) [47]. Excess redox stress against

cells with deficient intracellular antioxidant protection will induce the accumulation of irreparable oxidative damage and trigger ferroptosis [48,49].

The accelerated metabolism of cancer cells is linked to large intracellular ROS concentrations. This yields a delicate state of redox homeostasis that can be exploited by oxidative stress-inducing therapies [4]. To evaluate their susceptibility to ferroptosis cell death, murine melanoma B16-F10(OVA) were treated with cystine depleting agent Erastin. Erastin binds to cysteine-glutamate antiporter and impedes intracellular cysteine uptake (Fig. 4.8, a). After a 24-hour treatment, melanoma viability was evaluated using previously described colorimetric MTT assays (see Materials and Methods). The experiments showed that Erastin-mediated cystine depletion triggered significantly higher melanoma cell death. In comparison, murine macrophages RAW264.7 demonstrated higher oxidative resistance towards ROS-mediated damage (Fig. 4.8, b). This is consistent with previous research, which reports that macrophages are designed to survive and achieve self-protection against oxidative stress [37,50]. Hence, these results confirm the tumor-specific character of ferroptosis-inducing cancer therapies.

It was thus sought to evaluate the ferroptosis-inducing features of mIONPs. The melanoma cells were first administered increasing concentrations of Erastin for 24-hours and then treated with mIONP-COOH ([Fe] = 0.5 mM) for another 24 hours. Cell viability was evaluated using MTT assays after treatment. The results showed that mIONP administration alone was unable to trigger strong cytotoxic effects in the melanoma cells. However, these cytotoxic effects were significantly enhanced in melanoma cells previously treated with Erastin (Fig. 4.8, c). Accumulation of lipid hydroperoxides in the cell membrane could be revealed by previously described Flow Cytometry assays (see Materials and Methods). Liperfluo™ dye was loaded into the cells after treatment. Once loaded, the dye turns fluorescent when selectively oxidated by lipid hydroperoxides as a sign of accumulated oxidative damage (see Chapter 3). Cancer cells showed increasing signs of membrane lipid peroxidation following cysteine depletion by Erastin and oxidative mIONP treatments (Figure 4.8, d).

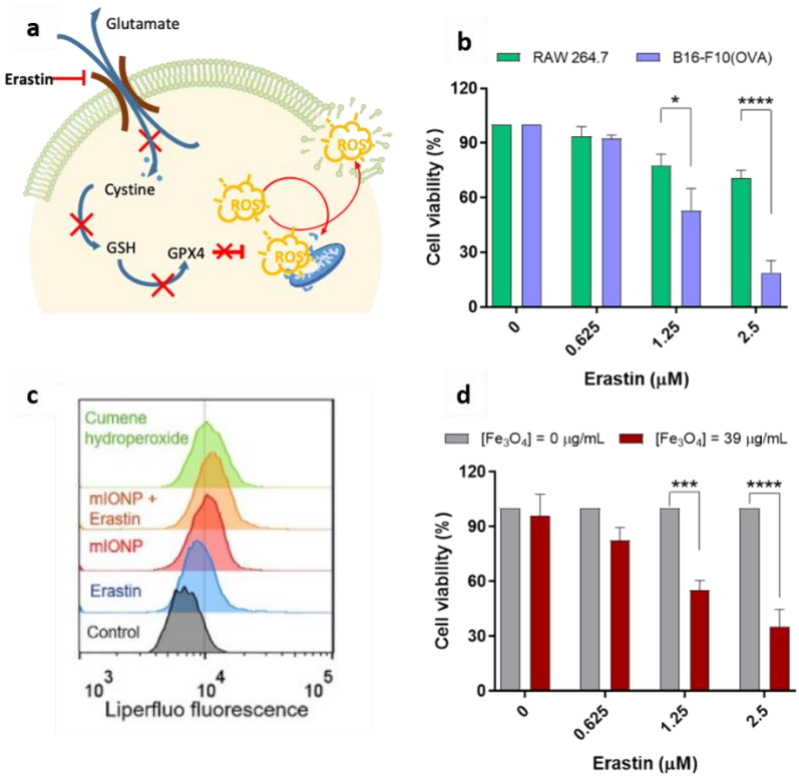

Figure 4.8. mIONP induce cancer-specific sensitization towards ferroptosis. *a) Effects of Erastin on the cell viability of RAW 264.7 (blue bars) and B16-F10(OVA) (green bars) in their respective monocultures, after 24 h of exposure as determined by MTT assay. Data was normalized to the absence of treatment. b) Effects of mIONPs on the cell viability of B16-F10(OVA) after 24 hours of exposure upon 24 h preconditioning with increasing concentrations of Erastin (stripped red bars). Concentration used for IONP was 39 μg/mL. Data was normalized to the absence of mIONP treatment for each Erastin concentration (solid green bars). Data are shown as mean ± SEM (n = 4). c) Effects of mIONPs on cell lipid peroxidation as measured by fluorescent positive cell populations using Liperfluo. Concentrations used for IONP was 78 μg/mL, for Erastin was 1.25 μM. Cumene hydroperoxide (100 μM) was used as positive control.*

4.2.3.2. Effects on macrophage-melanoma co-cultures

In the sections that follow, mIONP-based therapies are evaluated in different murine melanoma B16-F10(OVA) and murine macrophage RAW264.7 co-culture set-ups. Previous research has reported that M2-to-M1 macrophage repolarization is crucial to immunotherapy success [14–16]. Pro-tumoral TAMs constitute a major fraction of the cells found in the TME and take an active role in facilitating tumor growth and in mechanisms of immune suppression [1,13]. Hence, macrophage-melanoma co-cultures offer a closer resemblance to the reality of the TME than cell monocultures. To better elucidate the

effects of mIONPs on macrophage-melanoma dynamics, the two cell lines will be co-cultured maintaining two different degrees of intercellular contact: (i) non-contacting cell co-cultures, where the two cell lines are separated by a membrane but left to communicate through long-distance signalling; and (ii) contacting co-cultures, where close-range cell-to-cell contact is enabled (see Materials and Methods).

B16-F10(OVA) cells are derived from a cell strand known for their distinctively aggressive and low immunogenic character [51,52] and RAW264.7 cells are also one of the most used cell lines for investigating the antitumor effects of macrophages [53]. Anticancer macrophage activation will be estimated by quantifying the production of M1-like immunostimulatory tumor necrosis factor-α (TNF-α) and M2-like immunosuppressive interleukin 10 (IL-10) cytokines [13].

4.2.3.2.1. Non-contacting cell co-cultures

B16-F10-OVA and RAW264.7 cells were co-cultured in separate compartments in a transwell system (Fig. 4.9, a). The cells were separated by a porous membrane (<300nm) that impeded cell-to-cell contact and migration but allowed for long-distance biochemical signalling.

In these conditions, gold-standard chemotherapy drug cisplatin triggered very high rates of macrophage cell death while inducing none-to-low cytotoxicity to cancer cells (Fig. 4.9, b-c). Although treatment with pIC led to high increases in pro-inflammatory TNFα secretion (Fig. 4.9, c), indicative of M1-macrophage polarization, this rendered no effects on cancer cell viability. mIONPs were the only treatment providing for a slight decrease in cancer cell viability, comparable to cisplatin at highest dosage (100 μM) (Fig. 4.9, b), while maintaining macrophage viability. All treatments remained at baseline levels for immunosuppressive IL-10 release (Fig. 4.9, e). Overall, indirect co-cultures rendered therapeutic effects equivalent to monocultures.

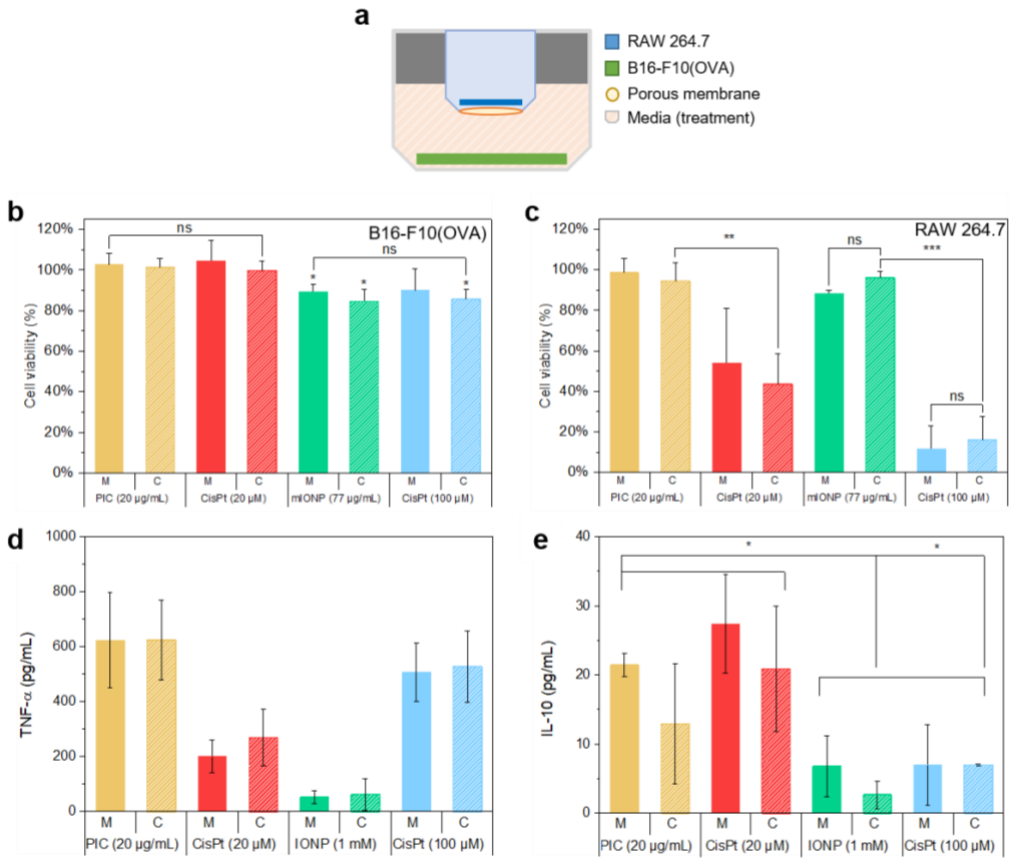

Figure 4.9. Distant cancer and immune cell co-culture limits the therapeutic action of mIONP treatments*. (a) Schematic representation of B16-F10(OVA) and RAW 264.7 transmembrane co-culture set-up. Comparison of b) B16-F10(OVA) and c) RAW 264.7 cell viability in monoculture (M, solid bars) or transmembrane co-culture (C, stripped bars), represented as subtraction from normalized necrotic cell death triggered upon treatment. TNF-α and IL-10 cytokine levels were measured using commercial ELISA kits (see Materials and Methods).*

4.2.3.2.2. Contacting co-cultures

B16-F10-OVA and RAW264.7 cells were co-cultured in the same well (Fig. 4.10, a). The cells were under direct cell-to-cell contact allowing immediate biochemical signalling and intercellular interaction (see Materials and Methods).

Again, cisplatin triggered very high levels of macrophage cell death but it was unable to induce cytotoxic effects in the melanoma cells (Fig. 4.10, a-b). However, mIONP administration now was able to decrease cell viability to a similar extent in both the cancer cells and the macrophages. Individual treatments of pIC or R837, although immunostimulatory (Fig. 4.10, c), did not affect cell viability. However, pIC-R837

treatment resulted in increased levels of TNFα and cancer cell death without affecting macrophage cell viability. mIONP-pIC-R837 treatments maximized the effects of its individual components, resulting in a synergistic response that killed the cancer cell population retaining high (ca. 70%) macrophage cell viability. Although the pIC-R837 treatment resulted in increased levels of pro-inflammatory TNFα, it also increased the levels of IL-10, a cytokine traditionally considered *immunosuppressive* due to its anti-inflammatory properties (Fig. 4.10, d). Instead, mIONP-pIC-R837 treatment resulted in increased production of TNF-α without increasing IL-10 levels.

These studies showed that the mIONP-pIC-R837 system is more effective inducing anticancer effects under the cell-cell contact interactions that can take place in the TEM. Indeed, the short-lived ROS reactivity cannot survive long distances [54] and direct phagocytotic action by M1-activated macrophages is prevented by the membrane. IONP administration sensitized cancer cells to ferroptosis and synergized with powerful immunostimulatory cocktails to drive macrophage activation for cancer cell cytotoxicity.

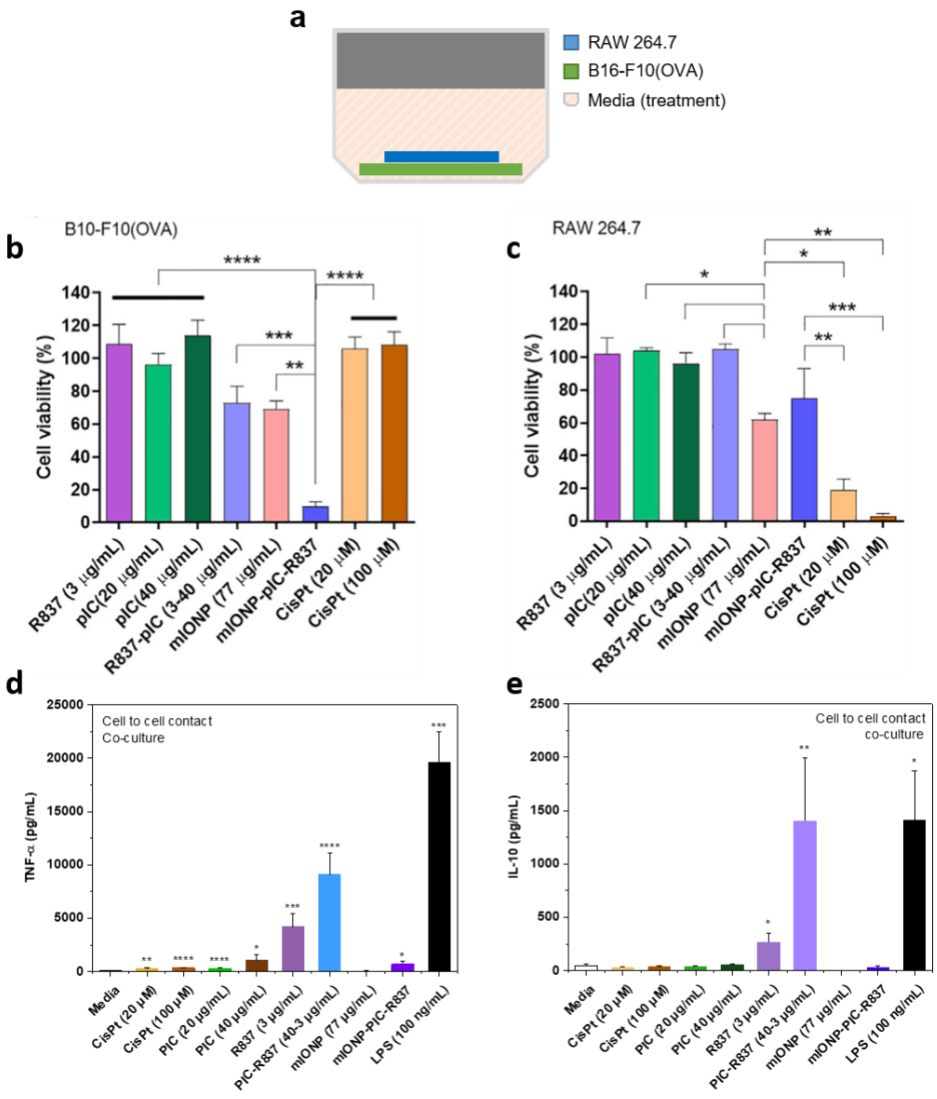

Figure 4.10. Treatments of mIONP-pIC-R837 enable powerful anticancer action leading to tumor cell annihilation. *(a) schematic representation of B16-F10(OVA) and RAW 264.7 direct co-culture set-up. Cell viability was measured by flow cytometry following 24 h treatment. b) B16-F10(OVA) melanoma cells and c) RAW 264.7 macrophages in cell-to-cell contact co-culture approach (77 µg/mL magnetite = 1 mM of [Fe]). Data are shown as mean ± SEM (n = 3). d,e) Cytokine levels elicited upon treatment under cell-to-cell contact co-culture approaches for d) TNF-α and e) IL-10. 77 µg/mL magnetite = 1 mM of Fe. Data are shown as mean ± SEM (n =3). TNF-α and IL-10 cytokine levels were measured using commercial ELISA kits (see Materials and Methods). mIONP-pIC-R837 was administered at concentrations of 77 µg/mL magnetite (1 mM of [Fe]), 40 µg/mL pIC and 3 µg/mL R837.*

4.2.3.3. In Vivo molecular imaging studies and anticancer therapy

Immunostimulatory mIONP-pIC-R837 particles formed and characterized above were administered *in vivo* in combination with various state-of-the-art immunotherapies. These studies were performed by Dr. Ane Ruiz-de-Angulo and Dr. Jordi Llop's research group at CIC biomaGUNE (Spain) [33]. These studies included strategies for:

- **IONP radiolabelling for biodistribution imaging studies:** As discussed in previous chapters, the magnetite core of our mIONPs can be doped with ^{67}Ga radiotracers for IONP biodistribution to be monitored and characterized by non-invasive MRI and PET/SPECT *in vivo* (see Chapter 2) [25].
- **Elucidating the contribution of "stealth" immunomodulatory drug delivery:** Redox catalysed mIONP disassembly will reveal the "stealth" immunostimulatory features of the device (see Chapter 2). As previously discussed, the inner hydrophobic core of our mIONPs can be recognized by the innate immune system as immunostimulatory DAMP [35]. Accessibility to the hydrophobic sites is sought to stimulate the immune system reaction and enhance immunotherapy.
- **IONVs designed to enhance tumor antigen cross presentation by DCs :** In an attempt to expand on the previous work of our group[25], the melanoma B16-F10(OVA) cells used in vivo studies are engineered to express ovalbumin (OVA) as model tumor antigen. Our previous studies showed that OVA-presenting mIONPs nanovaccines (mIONP-OVA) promoted potent OVA-specific antitumor immune responses [25]. Combinations of the mIONP-TLRa systems described above with variations of the mIONP-OVA system (synthetized by our collaborator Dr. Ane Ruiz-De-Angulo in CIC biomaGUNE, Spain) is now studied to optimise the efficacy of these nanovaccines.
- **ICB antibody combination therapies:** B16-F10(OVA) melanomas are known to be PD-L1^{+} (Fig. S4.3) and thus potentially susceptible to anti-PD-L1 ICB therapy. Hence, ICB and IONVs combination therapies are sought to maximize immunotherapy benefits.

4.2.3.3.1. Treatment biodistribution

Previous studies from our group showed that magnetite can accommodate ^{67}Ga radiotracers given the comparable size of Ga(III) and Fe(III) to ions [25]. This process involved the reaction of the radiocation $[^{67}Ga][Ga(H_2O)_6]Cl_3$ (aq.) obtained on-site with mIONPs at 70 °C for 30 min. Following purification by ultracentrifugation, IONP ^{67}Ga-doping could be achieved with very good yield (Fig. 4.11, a-b). The ^{67}Ga-doped mIONPs showed excellent stability, as less than 10% of the bound ^{67}Ga was released over 24 h even when challenged with 10^6-fold molar excess of DOTA chelator (Fig. 4.11, a, c).

Different TLRa-loaded mIONP systems (mIONP-TLRa), including mIONP-pIC-R837, and mIONP-OVA were confirmed to accumulate in the targeted tumor-site as well as in crucial immune cell-rich tissues such as spleen and lymph nodes, indicative of effective lymphatic trafficking, immune cell activation and processing [55] (Fig. 4.11, d-f; S4.2).

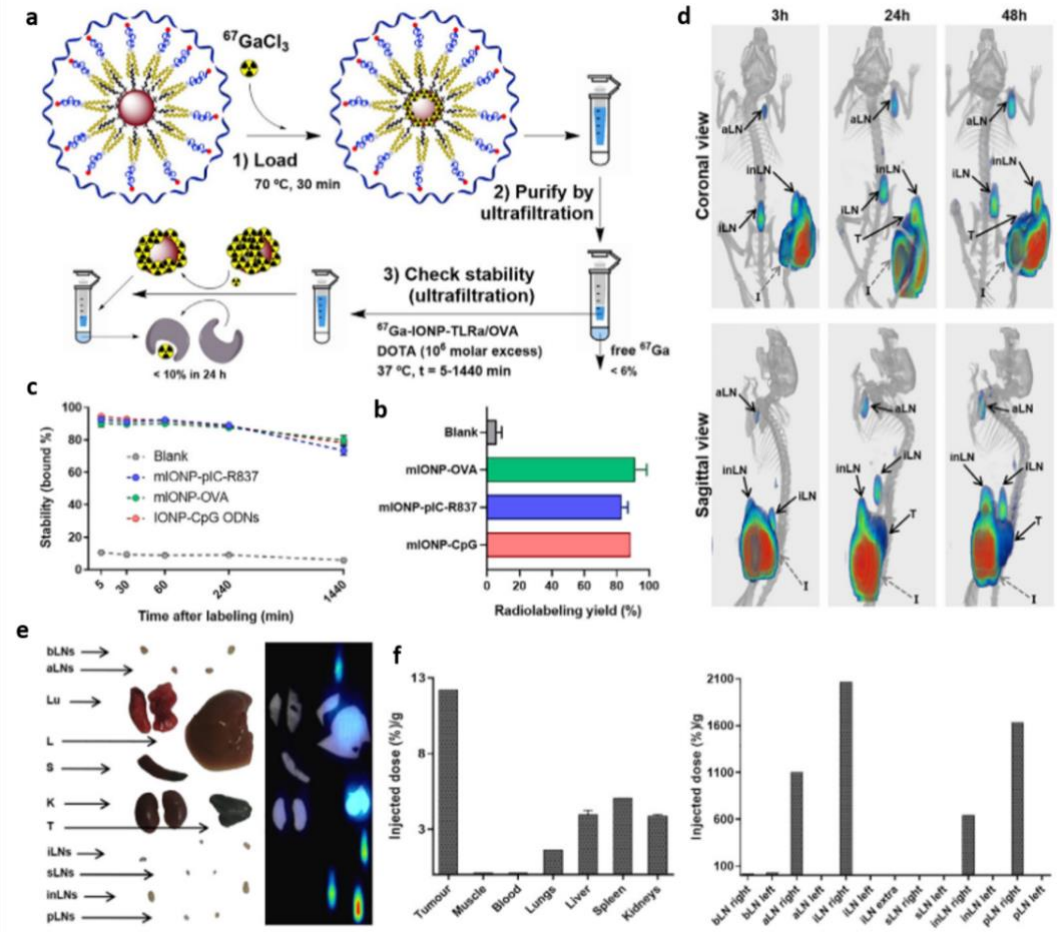

Figure 4.11. Radiolabelling and SPECT/CT tracking of mIONP-TLRa/OVA. *(a-c) The radiocation [^{67}Ga][Ga(H_2O)$_6$]Cl_3(aq.) is loaded by heating with the OVA/TLRa-IONP micelles and following purification by ultrafiltration. (c) The chelator DOTA (in 10^6 molar excess relative to IONP) is able to remove < 10% of the IONP-bound ^{67}Ga over a 24 h period. (d-f) Biodistribution study of ^{67}Ga labeled mIONP-TLRa (23.6 μg of magnetite) injected in the hock of melanoma tumor bearing mice by subcutaneous administration. d) SPECT/CT images 3 h, 24 h and 48 h post injection (coronal and sagittal views). Ex vivo analysis by (e) SPECT/CT and (f) gamma counter 48 h after injection. T, tumor; bLN, brachial LN; aLN, axillary LN; Lu, lungs; L, liver; S, spleen; K, kidneys; iLN, iliac LN; sLN, sciatic LN; inLN, inguinal LN; pLN, popliteal LN; injection site (I). These studies were performed and published with the help of our collaborators in the research institutes of CIC bioGUNE, in Derio (Spain), and CIC biomaGUNE, in Donostia (Spain)* [33].

4.2.3.3.2. "Stealth" DAMP delivery and particle size

To evaluate the effects of "stealth" DAMP delivery by the mIONPs, administration of mIONPs coated with PEG-OMe phospholipids (see Materials and Methods) was

compared to mIONPs coated with more strongly micelle stabilising PEGylated poly(maleic anhydride-alt-1-octadecene) phospholipids (PMAO-PEG) (mIONP-trapped; synthetized by Dr. Ane Ruiz de Angulo, CIC biomaGUNE). The maleic acid-rich structure of the mIONP-trapped coating is expected to form dense, close-packed polymeric micelles [56], thus limiting accessibility to inner hydrophobic sites. mIONP-trapped synthesis followed previously stablished methods of self-assembly through dry film hydration [57].

Indeed, the much more accessible hydrophobic core of mIONPs promoted an enhanced therapeutic response (Fig 4.12, b). mIONPs also provided improved therapeutic response compared to ferumoxytol, which consists of IONPs coated with hydrophilic carboxymethyl-dextran, confirming the importance of the "stealth" hydrophobic IONP coating (Fig. 4.12, c) [58]. Finally, large mIONP particles (mIONP-big; synthetized by Dr. Ane Ruiz de Angulo, CIC biomaGUNE) containing IONP cores of 20 nm instead of 6-7 nm (see Chapter 2) abrogated the therapeutic effects of mIONPs due to inefficient biodistribution (Figure 4.12, b; S4.1) [33].

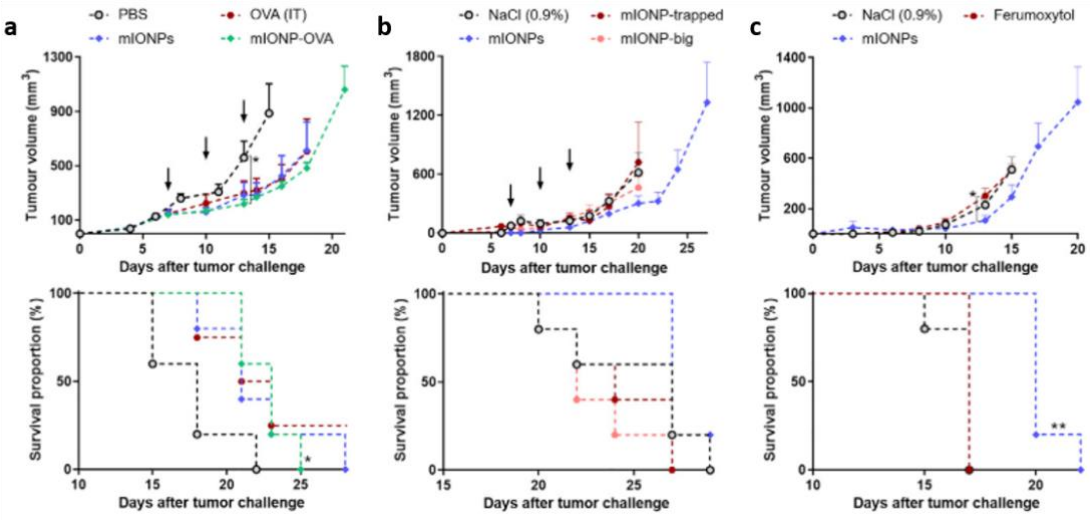

Figure 4.12. In vivo therapeutic effects derived from ''stealth'' hydrophobic IONP coating and size. *C57BL/6 mice (n = 5) were treated on days 7, 10, and 13 after B16-F10(OVA) cells injection in the right back. (a) intrinsic adjuvant activity of mIONP was analyzed by treating animals with 10 mg of OVA antigen alone (IT) or in combination (as protein corona adsorbed by the nanoparticle) with mIONP (SC injection into the hock [ankle]; 61 mg magnetite); (c) nanoparticle size and exposure of coating was studied by injecting animals with different IONP-filled micelle designs (101 mg magnetite)*

peritumorally (SC, 2 cm from tumor); and (c) the effect of IONP coating nature was examined by comparing the co-administration (SC, right back) of B16-F10(OVA) cancer cells with ferumoxytol or mIONPs (12 mg Fe/kg, 332 mg magnetite). (a–c) Results are shown as average tumor growth curves (upper graphs) and Kaplan-Meier survival curves for each case group (lower graphs). Arrows indicate the days of therapy administration. Data are shown as mean ± SEM. These studies were performed and published with the help of our collaborators in the research institutes of CIC bioGUNE, in Derio (Spain), and CIC biomaGUNE, in Donostia (Spain) [33].

4.2.3.3.3. Antigen cross-presentation and immunostimulatory improvement by IONVs

As previously discussed, ROS-mediated endosome destabilization in activated DCs can facilitate antigen release for cross-presentation improving the activation of CD8+ cytotoxic T cells [19]. Hence, it is reasonable that the peroxidative-like features of the IONP could be contributing to the improved DC activation and enhanced CD8+ cytotoxic T cell responses achieved by previous mIONP-OVA systems [25]. These new *in vivo* studies show that the mIONP-OVA system improves the therapeutic outcomes, even that mIONP alone is as effective as intratumorally administered OVA-antigen (Fig. 4.12, a). IONVs were shown to elicit long-term adaptive immunity as shown by increased OVA antigen presentation by immune cells as well as increased TNFα and IFNγ production (Fig. S4). To investigate the importance of the antigen attachment mode, mice were treated with IONVs based on OVA adsorbed to the mIONPs as a corona (mIONP-OVA(ads)) and its covalent conjugation by hydrazone linkages (mIONP-OVA(hyd)). Hydrazones are moieties sensitive to the pH of endolysosomes and thus used for site-specific drug-delivery [59] (see Chapter I). Although co-administration with adjuvant mIONP-polyIC-R837 for both mIONP-OVA(ads) or mIONP-OVA(hyd) significantly suppressed tumor growth (Fig. 4.13, a), only mice in the mIONP-OVA(hyd)-treated group achieved complete tumor regression (CR 40%) (Fig. 4.13, b-c). These findings reveal that hydrazone bioconjugation chemistry optimizes therapeutic immune responses to the IONVs. Having established these therapeutic IONV features, other biocompatible nanoparticles like AuNPs were considered as they had been previously used for nanovaccine development [60]. PEI is a well-studied cationic polymer shown to promote diverse immunostimulatory mechanisms, including the triggering of adjuvant "danger signals" and ROS [61,62]. Our group developed PEI-modified AuNPs

suitable for capturing the anionic polyIC-R837 adjuvant (Au@PEI-pIC-R837; synthetized by Dr. Ane Ruiz de Angulo, CIC biomaGUNE) by exploiting PEI´s positive charge. The AuNPs@PEI-polyIC-R837 complexes had an optimal size for effective lymphatic delivery [33]. However, AuNP@PEI- polyIC-R837 complexes were not able to replicate the adjuvant effects of mIONP-polyIC-R837 in neither average tumor growth decrease (4.13, a, c) nor survival rates (4.13, b). Hence, these findings highlight the intrinsic contributions to therapy arising from the IONP core. As it was observed in sections above, PEI-coated gold nanoparticles displayed little peroxidative activity in comparison to the IONP (Fig. 4.5).

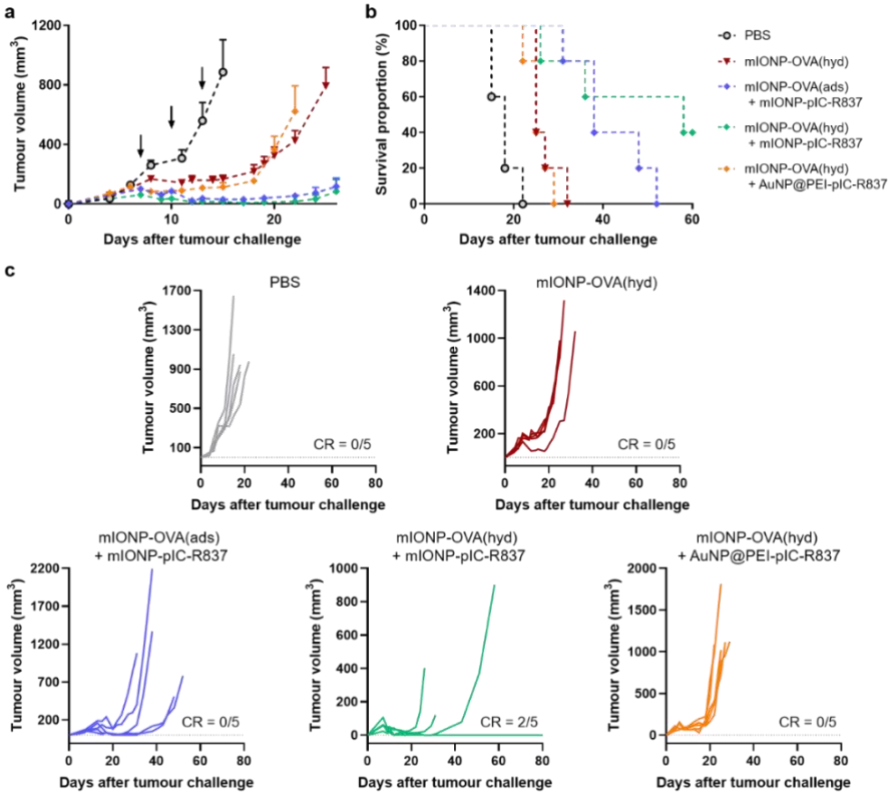

Figure 4.13. Therapeutic contribution of adjuvant "stealth" material and optimized antigen nanoparticle attachment. *C57BL/6 mice (n = 5) treated after B16-F10(OVA) cells injection in the right back with OVA protein adsorbed onto mIONPs (mIONP-OVA(ads)) or conjugated to mIONP by hydrazone linkages (mIONP-OVA(hyd)), either alone or co-administered with adjuvants (mIONP-pIC-R837 or AuNP@PEI-pIC-R837). (a) Average tumor growth, (b) Kaplan-Meier survival plot and (c) individual tumor growth curves. CR: complete regression. Arrows indicate the days (day 7, 10 and 13) of therapy administration. Data are shown as mean ± SEM. These studies were performed and published with the help of our collaborators in the research institutes of CIC bioGUNE, in Derio (Spain), and CIC biomaGUNE, in Donostia (Spain)* [33].

4.2.3.3.4. State-of-the-art ICB combination therapy synergies

ICB immunotherapies have recently emerged as a relevant pillar of cancer treatment. As discussed above, the blockade of the inhibitory PD-L1/PD-1 checkpoint offers crucial means to "release the brake" of T-cell activity in the TME. Immunotherapy-activated T-cells secrete IFN-γ, which promotes tumor cell lipid peroxidation and sensitizes tumors to ferroptosis [63]. Hence, targeting ferroptosis offers a new perspective for ICB immunotherapy improvement. Also, new generations of ICB therapies have moved to integrate agents that can stimulate and promote activation pathways to boost antitumor immunity [64]. In this context, agonistic anti-OX40 antibodies (aOX40) are being evaluated as means to favor $CD8^+$ T-cell expansion while inhibiting immunosuppressive Tregs [65,66]. Immunotherapies that simultaneously stimulate and deactivate suppressing mechanisms of the immune system system have reported very promising benefits in the clinic (see Chapter I) [67,68]. On the basis of these studies, we explored the combination of IONVs with an antagonistic anti-PD-L1 (aPD-L1) and aOX40 antibodies.

To confirm the expression of OX40 and PD-L1 in the TME, aPD-L1 and aOX40 monoclonal antibodies were radiolabeled with ^{89}Zr following previously stablished methods using p-isothiocyanatobenzyl-desferrioxamine chelators [69]. ^{89}Zr-immuno-positron emission tomography (PET) imaging revealed high uptake of both radiolabeled antibodies in the tumor and in the spleen (Fig. S4.3), thus suggesting susceptibility to the combination immunotherapy.

To study the eradication of established melanoma tumors, mice were treated with IONVs, and, on days 1 and 4 after each vaccination, with aPD-L1 administered (100 mg) intraperitoneally. Although IONVs alone induced delayed tumor growth, all mice eventually developed the tumor. However, when IONVs were combined with the aPD-L1 treatment, 40% of mice remained tumor-free after 90 days (Fig. 4.14, a-c). To evaluate the efficacy of IONVs in combination with aOX40 antibodies against stablished tumors, mice were co-treated with an ultra-low dose of aOX40 antibody (10 mg) intratumorally and the IONVs administered subcutaneously at a tumor-distant site. Again, the results show complete tumor regression for 20% of the mice (4.14, b) and significantly reduced tumor growth (4.14, a, c) compared to monotherapy or aOX40 and aPD-L1 combination controls. In addition, the surviving mice populations acquired long-term protection

against tumor rechallenge (90 days after first tumor challenge) and remained tumor-free for 30 days (Fig 4.14, d-e). It is reasonable to consider that complete IONV, aPD-L1 and aOX40 combination therapies could provide even better results.

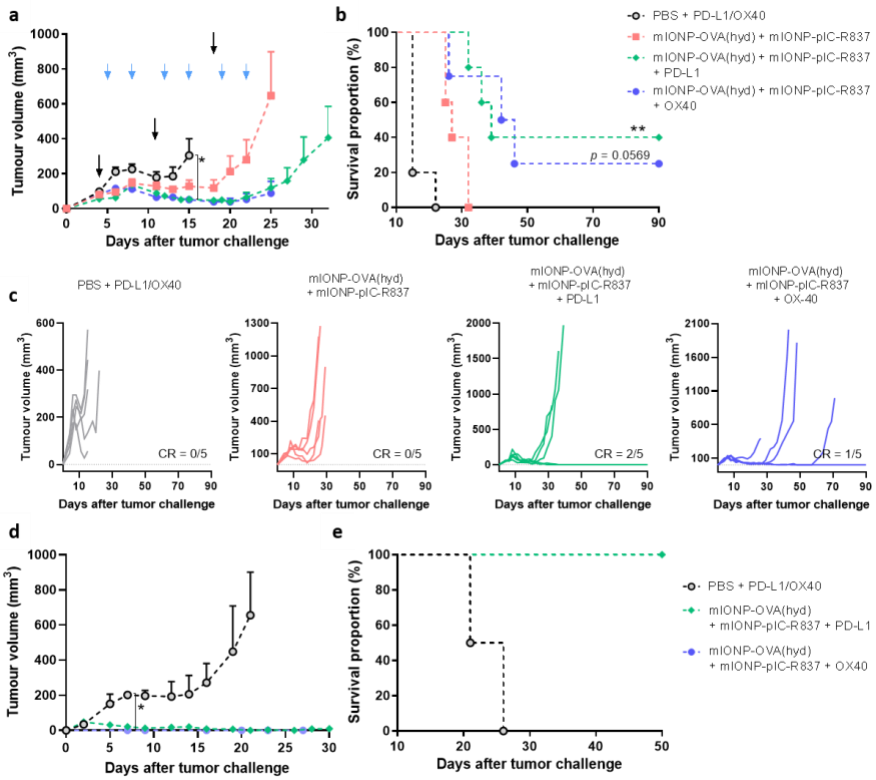

Figure 4.14. Synergistic combination of IONV treatment with state-of-the-art ICB therapies. *C57BL/6 mice (n = 5) were inoculated with 3 × 10^5 B16-F10(OVA) cells and treated with nanovaccines (10 μg of OVA, 4 μg of pIC, and 2 μg of R837; 42 μg of magnetite) on days 4, 11, and 18. 100 μg of anti-PD-L1 and 10 μg of anti-OX40 were administered on days 1 and 4 after each immunization. (a) Average tumor growth, (b) Kaplan-Meier survival plot, and (c) individual tumor growth curves. (d) Average tumor growth and (e) Kaplan-Meier survival plot following re-challenge of melanoma cells in the contralateral back of cured mice. CR, complete regression. Arrows indicate the days of nanovaccines (black) and checkpoint inhibitors (blue) administration. Data are shown as mean ± SEM. These studies were performed and published with the help of our collaborators in the research institutes of CIC bioGUNE, in Derio (Spain), and CIC biomaGUNE, in Donostia (Spain)* [33].

4.3. Conclusions

The work in this chapter is indicative of how IONV engineering offers feasible means to unite and synergise concurrently state-of-the-art strategies for cancer immunotherapy. IONV features that contributed to therapy enhancement can be itemized to rationalize further approaches of optimization. In summary:

- Positively charged mIONP-TAP suspensions were formed using well-stablished dry film hydration methods. Through electrostatic self-assembly strategies, mIONP-TAP could capture and deliver potent pIC and R837 immunotherapy TLRa cocktails. The resulting mIONP-pIC-R837 demonstrated optimal size and stability for systemic administration *in vivo*. The magnetite structure allows radiolabelling through Ga(III) doping for non-invasive SPECT studies, which confirmed that IONP-based treatments accumulated into the tumor and other key immunological sites (spleen and lymph nodes).
- The IONP core showed strong peroxidase-like activity. Its administration *in vitro* was shown to induce membrane lipid hydroperoxide accumulation and cancer-specific sensitization to cell death induction by oxidative damage and ferroptosis whilst remaining well-tolerated by macrophages.
- In cancer cell-macrophage co-cultures, the mIONP enhanced macrophage activation for antitumor cytotoxicity and synergized with potent TLRa adjuvants culminating in cancer cell killing efficacy that was near 100% while retaining high (ca. 70%) macrophage viability. mIONP-pIC-R837 treatments induced the release of immunostimulatory TNFα while maintaining baseline levels of immunosuppressive IL-10, thus indicating M1-like macrophage activation. In sharp contrast, widely-used chemotherapy drug cisplatin killed the macrophage cell population without compromising the melanoma cell viability.
- Iron catalysis offers the possibility to induce site-specific mIONP breakdown, ROS and “stealth” DAMP delivery. Indeed, the absence of hydrophobicity and limited peroxidative-like properties of ferumoxytol or Au@PEI NPs failed to reproduce the therapeutic benefits of mIONPs.
- Our results suggest that IONP-enabled peroxidase-like activity and smart pH-responsive hydrazone bioconjugation can provide enhanced antigen delivery and

cross-presentation. The studies showed increased immune cell maturation and cytotoxic cytokine signalling.

- IONV synergized with suboptimal state-of-the-art ICB therapies achieving complete cancer regression and long-lasting immunity protection against rechallenge.

Our findings demonstrate the suitability of our chemically programmable IONVs to act as generalizable platforms for effective cancer immunotherapy

4.4. Supporting information

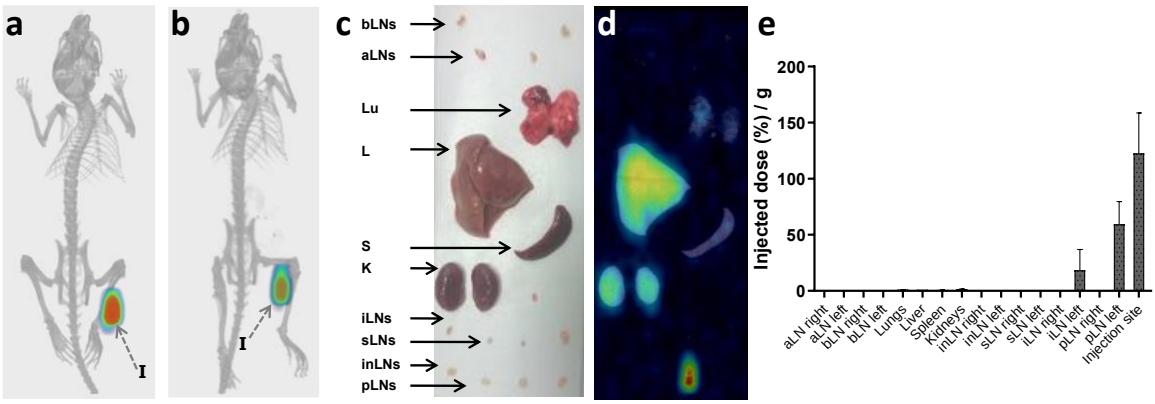

Figure S4.1. Changes in IONP size affect vaccine biodistribution. *C57BL/6 mice (n = 2) were administered with mIONP-big micelles (9.2 µg of magnetite) subcutaneously in the left hock. SPECT/CT images of representative mouse (a) 3 h and (b) 24 h after injection. (c) Photograph of selected harvested organs, (d) SPECT/CT images of the extracted organs and (e) biodistribution expressed as injected dose percentage per gram of tissue. bLN, brachial LN; aLN, axillary LN; Lu, lungs; L, liver; S, spleen; K, kidneys; iliac LN; sLN, sciatic LN; inLN, inguinal LN; pLN, popliteal LN; injection site (I). Image extracted from* [33].

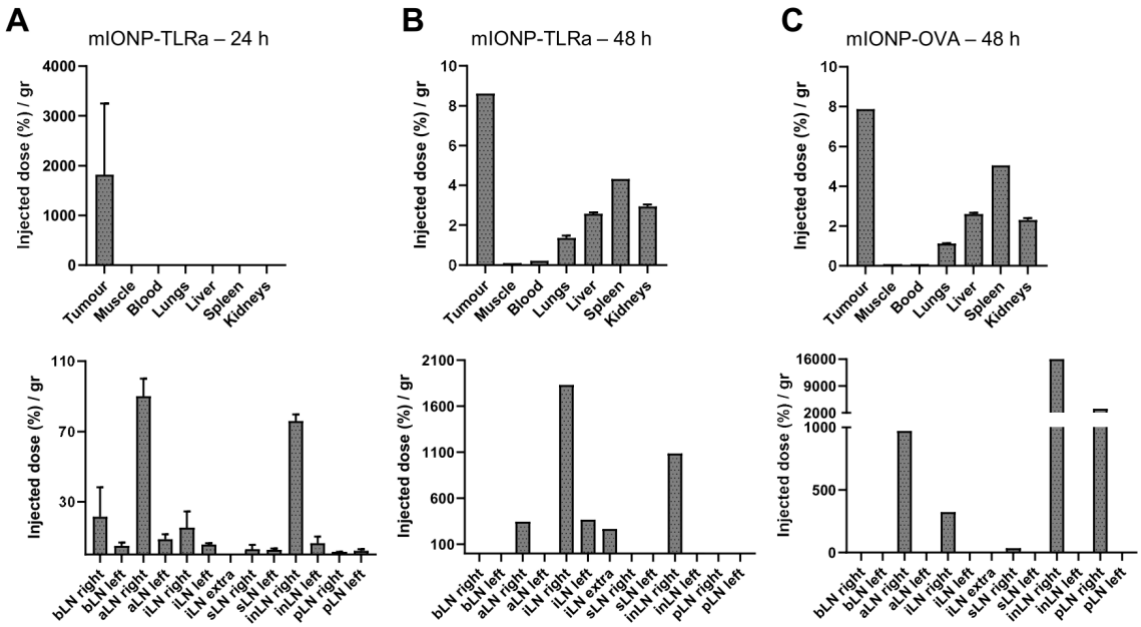

Figure S4.2. Biodistribution analysis of differently functionalized nanovaccines administered subcutaneously in tumor bearing mice*. (a) mIONP-pIC-R837 micelles administered peritumorally (4.68 µg of magnetite) and analyzed after 24 h; (b) mIONP-CpG micelles injected in the right flank (23.6 µg of magnetite, 48 h); and (c) mIONP-OVA micelles injected in the right hind limb (hock, 15.6 µg of magnetite, 48h). bLN, brachial LN; aLN, axillary LN; iLN, iliac LN; sLN, sciatic LN; inLN, inguinal LN; pLN, popliteal LN. Image extracted from* [33].

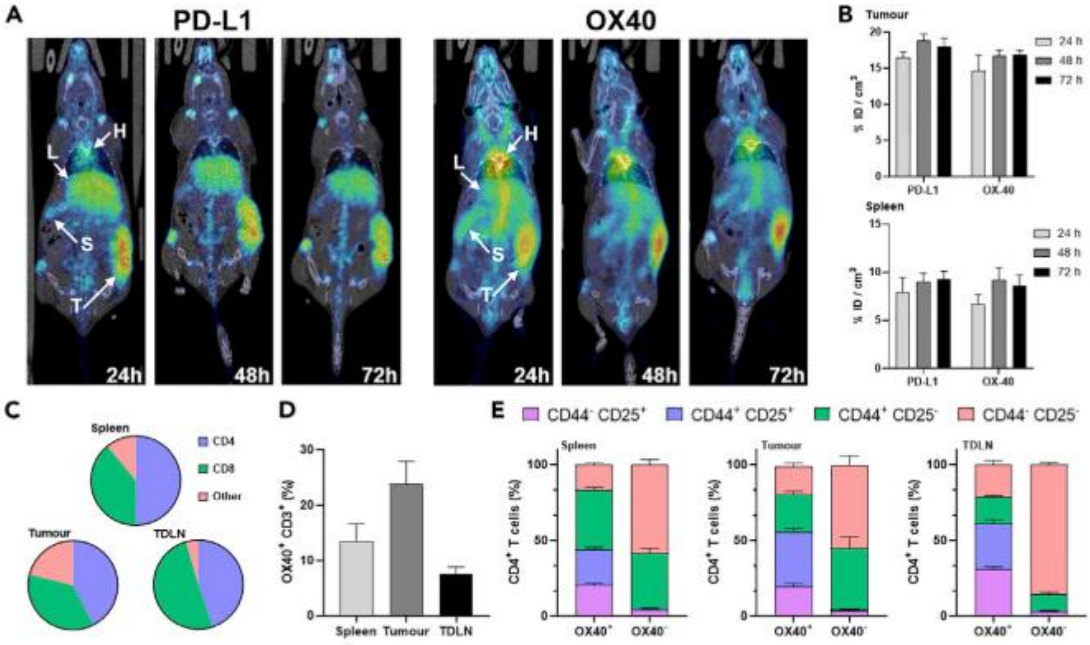

Figure S4.3. In vivo detection PD-L1 and OX40 immune receptors expression by immuno-PET imaging and subsequent analysis of infiltrating immune cells allowed characterization of TME status *(a) PET images were acquired 24, 48, and 72 h after administration of the radiolabeled anti-PD-L1 and anti-OX40 antibodies (80–100 mg). (b–e) (c) Antibody accumulation in tumor and spleen expressed as injected dose percentage per cm^3 (% ID/cm^3). Analysis of immune cells phenotype found in the spleen, TME and TDLN: (C) CD4$^+$ and CD8$^+$ T cell percentages, (d) OX40$^+$ T cell percentages, and (e) activation profile of CD4$^+$OX40$^+$ T cells. Data are shown as mean ± SEM (n = 7). Image extracted from* [33].

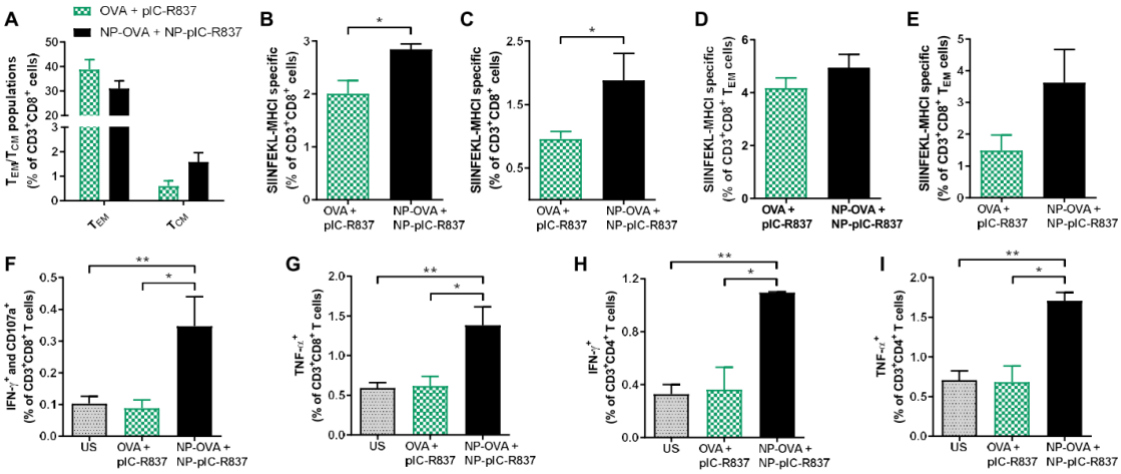

Figure S4.4. Long-term adaptive immune response elicited by nanovaccines. *C57BL/6 female mice (n = 5) were subcutaneously immunized with 5 µg of OVA, 12 µg of polyIC, 4 µg of R837 alone or adsorbed to mIONPs on day 0 and 14 and, on day 21 were challenged with 3 x 105 B16-F10(OVA) cells. On day 84 after first immunization, animals were rechallenged with melanoma cells in the contralateral side. Six weeks later, mice were sacrificed, and blood and spleens were collected for further immune analysis. A) Effector (TEM) and central memory (TCM) CD8$^+$ T cell percentages in spleen. SIINFEKL-specific (B, C) CD8$^+$ and (D, E) TEM cells in (B, D) spleen and (C, E) blood. (F-I) Intracellular IFN-γ and TNF-α production and CD107a expression in (F, G) CD8$^+$ and (H, I) CD4$^+$ T cells after 5 h of incubation with 10 µg/mL of SIINFEKL peptide. Image extracted from* [33].

4.5. References

(1) Galon, J.; Bruni, D. Approaches to Treat Immune Hot, Altered and Cold Tumours with Combination Immunotherapies. *Nat. Rev. Drug Discov.* **2019**, *18* (3), 197–218. https://doi.org/10.1038/s41573-018-0007-y.

(2) Quail, D. F.; Joyce, J. A. Microenvironmental Regulation of Tumor Progression and Metastasis. *Nat. Med.* **2013**, *19* (11), 1423–1437. https://doi.org/10.1038/nm.3394.

(3) Vaupel, P.; Multhoff, G. Accomplices of the Hypoxic Tumor Microenvironment Compromising Antitumor Immunity: Adenosine, Lactate, Acidosis, Vascular Endothelial Growth Factor, Potassium Ions, and Phosphatidylserine. *Front. Immunol.* **2017**, *8* (DEC), 1887. https://doi.org/10.3389/fimmu.2017.01887.

(4) Mou, Y. et al. Ferroptosis, a New Form of Cell Death: Opportunities and Challenges in Cancer. *J. Hematol. Oncol.* **2019**, *12* (1), 34. https://doi.org/10.1186/s13045-019-0720-y.

(5) Rodriguez-Ruiz, M. E.; Vitale, I.; Harrington, K. J.; Melero, I.; Galluzzi, L. Immunological Impact of Cell Death Signaling Driven by Radiation on the Tumor Microenvironment. *Nat. Immunol.* **2020**, *21* (2), 120–134. https://doi.org/10.1038/s41590-019-0561-4.

(6) Zhou, Y. et al. Iron Overloaded Polarizes Macrophage to Proinflammation Phenotype through ROS/Acetyl-P53 Pathway. *Cancer Med.* **2018**, *7* (8), 4012–4022. https://doi.org/10.1002/cam4.1670.

(7) Pal, R. et al. Noble Metal Nanoparticle-Induced Oxidative Stress Modulates Tumor Associated Macrophages (TAMs) from an M2 to M1 Phenotype: An in Vitro Approach. *Int. Immunopharmacol.* **2016**, *38*, 332–341. https://doi.org/10.1016/j.intimp.2016.06.006.

(8) Shi, C. et al. Reprogramming Tumor-Associated Macrophages by Nanoparticle-Based Reactive Oxygen Species Photogeneration. *Nano Lett.* **2018**, *18* (11), 7330–7342. https://doi.org/10.1021/acs.nanolett.8b03568.

(9) Liu, L. et al. ROS-Inducing Micelles Sensitize Tumor-Associated Macrophages to TLR3 Stimulation for Potent Immunotherapy. *Biomacromolecules* **2018**, *19* (6), 2146–2155. https://doi.org/10.1021/acs.biomac.8b00239.

(10) Yang, B.; Chen, Y.; Shi, J. Reactive Oxygen Species (ROS)-Based Nanomedicine. *Chemical Reviews*. American Chemical Society April 24, 2019, pp 4881–4985. https://doi.org/10.1021/acs.chemrev.8b00626.

(11) Zhang, F. et al. Engineering Magnetosomes for Ferroptosis/Immunomodulation Synergism in Cancer. *ACS Nano* **2019**, *13* (5), 5662–5673. https://doi.org/10.1021/acsnano.9b00892.

(12) Zou, Z.; Chang, H.; Li, H.; Wang, S. Induction of Reactive Oxygen Species: An

Emerging Approach for Cancer Therapy. *Apoptosis* **2017**, *22* (11), 1321–1335. https://doi.org/10.1007/s10495-017-1424-9.

(13) Sica, A. et al. Macrophage Polarization in Tumour Progression. *Seminars in Cancer Biology*. 2008, pp 349–355. https://doi.org/10.1016/j.semcancer.2008.03.004.

(14) Lian, G. et al. Colon Cancer Cell Secretes EGF to Promote M2 Polarization of TAM Through EGFR/PI3K/AKT/MTOR Pathway. *Technol. Cancer Res. Treat.* **2019**, *18*. https://doi.org/10.1177/1533033819849068.

(15) Zhang, F. et al. TGF-β Induces M2-like Macrophage Polarization via SNAILmediated Suppression of a pro-Inflammatory Phenotype. *Oncotarget* **2016**, *7* (32), 52294–52306. https://doi.org/10.18632/oncotarget.10561.

(16) Kohno, K. et al. Inflammatory M1-like Macrophages Polarized by NK-4 Undergo Enhanced Phenotypic Switching to an Anti-Inflammatory M2-like Phenotype upon Co-Culture with Apoptotic Cells. *J. Inflamm. (United Kingdom)* **2021**, *18* (1), 1–14. https://doi.org/10.1186/s12950-020-00267-z.

(17) Qi, Y.; Yan, X.; Xia, T.; Liu, S. Use of Macrophage as a Trojan Horse for Cancer Nanotheranostics. *Mater. Des.* **2021**, *198*, 109388. https://doi.org/10.1016/j.matdes.2020.109388.

(18) Chen, Y. et al. Tumor-Associated Macrophages: An Accomplice in Solid Tumor Progression. *J. Biomed. Sci.* **2019**, *26* (1), 1–13. https://doi.org/10.1186/s12929-019-0568-z.

(19) Dingjan, I. et al. Lipid Peroxidation Causes Endosomal Antigen Release for Cross-Presentation. *Sci. Rep.* **2016**, *6* (1), 22064. https://doi.org/10.1038/srep22064.

(20) Saeed, M.; Ren, W.; Wu, A. Therapeutic Applications of Iron Oxide Based Nanoparticles in Cancer: Basic Concepts and Recent Advances. *Biomater. Sci.* **2018**, *6* (4), 708–725. https://doi.org/10.1039/c7bm00999b.

(21) Gao, L.; Fan, K.; Yan, X. Iron Oxide Nanozyme: A Multifunctional Enzyme Mimetic for Biomedical Applications. *Theranostics* **2017**, *7* (13), 3207–3227. https://doi.org/10.7150/thno.19738.

(22) Zanganeh, S. et al. Iron Oxide Nanoparticles Inhibit Tumour Growth by Inducing Pro-Inflammatory Macrophage Polarization in Tumour Tissues. *Nat. Nanotechnol.* **2016**, *11* (11), 986–994. https://doi.org/10.1038/nnano.2016.168.

(23) da Silva, M. C. et al. Iron Induces Anti-Tumor Activity in Tumor-Associated Macrophages. *Front. Immunol.* **2017**, *8* (NOV), 1479. https://doi.org/10.3389/fimmu.2017.01479.

(24) Laskar, A.; Eilertsen, J.; Li, W.; Yuan, X. M. SPION Primes THP1 Derived M2 Macrophages towards M1-like Macrophages. *Biochem. Biophys. Res. Commun.*

2013, *441* (4), 737–742. https://doi.org/10.1016/j.bbrc.2013.10.115.

(25) Ruiz-De-Angulo, A.; Zabaleta, A.; Gómez-Vallejo, V.; Llop, J.; Mareque-Rivas, J. C. Microdosed Lipid-Coated 67Ga-Magnetite Enhances Antigen-Specific Immunity by Image Tracked Delivery of Antigen and Cpg to Lymph Nodes. *ACS Nano* **2016**, *10* (1), 1602–1618. https://doi.org/10.1021/acsnano.5b07253.

(26) Hernández-Gil, J. et al. An Iron Oxide Nanocarrier Loaded with a Pt(IV) Prodrug and Immunostimulatory DsRNA for Combining Complementary Cancer Killing Effects. *Adv. Healthc. Mater.* **2015**, *4* (7), 1034–1042. https://doi.org/10.1002/adhm.201500080.

(27) Traini, G. et al. Cancer Immunotherapy of TLR4 Agonist–Antigen Constructs Enhanced with Pathogen-Mimicking Magnetite Nanoparticles and Checkpoint Blockade of PD-L1. *Small* **2019**, *15* (4). https://doi.org/10.1002/smll.201803993.

(28) Peng, W. et al. PD-1 Blockade Enhances T-Cell Migration to Tumors by Elevating IFN-γ Inducible Chemokines. *Cancer Res.* **2012**, *72* (20), 5209–5218. https://doi.org/10.1158/0008-5472.CAN-12-1187.

(29) Chen, H. et al. Anti-CTLA-4 Therapy Results in Higher CD4 +ICOS Hi T Cell Frequency and IFN-γ Levels in Both Nonmalignant and Malignant Prostate Tissues. *Proc. Natl. Acad. Sci. U. S. A.* **2009**, *106* (8), 2729–2734. https://doi.org/10.1073/pnas.0813175106.

(30) Zitvogel, L.; Kroemer, G. Interferon-γ Induces Cancer Cell Ferroptosis. *Cell Res.* **2019**, *29* (9), 692–693. https://doi.org/10.1038/s41422-019-0186-z.

(31) Stockwell, B. R.; Jiang, X. A Physiological Function for Ferroptosis in Tumor Suppression by the Immune System. *Cell Metab.* **2019**, *30* (1), 14–15. https://doi.org/10.1016/j.cmet.2019.06.012.

(32) Wang, W. et al. CD8+ T Cells Regulate Tumour Ferroptosis during Cancer Immunotherapy. *Nature* **2019**, *569* (7755), 270–274. https://doi.org/10.1038/s41586-019-1170-y.

(33) Ruiz-de-Angulo, A. et al. Chemically Programmed Vaccines: Iron Catalysis in Nanoparticles Enhances Combination Immunotherapy and Immunotherapy-Promoted Tumor Ferroptosis. *iScience* **2020**, *23* (9). https://doi.org/10.1016/j.isci.2020.101499.

(34) Szatrowski, T. P.; Nathan, C. F. Production of Large Amounts of Hydrogen Peroxide by Human Tumor Cells. *Cancer Res.* **1991**, *51* (3), 794–798.

(35) Seong, S. Y.; Matzinger, P. Hydrophobicity: An Ancient Damage-Associated Molecular Pattern That Initiates Innate Immune Responses. *Nature Reviews Immunology*. Nature Publishing Group 2004, pp 469–478. https://doi.org/10.1038/nri1372.

(36) Hernandez, C.; Huebener, P.; Schwabe, R. F. Damage-Associated Molecular

Patterns in Cancer: A Double-Edged Sword. *Oncogene* **2016**, *35* (46), 5931–5941. https://doi.org/10.1038/onc.2016.104.

(37) Tan, H. Y. et al. The Reactive Oxygen Species in Macrophage Polarization: Reflecting Its Dual Role in Progression and Treatment of Human Diseases. *Oxid. Med. Cell. Longev.* **2016**, *2016*, 1–16. https://doi.org/10.1155/2016/2795090.

(38) Mac Cheever, M. A. Twelve Immunotherapy Drugs That Could Cure Cancers. *Immunol. Rev.* **2008**, *222* (1), 357–368. https://doi.org/10.1111/j.1600-065X.2008.00604.x.

(39) Napolitani, G.; Rinaldi, A.; Bertoni, F.; Sallusto, F.; Antonio, L. Selected TLR Agonist Combinations Synergistically Trigger a TH1 Polarizing Program in Dendritic Cells. *Nat. Immunol.* **2005**, *6* (8), 769–776. https://doi.org/10.1038/ni1223.Selected.

(40) Bianchi, F.; Pretto, S.; Tagliabue, E.; Balsari, A.; Sfondrini, L. Exploiting Poly(I:C) to Induce Cancer Cell Apoptosis. *Cancer Biol. Ther.* **2017**, *18* (10), 747–756. https://doi.org/10.1080/15384047.2017.1373220.

(41) Hu, Y. et al. Synergy of TLR3 and 7 Ligands Significantly Enhances Function of DCs to Present Inactivated PRRSV Antigen through TRIF/MyD88-NF-KB Signaling Pathway. *Sci. Rep.* **2016**, *6* (1), 23977. https://doi.org/10.1038/srep23977.

(42) Cobaleda-Siles, M. et al. An Iron Oxide Nanocarrier for DsRNA to Target Lymph Nodes and Strongly Activate Cells of the Immune System. *Small* **2014**, *10* (24), 5054–5067. https://doi.org/10.1002/smll.201401353.

(43) Bocanegra Gondan, A. I. et al. Effective Cancer Immunotherapy in Mice by PolyIC-Imiquimod Complexes and Engineered Magnetic Nanoparticles. *Biomaterials* **2018**, *170*, 95–115. https://doi.org/10.1016/j.biomaterials.2018.04.003.

(44) Ma, F.; Zhang, J.; Zhang, J.; Zhang, C. The TLR7 Agonists Imiquimod and Gardiquimod Improve DC-Based Immunotherapy for Melanoma in Mice. *Cell. Mol. Immunol.* **2010**, *7* (5), 381–388. https://doi.org/10.1038/cmi.2010.30.

(45) Huang, S. W. et al. Imiquimod Activates P53-Dependent Apoptosis in a Human Basal Cell Carcinoma Cell Line. *J. Dermatol. Sci.* **2016**, *81* (3), 182–191. https://doi.org/10.1016/j.jdermsci.2015.12.011.

(46) Cho, J. H. et al. *The TLR7 Agonist Imiquimod Induces Anti-Cancer Effects via Autophagic Cell Death and Enhances Anti-Tumoral and Systemic Immunity during Radiotherapy for Melanoma*; 2017; Vol. 8. https://doi.org/10.18632/oncotarget.15326.

(47) Abdalkader, M.; Lampinen, R.; Kanninen, K. M.; Malm, T. M.; Liddell, J. R. Targeting Nrf2 to Suppress Ferroptosis and Mitochondrial Dysfunction in Neurodegeneration. *Front. Neurosci.* **2018**, *12* (JUL).

https://doi.org/10.3389/fnins.2018.00466.

(48) Shan, X. et al. Ferroptosis-Driven Nanotherapeutics for Cancer Treatment. *J. Control. Release* **2020**, *319*, 322–332. https://doi.org/10.1016/j.jconrel.2020.01.008.

(49) Badgley, M. A. et al. Cysteine Depletion Induces Pancreatic Tumor Ferroptosis in Mice. *Science (80-.).* **2020**, *368* (6486), 85–89. https://doi.org/10.1126/science.aaw9872.

(50) Wang, P. et al. Macrophage Achieves Self-Protection against Oxidative Stress-Induced Ageing through the Mst-Nrf2 Axis. *Nat. Commun.* **2019**, *10* (1), 1–16. https://doi.org/10.1038/s41467-019-08680-6.

(51) Danciu, C. et al. Behaviour of Four Different B16 Murine Melanoma Cell Sublines: C57BL/6J Skin. *Int. J. Exp. Pathol.* **2015**, *96* (2), 73–80. https://doi.org/10.1111/iep.12114.

(52) Xu, D. et al. NK and CD8+ T Cell-Mediated Eradication of Poorly Immunogenic B16-F10 Melanoma by the Combined Action of IL-12 Gene Therapy and 4-1BB Costimulation. *Int. J. Cancer* **2004**, *109* (4), 499–506. https://doi.org/10.1002/ijc.11696.

(53) Taciak, B. et al. Evaluation of Phenotypic and Functional Stability of RAW 264.7 Cell Line through Serial Passages. *PLoS One* **2018**, *13* (6). https://doi.org/10.1371/journal.pone.0198943.

(54) Ranji-Burachaloo, H.; Gurr, P. A.; Dunstan, D. E.; Qiao, G. G. Cancer Treatment through Nanoparticle-Facilitated Fenton Reaction. *ACS Nano* **2018**, *12* (12), 11819–11837. https://doi.org/10.1021/acsnano.8b07635.

(55) Perrin, J. et al. Cell Tracking in Cancer Immunotherapy. *Front. Med.* **2020**, *7*, 34. https://doi.org/10.3389/fmed.2020.00034.

(56) Yu, W. W.; Chang, E.; Sayes, C. M.; Drezek, R.; Colvin, V. L. Aqueous Dispersion of Monodisperse Magnetic Iron Oxide Nanocrystals through Phase Transfer. *Nanotechnology* **2006**, *17* (17), 4483–4487. https://doi.org/10.1088/0957-4484/17/17/033.

(57) Moros, M. et al. Engineering Biofunctional Magnetic Nanoparticles for Biotechnological Applications. *Nanoscale* **2010**, *2* (9), 1746–1755. https://doi.org/10.1039/c0nr00104j.

(58) Trujillo-Alonso, V. et al. FDA-Approved Ferumoxytol Displays Anti-Leukaemia Efficacy against Cells with Low Ferroportin Levels. *Nat. Nanotechnol.* **2019**, *14* (6), 616–622. https://doi.org/10.1038/s41565-019-0406-1.

(59) Liu, J. et al. PH-Sensitive Nano-Systems for Drug Delivery in Cancer Therapy. *Biotechnol. Adv.* **2014**, *32* (4), 693–710. https://doi.org/10.1016/j.biotechadv.2013.11.009.

(60) Almeida, J. P. M.; Figueroa, E. R.; Drezek, R. A. Gold Nanoparticle Mediated Cancer Immunotherapy. *Nanomedicine Nanotechnology, Biol. Med.* **2014**, *10* (3), 503–514. https://doi.org/10.1016/j.nano.2013.09.011.

(61) Shen, C. et al. Polyethylenimine-Based Micro/Nanoparticles as Vaccine Adjuvants. *Int. J. Nanomedicine* **2017**, *12*, 5443–5460. https://doi.org/10.2147/IJN.S137980.

(62) Liang, X. et al. Improved Vaccine-Induced Immune Responses: Via a ROS-Triggered Nanoparticle-Based Antigen Delivery System. *Nanoscale* **2018**, *10* (20), 9489–9503. https://doi.org/10.1039/c8nr00355f.

(63) Wang, W. et al. CD8+ T Cells Regulate Tumour Ferroptosis during Cancer Immunotherapy. *Nature* **2019**, *569* (7755), 270–274. https://doi.org/10.1038/s41586-019-1170-y.

(64) Mahoney, K. M.; Rennert, P. D.; Freeman, G. J. Combination Cancer Immunotherapy and New Immunomodulatory Targets. *Nat. Rev. Drug Discov.* **2015**, *14* (8), 561–584. https://doi.org/10.1038/nrd4591.

(65) Aspeslagh, S. et al. Rationale for Anti-OX40 Cancer Immunotherapy. *Eur. J. Cancer* **2016**, *52*, 50–66. https://doi.org/10.1016/j.ejca.2015.08.021.

(66) Linch, S. N.; McNamara, M. J.; Redmond, W. L. OX40 Agonists and Combination Immunotherapy: Putting the Pedal to the Metal. *Front. Oncol.* **2015**, *5* (FEB). https://doi.org/10.3389/fonc.2015.00034.

(67) Gong, J.; Chehrazi-Raffle, A.; Reddi, S.; Salgia, R. Development of PD-1 and PD-L1 Inhibitors as a Form of Cancer Immunotherapy: A Comprehensive Review of Registration Trials and Future Considerations. *J. Immunother. Cancer* **2018**, *6* (1), 8. https://doi.org/10.1186/s40425-018-0316-z.

(68) Messenheimer, D. J. et al. Timing of PD-1 Blockade Is Critical to Effective Combination Immunotherapy with Anti-OX40. *Clin. Cancer Res.* **2017**, *23* (20), 6165–6177. https://doi.org/10.1158/1078-0432.CCR-16-2677.

(69) Vosjan, M. J. W. D. et al. Conjugation and Radiolabeling of Monoclonal Antibodies with Zirconium-89 for PET Imaging Using the Bifunctional Chelate p-Isothiocyanatobenzyl-Desferrioxamine. *Nat. Protoc.* **2010**, *5* (4), 739–743. https://doi.org/10.1038/nprot.2010.13.

Chapter 5 . **Neoantigen-and linoleic acid -presenting IONVs towards immunogenic cancer cell ferroptosis and personalized cancer immunotherapy**

5.1. Introduction

Therapeutic cancer vaccines have seen renewed interest in recent years. Their aim is to induce antitumor cytotoxic immunity and establish long-term protection memory while showing minimal adverse reactions. However, tumor heterogeneity and tumor-induced immunosuppression pose strong challenges to this goal. The patient-specific characteristics of the tumor limits the prediction of generalizable targets for "off the shelf" vaccination. Better understanding on the tumor-immune system dynamics, the identification of new tumor-associated antigens (TAAs) and neoantigen targets, and the development of new drug delivery technologies have improved vaccine design. The improved availability of rapid and cost-effective sequencing, clinical bioinformatics technology and nanotechnology provide new opportunities for the identification, prediction and delivery of immunogenic tumor neoantigens which are highly specific to tumors of individual patients. We reasoned there is considerable potential in combining redox stress-inducing therapies with potential to induce reprogramming of the tumor microenvironment and immunogenic cell death (ICD) with nanovaccines formulated with potent adjuvants and designed to enhance neoantigen processing and presentation. In this chapter, a new generation of mIONPs is developed, which by catalytic oxidative coupling between Fenton chemistry and polyunsaturated fatty acid (PUFA) lipid peroxidation is shown to induce oxidative stress and enhance ferroptosis. These new PUFA-bearing mIONPs are proven to be very effective triggering cell death in a panel of human and murine cancer cell lines *in vitro*. Neoantigen-presenting PUFA-bearing IONVs are developed and characterized. They are created exploiting thiol-maleimide linkages between the INOVs and the peptide neoantigens. These provide proof-of-concept demonstration of the suitability of mIONPs for development of both agents that catalyse ferroptosis and creating peptide-based, personalized neoantigen-based vaccines. The neoantigen vaccines are evaluated *in vivo* in the B16-F10 mouse melanoma model in a preliminary study.

5.1.1. Neoantigen cancer vaccines

The aberrant growth of the cancer tissue results in progressive accumulation of mutations and tumor-associated antigens (TAAs). TAAs are antigens overexpressed in tumors and thus can serve as potential targets for antigen specific cancer immunotherapy. A

subcategory of TAAs are tumor-specific antigens (TSAs) or neoantigens [1], which are unique of the tumor tissue. Thus, the major advantage of creating neoantigen-based vaccines is that they will not be subjected to the immune dampening effects of self-central tolerance or autoimmunity. However, not all antigens are immunogenic - not all antigens can be processed by the immune system to induce an immune response. The tumor mutation burden (TMB) is a recently defined calculation that accounts for the number of mutations per million nucleic acid bases found in the cancerous tissue. Since tumors with higher TMB are more likely to have higher immunogenic TAA and TSA loading, the TMB has been proposed as important predictive biomarker for immunotherapy success [2]. Indeed, upon the accumulation of immunogenic TAAs and TSAs, the immune system surveillance is expected to recognize the malignant tissue and attack it. However, through the process known as immunoediting, the tumor acquires numerous protective mechanisms to contain and overcome cytotoxic immune system reactions [3]. With the progression of the disease, the tumor becomes increasingly heterogeneous and develops cancer type- and patient-specific characteristics. All in all, these processes limit the identification of universal immunogenic targets for generalizable cancer immunotherapy and therapeutic vaccine development.

The increasing potency of bioinformatics and the development of novel nanotechnology approaches enabled a boom in therapeutic cancer vaccine research (Fig. 5.1, a). By pooling large clinical databases, algorithm-based neoantigen identification and prediction provides increasing insights towards the finding of semi-universal neoantigens for "off the shelf" cancer vaccine production. Still, the immunogenicity of the predicted antigen load can be limited by tumor heterogeneity and immunoediting [4,5]. Instead, personalized vaccine approaches are aimed at the identification of highly immunogenic neoantigens directly from the particularities of the patient tumor. However, these strategies can suffer from extended time delay as the process consists of several steps from diagnosis to therapy, including tumor tissue biopsy, neoantigen isolation, vaccine assembly and final vaccination (Fig. 5.1, b) [6]. Therefore, there is a pressing medical need for the development of versatile vaccine scaffolds that can readily accommodate and deliver immunogenic antigens for cancer immunotherapy.

This chapter studies establishes proof-of-concept demonstration of some strategies for using and potentially enhancing the efficacy of iron oxide nanovaccines (IONVs) as

carriers of predicted peptide neoantigens. The study uses the aggressive, poorly immunogenic, and widely used B16-F10 mouse melanoma model for the development of the rationally designed peptide-based neoantigen vaccine [7,8]. B16-M30 and B16-M27 have been identified as two immunogenic neoantigens for B16-F10 melanomas (Fig. 5.1, c-d) [9]. The neoantigen-presenting IONVs are assembled using a click chemistry strategy based on thiol-maleimide linkages, [10] which will be easy to implement with any peptide neoantigen target(s) in future applications (see Chapter 2).

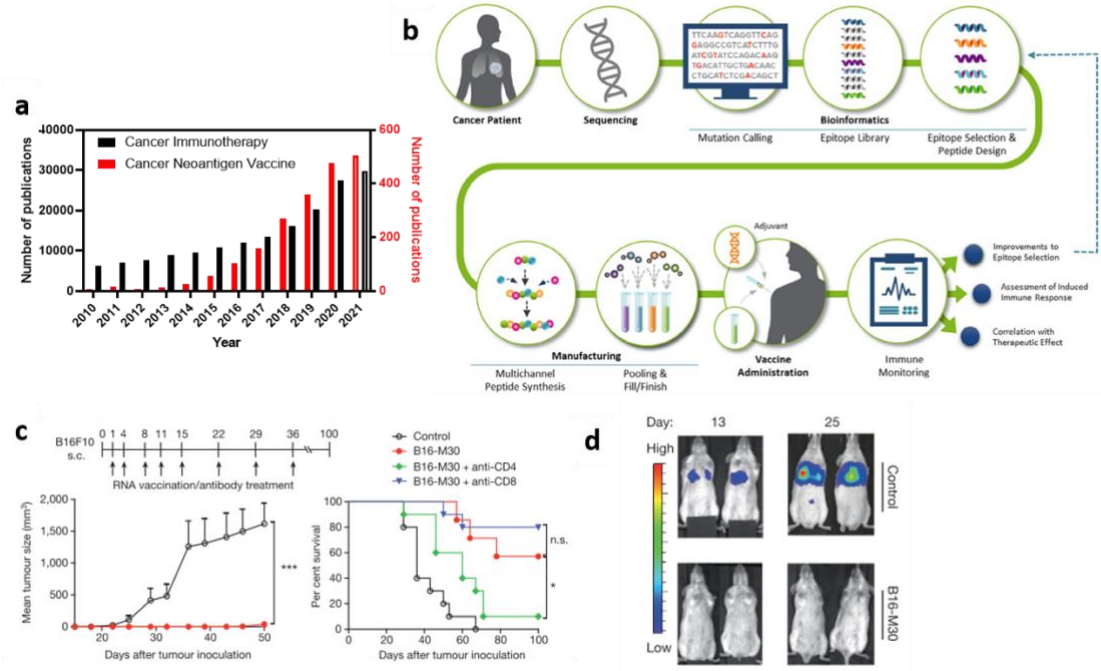

Figure 5.1. Efficient tumor control and survival using cancer neoantigen vaccines. *(a) Interest in cancer neoantigen vaccine research shown as number of scientific publications per year since year 2010. Data as sum of publications (limited to research articles only) registered in Scopus database using keywords: "cancer AND immunotherapy" (black bars) or "neoantigen AND cancer AND vaccine" (red bars). For 2021 data compiled as of 19th October. (b) Workflow diagram for personalized neoantigen peptide vaccine development. (c-d) successful immunization against B16-F10 murine melanoma using neoantigen vaccines showing (c) decreased tumor growth rates and increased survival rates, (d) prevention of lung metastasis. Image (b) extracted from [11]. Images (c-d) extracted from [9].*

5.1.2. Fenton chemistry and PUFA catalytic oxidative coupling

Lipid peroxidation is a reactive oxygen species (ROS)-mediated chain reaction that results in increased lipid unsaturation and degradation. The reaction is initiated by free

electron radical stabilization between π-conjugated polyunsaturated hydrocarbons. Subsequent radical reaction with O_2 yields a lipid peroxyl radical that can further propagate and oxidise the surrounding tissue. Free Fe^{2+} ions and iron oxide nanoparticles (IONPs) can further expand this oxidative reactivity through Fenton chemistry ROS regeneration (Fig. 5.2, a; see Chapter 2) [12,13].

ROS generation has shown key connections with various pathways of intracellular redox stress, cancer cell killing and immunotherapy enhancement. Ferroptosis is ROS- and iron-mediated mechanism of cell death triggered upon the accumulation of irreparable intracellular oxidative damage [14]. Ferroptosis has been reported to offer safer mechanisms of cancer-specific cell death in comparison to classic cancer chemotherapy [15]. Ferroptosis can lead to ICD and release TAA and immunostimulatory damage-associated molecular patterns (DAMP), which can act as an *in situ* tumor vaccine [16–18]. ROS may also serve as "eat me" signals to induce immunogenic phagocytosis, a process by which immune cells can kill and scavenge cancer cells from the tumor-site [18–21]. Indeed, PUFAs have been reported to induce ROS-mediated cancer cell killing through ferroptosis and potentiating cancer immunotherapies [22–24].

Linoleic acid is an essential fatty acid that is readily obtained from vegetable oils, nuts and seeds. It has two π-conjugated double bonds (C18:2, $\Delta^{9,12}$) that facilitate free electron radical stabilization. Linoleic acid has been shown to enhance intracellular lipid peroxidation rates resulting in cancer cell mitochondrial dysfunction, chemotherapy enhancement and increased cancer cell death (Fig. 5.2, b-c) [24–26]. In previous chapters, catalytic IONP Fenton chemistry has been demonstrated to enhance cancer therapies through cancer-specific oxidative damage, increased macrophage cytotoxic activation and improved antigen cross-presentation mechanisms [27]. In this chapter, IONP Fenton chemistry will be coupled to linoleoyl lipid peroxidation as a boost for tumor ICD and IONVs immunotherapies.

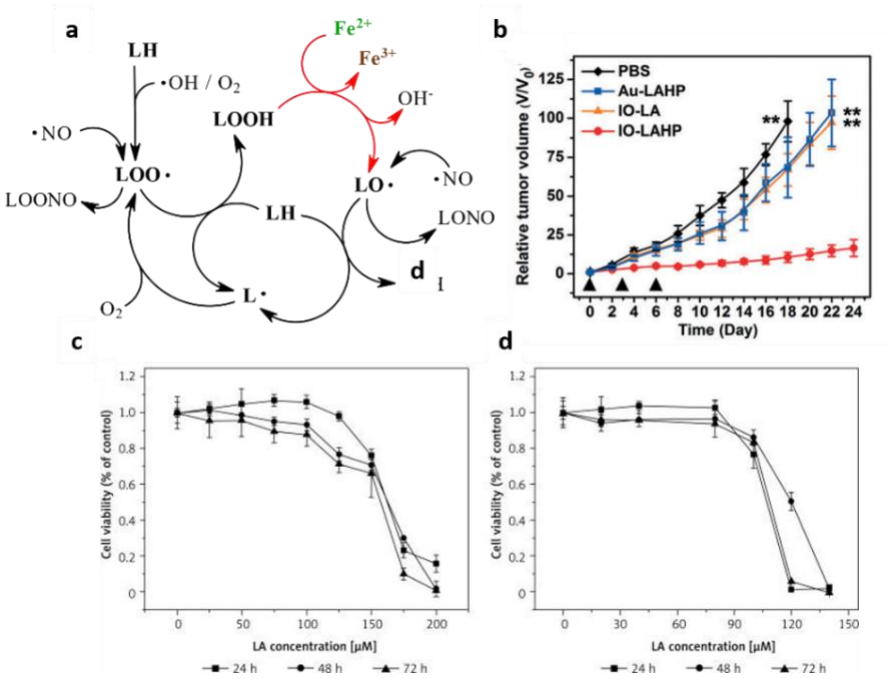

Figure 5.2. Fenton chemistry and PUFA oxidative coupling. *(a) Schematic representation of lipid peroxidation (LOOH) initiated by ROS and amplified by Fenton chemistry; (b) iron oxide (IO) and linoleic acid (LA and LAHP)-enabled lipid peroxidation yield significant decrease in brain tumor growth* in vivo*; (c-d) increasing linoleic acid concentrations decrease viability for (c) LoVo and (d) RKO colon cancer cells. Image (a) adapted from* [12]*. Image (b) adapted from* [13]*, Images (c-d) adapted from* [24]*.*

5.2. Results and discussion

5.2.1. IONP-based scaffolds: synthesis and characterization

5.2.1.1. PUFA-rich IONVs

PUFA-rich polyethylene glycol (PEG)-stabilized mIONP formation followed previously described methods of dry film hydration (see Materials and Methods). Typically, 1 mg of IONP would be mixed with 2 mg of PEG(2000 kDa)-phospholipids (PEG-PLs) of various chemical terminations (-COOH, -NH_2 or -OMe) and 1 mg of dilinoleylmethyl-4-dimethylaminobutyrate (DLin-MC3-DMA or DLin). DLin is an ionizable cationic compound (apparent pKa = 6.44) that contains two covalently bound polyunsaturated linoleoyl chains [28,29] (Fig. 5.3, b). DLin loading constituted a 66% molar fraction of the IONP lipid/phospholipid coating (linoleoyl loading equivalent to an 80% molar fraction).

DLin was successfully loaded into mIONPs (mIONP-DLin) alongside PEG-PLs of various chemical terminations without compromising the stability of the system (Fig. 5.3, a). Qualitative PUFA mIONP enrichment was confirmed using previously described colorimetric methods based on 3,3′,5,5′-tetramethylbenzidine (TMB) oxidation (TMB^+ shows a characteristic absorbance peak at 652 nm) (see Materials and Methods). TMB oxidation can be triggered by Ag^+ reduction. However, polyunsaturated lipid chains can chelate free Ag^+ ions in solution, thus preventing TMB oxidation (Fig. 5.3, c; see Chapter 2) [30].

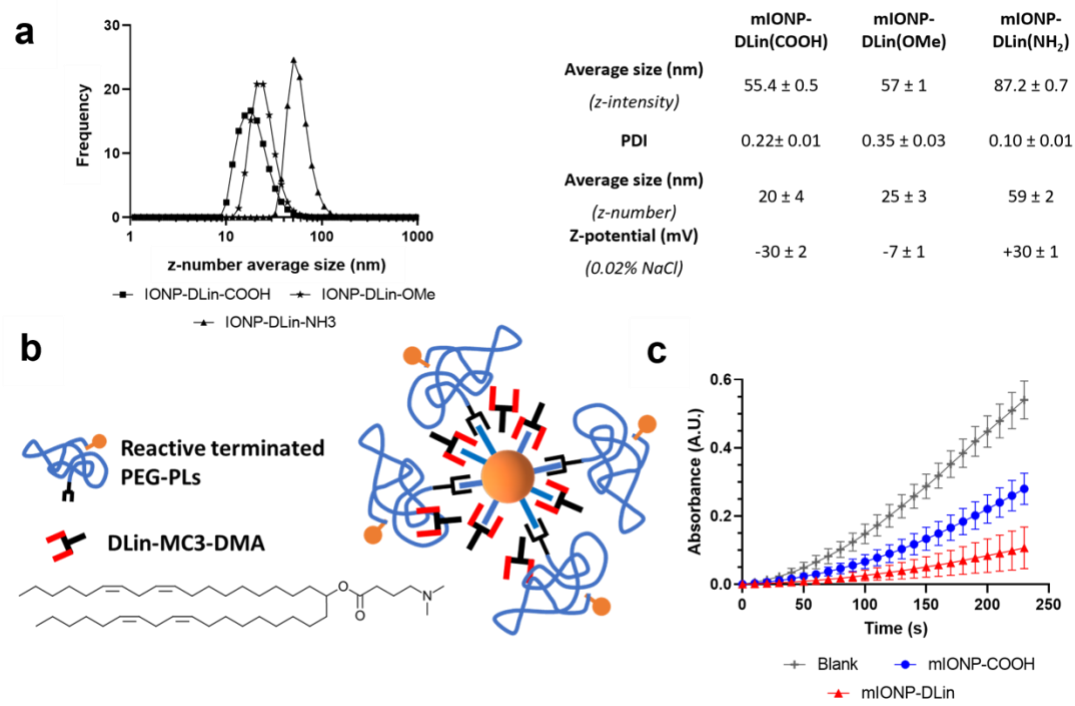

Figure 5.3. Characterization of dilinoleyl-enriched mIONP-DLin formulations. *(a) Nanoparticle size distribution as percentage (%) of events by z-number from DLin-MC3-DMA-rich IONP-filled suspensions combined with PEG-COOH-PL, PEG-OMe-PL or PEG-NH3-PL and physicochemical characterization summary. Representative values as mean ± SEM for at least three independent experiments as characterized by Dynamic Light Scattering (DLS). (b) Proposed schematic structure of mIONP-DLin-PEG particles. (c) Time course curves assessing TMB oxidation at 37°C by mIONP(COOH) (synthetized and characterized in Chapter 2) and mIONP-DLin(COOH) at [TMB] = 830 uM and [Ag+] = 175 uM. Concentrations were [Fe] = 150 µM for both mIONPs systems. pH was controlled with sodium acetate (0.1M) buffer (pH=4.5). Representative values as mean ± SEM for at least three independent experiments as characterized by UV-Vis.*

5.2.1.1.1. Immunostimulatory drug capture

Polyinosinic:polycytidylic acid (poly(I:C) or pIC) is a double-stranded ribonucleic acid chain that has demonstrated powerful immunostimulatory capacity for immune cell activation [31]. Its phosphate-rich structure confers pIC a net negative charge. Following our previous studies, positively charged 2-dioleoyl-3-trimethylammonium-propane (DOTAP)-rich mIONPs (mIONP-TAP) can be used for pIC loading and successful systemic delivery *in vivo* (see Chapter 4) [27].

First, DLin-rich mIONP-TAP micelles (mIONP-DLin-TAP) were formed. The procedure used was based on the previously described methods of dry film hydration (see Materials and Methods). Typically, 1 mg of IONP would be mixed with 1.5 mg of PEG-OMe-PL, 0.7 mg DOTAP and 0.8 mg of DLin-MC3-DMA. This resulted in the formation of positively charged mIONP-DLin-TAP nanoparticles of approximately 34 nm in size (Fig. 5.4, d). Then, a range poly(I:C) (0-250 µg/mL) concentrations were combined with mIONP-DLin-TAP ([Fe] =2 mM) (Fig. 5.4, a-d) and left to self-assemble overnight. Excess non-bound pIC was removed by discarding the supernatant after ultracentrifugation (see Materials and Methods). The pellet, mIONP-DLin-TAP-pIC, was resuspended in aqueous media. UV-Vis characterization confirmed pIC capture (Fig. 5.4, e). Increasing polydispersity and particle size could be observed as a result of increasing pIC loading (Fig. 5.4, a-c). Transmission Electron Microscopy (TEM) imaging showed absence of particle aggregates for mIONP-DLin-TAP-pIC (Fig. 5.4, e-f) (see Materials and Methods).

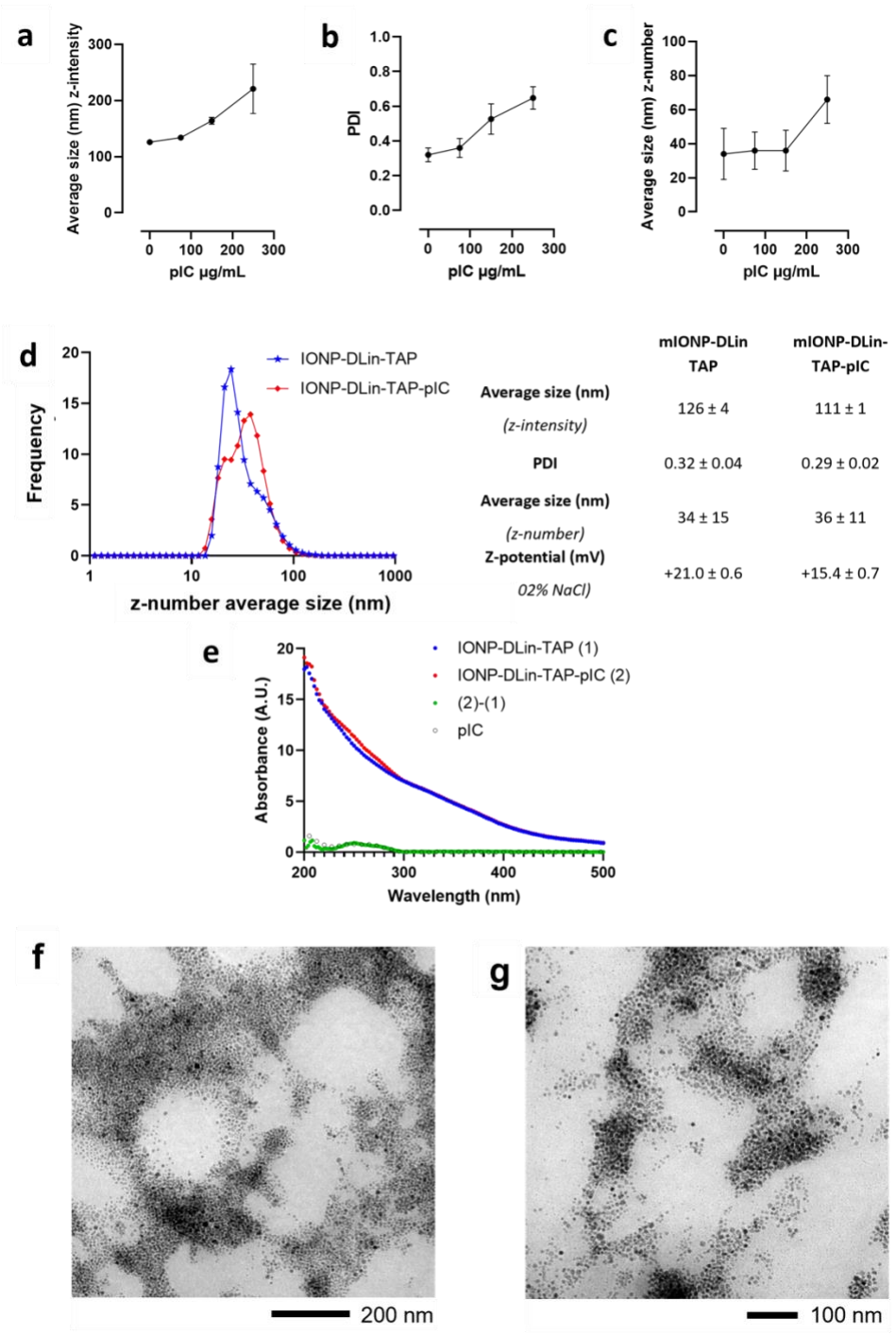

Figure 5.4. Characterization of pIC-capturing dilinoleyl-enriched mIONP-DLin-TAP formulations. Nanoparticle *size characterization by DLS mIONP-DLin-TAP functionalized with increasing amounts of pIC (mIONP-DLin-TAP-pIC) showing (a) particle size mean by z-intensity and (b) polydispersity index (PDI); (c) particle size mean by z-number. (d) Nanoparticle size distribution as percentage (%) of events by z-number, physicochemical characterization summary and (e) UV-Vis absorbance spectra before and after pIC functionalization of mIONP-DLin-TAP. (f-g) Representative mIONP-DLin-*

TAP-pIC imaging by TEM. DLS characterization data shown as mean ± SEM for at least three independent experiments.

5.2.1.1.2. Neoantigen-decoration of mIONP-DLin

Functionalization of the mIONPs with the neoantigen peptide cocktail was achieved using previously described thiosuccinimide linkage strategies by the Michael addition reaction between a reduced thiol and maleimide (see Chapter 2). This bioconjugation route offers versatile and stable click chemistry cross-linking and is already present in various clinically-approved cancer therapy treatments [32,33].

First, maleimide-presenting mIONP-DLin (mIONP-DLin(Mal)) were formed following previously described methods of dry-film hydration (see Materials and Methods). Typically, 1 mg of IONP would be mixed with: 2.5 mg of PEG(2000 kDa)-Maleimide (PEG-Mal) and 0.2 mg DLin-MC3-DMA. In the formulations described above, DLin proportion accounted for a molar 66% fraction of the IONP coating. To ensure an excess of reactive maleimide moieties in the PEGylated surface of our mIONPs, DLin content was limited to a molar 20% fraction. The procedure resulted in the formation of mIONP-DLin(Mal) of ca. 40 nm (Fig. 5.5).

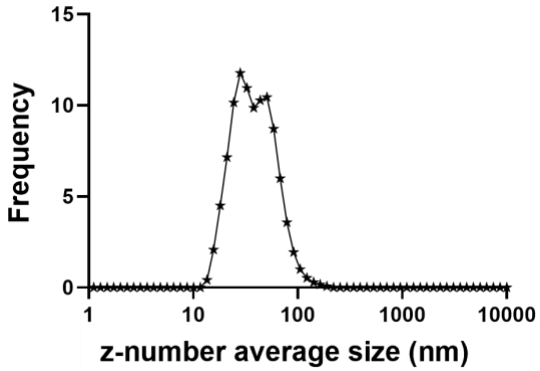

	IONP-DLin(Mal)
Average size (nm) *(z-intensity)*	164 ± 19
Average size (nm) *(z-number)*	42 ± 17
PDI	0.43 ± 0.05
Z-potential (mV) *(0.02% NaCl)*	-11.4 ± 0.8

Figure 5.5. Characterization of mIONP-DLin(Mal) formulations *Nanoparticle size distribution as percentage (%) of events by z-number from mIONP-DLin-Mal suspensions and physicochemical characterization summary. Representative values as mean ± SEM for at least three independent experiments as characterized by DLS.*

B16-M30 and B16-M27 neoantigen proteins used for IONV development were custom-synthetized (Sinopharma) to include a N-terminal thiol moiety. Following the previously described method of thiol-maleimide bioconjugation (see Materials and Methods),

mIONP-Mal (synthetized and characterized in Chapter 2) or mIONP-DLin(Mal) were combined with fresh solutions of thiol-containing peptide neoantigen cocktails. Mal-presenting particles and neoantigens were mixed in a 1 : 9 : 9 molar ratio (IONP : B16-M30 : B16-M27) and were left to react overnight at room temperature in PBS buffer (pH = 7.6) previously purged with N_2 for a few minutes to remove the dissolved oxygen and supplemented with 5 mM EDTA to avoid metal-induced thiol oxidation. Free neoantigen excess was removed from neoantigen-decorated IONVs, mIONP-NeoA or mIONP-DLin-NeoA, by ultracentrifugation (see Materials and Methods). The IONVs resuspended in PBS showed little to no changes in PDI or average particle size (by z-number) for at least 2 weeks, which is indicative of good stability (Fig. 5.6, b-f). TEM imaging also showed well dispersed particles and absence of aggregates (Fig. 5.6, g-h).

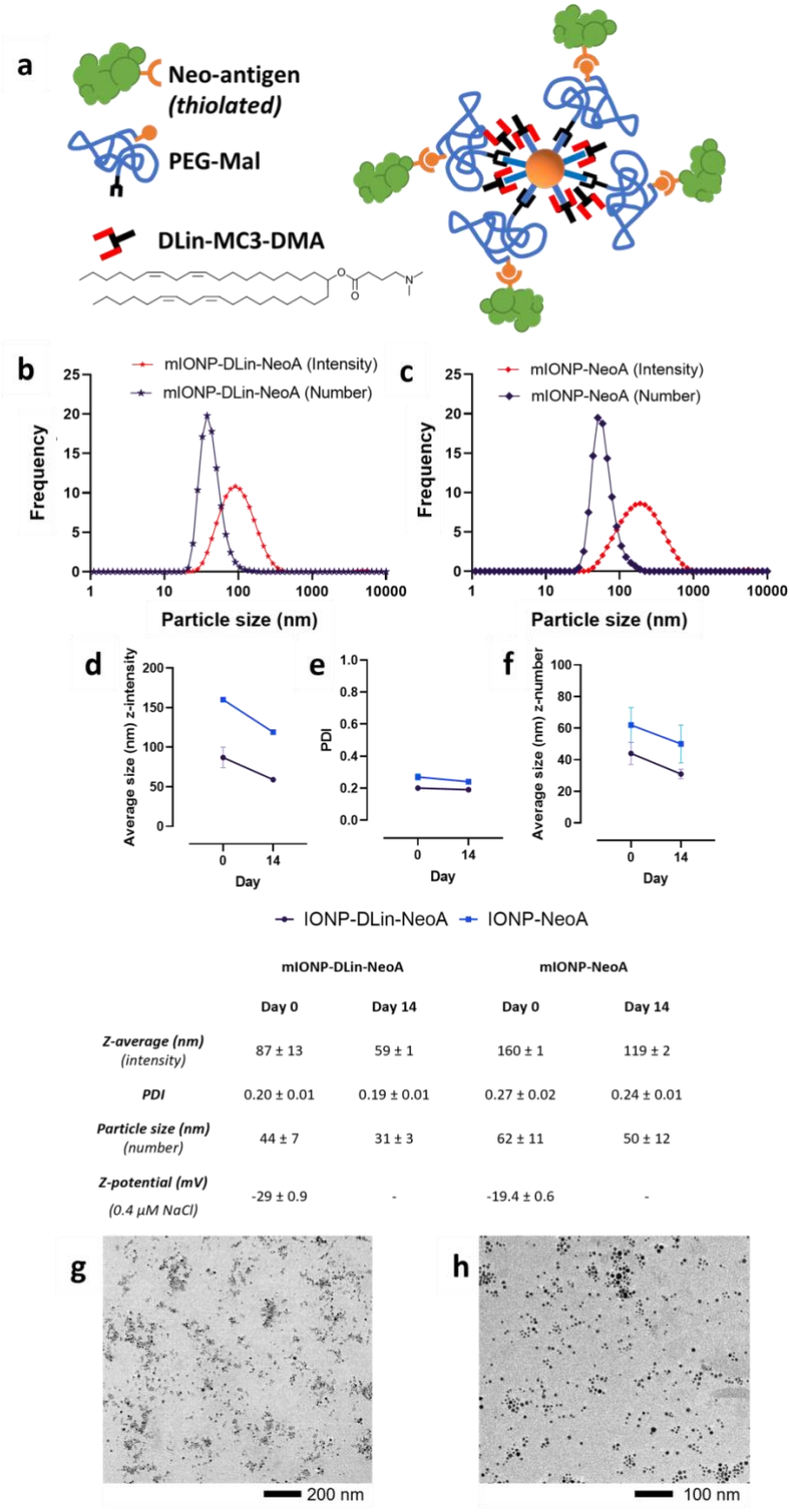

Figure 5.6. Characterization of neoantigen-decorated mIONP-DLin-NeoA and mIONP-NeoA *(a) Schematic representation of the mIONP-DLin-NeoA system. (b) Nanoparticle size distribution as percentage (%) of events by z-number before and after neoantigen-decoration for mIONP-DLin-Mal and mIONP-Mal suspensions. Particle suspension stability characterization of mIONP-DLin-NeoA and mIONP-NeoA at days 0*

and 14 showing (c) particle size mean by z-intensity and (d) polydispersity index (PDI); (e) particle size mean by z-number. (f) physicochemical characterization summary. (g-h) Representative mIONP-DLin-NeoA imaging by TEM. DLS characterization data shown as mean ± SEM for at least three independent experiments.

Neoantigen capture was measured by indirect analytical methods. Unbound neoantigen excess removed by ultracentrifuge was quantified by HPLC (see Materials and Methods) (Fig. 5.7). Regardless of DLin content, mal-decorated mIONPs retained 5.5 ± 0.5 µg of total neoantigen mix per µg of Fe_3O_4 comprized of 57 ± 2 % B16-M27 (N = 2). The lack of neoantigen capture by maleimide-free mIONPs provided further evidence of the specific nature of the reactions leading to the covalent bioconjugation of the neoantigens (Fig. 5.7, e-f).

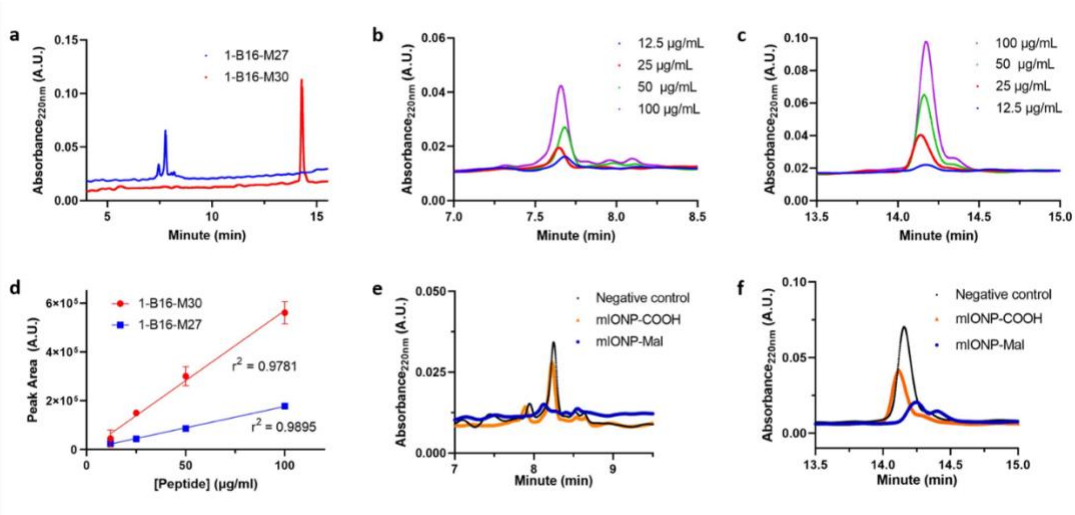

Figure 5.7. mIONP neoantigen-decoration quantification using indirect HPLC analytical methods*. (a) HPLC absorbance peaks for B16-M27 and B16-M30; HPLC UV-Vis absorbance peaks from increasing concentrations of (b) B16-M27 and (c) B16-M30 and (d) respective linear calibration curves. Representative values as mean ± SEM for at least two independent experiments as characterized by HPLC. Mobile phase gradient elution conditions specified in Table 7.1 (see Materials and Methods). Comparative representative decrease in absorbance peak intensity after neoantigen capture by maleimide-rich mIONP-Mal and maleimide-less mIONP-COOH (synthetized and characterized in Chapter 2) (e) for B16-M27 and (f) B16-M30.*

5.2.1.2. Small PUFA-free Fenton reaction inducers

Hydrophobic oleic acid-coated IONPs have been used as the core of every therapeutic carrier developed throughout this thesis (see Chapter 2). PEGylation was used to achieve water solubility of the mIONP-based systems, yielding controllable size, surface charge and stability optimum for applications in cancer chemoimmunotherapy (see Chapter 3) and immunotherapy (See Chapter 4) *in vivo*. In these systems, the hydrophobic rich mIONP core resulting from its self-assembly and programmable disassembly was also important to improve the immunostimulatory properties [27]. However, oleic acid has been reported to protect metastasizing cancer cells in the lymph from ferroptosis [34]. In addition, bulky PEG chains have been reported to limit cellular uptake, which could condition intracellular Fenton chemistry and drug delivery [35]. Therefore, alternative routes for IONP synthesis can be selected to as a way to potentially improve the therapeutic properties of the IONP as Fenton reaction inducers [36].

Iron (II) and iron (III) co-precipitation is one of the most conventional methods for iron oxide nanoparticle synthesis [37]. This method uses 2:1 $Fe^{2/3+}$ molar mixtures which in basic aqueous solution precipitate in the form of IONPs. The particle can then be coated with small hydrophilic molecules to enable aqueous suspension. Synthesis of hydrophilic citric acid-coated IONPs was adapted from well-stablished methods [38,39]. $FeCl_3 \cdot 6H_2O$ (6 mmol) and $FeCl_2 \cdot 4H_2O$ (3 mmol) would be dissolved in distilled water and ammonium hydroxide excess added to reach strong basic aqueous pH (pH > 10). The reaction mixture leads to the immediate precipitation of a black solid product, the IONP (Fig. 5.8, b). Citrate-coating was achieved following nanoparticle incubation with sodium citrate excess solution at 90°C for 1 hour. The product was purified by centrifugation to obtain clean citrate-coated IONPs (Figure 5.8) (*Materials and methods).*

STEM characterization of the citrate-coated IONPs demonstrated the obtention of very small particles of 3.3 ± 0.6 nm (Fig. 5.8, a-b). FTIR characterization showed presence of characteristic peaks from sodium citrate (COO^- stretching bands 1579 cm^{-1}, 1393 cm^{-1}) and bare naked IONPs (Fe-O stretching band 550 cm^{-1}) in purified IONP-Cit samples (Fig. 5.8, c). Broad bands seen at ca. 3400 cm^{-1} can be assigned to O-H stretching and bending vibrations from magnetite surface and water molecules [40]. The IONP-Cit samples formed particles of approximately 8 nm, which remained suspended stably in aqueous

solution for months. Previously described methods of time-based 3,3′,5,5′-tetramethylbenzidine (TMB) oxidation assays were used to evaluate the catalytic features of mIONP-Cit particles (see Materials and Methods). The particles displayed catalytic oxidative properties that are very similar to that of the PEGylated mIONP particles reported in previous chapters: K_M (H_2O_2) = 393 µM; V_{max} = 5.9 × 10^{-8} M/s; k_{cat} = 0.3 s^{-1} (Fig. 5.8, e-f).

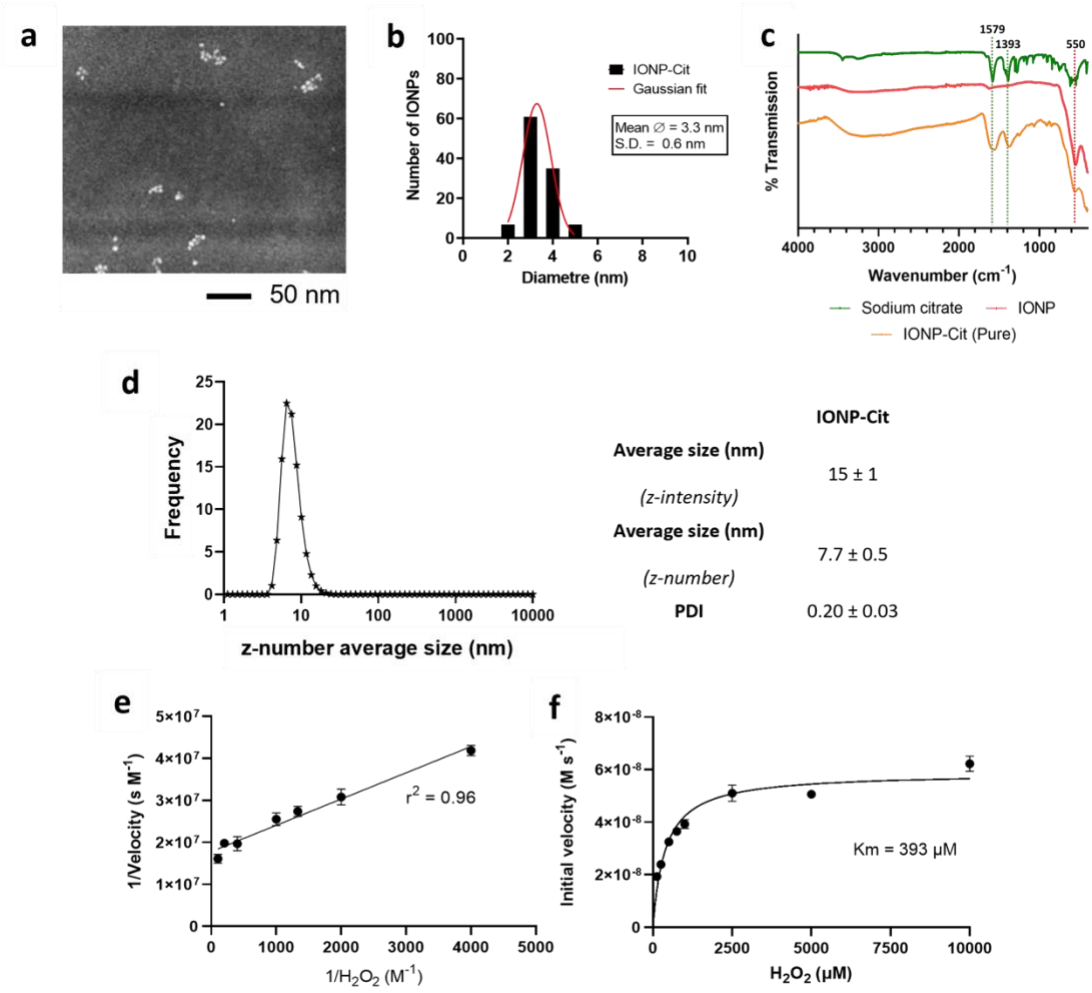

***Figure 5.8. Characterization of the IONP-Cit employed in this work**: (a) Representative scanning transmission electron microscope (STEM) images and (b) size distribution analysis of more than 100 IONPs; (c) FTIR characterization of sodium citrate (green line), IONP (red line) and IONP-Cit (orange line); (d) Nanoparticle size distribution as percentage (%) of events by z-number from mIONP-Cit suspensions and physicochemical characterization summary. Representative values as mean ± SEM for at least three independent experiments as characterized by DLS. (e) Michaelis-Menten and (f) Lineweaver-Burk kinetics plots for TMB oxidation ([TMB] = 830 µM) catalysed by IONP-Cit ([Fe] = 150 µM) at increasing concentrations of H_2O_2 ([H_2O_2] = 0 - 10*

μM). Results are shown as mean ± SEM from three independent experiments as characterized by UV-Vis.

5.2.2. Biological activity evaluation

5.2.2.1. Effects on melanoma and macrophage cell viability

As mentioned in previous chapters, the tumor microenvironment (TME) is characterized by elevated levels of ROS and H_2O_2 [41]. In the presence H_2O_2, lipid peroxidative reactivity of both PUFAs and Fenton chemistry agents can be expected to increase (See Fig. 4.2). As previously discussed, high levels of oxidative stress can lead to the induction of cell kiling through the activation of ferroptosis. However, preventing cytotoxicity towards local immune cells is key to favor ICD and activation of the immune system against the cancer cells,[16–18]. Indeed, the TME is rich in various immune cell populations [42]. Among them, macrophages represent a predominant fraction [43]. The activation and recruitment of anticancer macrophages in the TME has been reported as crucial for the success of cancer immunotherapy [44]. Hence, the cytotoxic effects of PUFA and IONP-mediated peroxidative activity were evaluated in melanoma cells and macrophages.

To evaluate IONP-mediated cancer cell sensitization towards ferroptosis, B16-F10(OVA) mouse melanoma cells were treated with IONP-Cit for 24 hours to ensure particle uptake. Non-internalized nanoparticles were then removed and the IONP-loaded melanoma cells were treated with increasing H_2O_2 concentrations ($[H_2O_2]$ = 0 – 75 μM) for another 24 hours. These are physiologically relevant H_2O_2 concentrations as human blood can reach a range of 30 – 50 μM during inflammation [45]. Cell viability was finally evaluated using MTT assays (see Materials and Methods). The results showed that pre-treatment with IONP-Cit sensitized cancer cells towards H_2O_2-mediated oxidative damage and cell death whilst remaining well-tolerated by macrophages (Fig. 5.9).

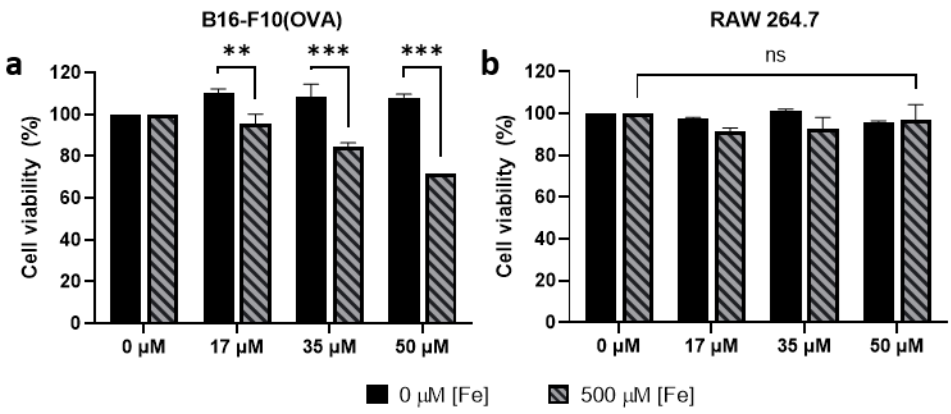

Figure 5.9. IONP-Cit suspensions trigger cancer-specific sensitization towards oxidative damage. *Cell viability for (a) B16-F10(OVA) melanoma and (b) RAW264.7 macrophage cells after (i) 24-hour pre-treatment with IONP-Cit ([Fe] = 0.5 mM) suspensions and (ii) 24-hour exposure to increasing H_2O_2 concentrations ([H_2O_2] = 0 - 50 µM).*

Cystine is a key precursor of intracellular antioxidant glutathione (GSH) production and ROS detoxification. Depletion of intracellular cystine has been reported to induce intracellular ROS accumulation, oxidative damage and ferroptosis [46]. Erastin is a compound that binds to the cysteine-glutamate antiporter and impedes cysteine uptake (Fig. 5.11, a). Hence, the compound can be used to evaluate cell susceptibility to ferroptosis [47] [48]. [49].

B16-F10(OVA) melanoma cells were treated with Erastin for 24 h. To evaluate PUFA contributions to ferroptosis induction, excess Erastin was then removed, and the melanoma cells were treated with PUFA-rich IONP-based systems for another 24 h. Cell viability was evaluated by MTT assays. In previous chapters we described the formation of linoleic acid-rich mIONP-PEG-Lin formulations (see Chapter 2). The ability of mIONP-PEG-Lin formulations administered to erastin-treated melanoma cells to enhance cell killing was directly proportional to their linoleic acid content (Fig. 5.10, a). Similarly, previously described PEG-free linoleic acid-coated mIONP-Lin formulations (see Chapter 2) showed an ability to trigger cell death preferentially in the melanoma cells (Fig. 5.10, b) as at the concentrations used they were well-tolerated by macrophages (Fig. 5.10, c).

In summary, these findings show that Fenton chemistry and PUFA delivery enabled by mIONPs provides an effective strategy to trigger cancer cell-specific sensitization towards oxidative damage and cell death.

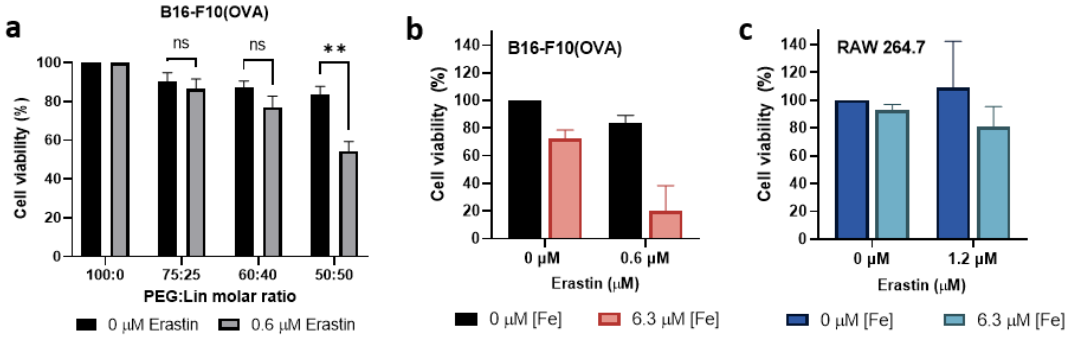

Figure 5.10. mIONP-enabled PUFA delivery induces cancer cell-specific sensitization towards oxidative damage*. Cell viability for (a) B16-F10(OVA) melanoma cell viability following (i) 24 h Erastin pre-treatment (0.6 μM) and (ii) 24-hour exposure to mIONP-PEG-Lin formulations of increasing Linoleic content. Cell viability for (b) B16-F10(OVA) melanoma and (c) RAW264.7 macrophage cells after (i) 24 h Erastin pre-treatment (0.6 μM) and (ii) 24-hour exposure to mIONP-Lin ([Fe] = 6.3 μM). Data is shown as (a-c) mean ± SEM (N = 3). Data for (b-c) is shown as mean ± SEM (N=2), small sample size does not allow for reliable statistical analysis. Cell studies were performed with the help of Ph.D. candidate Rhiannon Beadman (Swansea University).*

5.2.2.2. Cancer cell screening of IONP-induced cytotoxicity and sensitization to ferroptosis

Like Erastin, RSL3 is a known inhibitor of the antioxidant intracellular protection system [50]. RSL3 inhibits GPX4 production, an enzyme responsible for catalyzing lipid hydroperoxide reduction (Fig. 5.11, a). Depletion of antioxidant protection with either Erastin or RSL3 pre-treatment in cancer cells provide complementary evidence of ferroptosis induction. Herein, cancer cell sensitization to ferroptosis was screened in a panel of human and mouse cancer cell lines: LC-2 (human lung cancer) [51], MC-38 (murine colon cancer) [52,53], OVCAR8 (human ovarian cancer) [54], PEO1 (cisplatin-sensitive human ovarian cancer), PEO4 (cisplatin-resistant human ovarian cancer) [55] and 4T1 (murine breast cancer) [56] (Fig. 5.11, b-g).

Cancer cells were pre-treated for 24 h with Erastin or RLS3. Then, these treatments were removed and the IONP-based systems were administered for 24 h prior to cell viability

assessment by MTT assays. PUFA-enriched mIONP-DLin systems induced the highest levels of cancer cell killing. Administration of mIONP-DLin alone induced very high levels (> 70%) of cell death in LC-2, MC-38, OVCAR8 cell lines. Their strong cytotoxic effect could be increased through GXP4 inhibition for cell lines PEO1, PEO4 and 4T1. IONP-Cit administration also triggered significant rates of cytotoxicity. Cancer cell pretreatment with RSL3 induced a very strong increase in IONP-induced cytotoxicity, leading to very high levels of cell death for most cancer cell lines. In comparison, the PEGylated linoleoyl-free mIONP systems were less effective and inducing cancer cell death.

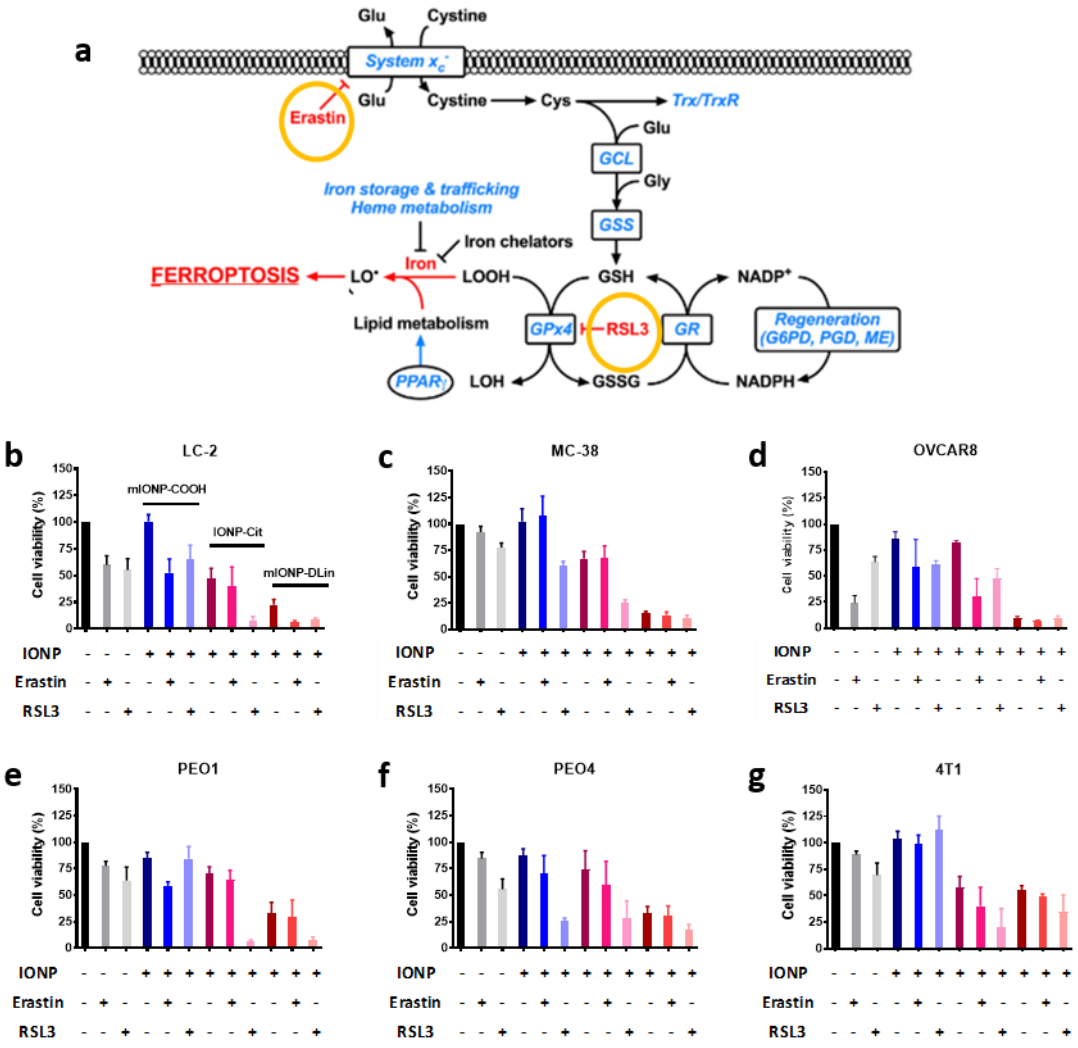

Figure 5.11. Small IONP-Cit and linoleoyl-rich mIONP-DLin are strong inducers of cancer cell ferroptosis*. Schematic summary of biochemical ferroptosis pathway and antioxidant protection. Cell viability evaluated by MTT assay for (b) LC-2 , (c) MC-38, (d) OVCAR8, (e) PEO1, (f) PEO4 and (g) 4T1 cancer cells following (i) 24 h pre-*

treatment with Erastin or RSL3 and (ii) 24 h exposure to mIONP-COOH (solid blue bars), IONP-Cit (solid pink bars) or mIONP-DLin (solid red bars). Data is shown as mean ± SEM (n = 3). Concentration of IONP was [Fe] = 500 µM. Concentrations of Erastin and RSL3 had been previously optimized per each cell line: [Erastin] = 0.156 µM for Lc-2, MC-38 and 4T1; 0.625 µM for PEO 1 and PEO 4; 2.5 µM for OVCAR8; [RSL3] = 0.039 µM for Lc-2, MC-38, PEO1, PEO4 and 4T1; 0.156 µM for OVCAR8. Image (a) adapted from [50].

5.2.2.3. Effects in macrophage-melanoma co-cultures

As in previous chapters, the cancer cell killing capacity of IONP-based therapies was also assessed in co-cultures of B16-F10(OVA) melanoma cells with RAW 264.7 macrophages. (see Materials and Methods). The cells were cultured together allowing for direct cell-to-cell contact and signalling. In this way, we aimed to study both combined effect of macrophage and IONP-induced cancer cell killing and the selectivity of the effects (lipid peroxide and cell death) induced with these new INOPs.

5.2.2.3.1. Effects on intracellular melanoma redox stress

Accumulation of lipid hydroperoxides serves as an indication of redox stress imbalance and oxidative damage. Lipid hydroperoxide accumulation was studied using previously described methods of Flow Cytometry using Liperfluo™ (*Materials and Methods*).

The cells were treated for 24 h with the IONP-based treatments prior to assessment of membrane lipid peroxidation using Liperfluo The results showed that all IONP-based treatments trigger increased lipid peroxidation in the melanoma cells (Fig. 5.12). The smaller PEG- and oleic acid-free IONP-Cit nanoparticles were expected to facilitate intracellular oxidative reactivity and, indeed, these systems increased membrane lipid hydroperoxide accumulation when compared to the mIONP-based systems. However, PUFA delivery through mIONP-DLin triggered the highest lipid hydroperoxide accumulation levels among these treatments. The peroxidative mIONP-DLin activity was also evaluated in melanoma cell monocultures, showing the same effects (Fig. 5.12, b).

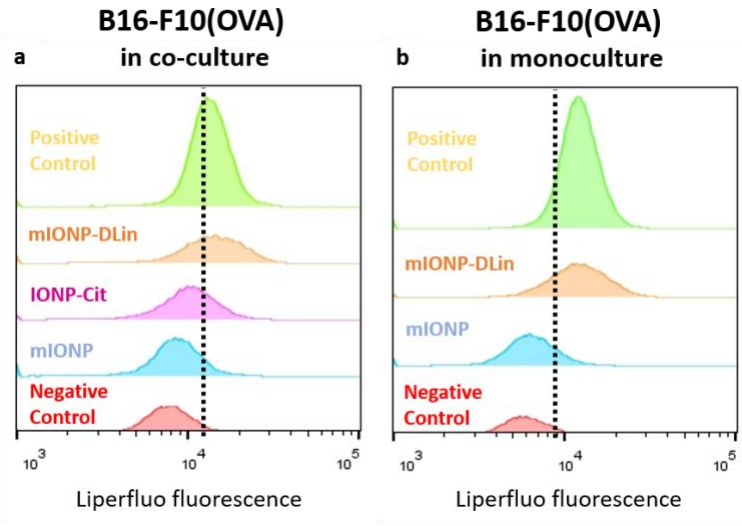

Figure 5.12. Fenton chemistry and PUFA delivery increase cancer cell lipid peroxidation. *Fluorescent-positive B16-F10(OVA) melanoma populations using Liperfluo dye following 24-hour exposure to mIONP-DLin, IONP-Cit, mIONP-COOH ([Fe] = 500 µM) when cells were cultured in (a) murine macrophage-melanoma (RAW264.7 – B16-F10(OVA)) direct cell-to-cell co-cultures and (b) melanoma-only monocultures. Cumene hydroperoxide (100 µM) for a 1-hour treatment was used as positive control.*

5.2.2.3.2. Effects on melanoma and macrophage viability

Finally, cell viability for each type after the different IONP-based treatments were measured following the previously described methodology by Flow Cytometry (see Materials and Methods). The cells were treated for 24 h with IONP-based treatments prior to cell viability evaluation.

Although oxidative damage triggered by IONP-Cit was well-tolerated in macrophages (Fig. 5.9, b) while inducing high rates of ferroptosis against various cancer cell lines in monoculture (Fig. 5.11), their administration in the macrophage-melanoma co-cultures proved surprisingly pro-tumoral (Fig. 5.13). These results demonstrate the complex nature of the interaction and effects that can take place in the cell co-cultures and of redox regulation in cells [57]. In absence of co-stimulation, uncontrolled oxidative damage can induce immune-mediated tumor tissue repair mechanisms and cancer cell proliferation [58]. Previous chapters demonstrated that simultaneous delivery of Fenton chemistry and DAMP-like "danger signals" resulting from mIONP self-assembly/programmed disassembly synergized to induce potent anticancer immune cell stimulation (see Chapter

4) [19,21]. This immunostimulatory feature is absent in the IONP-Cit treatments. Additional testing showed that IONP-Cit administration to macrophage monocultures induced significant increases in cell proliferation, which could be indicative of pro-tumoral tissue-repairing macrophage activation (Fig. S5.1) [59]. In sharp contrast, PUFA and DAMP-rich mIONP-DLin formulations triggered a significant decrease in melanoma viability in comparison to PUFA-free mIONPs, whilst maintaining macrophage viability.

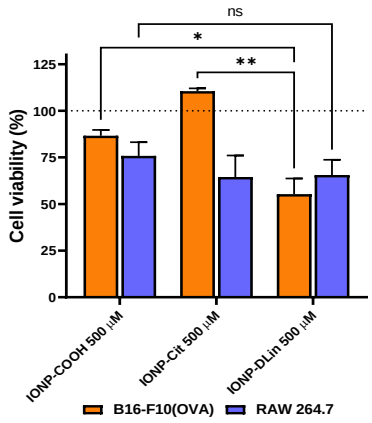

Figure 5.13. PUFA and DAMP-bearing mIONP-DLin suspensions enhance anticancer cytotoxicity in complex environments. *Cell viability as necrosis-negative stained cell populations measured by Flow Cytometry following 24 h of the indicated treatments in RAW 264.7 (blue solid bars) and B16-F10(OVA) (orange solid bars) cells in direct cell-to-cell contact co-culture. Co-culture cell viability is normalized to the absence of treatment and shown as mean ± SEM (n = 3).*

5.2.2.4.In vivo evaluation of neoantigen vaccines for cancer therapy

A preliminary *in vivo* study was carried out to evaluate the therapeutic efficacy of vaccination with a neoantigen cocktail (B16-F10 melanoma neoantigen peptides M27 and M30) co-administered with the potent adjuvant used in Chapter IV and previous generations of mIONVs developed in the group [27]. The main goal was to identify a suitable dose to induce therapeutic effects in mice bearing established *B16F10* melanoma tumors. Hence, peritumoral administration was used to ensure that the entirety of the therapeutic cargo reached the tumor tissue and thus avoid variabilities derived from the vaccine biodistribution.

In this initial study, C57BL/6 mice were inoculated with 1×10^5 B16-F10 tumor cells on day 0 and initiated treatments on day 4 when tumors were established (Fig 5.14, a). On

days 4, 7, and 10, animals were treated with different neoantigen-containing vaccines, containing 4 μg/dose of pIC and 3 μg/dose of imiquimod and 75 μg/dose of the two neoantigen peptides (NeoA + pIC-R837 group), and PBS (as non-treatment control group). The B16F10-specific M27 and M30 peptide neoantigens were administered in a 1:1 ratio. For the two IONP groups, we administered the equivalent dose of peptides and pIC-R837 adjuvants loaded onto 25 μg of Fe_3O_4/dose. IONP-enabled therapeutic delivery was studied with and without PUFA enrichment (mIONP-DLin-NeoA + mIONP-DLin-pIC-R837; or mIONP-NeoA + mIONP-pIC-R837) (Fig. 5.14). Our results show that neoantigen therapies induced clear therapeutic benefits in comparison to the non-treatment control group. The three vaccine formulations displayed non-significant differences among them. Regardless of IONP or DLin content, neoantigen delivery decreased tumor growth rates (Fig. 5.14, a, c-f) and extended median survival to over 30 days (Fig. 5.14, b). This first set of results confirms that the selected neoantigens-adjuvant cocktails are strongly immunogenic and that they successfully retained their immunogenicity after mIONP surface loading. Further studies will need to explore different routes of administration to elucidate the effect of the PUFA content and INOV delivery and also explore further therapy improvement, potentially through state-of-the-art antibody-based combination therapies [27,60–62] (see Chapter 4).

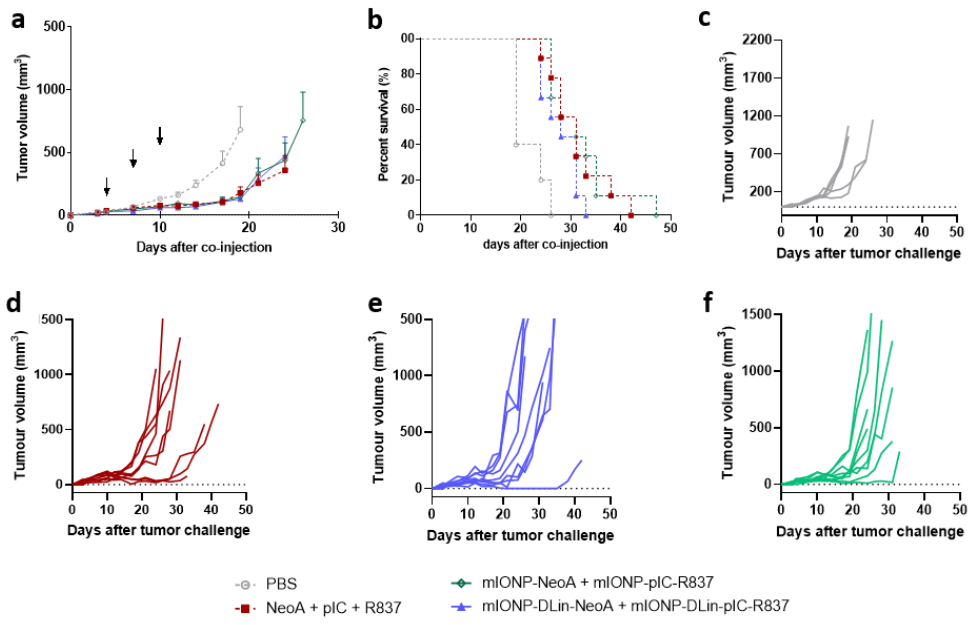

Figure 5.14. In Vivo evaluation of the therapeutic effect from neoantigen-decorated IONV immunotherapies. *C57BL/6 mice (n = 9) were inoculated subcutaneously with 3*

x 10^5 B16-F10 cells and treated with nanovaccines (73 µg of neoantigen mix, 4 µg of pIC and 3 µg R837; 27 µg Fe_3O_4) on days 4, 7, and 10 (peritumoral injection). Results are shown as (a) Average tumor growth curve for each case group; (b) Kaplan-Meier survival plot curves; and (c-f) individual tumor growth curves. Arrows indicate the days of therapy administration. These studies were performed with the help of our collaborators in the research institutes of CIC bioGUNE, in Derio (Spain), and CIC biomaGUNE, in Donostia (Spain).

5.3. Conclusions

The results presented in this chapter expand on the study of IONVs to enable tumor-specific activation of ferroptosis and effective antigen/adjuvant delivery for cancer immunotherapy. Several IONP-based treatment features that contributed to therapy enhancement can be highlighted to rationalize further approaches of optimization. In summary:

- mIONP self-assembly allowed stable PUFA loading into the micelle coating. Iron-enabled peroxidative activity is coupled with delivery of PUFA units in mIONP-DLin and resulted in a strong potentiation of the redox stress-inducing features of mIONPs. *In vitro* mIONP-DLin administration yielded very effective cell killing in several mouse and human cancer cell lines. Notably, increased cancer cell killing capacity was gained without compromising macrophage viability.
- Alternative IONP synthesis routes of iron co-precipitation enabled the formation of hydrophilic IONP-Cit particles. Their small, PEG- and oleic acid-free composition showed stronger ferroptosis-inducing features than the mIONPs. However, IONP-Cit administration in melanoma-macrophage co-cultures *in vitro* resulted in increased melanoma cell viability, which could be relate to their oxidative reactivity being devoid of DAMP-like co-stimulation thus triggering pro-tumoral macrophage polarization and activation of tumor tissue repair mechanisms. Thus, these findings highlighted the favorable therapeutic properties of the self-assembled micelle coating in mIONP and mIONP-DLin systems.
- The mIONP-DLin systems were successfully decorated with peptide neoantigens (B16-M27 and B16-M30 for B16-F10 melanoma tumors). The bioconjugation route used covalent click chemistry to form maleimide-thiol linkages between the micelles and peptides, respectively. The resulting neoantigen-presenting IONVs maintained optimal particle size and stability for *in vivo* systemic administration.
- B16-M27 and B16-M30 neoantigens retained immunogenicity after IONV conjugation. Therapeutic IONV administration *in vivo* decreased cancer cell growth rates for established B16-F10 tumors in mice. However, this first set of *in vivo* experiments did not show any noticeable therapeutic improvements arising

from PUFA and mIONP delivery. Additional experiments are thus required to fully evaluate and exploit the potent cancer killing features demonstrated for these systems *in vitro*.

In conclusion, these results serve as a step forward towards the development of potent redox stress-inducing therapies and personalized neoantigen IONVs for cancer immunotherapy enhancement.

5.4.Supporting information

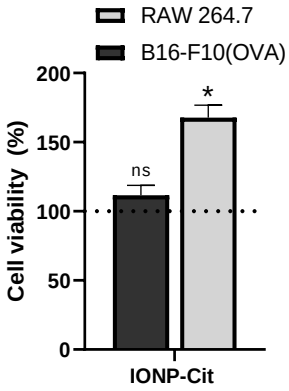

Figure S5.1. IONP-Cit administration triggers pro-tumoral-like proliferative effects to macrophage monocultures. *Cell viability evaluated by MTT assay for melanoma B16-F10(OVA) or macrophage RAW264.7 cancer cells in monoculture following 24 h treatment with IONP-Cit suspensions. Concentration of IONP was [Fe] = 500 µM. Data is normalized to absence of treatment and shown as mean ± SEM (n = 3).*

5.5. References

(1) Jiang, T. et al. Tumor Neoantigens: From Basic Research to Clinical Applications. *J. Hematol. Oncol.* **2019**, *12* (1), 1–13. https://doi.org/10.1186/s13045-019-0787-5.

(2) Samstein, R. M. et al. Tumor Mutational Load Predicts Survival after Immunotherapy across Multiple Cancer Types. *Nat. Genet.* **2019**, *51* (2), 202–206. https://doi.org/10.1038/s41588-018-0312-8.

(3) Schreiber, R. D.; Old, L. J.; Smyth, M. J. Cancer Immunoediting: Integrating Immunity's Roles in Cancer Suppression and Promotion. *Science (80-.).* **2011**, *331* (6024), 1565–1570. https://doi.org/10.1126/science.1203486.

(4) Blass, E.; Ott, P. A. Advances in the Development of Personalized Neoantigen-Based Therapeutic Cancer Vaccines. *Nat. Rev. Clin. Oncol.* **2021**, *18* (4), 215–229. https://doi.org/10.1038/s41571-020-00460-2.

(5) Hartmaier, R. J. et al. Genomic Analysis of 63,220 Tumors Reveals Insights into Tumor Uniqueness and Targeted Cancer Immunotherapy Strategies. *Genome Med.* **2017**, *9* (1), 1–9. https://doi.org/10.1186/s13073-017-0408-2.

(6) Shetty, K.; Ott, P. A. Personal Neoantigen Vaccines for the Treatment of Cancer. *Annu. Rev. Cancer Biol.* **2020**, *5*, 259–276. https://doi.org/10.1146/annurev-cancerbio-060820-111701.

(7) Danciu, C. et al. Behaviour of Four Different B16 Murine Melanoma Cell Sublines: C57BL/6J Skin. *Int. J. Exp. Pathol.* **2015**, *96* (2), 73–80. https://doi.org/10.1111/iep.12114.

(8) Xu, D. et al. NK and CD8+ T Cell-Mediated Eradication of Poorly Immunogenic B16-F10 Melanoma by the Combined Action of IL-12 Gene Therapy and 4-1BB Costimulation. *Int. J. Cancer* **2004**, *109* (4), 499–506. https://doi.org/10.1002/ijc.11696.

(9) Kreiter, S. et al. Mutant MHC Class II Epitopes Drive Therapeutic Immune Responses to Cancer. *Nature* **2015**, *520* (7549), 692–696. https://doi.org/10.1038/nature14426.

(10) Ravasco, J. M. J. M.; Faustino, H.; Trindade, A.; Gois, P. M. P. Bioconjugation with Maleimides: A Useful Tool for Chemical Biology. *Chem. - A Eur. J.* **2019**, *25* (1), 43–59. https://doi.org/10.1002/chem.201803174.

(11) Aldous, A. R.; Dong, J. Z. Personalized Neoantigen Vaccines: A New Approach to Cancer Immunotherapy. *Bioorganic Med. Chem.* **2018**, *26* (10), 2842–2849. https://doi.org/10.1016/j.bmc.2017.10.021.

(12) Girotti, A. W.; Korytowski, W. Nitric Oxide Inhibition of Chain Lipid Peroxidation Initiated by Photodynamic Action in Membrane Environments. *Cell Biochem. Biophys.* **2020**, *78* (2), 149–156. https://doi.org/10.1007/s12013-020-

00909-2.

(13) Zhou, Z. et al. Activatable Singlet Oxygen Generation from Lipid Hydroperoxide Nanoparticles for Cancer Therapy. *Angew. Chemie - Int. Ed.* **2017**, *56* (23), 6492–6496. https://doi.org/10.1002/anie.201701181.

(14) Dixon, S. J. et al. Ferroptosis: An Iron-Dependent Form of Nonapoptotic Cell Death. *Cell* **2012**, *149* (5), 1060–1072. https://doi.org/10.1016/j.cell.2012.03.042.

(15) Friedmann Angeli, J. P.; Krysko, D. V.; Conrad, M. Ferroptosis at the Crossroads of Cancer-Acquired Drug Resistance and Immune Evasion. *Nat. Rev. Cancer* **2019**, *19* (7), 405–414. https://doi.org/10.1038/s41568-019-0149-1.

(16) Sarhan, M.; Von Mässenhausen, A.; Hugo, C.; Oberbauer, R.; Linkermann, A. Immunological Consequences of Kidney Cell Death Review-Paper. *Cell Death Dis.* **2018**, *9* (2). https://doi.org/10.1038/s41419-017-0057-9.

(17) Xie, Y. et al. Ferroptosis: Process and Function. *Cell Death Differ.* **2016**, *23* (3), 369–379. https://doi.org/10.1038/cdd.2015.158.

(18) Zhou, J. et al. Immunogenic Cell Death in Cancer Therapy: Present and Emerging Inducers. *J. Cell. Mol. Med.* **2019**, *23* (8), 4854–4865. https://doi.org/10.1111/jcmm.14356.

(19) Vernon, P. J.; Tang, D. Eat-Me: Autophagy, Phagocytosis, and Reactive Oxygen Species Signaling. *Antioxidants Redox Signal.* **2013**, *18* (6), 677–691. https://doi.org/10.1089/ars.2012.4810.

(20) Mittal, M.; Siddiqui, M. R.; Tran, K.; Reddy, S. P.; Malik, A. B. Reactive Oxygen Species in Inflammation and Tissue Injury. *Antioxidants Redox Signal.* **2014**, *20* (7), 1126–1167. https://doi.org/10.1089/ars.2012.5149.

(21) Garg, A. D.; Romano, E.; Rufo, N.; Agostinis, P. Immunogenic versus Tolerogenic Phagocytosis during Anticancer Therapy: Mechanisms and Clinical Translation. *Cell Death Differ.* **2016**, *23* (6), 938–951. https://doi.org/10.1038/cdd.2016.5.

(22) Ilag, L. Are Long-Chain Polyunsaturated Fatty Acids the Link between the Immune System and the Microbiome towards Modulating Cancer? *Medicines* **2018**, *5* (3), 102. https://doi.org/10.3390/medicines5030102.

(23) Das, U. N. Can Bioactive Lipid(s) Augment Anti-Cancer Action of Immunotherapy and Prevent Cytokine Storm? *Arch. Med. Res.* **2019**, *50* (6), 342–349. https://doi.org/10.1016/j.arcmed.2019.10.004.

(24) Zhang, C. et al. Polyunsaturated Fatty Acids Trigger Apoptosis of Colon Cancer Cells through a Mitochondrial Pathway. *Arch. Med. Sci.* **2015**, *11* (5), 1081–1094. https://doi.org/10.5114/aoms.2015.54865.

(25) Jóźwiak, M.; Filipowska, A.; Fiorino, F.; Struga, M. Anticancer Activities of

Fatty Acids and Their Heterocyclic Derivatives. *Eur. J. Pharmacol.* **2020**, *871* (August 2019). https://doi.org/10.1016/j.ejphar.2020.172937.

(26) Huang, L. et al. Quantitative Self-Assembly of Photoactivatable Small Molecular Prodrug Cocktails for Safe and Potent Cancer Chemo-Photodynamic Therapy. *Nano Today* **2021**, *36*, 101030. https://doi.org/10.1016/j.nantod.2020.101030.

(27) Ruiz-de-Angulo, A. et al. Chemically Programmed Vaccines: Iron Catalysis in Nanoparticles Enhances Combination Immunotherapy and Immunotherapy-Promoted Tumor Ferroptosis. *iScience* **2020**, *23* (9). https://doi.org/10.1016/j.isci.2020.101499.

(28) Jayaraman, M. et al. Maximizing the Potency of SiRNA Lipid Nanoparticles for Hepatic Gene Silencing in Vivo. *Angew. Chemie - Int. Ed.* **2012**, *51* (34), 8529–8533. https://doi.org/10.1002/anie.201203263.

(29) Hu, B.; Weng, Y.; Xia, X. H.; Liang, X. jie; Huang, Y. Clinical Advances of SiRNA Therapeutics. *J. Gene Med.* **2019**, *21* (7). https://doi.org/10.1002/jgm.3097.

(30) Zhang, F.; Wang, X.; Jie, X.; Wei, W. Test Paper for Colorimetric Inspection of Fatty Acids and Edible Oils. *Sensors (Switzerland)* **2018**, *18* (10), 3252. https://doi.org/10.3390/s18103252.

(31) Mac Cheever, M. A. Twelve Immunotherapy Drugs That Could Cure Cancers. *Immunol. Rev.* **2008**, *222* (1), 357–368. https://doi.org/10.1111/j.1600-065X.2008.00604.x.

(32) Boutureira, O.; Bernardes, G. J. L. Advances in Chemical Protein Modification. *Chem. Rev.* **2015**, *115* (5), 2174–2195. https://doi.org/10.1021/cr500399p.

(33) Lu, J.; Jiang, F.; Lu, A.; Zhang, G. Linkers Having a Crucial Role in Antibody–Drug Conjugates. *Int. J. Mol. Sci.* **2016**, *17* (4), 852–3411. https://doi.org/10.3390/ijms17040561.

(34) Ubellacker, J. M. et al. Lymph Protects Metastasizing Melanoma Cells from Ferroptosis. *Nature* **2020**, *585* (7823), 113–118. https://doi.org/10.1038/s41586-020-2623-z.

(35) Verhoef, J. J. F.; Anchordoquy, T. J. Questioning the Use of PEGylation for Drug Delivery. *Drug Deliv. Transl. Res.* **2013**, *3* (6), 499–503. https://doi.org/10.1007/s13346-013-0176-5.

(36) Zhu, N. et al. Surface Modification of Magnetic Iron Oxide Nanoparticles. *Nanomaterials* **2018**, *8* (10). https://doi.org/10.3390/nano8100810.

(37) Tanaka, S. et al. A Review on Iron Oxide-Based Nanoarchitectures for Biomedical, Energy Storage, and Environmental Applications. *Small Methods* **2019**, *3* (5), 1800512. https://doi.org/10.1002/smtd.201800512.

(38) Sahoo, Y. et al. Aqueous Ferrofluid of Magnetite Nanoparticles: Fluorescence Labeling and Magnetophoretic Control. *J. Phys. Chem. B* **2005**, *109* (9), 3879–3885. https://doi.org/10.1021/jp045402y.

(39) Saraswathy, A. et al. Citrate Coated Iron Oxide Nanoparticles with Enhanced Relaxivity for in Vivo Magnetic Resonance Imaging of Liver Fibrosis. *Colloids Surfaces B Biointerfaces* **2014**, *117*, 216–224. https://doi.org/10.1016/j.colsurfb.2014.02.034.

(40) Duszyńska, A. et al. Influence of Electron-Beam Irradiation on Surface Properties of Magnetic Iron Oxide Nanoparticles Stabilized with Citrate. *Radiat. Phys. Chem.* **2020**, *169*. https://doi.org/10.1016/j.radphyschem.2018.03.009.

(41) Vaupel, P.; Multhoff, G. Accomplices of the Hypoxic Tumor Microenvironment Compromising Antitumor Immunity: Adenosine, Lactate, Acidosis, Vascular Endothelial Growth Factor, Potassium Ions, and Phosphatidylserine. *Front. Immunol.* **2017**, *8* (DEC), 1887. https://doi.org/10.3389/fimmu.2017.01887.

(42) Quail, D. F.; Joyce, J. A. Microenvironmental Regulation of Tumor Progression and Metastasis. *Nat. Med.* **2013**, *19* (11), 1423–1437. https://doi.org/10.1038/nm.3394.

(43) Sica, A. et al. Macrophage Polarization in Tumour Progression. *Seminars in Cancer Biology*. 2008, pp 349–355. https://doi.org/10.1016/j.semcancer.2008.03.004.

(44) Chen, Y. et al. Tumor-Associated Macrophages: An Accomplice in Solid Tumor Progression. *J. Biomed. Sci.* **2019**, *26* (1), 1–13. https://doi.org/10.1186/s12929-019-0568-z.

(45) Gao, L.; Fan, K.; Yan, X. Iron Oxide Nanozyme: A Multifunctional Enzyme Mimetic for Biomedical Applications. *Theranostics* **2017**, *7* (13), 3207–3227. https://doi.org/10.7150/thno.19738.

(46) Abdalkader, M.; Lampinen, R.; Kanninen, K. M.; Malm, T. M.; Liddell, J. R. Targeting Nrf2 to Suppress Ferroptosis and Mitochondrial Dysfunction in Neurodegeneration. *Front. Neurosci.* **2018**, *12* (JUL). https://doi.org/10.3389/fnins.2018.00466.

(47) Shan, X. et al. Ferroptosis-Driven Nanotherapeutics for Cancer Treatment. *J. Control. Release* **2020**, *319*, 322–332. https://doi.org/10.1016/j.jconrel.2020.01.008.

(48) Badgley, M. A. et al. Cysteine Depletion Induces Pancreatic Tumor Ferroptosis in Mice. *Science (80-.).* **2020**, *368* (6486), 85–89. https://doi.org/10.1126/science.aaw9872.

(49) Mou, Y. et al. Ferroptosis, a New Form of Cell Death: Opportunities and Challenges in Cancer. *J. Hematol. Oncol.* **2019**, *12* (1), 34. https://doi.org/10.1186/s13045-019-0720-y.

(50) Abdalkader, M.; Lampinen, R.; Kanninen, K. M.; Malm, T. M.; Liddell, J. R. Targeting Nrf2 to Suppress Ferroptosis and Mitochondrial Dysfunction in Neurodegeneration. *Front. Neurosci.* **2018**, *12* (JUL), 466. https://doi.org/10.3389/fnins.2018.00466.

(51) Okita, R.; Shimizu, K.; Nojima, Y.; Saisho, S.; Nakata, M. Tofacitinib Overcomes an IFNγ-Induced Decrease in NK Cell-Mediated Cytotoxicity via the Regulation of Immune-Related Molecules in LC-2/Ad. *Thorac. Cancer* **2021**, *12* (6), 775–782. https://doi.org/10.1111/1759-7714.13847.

(52) Juneja, V. R. et al. PD-L1 on Tumor Cells Is Sufficient for Immune Evasion in Immunogenic Tumors and Inhibits CD8 T Cell Cytotoxicity. *J. Exp. Med.* **2017**, *214* (4), 895–904. https://doi.org/10.1084/jem.20160801.

(53) Lau, J. et al. Tumour and Host Cell PD-L1 Is Required to Mediate Suppression of Anti-Tumour Immunity in Mice. *Nat. Commun.* **2017**, *8* (1), 1–11. https://doi.org/10.1038/ncomms14572.

(54) Mitra, A. K. et al. In Vivo Tumor Growth of High-Grade Serous Ovarian Cancer Cell Lines. *Gynecol. Oncol.* **2015**, *138* (2), 372–377. https://doi.org/10.1016/j.ygyno.2015.05.040.

(55) Hallas-Potts, A.; Dawson, J. C.; Herrington, C. S. Ovarian Cancer Cell Lines Derived from Non-Serous Carcinomas Migrate and Invade More Aggressively than Those Derived from High-Grade Serous Carcinomas. *Sci. Rep.* **2019**, *9* (1), 1–10. https://doi.org/10.1038/s41598-019-41941-4.

(56) Tao, K.; Fang, M.; Alroy, J.; Gary, G. G. Imagable 4T1 Model for the Study of Late Stage Breast Cancer. *BMC Cancer* **2008**, *8* (1), 1–19. https://doi.org/10.1186/1471-2407-8-228.

(57) Raza, M. H. et al. ROS-Modulated Therapeutic Approaches in Cancer Treatment. *J. Cancer Res. Clin. Oncol.* **2017**, *143* (9), 1789–1809. https://doi.org/10.1007/s00432-017-2464-9.

(58) Tham, M. et al. Melanoma-Initiating Cells Exploit M2 Macrophage TGFβ and Arginase Pathway for Survival and Proliferation. *Oncotarget* **2014**, *5* (23), 12027–12042. https://doi.org/10.18632/oncotarget.2482.

(59) Xiao, X. et al. M2 Macrophages Promote Beta-Cell Proliferation by up-Regulation of SMAD7. *Proc. Natl. Acad. Sci. U. S. A.* **2014**, *111* (13), E1211–E1220. https://doi.org/10.1073/pnas.1321347111.

(60) Zitvogel, L.; Kroemer, G. Interferon-γ Induces Cancer Cell Ferroptosis. *Cell Res.* **2019**, *29* (9), 692–693. https://doi.org/10.1038/s41422-019-0186-z.

(61) Stockwell, B. R.; Jiang, X. A Physiological Function for Ferroptosis in Tumor Suppression by the Immune System. *Cell Metab.* **2019**, *30* (1), 14–15. https://doi.org/10.1016/j.cmet.2019.06.012.

(62) Wang, W. et al. CD8+ T Cells Regulate Tumour Ferroptosis during Cancer Immunotherapy. *Nature* **2019**, *569* (7755), 270–274. https://doi.org/10.1038/s41586-019-1170-y.

Chapter 6 . **Summary of Results**

In summary:

- A systematic engineering rationale was successfully stablished for IONP-filled micelle design and customization. The approach enabled multilevel device optimization and personalization. Variations in the mIONP assembly provided control over distinguishable device properties (i.e. size, charge, stability and chemical reactivity) as well as bioactive molecule loading and particle surface functionalization.

- The IONP core demonstrated strong peroxidase-like catalytic activity. The IONzyme activity peaked at pH conditions typical of specific biological compartments of therapeutic interest (i.e. TME and endolysosomes) while remaining safely inactive in normal physiological conditions. pH-catalysed IONP degradation is a key feature to trigger drug delivery and reveal "stealth" bioactive properties of the vehicle.

- mIONP administration induced membrane lipid peroxidation and cell death, indicating cancer-specific sensitization to ferroptosis. IONzyme coupling to PUFA lipid peroxidation was proven to further potentiate its cancer cell killing features.

- mIONP-Pt enhanced Pt(IV) prodrug activation and increased cancer-specific cell killing suggestive of ferroptosis sensitization. mIONP-Pts were tolerated by macrophages, thus suggesting they can be used in immunotherapy strategies of cytotoxic macrophage activation and immune cell-mediated drug delivery. Antitumor cell killing discrimination was further enhanced by exploiting maltose-rich amphiphile incorporation onto the mIONP surface. These features are suitable to overcome the antioxidant protection provided by the lymph to metastasizing melanoma cells.

- Combination of TLRa delivery, ROS generation and DAMP-like hydrophobicity features in mIONP-TLRas were shown to induce strong antitumor immunity. mIONP-pIC-R837 systems triggered complete melanoma cell death while

maintaining high macrophage viability rates in *in vitro* co-cultures. Direct cell-to-cell contact between melanoma and macrophage cells was shown key to enable these effects. High TNFα and low IL-10 cytokine levels secreted by macrophages were indicative of cytotoxic activation. In synergy with antigen-presenting IONVs and antibody-based therapies, immunostimulatory mIONP-pIC-R837 administration achieved complete tumor regression of established and aggressive melanoma allografts and long-term protective immunity in vivo.

- Maleimide-thiol click-chemistry enabled stable, covalent surface particle functionalization for proof-of-concept development of immune checkpoint-targeting mIONP-aPDL1s and neoantigen-presenting IONVs with no observable functionality loss. mIONP-aPDL1s retained antibody binding activity and triggered cancer-specific cell death in complex *in vitro* co-cultures. A preliminary set of *in vivo* experiments showed that neoantigen-IONVs retained neoantigen immunogenicity and decreased cancer growth rates for established melanoma tumors in mice.

Therefore, two intriguing routes for future work are:

- Studies on the combination of Pt(IV) prodrug mIONP-enabled delivery (mIONP-Pt) with PUFA-enhanced ferroptotic properties. Both strategies, studied in Chapters II and V respectively, demonstrated very positive potential towards cancer cell death induction in the context of cancer immunotherapy. Their combination could provide for a further level of enhancement, as facilitated by the simple yet multifunctional mIONP nanoformulation rationale studied in this thesis.
- Studies on the long-distance administration of mIONP-DLin-NeoAs systems. When administered peritumorally, our IONV formulations demonstrated that the Neoantigen loaded onto the mIONP-based systems retained immunogenicity comparable to the unprocessed, naked neoantigen. By using a long-distance administration route, preferably subcutaneous, we expect to highlight the nanotechnology aspects of the formulation studied in Chapter IV (protection against early degradation, pH-catalysed disassembly, etc.) together with the potential NP-assisted lymphatic delivery as studied in Chapter III.

Chapter 7 . **Materials and Methods**

Laboratory consumables, chemicals and reagents

All commercially available reagents were used without further purification.

Synthesis of hydrophobic IONPs: Hexane (99%; LABSCAN), chloroform (water 0.005%; LABSCAN), diphenyl ether (99%; Sigma Aldrich), dibenzyl ether (>98%; Alfa Aesar), 1,2-hexadecanediol (>98%; Tokyo Chemical Industry Co. Ltd), oleic acid (90%; Alfa Aesar), oleylamine (70%; Sigma Aldrich), iron(III) acetylacetonate (99%; Strem Chemicals), ethanol (99%+; Fisher Chemical™). *Synthesis of citrate-coated IONPs:* Iron(II) chloride (tetrahydrate, 99+%), Iron (III) chloride hexahydrate (99%+), trisodium citrate dihydrate (99%) and ammonium hydroxide (35%) were purchased from Thermo Fisher Scientific. *Synthesis of mIONP nanovehicles:* 1,2-dipalmitoyl-sn-glycero-3-phosphoethanolamine-N-[methoxy(polyethylene glycol)-2000] (ammonium salt) (PEG-OMe), 1,2-distearoyl-sn-glycero-3-phosphoethanolamine-N-[carboxy(polyethylene glycol)-2000] (ammonium salt) (PEG-COOH), 1,2-dipalmitoyl-3-trimethylammonium-propane (chloride salt) (DOTAP or TAP), 1,2-distearoyl-sn-glycero-3-phosphoethanolamine-N-[amino(polyethylene glycol)-2000] (ammonium salt) (PEG-NH_2), 1,2-distearoyl-sn-glycero-3-phosphoethanolamine-N-[maleimide(polyethylene glycol)-2000] (ammonium salt) (PEG-MAL) lipids were purchased from Avanti Polar Lipids, Inc. Linoleic acid (99%) was purchased from Thermo Fisher Scientific, Dlin-mc3-dma (DLin; ≥ 98%) was purchased from Cambridge Bioscience. polyIC and R837 TLRas were purchased from InvivoGen. Disodium ethylenediaminetetraacetate (EDTA; dihydrate) was purchased from Merck. Neoantigens 1-B16-M27 (CSSREGVELCPGNKYEMRRHGTTHSLVIHD) and 1-B16-M30 (CSSPSKPSFQEFVDWENVSPELNSTDQPFL) were custom-synthetized (Shanghai RoyoBiotech Co.,Ltd). *Catalytic assays:* 3,3',5,5'-Tetramethylbenzidine (TMB; 98%) was purchased from Alpha Aesar (VWR), ortho-Phenylenediamine (OPD; 98%) from Sigma-Aldrich, Silver Nitrate ($AgNO_3$; 99.85%) Sodium Acetate (anhydrous) and hydrogen peroxide (H_2O_2; 30%) were purchased from Thermo Fisher Scientific. In vitro *experiments:* Phosphate buffer saline (PBS) were purchased from Life Technologies (Thermo Fisher Scientific). Erastin was purchased from Cayman Chemicals (Cambridge Bioscience, UK). Cell proliferation kit I (MTT) was purchased from Roche. Liperfluo® was purchased from Dojindo Molecular Technologies Inc. and Cumene Hydroperoxide

(80%) from Sigma-Aldrich. TNF-α ELISA kits were purchased from PeproTech. IL-10 ELISA kits were purchased from BioLegend. PD-L1 ELISA kit was purchased from Abcam. All fluorescently labeled antibodies were obtained from BioLegend unless specified otherwise. Thermo Scientific™ Pierce™ bicinchoninic acid (BCA) Protein Assay Kit was purchased from Thermo Fisher Scientific.

Instrumentation

Transmission Electron Microscopy (TEM)

TEM studies were conducted on a TEM JOEL 1400 electron microscope operating at 120 kV. The samples were prepared by depositing a drop of a solution of IONPs (0.5 mg/mL, 2 µL) onto a copper specimen grid coated with a holey carbon film and allowing it to dry. For IONP size determination using TEM, a minimum of 200 particles were measured using the *Image J* software. Secondary Transmission Electron Microscopy (STEM) characterization was kindly performed by Dr. S. Evans (Swansea University), following the same sample preparation.

DLS and zeta potential

Hydrodynamic diameter and zeta-potential of water soluble micelles were characterized with a NanoSizer (Malvern Nano-Zs, UK) at a particle concentration of [Fe] = 200 µM Particle size analysis was measured with a NanoSizer (Malvern Nano-Zs, UK) with 173° scattering angle at 25 °C. The correlation function was measured at least three times for each sample and the average value was used for data fitting. Zeta potential measurements were performed with the mentioned NanoSizer instrument at 25 °C with a cell drive voltage of 150 mV using a Smoluchowski model. Unless indicated, zeta potential samples contained 3.4 µM of NaCl. The results are shown as a mean of at least three measurements matching quality criteria.

UV-visible spectrophotometry

UV-visible absorption spectra were recorded on a NanoDrop™ One (ThermoFisher Scientific) and on Lambda 265/365 (Perkin Elmer) spectrophotometers. Absorbance measurement using Thermo Scientific Nunc™ 96-well microplates was performed on a

TECAN Infinite M Nano+ (LifeSciences) and on a POLARstar Omega (BMG Labtech) multifunction microplate readers.

Fourier-transformed infrared spectroscopy (FTIR)

IR spectra were recorded using a Spectrum two™ (PerkinElmer) spectrophotometer. Samples, solid or liquid, were scanned following manufacturer instructions. A background scan was always performed prior to data collection. Background-corrected data was analysed using Spectrum 10™ software (PerkinElmer).

Flow cytometry

Flow cytometry experiments were carried out in a NovoCyte Flow Cytometer (ACEA Biosciences) system. Samples were prepared and fluorescently labeled as specified in the methods section. All samples were finally resuspended in FACS buffer (1% FBS in PBS) prior to evaluation. Collected data was analysed using the FlowJo, LCC software. Cell populations were electronically gated based on the forward and side scatter parameters and the not-single events leaved out based on forward area and height scatter parameters. For data analysis, at least 10,000 events of the population of interest were acquired.

Every two weeks, the flow cytometer was calibrated using BD Cytometer and Tracking beads (BD Biosciences) following manufacturer instructions. Briefly, one drop of beads was added to 0.5 mL of PBS and the Quality Control program was initialized to verify instrument functionality.

High performance liquid chromatography (HPLC)

Reversed phase HPLC experiments were performed using PerkinElmer Altus™ HPLC system with an A-10 solvent and sample module and a A-10 photodiode array (PDA) detector. Experiment runs, methodology and data acquisition were operated using Empower® 3 software. All the samples in this work were run on a Brownlee SPP C-8 Column 150 mm x 4.6 mm ID (Perkin Elmer) using the settings specified in the methods section.

Fluorescence microscopy

Fluorescent cell imaging studies were performed using a Zeiss Axio Imager M1 microscope. The system was equipped with an HBO 103 mercury vapor short-arc lamp and a AxioCam MRm monochrome digital camera. Samples were prepared as specified in the methods section. The instrument was operated with AxioVision software. Images were processed on Zeiss Zen lite software.

Confocal laser scanning microscopy (CSLM)

Fluorescent cell imaging studies were also performed using a Carl Zeiss LSM 710 confocal microscope. The system was equipped with an HBO 100 mercury vapor short-arc lamp (Osram) and a QUASAR multichannel detector unit (Zeiss). Samples were prepared as specified in the methods section. Images were processed on Zeiss ZEN blue edition software.

Experimental Methods

Synthesis of IONPs

Synthesis of hydrophobic oleic-coated IONPs

Synthesis of the oleic acid-coated IONPs (magnetite; Fe_3O_4) was carried out following previously stablished methods of thermal decomposition[1,2]. $Fe(acac)_3$ (2 mmol), 1,2-hexadecanediol (10 mmol), oleic acid (6 mmol), oleylamine (6 mmol), and benzyl ether (20 mL) were mixed under nitrogen and constant stirring. The mixture was heated to 210 °C (5.7°C / min temperature increase), maintained for 2 h and then brought to 300 °C (3.2°C / min temperature increase) for 1 h. The product was cooled to room temperature by removing the heat source. Purification was performed under ambient conditions: Ethanol (40 mL) was added to the mixture, the material was precipitated and separated via centrifugation (3,000 x g, 30 min). The black pellet was dissolved in hexane (10 mL) containing oleic acid (0.05 mL) and oleylamine (0.05 mL). Centrifugation (3,000 x g, 10 min) was applied to remove any undispersed residue. The product, c.a. 7 nm Fe_3O_4 nanoparticles, was then precipitated with ethanol and isolated by centrifugation (3,000 x g, 10 min). The dried powder was stored at room temperature until use. The dried powder was redispersed in chloroform for TEM characterization or micelle formation.

High-resolution X-ray photoelectron spectroscopy (XPS) measurements were kindly performed by Dr. A Ruiz-de-Angulo (CIC BiomaGUNE, Spain) to determine the elemental composition of Fe_3O_4 nanoparticles.

Synthesis of hydrophilic citrate-coated IONPs (IONP-Cit)

Synthesis of hydrophilic citric acid-coated IONPs (IONP-Cit) followed previously stablished methods [3,4]. $FeCl_3 \cdot 6H_2O$ (6 mmol) and $FeCl_2 \cdot 4H_2O$ (3 mmol) were dissolved in distilled water (25 mL) under constant mechanical (non-magnetic) stirring. An excess of ammonium hydroxide (20 mL; 7.2 M) was added to reach strong basic aqueous pH (pH > 10). The reaction mixture leads to the immediate precipitation of a black solid product, the IONP. Citrate-coating was achieved following nanoparticle incubation with sodium citrate excess solution (100 mL; 1.0 M) at 90°C for 1 hour. The product was left to cool down to ambient temperature prior to purification. The material was first centrifuged (10,000 x g, 5 min) to remove large aggregates. Any remaining soluble impurities were removed after ultracentrifugation (3 cycles, 160.000 x g for 50 min) by discarding the supernatant. The nanoparticle pellet was resuspended in Milli Q water and stored at 4°C until use.

mIONP formation by dry film hydration methods

PEGylated IONP-filled micelles (mIONPs) were formed following well-stablished methods of amphiphilic self-assembly and dry-film hydration [5]. Typically, hydrophobic IONPs (1 mg) were dissolved in chloroform (500 μL) with experimentally optimized amounts of PEG-PLs, linoleic acid, DLin or glucose-rich amphiphiles as indicated in the discussion sections. The solvent was left to evaporate overnight at room temperature. Any remaining solvent was removed by placing the dried film under vacuum for 1 hour. The film was finally heated for 30 seconds at 80 °C and hydrated by adding 1 mL of nanopure MilliQ water. To maximize the yield of product formation, mIONPs were left to hydrate at room temperature for 2 h (vortexing gently every 20 minutes). Large aggregates were removed by centrifugation (1 cycle, 9,800 × g, 5 min) and the supernatant was passed through a 0.45 μm PTFE syringe-filter. Any remaining empty micelles were removed by ultracentrifugation (3 cycles, 160,000 g, 50 min) by discarding the supernatant.

For the formation of mIONP-Pt and mIONP-Pt-Malt nanovehicles (Chapter 3), PEG-Pt was kindly synthetized and characterized by Saul Michue Seijas (Ph.D candidate, Swansea University) and maltose-rich amphiphiles (Malt-T9) were a gift from Dr. Lubna Ghani (Hanyang University).

IONP-Lin formation by phase-transfer

Linoleic-coated IONP-filled micelles were formed following previously stablished methods of organic-to-aqueous phase transfer [6]. Oleic-coated IONPs were homogeneously dispersed in linoleic acid (10 mg/mL) and deposited on top of a 50 mM sodium linoleate aqueous solution (2:1 H_2O: EtOH). Under very gentle stirring, linoleate chains rearranged to coat the IONP-oleic particles in the interphase. Linoleic-coated IONP-filled micelles (IONP-Lin) transferred into the aqueous phase. Large aggregates were removed by centrifugation (1 cycle, 9,000 × g for 5 min). Removal of linoleic acid excess and solvent exchange to MilliQ H_2O is achieved after centrifugal spin-filter devices (5,000 g, 5 min; 50 kDa MWCO, Amicon).

Elemental analysis: Iron quantification

Iron content in suspension was quantified by UV-Vis spectrometry (Fig. 7.1, a). Although no absorbance peak can be clearly distinguished, light absorbance at 380 nm was selected for iron quantification. It was reasoned that this wavelength provided good absorbance intensity while avoiding potential interferences coming from proteins (220 nm and 280 nm), poly(I:C) (260 nm) or R837 (320 nm). Quantification by UV-Vis (Fig. 7.1, b) was calibrated to iron determined by inductively coupled plasma atomic emission spectroscopy (ICP-AES). ICP-AES experiments were kindly realized by Dr. Ane Ruiz de Angulo (CIC biomaGUNE, Spain).

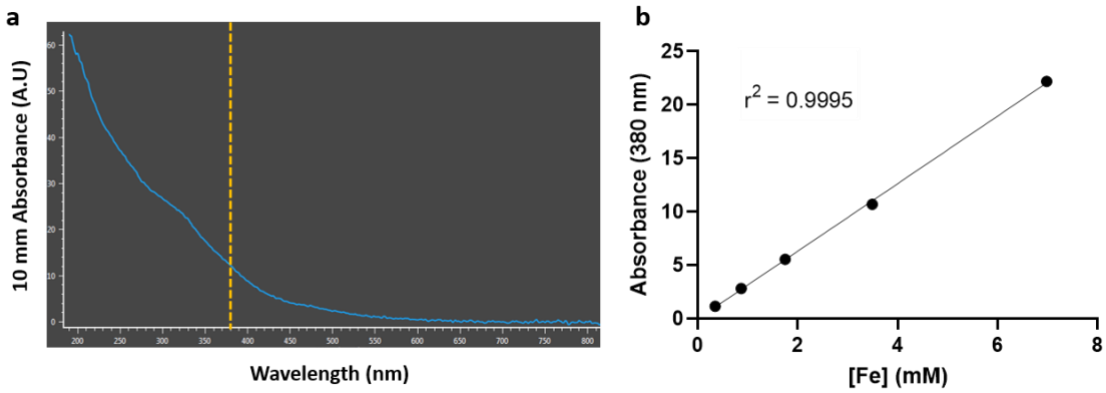

Figure 7.1. UV-Vis spectrometry for iron quantification. *(a) Typical UV-Vis absorbance spectra from IONP-based systems as recorded by a NanoDrop™ One. Yellow dashed lines indicate wavelength 380 nm and (b) [Fe] quantification fit curve.*

Nanoparticle calculations

The following calculations are described to approximate IONP content (magnetite; Fe_3O_4) from Fe concentration. In this work we used spherical hydrophobic IONPs with an average diameter of approximately 7.0 nm:

V (IONP) = $4/3 \cdot \pi \cdot r^3 = 4/3 \cdot \pi \cdot (3.5 \times 10^{-7})^3 = 1.8 \times 10^{-19}$ cm^3;
ρ (magnetite) = 5.17 g · cm^{-3}; m = ρ (magnetite) · V (IONP) = 9.29 x 10^{-19}g;
moles of Fe_3O_4 = m / MW (Fe_3O_4) = 9.25×10^{-19} / 231.5 = 4.01 x 10^{-21} mol
moles of Fe = 3 · moles of Fe_3O_4 = 3 · 4.01 x 10^{-21} = 1.20×10^{-20} mol
atoms of Fe per IONP = moles Fe in IONP · NA = $1.20 \times 10^{-20} \cdot 6.022 \times 10^{23}$ = 7244 atoms

Elemental analysis: Platinum quantification

Platinum loading in our mIONP samples was quantified following well established colorimetric methods [7]. The assay is based on the substitution of labile cis-chloride ligands in Pt(II)-complexes by OPD to yield Pt-OPD (the compound shows a strong absorbance peak at 706 nm). An aliquot of a Pt-containing sample was dissolved in 100 µL of DMF. Then, 50 µL of PBS and 500 µL of a fresh solution of 10 mg/mL of OPD in DMF were added. The mix was left to react overnight (for at least 12 h), at 80 °C under continuous stirring. The rection was carefully sealed to prevent solvent evaporation. Once cooled down, the absorbance of the solution was fit to a linear calibration curve

containing increasing amounts of platinum ([Pt] = 0 - 10 μM). Light absorbance was recorded at room temperature in a total volume of 650 μL contained in quartz cuvettes (HellmaTM; path length: 10 mm) using PerkinElmer UV/VIS Lambda 265 spectrophotometer and applying a 2-point baseline correction (600 and 800 nm). The absorbance of all samples was blanked to a Pt-less control. Platinum colorimetric quantification was calibrated to ICP-AES experiments kindly realized by Dr. Ane Ruiz de Angulo (CIC biomaGUNE, Spain).

Studies on IONP peroxidase-like catalytic activity

The peroxidase-like activity of the mIONPs was studied by monitoring the oxidation of TMB and OPD substrates by UV-Vis spectroscopy, which yield a blue (TMB^+ λ = 652 nm) and yellow (OPD^+ λ = 450 nm) product respectively.

The Michaelis Menten kinetics assays were conducted with mIONP ([Fe] = 150 μM) in sodium acetate buffer (pH = 4.5) and in the presence of different concentrations of H_2O_2 (ranging from 0.060 to 30.3 mM) and TMB (ranging from 33.0 to 830 μM). These assays were performed in sodium acetate buffer (0.1 M, pH = 4.5) in a total volume of 200 μL contained in 96-well plates. Unless specified, these assays were monitored at 37 °C using TECAN Infinite M Nano+ (LifeSciences) spectrophotometer.

The kinetic parameters were calculated fitting the absorbance data using Lineweaver–Burk plots of the Michaelis–Menten kinetics.

$$\frac{1}{v} = \frac{Km}{Vmax}\left(\frac{1}{[S]} + \frac{1}{Km}\right)$$

Where v is the initial velocity, Vmax is the maximal reaction velocity, [S] is the concentration of substrate and Km is the Michaelis constant and the turnover number (k_{cat}) was calculated as,

$$k_{cat} = \frac{\mathrm{Vmax}}{[\mathrm{E}]}$$

Where [E] stands for enzyme concentration, in this work approximated to nanoparticle concentration [IONP].

Kinetic studies comparing different formulations of IONPs ([Fe] = 150 μM for mIONPs; [Fe] = 550 μM for Ferumoxytol), free Fe ions leached after acidic digestion (pH = 4.5 for 40 min) and AuNPs ([Au] = 150 μM) nanocatalysts were monitored in sodium acetate buffer (0.1 M, pH= 4.5, 5.5, 6.6) or PBS (0.01 M, pH = 7.4). The studies used either TMB ([TMB] = 830 μM) or OPD ([OPD] = 3 mM) as UV-Vis substrates. These reactions were monitored at room temperature in a total volume of 500 μL contained in quartz cuvettes (HellmaTM; path length: 10 mm) using PerkinElmer UV/VIS Lambda 365 spectrophotometer in time-scan mode.

Catalytic assays (Ag^+-TMB) on PUFA enrichment of mIONPs

Qualitative PUFA enrichment of mIONPs was studied by monitoring the oxidation of the peroxidase substrate TMB in the presence of Ag^+ [8]. Unless specified, the absorbance variation was monitored in the presence of TMB ([TMB] = 830 μM) and silver ([Ag^+] = 175 μM) in sodium acetate buffer (0.1 M, pH = 4.5) in a total volume of 200 μL contained in 96-well plates. Concentrations were [Fe] = 150 μM for the mIONPs formulations. Unless specified, the reactions were monitored at 37 °C temperature using TECAN Infinite M Nano+ (LifeSciences) spectrophotometer.

Synthesis of P1-Tx amphiphiles and P1-Tx-IONP formation

Synthesis of P1-Tx amphiphiles followed previously stablished methods of hydrazone bioconjugation [9]. The materials required for the reaction were kindly provided by J. Montenegro (University of Santiago de Compostela; CiQUS): hydrazine-rich peptide backbone (P1) and aldehyde-terminated hydrophobic chains cyclohexane-carboxaldehyde (T1), benzaldehyde (T3), dodecanal (T20) and oleic aldehyde (T25). All materials were stored at 4°C until use.

4 μL of P1 peptide solution (2.5 mM in dry DMSO) were combined with 2 μL of the desired aldehyde-terminated hydrophobic chain Tx (20 mM in dry DMSO) and 2 μL of acetic acid (20%) in DMSO. The mixture was left to react at 60 °C for 2 h under constant stirring. The mix was finally cooled down to room temperature. The reaction was expected to be quantitative and thus the product, hydrazone-linked peptides (P1-Tx), did not require further purification [9]. P1-Tx hydrazone formation was performed only when ready to use.

P1-Tx-IONP formation followed previously described methods of dry film hydration. P1-Tx, IONPs and PEG-PLs were mixed in chloroform (0.5 mL) as indicated in the discussion sections. The solvent was then made to evaporate quickly under a gentle nitrogen flow at room temperature. Once the solvent evaporated, Milli-Q water or PBS were added at room temperature. Large aggregates were removed by centrifugation (1 cycle, 9,800 × g, 5 min) and the supernatant was passed through a 0.45 μm PTFE syringe-filter. Any IONP-free micelles were removed by ultracentrifugation (3 cycles, 160,000 g, 50 min) by discarding the supernatant.

mIONP-TLR self-assembly

mIONP-TLR formation followed previously described methods of electrostatic self-assembly [5,10,11]. Cationic DOTAP- or T1-containing mIONPs were used to capture anionic Poly(I:C) chains. Typically, an aliquot of mIONP stock solution ([Fe] = 3.6 mM of Fe, or [IONP] = 0.5 μM) were mixed with poly(I:C) (pIC concentrations as specified in the discussion sections) in 1mM PBS in MilliQ water. The mix was allowed to self-assemble overnight under gentle stirring (800 RPM; using a Grant Bio PCMT Thermoshaker) at room temperature. Unbound poly(I:C) excess was removed by ultracentrifuge (160,000 x g for 50 min). The nanoparticle pellet could be resuspended in aqueous buffer and stored at 4 °C until use. mIONP-PIC was used to capture positively charged small R837 molecules. An aliquot of mIONP-pIC stock solution was mixed with R837 (concentrations as specified in the discussion sections) in 1mM PBS in MilliQ water. Final ligand excess was removed by spin-filter filtration (3 cycles, 1,844 × g for 5 min) through a NanoSep centrifugal device (MWCO 100 kDa, Amicon) followed by ultracentrifugation (1 cycle, 160,000 x g for 50 min). The mIONP-pIC-R837 pellet could be resuspended in aqueous buffer and stored at 4 °C until use.

To quantify the bound TLRa, an aliquot of the TLR-decorated mIONP stock suspension was digested overnight using 0.2 M NaOH under gentle stirring at room temperature. The hydrolysed IONPs were removed by ultracentrifugation (160,000 x g for 50 min) to obtain a solution of free TLR ligands. UV−vis absorbance of this solution (λ = 260 nm for poly(I:C) and λ = 320 nm for R837) could be converted to concentration by comparison to a linear fit curve.

PD-L1 antibody surface thiolation

PD-L1 agonist (aPDL1) antibodies (Atezolizumab, Tecentriq) were a gift from Dr. Zsuzsanna Tabi (Cardiff University). The antibody surface was thiolated using 2-Iminothiolane (Pierce™ Traut's Reagent; Thermo Fischer Scientific). Following manufacturer instructions, aPDL1 and 2-Iminothiolane were mixed at a 1:10 molar ratio. The mix was left to react for one hour at room temperature, under gentle stirring (800 RPM) in PBS buffer (pH = 7.6) previously purged with N_2 for a few minutes to remove the dissolved oxygen and supplemented with 5 mM EDTA to avoid metal-induced thiol oxidation. 2-Iminothiolane excess was removed by spin-filtration (3 cycles of 1,000 x g, 3 minutes; Amicon, 100 kDa MWCO;) to avoid interferences during subsequent thiosuccinimide linkage formation.

Thiol-maleimide neoantigen and antibody bioconjugation to mIONPs

Thiolated structures (aPDL1 antibodies and neoantigens 1-B16-M27 and 1-B16-M30) were mixed with mIONP-Mal using concentrations indicated in the respective discussion sections. The mix was left to react overnight at room temperature, under gentle stirring (800 RPM) in PBS buffer (pH = 7.6) previously purged with N_2 for a few minutes to remove the dissolved oxygen and supplemented with 5 mM EDTA to avoid metal-induced thiol oxidation.

mIONP-aPDL1 were purified by spin-filtration (Amicon, 300 kDa MWCO) to remove EDTA and non-bound aPDL1 excess. Centrifugation conditions were optimized to minimize particle aggregation. Three cycles of buffer exchange were used, each divided into 4 sub-runs of 500 g for 3 min. After each sub-run, the sample was vortexed to minimize IONP-aPDL1 adherence onto the filter membrane.

mIONP-NeoAs were purified by ultracentrifugation (160,000 x g; 50 min) to remove EDTA and non-bound neoantigen excess. The supernatant (neoantigen excess) was stored for analysis and the pellet (mIONP-NeoAs) was resuspended in aqueous media with the help of gentle ultra-sonication (< 1 min).

Non-bound neoantigen quantification

Non-bound neoantigen excess collected during mIONP-NeoA purification was quantified by HPLC-UV/Vis (PerkinElmer Altus™ HPLC connected to a A-10 PDA). Samples were diluted in PBS and 10 µL were injected into the HPLC. Samples were run at room temperature on a Brownlee SPP C-8 Column 150 mm x 4.6 mm ID. Mobile phase solvents were (a) 0.1% trifluoroacetic acid (TFA; Thermo Fisher Scientific) in acetonitrile and (b) 0.1% TFA in Milli Q water. The separation was carried out during 32 min using the mobile phase gradient elution conditions specified in Table 7.1. Analyte peaks were identified by comparison with solutions of each individual compound: 1-B16-M27 (elution peak at 7.5 min) and 1-B16-M30 (elution peak at 14 min). Peak intensities were integrated and converted to concentration by comparison to a linear fit curve.

Table 7.1. Mobile phase gradient elution conditions

Elution minute	Acetonitrile 0.1% TFA	Milli Q H_2O 0.1% TFA
0	15%	85%
15	40%	60%
22	100%	0%
27	15%	85%
32	15%	85%

Total run: 32 min; 1 ml/min

Protein quantification (BCA)

Protein levels in a sample were measured using Thermo Scientific™ Pierce™ BCA Protein Assay Kits following manufacturer instructions. The samples were loaded in 96-well plates. The optical density was measured in a POLARstar Omega (BMG Labtech) microplate reader at 560 nm. A second-order polynomial fit curve was used to quantify the protein present from blank-corrected absorbances.

In vitro studies

Cell lines

Murine melanoma B16-F10(OVA) and murine macrophage RAW264.7 were kindly provided by Dr. Ane Ruiz de Angulo (CIC biomaGUNE). Cell culture media, Dulbecco's Modified Eagle Medium (DMEM), Roswell Park Memorial Institute (RPMI)-1640 medium, as well as media supplements, fetal bovine serum (FBS),

Penicillin/Streptomycin (P/S, 50 U/mL), L-glutamine (200 mM) were all purchased from Gibco (UK). Accutase® was purchased from Biolegend, UK, and trypsin-EDTA (0.05%) from Gibco (UK).

Cell counting

Isolated cells were diluted based on anticipated cell number and 10 µl of the diluted cell suspension were mixed with 10 µl of trypan blue (0.4%; Gibco). Cell counting was then performed by either (i) applying the mix to an Eve™ cell counting slide (Cambridge Bioscience) and into a Countess™ 3FL automated cell counter (Invitrogen); or (ii) manually counting cells in four 1 mm x 1 mm squares using a standard haemocytometer. The total live cell count (via trypan blue exclusion) was used for experimentation.

Monoculture cell viability studies (MTT)

The cells were seeded at 5×10^3 cells/well (seeding density of 1.6×10^4 cells/cm^2) in flat bottom 96-well plates and cultured for 24 h in 200 µL of complete medium. After removing the medium, cells were treated as specified in quadruplicate. Negative controls were treated with medium only. For final cell viability quantification, supernatant was removed and 50 µL of MTT reagent in complete medium (0.5 mg/mL) were added to the cells. The plate was incubated for 2 h at 37 °C. The supernatant was then discarded and 100 µL of DMSO were added to solubilize the formazan crystals. Finally, the optical density of the samples was measured in a POLARstar Omega (BMG Labtech) microplate reader at 550 nm. Unless specified, cell viability data is represented as the relative absorbance intensity to the negative control.

MTT studies on the susceptibility to ferroptosis for LC-2, MC-38, OVCAR8, PEO1, PEO4 and 4T1 cancer cell lines (see Chapter 5) were kindly performed by Ph.D. candidate Rhiannon Beadman (Swansea University).

Co-culture studies

Non-contacting co-cultures

RAW 264.7 macrophages were co-cultured with B16-F10(OVA) melanoma cells separated by a 0.4 µm pore-size membrane in transwell plates (24-well plate). RAW264.7

cells were seeded on the apical chamber of the transwell plate at a density of 2.5×10^5 cells/cm^2 and in a volume of 100 µL of complete DMEM medium. B16-F10(OVA) cells were seeded on the basolateral chamber of the well at a seeding density of 4.2×10^2 cells/cm^2 and in a volume of 600 µL of complete RPMI 1640 medium. The cells were allowed to grow to 100% confluence for 48 h (final media mix ratio RPMI-1640:DMEM = 7:1). After removing the medium, cells were treated as specified. Indirect cell-to-cell co-cultures were accompanied by mono-culture controls exposed to the corresponding treatments used in the co-culture. For mono-culture controls, 8×10^4 RAW 264.7 cells were seeded on the bottom of a 96-well plate (seeding density of 2.5×10^5 cells/cm^2) in a volume of 200 µL of media mix (RPMI-1640:DMEM = 7:1) and 8×10^4 B16-F10(OVA) cells were seeded on the bottom of a 24-well plate (seeding density of 4.2×10^2 cells/cm^2) in a volume of 700 µL of media mix (RPMI-1640:DMEM = 7:1). After treatment, supernatants were collected and stored at -20 ℃ for cytokine analysis.

Contacting co-cultures

B16-F10(OVA) melanoma cells were seeded in 96-well plates at a density of 1.8×10^5 cells/cm^2 in a volume of 200 µL. After 24 h, B16-F10(OVA) formed a confluent monolayer and 8.5 x 10^4 RAW264.7 macrophage cells were seeded on top (seeding density of 2.7×10^5 cells/cm^2) in a volume of 100 µL. They were allowed to adhere for 2 h in complete medium (media mix ratio of RPMI-1640 : DMEM = 7:1). Medium was removed and fresh RPMI-1640 medium was added for 30 minutes to stabilize the cells. Finally, medium was removed and treatment was added as specified. Due to the small number of cells employed in each well, every treatment was performed in triplicate. Detached cells were pooled together for subsequent Flow Cytometry experiments. Supernatants were collected and stored at - 20 ℃ for cytokine analysis.

Contacting co-culture development

The contacting co-culture model was developed to: (i) to obtain a homogeneous monolayer of B16-F10(OVA) at the time of treatment to minimise uneven drug-distribution; and (ii) to obtain a macrophage-to-melanoma cell ratio of approximately 1:3 to 1:2, which corresponds to the relative macrophage-to-cancer cell presence observed in human tumors [12,13].

The obtention of a homogeneous B16-F10(OVA) melanoma monolayer was assessed using fluorescent microscopy and well-stablished methods of cell staining [14]. A first screening used 10,000-250,000 cell/cm^2 cell seeding densities. The cells were seeded on top of a retriable transwell membrane (surface equivalent to 96-well plate, 0.33 cm^2). After a 24-hour incubation, the cells were washed two times with PBS and fixed with paraformaldehyde (5% in PBS; 15 minutes at room temperature). Fixed cells were then washed two times with PBS and permeabilized with 2-[4-(2,4,4-trimethylpentan-2-yl)phenoxy]ethanol (Triton X-100) (0.2% in PBS; 15 minutes at room temperature). Fixed and permeabilized cells were finally washed two times with PBS. To visualize the cell layer, the transwell membrane was retrieved and nuclear staining was performed using Vectashield® mounting solution containing 4′,6-diamidino-2-phenylindole (DAPI) (abcam; staining for 45 minutes at room temperature). Our results indicated that only the highest seeding densities (above 150,000 cell/cm^2) provided a completely confluent layer of melanoma cells (Fig. 7.2, a-d). A narrower range of B16-F10(OVA) seeding densities between 150,000-250,000 cell/cm^2 was used to optimize cell seeding number. This time, intracellular actin filaments of the cytoskeleton were stained using Phalloidin Red (Biolegend; 1:20 working dilution; staining for 45 minutes at room temperature after permeation). Cells were mounted using Vectashield® mounting solution (abcam) and observed using confocal fluorescent microscopy. Cell seeding densities larger than >190,000 cell/cm^2 showed increasingly rough cell surfaces with large cell clumps (Fig. 7.2, e-h). Therefore, B16-F10(OVA) seeding densities of 170,000 cell/cm^2 were shown optimal for the obtention of a homogeneous monolayer after a 24 h incubation.

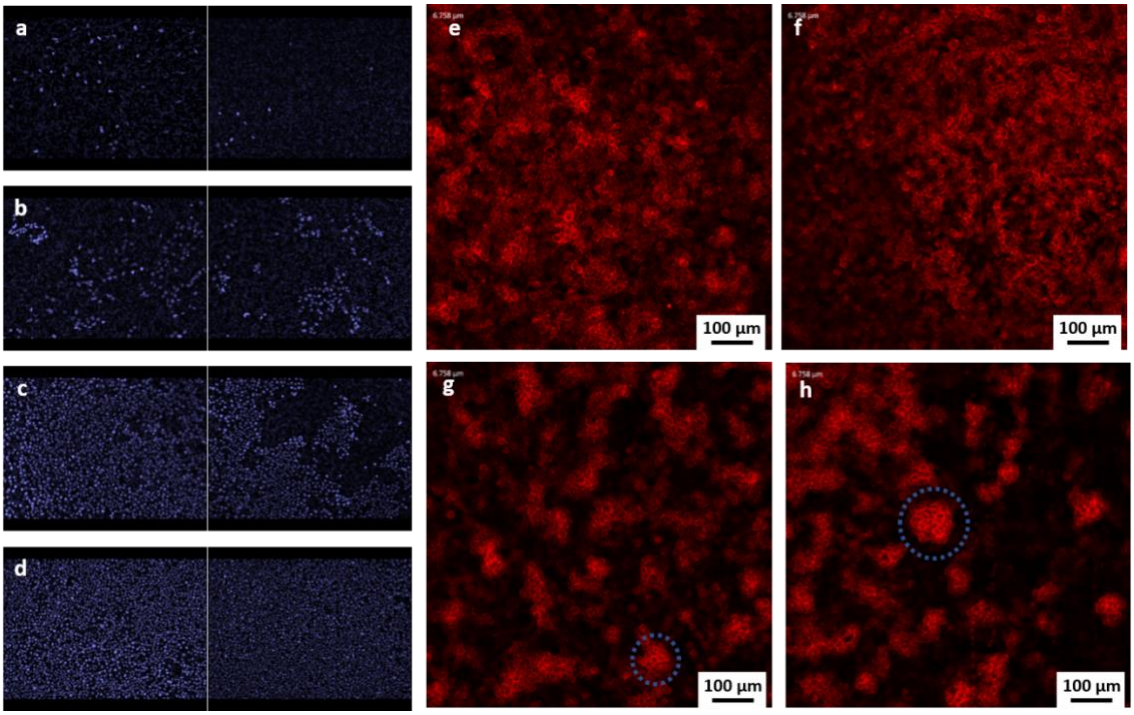

Figure 7.2. Fluorescent imaging of melanoma monolayers at the time of treatment. *(a-d) 2-fold fluorescent image sets of B16-F10-OVA melanoma cells stained with DAPI at cell seeding densities: (a) 10 x 10^3 cell/cm^2; (b) 40 x 10^3 cell/cm^2; (c) 150 x 10^3 cell/cm^2; (d) 250 x 10^3 cell/cm^2. (e-h) Confocal fluorescent imaging of B16-F10-OVA melanoma cells Phalloidin Red at cell seeding densities: (e) 150 x 10^3 cell/cm^2, (f) 170 x 10^3 cell/cm^2; (g) 210 x 10^3 cell/cm^2; (h) 250 x 10^3 cell/cm^2. Multi-layered cell clumps observed at same objective height (6.75 µm) are indicated inside blue intermittent lines. DAPI (365/448 nm) staining and Phalloidin Red staining (590/615 nm) were recorded using corresponding excitation lasers and detection filters.*

B16-F10(OVA) were seeded onto a 96-well plate at 170,000 cell/cm^2 and incubated for 24 h. The cells were then detached using 100 µL of accutase® or trypsin-EDTA and counted, resulting 88,300 ± 10,500 cells (Fig. 6.3). To optimize RAW264.7 cell seeding number, the macrophages were seeded onto a 96-well plate at cell densities ranging between 85,000 – 303,000 cell/cm^2. After 120 minutes, the supernatant was discarded and the remaining macrophages were detached and counted (Fig. 7.3). A RAW264.7 cell seeding density of 260.000 cell/cm^2 was shown to achieve 40 ± 5% of attached macrophages to melanoma at the time of treatment.

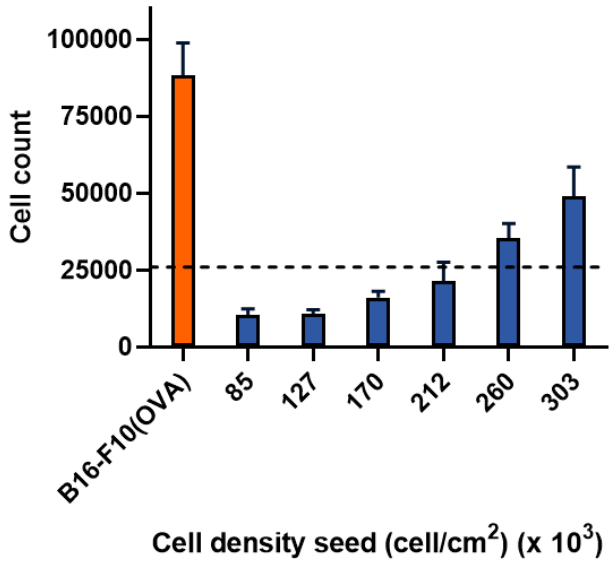

Figure 7.3. Total number of adhered RAW264.7 cells. *Murine macrophage 264.7 cells were seeded at the specified seeding censities and left to adhere onto the surface of a 96-well for 120 minutes. The cells were then detached and counted. Orange bar represents the cell number for B16-F10-OVA melanoma cells. Dashed lines represent the low-end objective of relative number of macrophages to melanoma cells (30%). Data shown as mean ± SEM (N=2).*

Flow cytometry studies

Cell viability

Cell viability assessment after treatment was conducted by Flow Cytometry. After treatment, RAW 264.7 and B16-F10(OVA) cells were detached using 100 µL of accutase® or trypsin. After 5 min at room temperature, the detachment solutions were neutralized with 100 µL of complete media. The resulting cell suspensions were washed with PBS and stained with 50 µL of Zombie NIR™ diluted 1:100 in PBS over 45 min at 4° C in the dark. For differentiation between RAW 264.7 from B16-F10(OVA), cells were then washed with 0.1.% BSA in PBS (and stained with Brilliant Violet-labeled anti-F4/80 antibody diluted 1:200 in the same buffer. Finally, the cell suspensions were washed with FACS buffer (1% FBS in PBS) by centrifugation (3 cycles, 800 g, 4 min) and suspended in 300 µL of the same buffer. Positive controls for necrotic cell death were heated to 80° C for 3 min prior to staining. Using a NovoCyte Flow Cytometer (ACEA Biosciences), cell populations were gated based on the forward and side scatter

parameters and the not-single events leaved out based on forward area and height scatter parameters (FlowJo, LCC software). Differentiation between cells was based on F4/80-positive fluorescent (fluorescent Pacific Blue channel, 445 nm). Necrotic cell populations were gated based on Zombie NIR™ positive fluorescent staining (fluorescent APC-Cy7 channel, 780 nm) (Fig. 7.4).

Flow cytometry studies on bone marrow-derived macrophage polarization and viability (see Chapter 3) were kindly performed by Arnold J. group in King´s College London (UK).

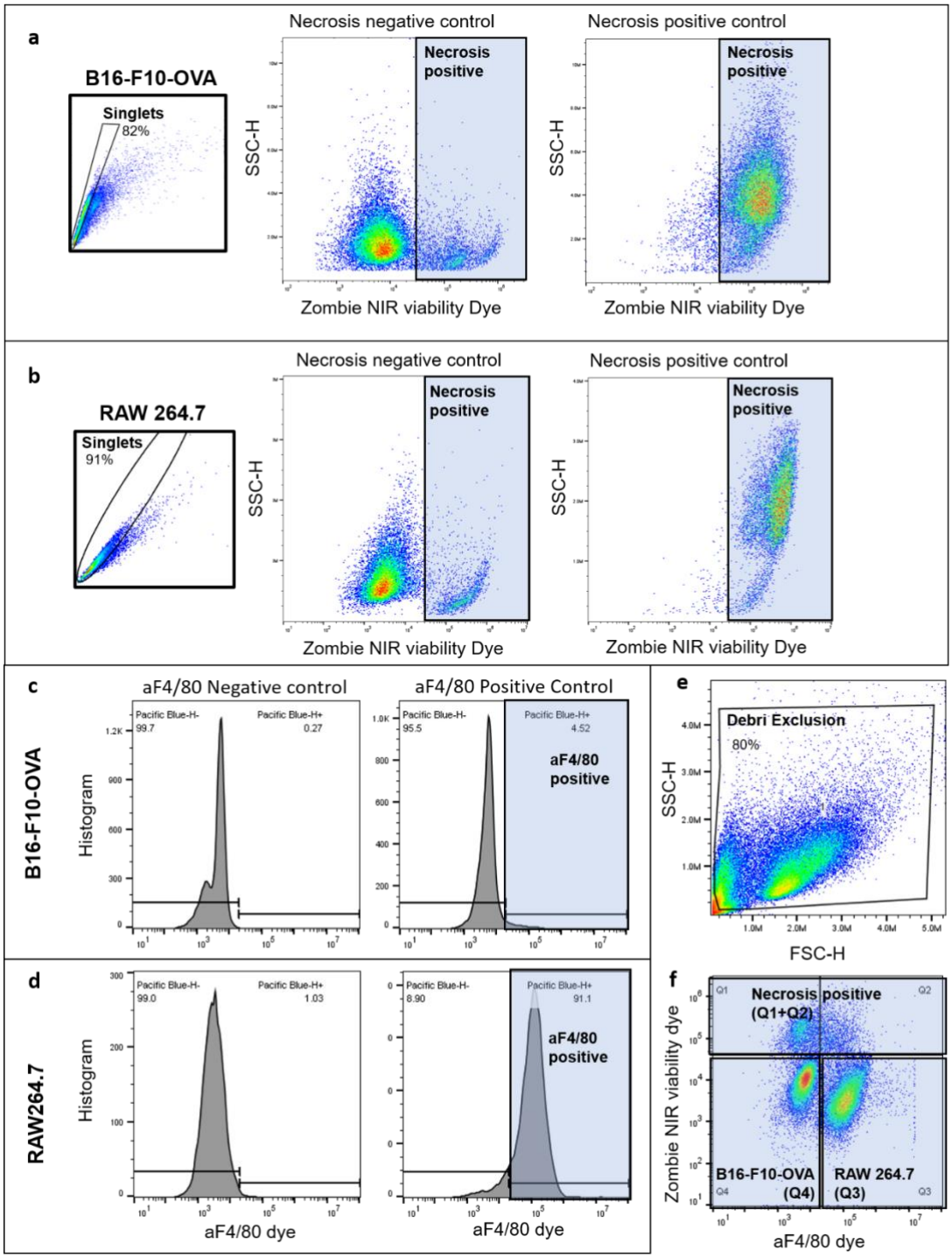

Figure 7.4. Cell gating strategy employed in this work. *(a-b) B16-F10-OVA and RAW263.7 murine melanoma cell line gating strategy for singlet discrimination and necrosis fluorescent staining; (c-d) B16-F10-OVA and RAW264.7 gating strategy for cell-line discrimination as negative and positive aF4/80 fluorescent staining, (e), Small debri exclusion prior to cell sorting; (f), Final gating strategy (2D) for direct cell-to-cell contact co-culture set-up.*

Membrane lipid peroxidation analysis in live cells

Lipid hydroperoxide accumulation after treatment could be revealed by Flow Cytometry. After treatment, supernatant was removed and cells were stained using Liperfluo® (10 μM) or DMSO vehicle control (1%) and incubated 30 min (at 37 °C, 5% CO_2). As a positive control for lipid peroxides, cells were incubated with Cumene Hydroperoxide (100 μM) in complete RPMI for 2 h at 37 °C, 5% CO_2 prior to Liperfluo® addition. Cells were detached using 100 μl accutase® and Flow cytometry sample preparation followed the steps described above. After not-single events were leaved out, differentiation between cells was based on lipid hydroperoxide-positive fluorescent staining (fluorescent Pacific Orange channel, 572 nm).

Quantification of IL-10, PD-L1 and TNF-α cytokines by ELISA

Cytokine levels were measured in cell supernatants using sandwich ELISA following manufacturer instructions. The optical density was measured in a POLARstar Omega (BMG Labtech) microplate reader at 450-550 nm. A 4-parameter sigmoidal (logistic) standard curve was used to quantify the cytokine present (GraphPad Prism software). Results are expressed as mean ± SEM in pg/mL or ng/mL, compared to untreated control wells. PD-L1 ELISA quantification was kindly performed by Saul Michue Seijas (Ph.D. candidate; Swansea University).

In vivo studies

All *in vivo* studies included in this work were kindly performed by Dr. Ane Ruiz-de-Angulo (CIC biomaGUNE, Spain) by Dr. Ane Ruiz-de-Angulo and Dr. Jordi Llop's research group at CIC biomaGUNE (Spain).

Statistical analysis

Data presented as mean ± SEM. The differences between the control and the experimental groups were assessed using two-tailed unpaired Student's t tests and the differences among groups > 2 by one-way ANOVA (GraphPad Prism, GraphPad Software, La Jolla, CA). Statistical significance was set at *$p < 0.05$; **$p < 0.01$; $p < 0.001$.

References

(1) Sun, S. et al. Monodisperse MFe2O4 (M = Fe, Co, Mn) Nanoparticles. *J. Am. Chem. Soc.* **2004**, *126* (1), 273–279. https://doi.org/10.1021/ja0380852.

(2) Blanco, N. G. et al. Iron Oxide-Filled Micelles as Ligands for Fac-[M(CO)3]+ (M = 99mTc, Re). *Chem. Commun.* **2012**, *48* (35), 4211–4213. https://doi.org/10.1039/c2cc31045g.

(3) Sahoo, Y. et al. Aqueous Ferrofluid of Magnetite Nanoparticles: Fluorescence Labeling and Magnetophoretic Control. *J. Phys. Chem. B* **2005**, *109* (9), 3879–3885. https://doi.org/10.1021/jp045402y.

(4) Saraswathy, A. et al. Citrate Coated Iron Oxide Nanoparticles with Enhanced Relaxivity for in Vivo Magnetic Resonance Imaging of Liver Fibrosis. *Colloids Surfaces B Biointerfaces* **2014**, *117*, 216–224. https://doi.org/10.1016/j.colsurfb.2014.02.034.

(5) Carion, O.; Mahler, B.; Pons, T.; Dubertret, B. Synthesis, Encapsulation, Purification and Coupling of Single Quantum Dots in Phospholipid Micelles for Their Use in Cellular and in Vivo Imaging. *Nat. Protoc.* **2007**, *2* (10), 2383–2390. https://doi.org/10.1038/nprot.2007.351.

(6) Wu, L. et al. A General and Facile Approach to Disperse Hydrophobic Nanocrystals in Water with Enhanced Long-Term Stability. *J. Mater. Chem. C* **2017**, *5* (12), 3065–3071. https://doi.org/10.1039/c7tc00586e.

(7) Golla, E. D.; Ayres, G. H. Spectrophotometric Determination of Platinum with O-Phenylenediamine. *Talanta* **1973**, *20* (2), 199–210. https://doi.org/10.1016/0039-9140(73)80267-X.

(8) Zhang, F.; Wang, X.; Jie, X.; Wei, W. Test Paper for Colorimetric Inspection of Fatty Acids and Edible Oils. *Sensors (Switzerland)* **2018**, *18* (10), 3252. https://doi.org/10.3390/s18103252.

(9) Louzao, I.; García-Fandiño, R.; Montenegro, J. Hydrazone-Modulated Peptides for Efficient Gene Transfection. *J. Mater. Chem. B* **2017**, *5* (23), 4426–4434. https://doi.org/10.1039/c7tb00179g.

(10) Ruiz-De-Angulo, A.; Zabaleta, A.; Gómez-Vallejo, V.; Llop, J.; Mareque-Rivas, J. C. Microdosed Lipid-Coated 67Ga-Magnetite Enhances Antigen-Specific Immunity by Image Tracked Delivery of Antigen and Cpg to Lymph Nodes. *ACS Nano* **2016**, *10* (1), 1602–1618. https://doi.org/10.1021/acsnano.5b07253.

(11) Bocanegra Gondan, A. I. et al. Effective Cancer Immunotherapy in Mice by PolyIC-Imiquimod Complexes and Engineered Magnetic Nanoparticles. *Biomaterials* **2018**, *170*, 95–115. https://doi.org/10.1016/j.biomaterials.2018.04.003.

(12) Gauci, C. L.; Alexander, P. The Macrophage Content of Some Human Tumours.

Cancer Lett. **1975**, *1* (C), 29–32. https://doi.org/10.1016/S0304-3835(75)94826-0.

(13) Qiu, S. Q. et al. Tumor-Associated Macrophages in Breast Cancer: Innocent Bystander or Important Player? *Cancer Treat. Rev.* **2018**, *70*, 178–189. https://doi.org/10.1016/j.ctrv.2018.08.010.

(14) Stadler, C.; Skogs, M.; Brismar, H.; Uhlén, M.; Lundberg, E. A Single Fixation Protocol for Proteome-Wide Immunofluorescence Localization Studies. *J. Proteomics* **2010**, *73* (6), 1067–1078. https://doi.org/10.1016/j.jprot.2009.10.012.

Published papers, Conferences and Research Experience

Publications

[1] *Chemically Programmed Vaccines: Iron Catalysis in Nanoparticles Enhances Combination Immunotherapy and Immunotherapy-Promoted Tumor Ferroptosis*. Ane Ruiz-de-Angulo, **Marc Bilbao-Asensio**, James Cronin, Stephen J. Evans, Martin J.D. Clift, Jordi Llop, Irene V.J. Feiner, Rhiannon Beadman, Kepa Zamacola Bascarán, Juan C. Mareque-Rivas. iScience (2020), 23 (9), 101499

[2] *Dinaciclib, a Bimodal Agent Effective against Endometrial Cancer.* David Howard, David James, Kate Murphy, Jezabel Garcia-Parra, Belen Pan-Castillo, Stuart Rex, Annemarie Moul, Eilir Jones, **Marc Bilbao-Asensio,** Saul Michue-Seijas, Kerryn Lutchman-Singh, Lavinia Margarit, Lewis W. Francis, Paul Rees, Deyarina Gonzalez and R. Steven Conlan. Cancers (2021), 13(5), 1135.

Conferences

[1] **M. Bilbao-Asensio**, Chemically programmed iron oxide-loaded nanovaccines for cancer immunotherapy. **Early Career Researcher Summer 2021 - British Society for Nanomedicine**, 2021, virtual meeting. (**Oral Presentation**)

[2] **M. Bilbao-Asensio**, Design, synthesis and evaluation of nanosystems for cancer immunotherapy. **Chemistry Department Research Seminar Series 2019-2020**, 2019, Swansea. (**Oral Presentation**)

Research experience during the PhD

Host institution: CIC biomaGUNE (Donostia, Spain)
Host investigator: Prof. Juan Mareque-Rivas
Period: 15-19, October, 2017

Funding Agency

Funding body: EPSRC (UK)
Project Reference: 2105067 (related to EP/N509553/1)
Period: 01/10/2017 to 30/09/2021